Dynamics and Evolution of Supermassive Black Holes in Merging Galaxies

Fazeel Mahmood Khan

Astronomisches Rechen-Institut

Zentrum für Astronomie der Universität Heidelberg

Heidelberg 2011

Cover picture: Gemini image of NGC 5426-27 (Arp 271).

Dissertation
submitted to the
Combined Faculties for the Natural Sciences and for Mathematics
of the Ruperto-Carola University of Heidelberg, Germany
for the degree of
Doctor of Natural Sciences

Put forward by
Fazeel Mahmood Khan
Born in: Azad Kashmir, Pakistan
Oral examination: January 25, 2012

Dynamics and Evolution of Supermassive Black Holes in Merging Galaxies

Referees: PD Dr. Andreas Just

         Prof. Dr. Volker Springel

Abstract

Supermassive black holes (SMBHs) are ubiquitous in galaxy centers and are correlated with their hosts in fundamental ways, suggesting an intimate link between SMBH and galaxy evolution. In the paradigm of hierarchical galaxy formation this correlation demands prompt coalescence of SMBH binaries, presumably due to dynamical friction, interaction of stars and gas with the binary and finally due to gravitational wave emission. If they are able to coalesce in less than a Hubble time, SMBH binaries will be a promising source of gravitational waves for gravitational wave detectors. However, it has been suggested that SMBH binaries may stall at a separation of 1 parsec. This stalling is sometimes referred to as the "Final Parsec Problem (FPP)". This study uses N-body simulations to test an improved formula for the orbital decay of SMBHs due to dynamical friction. Using a large set of N-body simulations, we show that the FPP does not occur in galaxies formed via mergers. The non spherical shape of the merger remnants ensures a constant supply of stars for the binary to interact with. On its way to coalescence, the SMBH binary ejects several times its total mass in stars and leads to the formation of the cores observed at the center of giant ellipticals. The results of this study also support a cosmological scenario where the prompt coalescence of SMBHs following galaxy mergers is common and where SMBH binaries are promising sources of gravitational waves at low and high redshifts.

Zusammenfassung

In vielen Galaxienzentren werden Supermassive Schwarze Löcher (SMBHs) detektiert. Ihre Massen korrelieren mit unterschiedlichen Eigenschaften dieser Galaxien, was als enge Verbindung in der Entwicklung der SMBHs und Galaxien interpretiert werden kann. Im Bild der hierarchischen Galaxienentstehung erfordert diese enge evolutionäre Koppelung ein schnelles Verschmelzen von Doppel-SMBHs, vermutlich verursacht durch dynamische Reibung, die Wechselwirkungen des Doppelsystems mit Sternen bzw. Gas und im finalen Stadium durch Abstrahlung von Gravitationswellen. Würden die Doppel-SMBHs schneller als in einer Hubble-Zeit verschmelzen, wären sie eine vielversprechende Quelle von Gravitationswellen für die entsprechenden Detektoren. Jedoch wird vermutet, dass die Entwicklung der Doppel-SMBHs bei Abständen von ungefähr einem Parsec zum Erliegen kommt. Dieser Effekt wird manchmal auch als "Finales Parsec Problem" (FPP) bezeichnet. In dieser Arbeit nutzen wir N-Körper-Simulationen für eine erweiterte Beschreibung des Herabsinkens von SMBHs als Folge dynamischer Reibung. Mit einer Vielzahl von N-Körper-Simulationen zeigen wir, dass das FPP in Galaxien, die durch Verschmelzungen entstehen, nicht auftritt. Die Abweichung von der Kugelsymmetrie der aus der Verschmelzung neu gebildeten Galaxie sorgt für einen kontinuierlichen Nachschub an Sternen, die mit dem SMBH-Doppelsystem wechselwirken. Auf dem Weg zu ihrer eigenen Verschmelzung schleudern die Doppel-SMBHs Sterne mit einem Vielfachen ihrer eigenen Masse aus der Galaxie heraus, wodurch sich flache Dichteprofile bilden, wie sie häufig in elliptischen Galaxien beobachtet werden. Die Ergebnisse dieser Arbeit unterstützen kosmologische Szenarien, in welchen das rasche Verschmelzen von SMBHs üblicherweise sowohl bei niedrigen als auch bei hohen Rotverschiebungen nach einer Galaxienverschmelzung eintritt und in denen Doppel-SMBHs eine vielversprechende Quelle von Gravitationswellen sind.

To my parents

Contents

List of Acronyms

AGN   Active Galactic Nuclei

BH   Black Hole

DF   Distribution Function

FPP   Final Parsec Problem

GW   Gravitational Wave

HST   Hubble Space Telescope

IMBH   Intermediate Mass Black Hole

IMF   Initial Mass Function

Λ CDM   Lambda Cold Dark Matter

PDF   Probability Distribution Function

POPIII   Population III

PTA   Pulsar Timing Array

SMBH   Super Massive Black Holes

VLBA   Very Long Base-line Array

Chapter 1

Introduction

Black holes are one of the most exotic predictions of physics described by Einstein's Theory of General Relativity (GR). In GR matter and energy cause spacetime curvature and the black holes which are the densest masses in the Universe are the objects of spacetime wrapped around themselves. Indirect astronomical observational evidence support that the astrophysical black holes exist in three mass ranges: stellar mass black holes (BH), having masses of 4-15 $M_\odot$, are formed as the end product of stellar evolution of massive stars for a wide range of stellar masses and metallicities. Intermediate mass black holes (IMBH), with masses $\sim 10^2 - 10^4$ $M_\odot$, are suggested to have been formed by the collapse of population III (PopIII) stars (Rees 1984, Madau & Rees 2001) or by runaway mergers of very massive stars in the center of dense stellar clusters (Portegies Zwart & McMillan 2002, Portegies Zwart et al. 2004, Gürkan et al. 2004). Supermassive black holes (SMBH), with masses ranging from $10^5 - 10^9$ $M_\odot$ reside at the center of massive galaxies. SMBH are suggested to grow to these enormous masses by starting as a seed black hole of few hundred solar masses as a remnant of a PopIII star and then accretion plays vital role in the growth of supermassive black hole. In another scenario a SMBH can form as the end product of dynamical instabilities setting in massive gaseous protogalactic disks (Koushiappas et al. 2004, Begelman et al. 2006, Volonteri & Begelman 2010) or in the mergers of gas rich disk galaxies (Mayer et al. 2010). Mergers between SMBHs can also assist the mass growth of black holes.

The idea of supermassive black holes was proposed in 1960s to explain the enormous luminosities of quasars (Salpeter 1964, Zel'Dovich & Novikov 1964). Quasars, the most powerful sources of energy in the universe, are believed to be powered by accretion of gas and stars onto SMBHs. This idea has also been generally accepted for the explanation of radiation and jets emission from all active galactic nuclei (AGN). The existence of SMBHs is now firmly established by measurements of velocities of stars and gas which have Keplarian rise near the centers of galaxies. Observations of distant quasars (redshift greater than 6) suggest that SMBHs with masses of up to a billion solar masses were already in place at the centers of galaxies in the first billion years after the Big Bang (Fan 2006). The presence of the SMBH at the center of a galaxy is correlated with the dynamics of its stellar component. There is a tight correlation between the mass of the SMBH and the central velocity dispersion of stars, the $M_\bullet - \sigma$ relation (Ferrarese & Merritt 2000, Gebhardt et al. 2000, Gültekin et al. 2009). Similarly the bulge or spheroid luminosity is correlated with the mass of the SMBH. These tight correlations indicate that the growth of the SMBH and its host galaxy are tightly interwined. Hence an understanding of the evolution of of SMBHs can assist to understand the evolution of the galaxies.

Dynamical friction causes orbital decay of satellite galaxies in the halo of larger galaxies. It is also responsible for star clusters and SMBHs sinking to the centers of galaxies. The cosmological growth of massive central black holes from minor and major mergers depends sensitively on dynamical friction of satellite galaxies and massive black holes in a background of stars and dark

matter. Dynamical friction can be seen as the drag induced on a massive body (satellite galaxy, star cluster, SMBH etc.) by the over-density raised behind the massive body due to the deflection of stars which interact with it. The principles of dynamical friction theory were formulated by Chandrasekhar in his classical work in 1943. Chandrasekhar assumed an infinite, homogeneous and isotropic background stellar distribution in which the massive body moves. The singularity at large impact parameters is cut off by the use of a so-called Coulomb logarithm $\ln \Lambda$ which is the ratio of maximum to minimum impact factors. Also all contributions to the dynamical friction force come from the stars moving slower than the massive body. The contributions to the dynamical friction force from particles moving faster than massive body cancel out due to symmetry. Despite these assumptions, dynamical friction theory has worked remarkably well in wide range of astrophysical situations since it was first formulated. The error made by the first assumption is usually absorbed by fitting a certain numerical value of the Coulomb logarithm to the results of numerical simulations; such a method has been very successful in plasma physics (Rosenbluth et al. 1957), star cluster dynamics (Spitzer 1987) and galactic dynamics (Weinberg 1989, Spinnato et al. 2003, Antonini & Merritt 2011). In order to determine the fraction of slow stars when compared to the motion of the massive body, a Maxwellian velocity distribution is adopted for the stars. There are two developments which have caused renewed interest in more accurate theoretical determinations of dynamical friction. One is the realization (both from theoretical structure formation models and Hubble Space Telescope (HST) observations of galaxy cores) that the cores of most galaxies in the standard picture of hierarchical structure formation are embedded in cuspy distributions of dark matter (Lauer et al. 1995, Navarro et al. 1997). This means that in many galaxies the density profile of the dark matter, which is the main background for dynamical friction of dwarf galaxies, star clusters and compact objects is nowhere constant as assumed in the standard Chandrasekhar theory. This problem has led to the suggestion of an empirical variation of the Coulomb logarithm with radius, so as to account for the different efficiency of dynamical friction (Tremaine 1976, Hashimoto et al. 2003, Peñarrubia et al. 2004). Secondly numerical investigations have identified few cases in which Chandrasekhar's dynamical friction theory appears to break down. These include the inspiral of the massive body in constant density (harmonic) cores (Hernandez & Gilmore 1998, Read et al. 2006, Inoue 2009), deceleration of rotating stellar bar (Weinberg 1985) and orbital evolution of SMBH in the core of galaxies (Gualandris & Merritt 2008, Just et al. 2011).

In the paradigm of Λ Cold Dark Matter (Λ CDM) cosmology, galaxies are formed via hierarchical merging. Galaxies grow in size and mass through the agglomeration of smaller galaxies. If both merging galaxies contain SMBHs at their centers then the two black holes will form a binary SMBH system in the merged galactic nucleus (Begelman et al. 1980). There are cases in which there is clear observational evidence for two widely separated SMBHs as well as some circumstantial evidence for a true SMBH binary (for detailed review see Komossa (2006)).

SMBH binary evolution, after the merger of the two galaxies, consists of three distinct phases (Begelman et al. 1980). First, the two SMBHs sink towards the center due to the dynamical friction exerted by the stars and the dark matter. Dynamical friction acts together with the "gravitational slingshot effect" as SMBHs form a bound pair. Dynamical friction stops being an effective driver of inspiral when the binary reaches a separation where the enclosed mass inside the binary orbit is much smaller than binary's mass itself. In the second phase, *slingshot* ejection of stars is the dominant mechanism for removing energy and angular momentum from the SMBH binary. The stars plunging into the orbit of SMBH binary are ejected with velocities compared to the binary's orbital velocity. Thirdly, if the binary eventually reaches a separation at which the loss of orbital energy due to gravitational wave (GW) emission becomes the dominant mechanism in extracting the binary's remaining energy and angular momentum , the two SMBHs will finally coalesce. It is also possible, however, that coalescence is delayed, perhaps for much longer than a Hubble time, if the massive binary is limited in its ability to exchange angular momentum with surrounding stars and gas.

With the rapid development in computer power, massive parallelization and special purpose hardware developed to run numerical codes efficiently, numerical modeling of astrophysical objects has become, "third pillar" of astrophysics beside pure theory and observations. Big supercomputer have become laboratories for astrophysicists to understand the formation and evolution of stars, galaxies and structures on a cosmological scale. In the past decade several numerical simulations have been carried out to study the dynamics of SMBHs at the center of galaxies (Makino 1997, Milosavljević & Merritt 2001, Makino & Funato 2004, Berczik et al. 2005, 2006, Merritt 2006*b*, Berentzen et al. 2009). It has been found that dynamical friction is very efficient in bringing two SMBHs close to form a binary, but the subsequent evolution, which is governed by the individual stars interacting with the massive binary, depends on number of the particles N used to represent the galaxy in these simulations (Makino & Funato 2004, Berczik et al. 2005). The maximum number of particles used in these studies is still several orders of magnitude less than the total number of stars in real galaxies and the results of these studies which depend on particle number, cannot be extrapolated to real galaxies. Also the direct N-dependence indicate that the evolution of SMBH binaries happen on relaxation time scales which are $O(10^{11}$ years) for real galaxies. The N- dependent evolution of massive binary occurs at separation of approximately one parsec and the SMBH binary should stop evolving beyond this point unless there is some other mechanism which ensures a constant supply of the stars to the massive binary. This sometimes is referred to as the "final parsec problem" (Milosavljević & Merritt 2003*b*). These studies, however, suffer a drawback in that the binary evolution was always studied using a spherical galaxy model while in reality the galaxy merger remnant where the binary evolution occurs is not spherically symmetric. Theoretical studies suggest that by introduction of flattening and non-axisymmetries stellar dynamics might suffice to bring SMBH binaries to GW dominated regime, since in these cases a significant fraction of orbits pass through the center (Merritt & Poon 2004). Motivated by this, rotating bar unstable galaxy models were used to study the evolution of SMBH binaries. These studies indicated that the evolution of SMBH binaries was N-independent, thus providing a potential stellar dynamical solution to final parsec problem (Berczik et al. 2006, Berentzen et al. 2009). In addition the torques from gas (Escala et al. 2005, Cuadra et al. 2009), if present, or re-population of stellar orbits due to "massive perturbers" (Perets & Alexander 2008) can assist the binary's loss of energy and angular momentum. It is thus important to perform numerical studies of the evolution of SMBH binaries in more realistic scenario of merging galaxies in order to obtain a clearer picture of this paradigm.

Gravitational waves were predicted by Einstein shortly after presenting his theory of General relativity. GWs are produced by accelerated masses, and according to GR, propagate with speed of light . The first indirect observational verification of the existence of GWs came through observations of the binary pulsar PSR B1913+16 by Hulse and Taylor starting in 1974 (Hulse & Taylor 1974). There are several interferometric ground based detectors for GW detection (such as LIGO, Virgo and GEO600) designed to observe neutron star or stellar-mass black hole binary coalescences in a frequency range from few Hz to few hundred Hz. Currently a space mission LISA[1] (Laser-Interferometer Space Antenna) is designed to measure gravitational waves for various sources over a range of frequencies (0.03 milli Hz - 0.1 Hz). The prospect of the detection of low-frequency gravitational radiation by LISA (Hughes 2003, Barack & Cutler 2004) has motivated theoretical studies into the formation and evolution of binary supermassive black holes. Such binaries would constitute the highest signal-to-noise ratio sources of low-frequency gravitational waves, but as is the case for virtually all potential LISA sources, the event rate is still poorly known, with estimates ranging from a few to a few thousand events per year (e.g. Wyithe & Loeb 2003, Rhook & Wyithe 2005, Sesana 2010). A common practice when estimating event rates for LISA is to equate the binary SMBH coalescence rate with the galaxy merger rate, the latter derived from models of structure formation in which galaxies merge hierarchically (Haehnelt 1994, Menou et al. 2001, Volonteri et al. 2003, Wyithe & Loeb 2003, Jaffe & Backer 2003). But as mentioned above, it is not clear whether prompt coalescence of SMBHs in galaxy

---

[1]http://www.esa.int/science/lisa

mergers is common, although observation may favor the prompt coalescence scenario. LISA can determine the luminosity distance of coalescing binaries. Assuming standard cosmology this can be converted to the redshift of the binary. Consequently, one can calculate the merger events as a function of redshift and hence trace the early history of galaxy mergers and the build-up of SMBHs[2].

Detailed surface photometry of elliptical galaxies has revealed that their surface brightness is well described by a Sérsic profile, $\log I(r) \propto r^{1/n}$, over most of the body of a bulge or early-type galaxy. However, systematic deviations from this profile are found in the innermost regions close to the central SMBH – either in the form of a light (mass) excess or deficit with respect to that would result from the extrapolation of the Sérsic profile towards the center. In other words, observations seem to reveal a dichotomy in the central density profiles of bulges and early-type galaxies: giant, high-luminosity objects have relatively shallow central density profiles while normal, low-luminosity ones show steeper density profiles in their center. The former are often called *core* galaxies and show density profiles ($\rho \propto r^{-\gamma}$) with central logarithmic slopes $\gamma < 1$, and typically harbor SMBH of mass $\gtrsim 10^8 M_\odot$; while the latter are normally called *power law* galaxies, have central $\gamma > 1$ and lighter SMBH $\lesssim$ few $\times 10^7 M_\odot$. Recent studies show that this mass excess or mass deficit can be as large as $10\times$ the mass of the supermasssive black hole. The inspiral of a binary SMBH is expected to leave a characteristic imprint in the morphological and dynamical properties of the newly formed galactic nucleus following the merger. The inspiraling binaries could carve a core in the centers of galaxies (Chapter 8) by ejecting stars on orbits that intersect the orbit of massive binary, thus providing an explanation for the mass deficits present in the centers of gas-poor giant elliptical galaxies.

Key scientific points to be addressed in this study

1. Use of self consistent distribution functions and an improved general form of the position and velocity dependent Coulomb logarithm to estimate dynamical friction and estimate the orbital decay of supermassive black holes in galaxies having different cuspy density profile.

2. Production of a large set of N-body simulations that can be compared to our improved dynamical friction formula in order to test its validity.

3. Investigations of the final parsec problem using more realistic models of merging galaxies with SMBHs at their centers and follow the evolution of SMBHs once the galaxies merge and a SMBH binary is formed.

4. Investigations of the shape of newly formed galactic nuclei following the merger of the galaxies by looking at the projected densities contours and calculating the axes ratios for the merged nucleus.

5. Investigations of the impact of mass ratios and density profiles of the merging galaxies on the SMBH binary evolution and on the shape of the merger remnant.

6. Estimates of the full time to coalescence of SMBH binaries for different masses of the merging black holes ($10^6 M_\odot - 10^9 M_\odot$) and the implications for gravitational wave detection by LISA.

7. Estimates of the mass ejected from the centers of galaxies by the massive SMBH binary in the process of merging and implications for the missing light observed at the centers of bright elliptical galaxies.

---

[2]Danzmann, K. et al., 2011, ESA LISA Yellow Book

Outlines

Chapter 2 reviews briefly the black hole galaxy relation, observational evidence of the SMBH binaries and evolution of the SMBH binary in galaxy merger. In Chapter 3, we discuss the galaxy models and the numerical codes used to evolve these models for various investigations concerning SMBHs and galaxy mergers. In Chapters 4 and 5 the improved formula of dynamical friction is discussed and used to estimate the orbital decay for power law cusps. Chapter 6, presents the results of our numerical study on dynamical friction and comparison of these results with analytic and semi-analytic estimates for standard dynamical friction formula and our improved formula. The results of numerical simulations to study the final parsec problem are discussed in Chapter 7. The evolution of SMBH binaries in the galaxy mergers having different mass ratios and density profile of merging galaxies are presented in Chapter 8. Chapter 9, presents the result of our study of the SMBH binary evolution starting from a late phase of the Milky Way type 1:10 galaxy merger. In the end, Chapter 10 concludes our study.

Chapter 2

Supermassive Black Holes in Galaxy Centers

<div style="background-color: yellow">

This Chapter reviews the following aspects of SMBHs evolution

1. Supermassive black holes, formation scenarios and the correlation of their properties with their host galaxies.

2. Observational evidence (direct and indirect) of binary supermassive black holes.

3. The formation and evolution of SMBH binaries in merging galaxies.

4. Stalling of SMBH binaries in spherical galaxy models and proposed scenarios to overcome this stalling.

</div>

Super Massive Black Holes are now a well established component of galaxies with a sizable bulge (Ferrarese et al. 2006). Since the 1960's it was understood that energetic processes taking place in quasars have gravitational origin (Salpeter 1964, Zel'Dovich & Novikov 1964, Robinson et al. 1965). Quasars, the most powerful sources of energy in the visible universe are powered by lurking SMBHs in the centers of galactic nuclei as they accrete stars and gas. The gravitational energy is released very efficiently from the accreted gas in the form of highly energy radiation and jets that sometimes extend to several kiloparsecs. The fact that quasar activity and galaxy mergers peak at approximately the same redshift supports the idea that the gas accretion on the SMBH is the source of triggering Active Galactic Nuclei activity since galaxy mergers are very efficient in driving the gas to the centers (Kauffmann & Haehnelt 2000, Mayer et al. 2010). Initially, SMBH masses in AGNs and quasars were deduced from the assumption of the Eddington limited luminosities where the gravitational attraction on electrons and protons is balanced by the radiation pressure of Thomson scattering:

$$L_{\text{Edd}} = 4\pi \frac{GM_\bullet m_p c}{\sigma_T} = 10^{39}(\frac{M_\bullet}{10^8 M_\odot})W. \tag{2.1}$$

Where σ_T is the cross-section for Thomson scattering, m_p is the mass of a proton and c is speed of the light. In the last few years we have witnessed the discovery of luminous quasars at z > 6 that are likely anchored by supermassive black holes of mass $> 10^9 M_\odot$ at the end of re-ionization epoch (Fan 2006). With the recent developments in ground and space based telescopes,
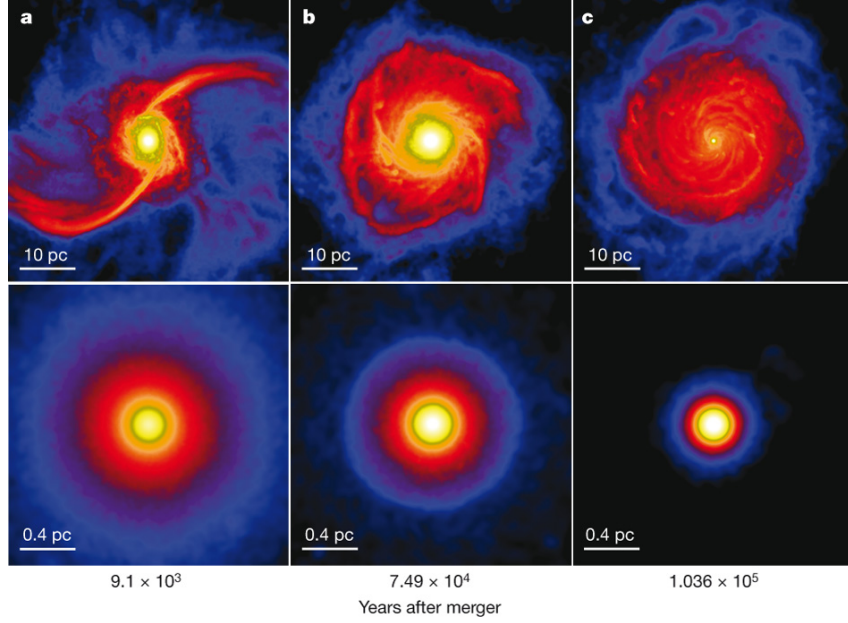
Figure 2.1: Evolution of central gas disk in the merger of two disk galaxies[Figure taken from Mayer et al. (2010)]. Figure shows the projected surface density maps of the central part of the gaseous disk formed as the result of the merger of two gas rich disk galaxies. A massive gas cloud with mass $\sim 10^8 M_\odot$ forms at the center.

the dynamics of gas and stars is used as a probe to measure the masses of even quiescent SMBHs in the nearby universe. One of the most compelling evidence involves the presence of a SMBH at the center of our own galaxy - the Milky Way. The motions of stars within $0.\acute{3}$ of Milky Way's SMBH have been monitored for more than a decade now (Eckart & Genzel 1997, Ghez et al. 1998). The full Keplarian orbit obtained for the short-period S-2 star has revealed a $4.1 \times 10^6 M_\odot$ mass SMBH at the center (Ghez et al. 2008).

Several scenarios are proposed in literature to explain the appearance of billion solar mass black holes within the first gigayear (Gyr) after the big bang:

- The conventional scenario involves the direct collapse of metal free population III star, leading to the formation of a seed black hole of about $100 M_\odot$ (Madau & Rees 2001). This seed black hole then needs to accrete steadily at or above the Eddington rate to grow to the billion solar mass supermassive black hole that is the power engine of a redshift 6 quasar (Volonteri & Rees 2006). There are several processes which can go against this high accretion rate, namely radiative feedback (Milosavljević et al. 2009) and/or low gas densities (Johnson et al. 2007) around the black hole. Also gravitational kicks due to asymmetric emission of gravitational waves received during the final phase of black hole mergers, may move the black hole off center (Haiman 2004) and hence can affect the accretion rates.

- Intermediate mass black holes, thought to be the remnants of very massive stars formed via runaway mergers between the stars at the centers of dense stellar clusters, can act as seed black holes and provide a possible route to SMBH growth (Portegies Zwart et al. 2004).

- Another interesting scenario involves the direct formation of SMBHs via multi-scale gas

inflows in galaxy mergers (Mayer et al. 2010). The collision of two galactic cores produce a massive turbulent, rotating nuclear disk (Figure 2.1) and more than 10^8 $M_\odot$ is accumulated in the central parsec. This supermassive cloud then can directly collapse to a SMBH or can partially collapse to form a supermassive star that can in turn collapse to an IMBH. The IMBH can then accrete from surrounding gas rich environment at high enough rates to become $10^9 M_\odot$ black hole.

Locally there is a tight correlation between the mass of the SMBH and the velocity dispersion σ of the stellar component of the host galaxy (Ferrarese & Merritt 2000, Gebhardt et al. 2000, Merritt & Ferrarese 2001, Tremaine et al. 2002, Ferrarese & Ford 2005, Gültekin et al. 2009). This correlation indicates that black hole evolution and galaxy formation are strongly coupled. The $M_\bullet - \sigma$ relation is given by (Gültekin et al. 2009)

$$\log(M_\bullet/M_\odot) = (8.12 \pm 0.08) + (4.24 \pm 0.41)\log(\frac{\sigma}{200 \text{ km s}^{-1}}) \tag{2.2}$$

Similar correlations exist between the bulge luminosity and the SMBH mass, and between the mass of the galaxy and the mass of the SMBH.

$$\log(M_\bullet/M_\odot) = (8.95 \pm 0.11) + (1.11 \pm 0.18)\log(\frac{L_V}{10^{11}L_{\odot,V}}) \tag{2.3}$$

The concordant evolution of SMBHs and their host galaxies suggest a paradigm in which SMBHs play an active role in shaping the cosmic environment.

Density profiles near the centers of elliptical and spiral galaxies exhibit a power law, $\rho \propto r^{-\gamma}$. Bright ellipticals have shallow cusps ($\gamma \simeq 0.5$) whereas faint ellipticals and spiral galaxies have steep density cusps ($\gamma > 1.5$). The formation of steep cusps is possible via collisional relaxation. In self gravitating cusps the encounter between stars result in driving the local velocity distribution to Maxwellian. But in the sphere of influence of SMBH where its gravitational potential dominates, the equilibrium density distribution has the $\rho \propto r^{-7/4}$ due to the exchange of energy between stars (Bahcall & Wolf 1976). A key timescale for the formation of the Bahcall-Wolf cusp is the relaxation timescale (Preto et al. 2004).

The bright elliptical galaxies with SMBH masses in the $10^8 - 10^9$ $M_\odot$ range, have relaxation times which are much longer than the age of the universe due to their relatively low stellar densities and high velocity dispersion (equation 2.2). So the nuclear density profile in these galaxies did not have enough time to evolve to a Bahcall-Wolf cusp and retain an imprint of their formation processes. On the other hand in galaxies like the Milky Way and M32 both having SMBH masses $\sim 10^6$ $M_\odot$, the central relaxation time is shorter than a Hubble time. Each of these galaxies exhibits a steep power law density profile $\gamma \sim 1.5$.

2.1 Observational Evidence for Binary Supermassive Black Holes

According to hierarchical galaxy formation models, the formation of Supermassive Black Holes Binaries (BBHs) should be common in galaxies. The search for BBHs is of great interests for understanding galaxy formation and evolution. The detection of a binary supermassive black hole would strengthen the idea that black holes can grow to high masses in the centers of galaxies by merging with other black holes. Here is a brief overview of several direct and indirect evidences which point to the presence of two supermassive black holes in the nucleus of a single galaxy.

Figure 2.2: SMBH masses as function of velocity dispersion σ based on 49 measurements [Figure from Gültekin et al. (2009)]. The line is the best fit relation to the sample: $M_\bullet = 10^{8.12}\mathrm{M}_\odot \left(\frac{\sigma}{200 \text{ km s}^{-1}}\right)^{4.24}$.
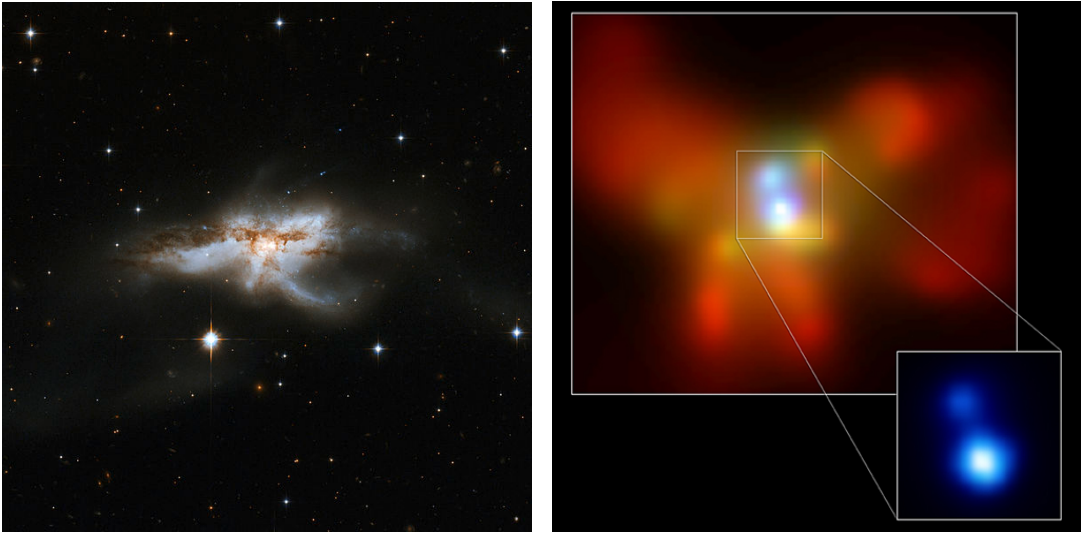
Figure 2.3: Left: Optical image of NGC6240 obtained by Hubble Space Telescope. Right: X-ray image of the central region of NGC6240 obtained by NASA's Chandra X-ray Observatory showing two accreting supermassive black holes: red color corresponds to soft X-rays (0.5-1.5 keV), green to medium X-rays(1.5-5 keV), and blue to hard X-rays(5-8 keV). Credit: NASA/CXC/M-PE/S.Komossa et al. 2003.

2.1.1 Direct Evidence for Dual SMBHs: Spatially Resolved Systems

In this section cases in which both SMBHs can be spatially resolved in a single galaxy are described.

Starburst Galaxy NGC 6240

NGC 6240 is a result of the merger of two galaxies and belongs to the ultra luminous infrared galaxy (ULIRG) class. It harbors two optical nuclei (Figure 2.3-left). Due to the recent collision and merger of two galaxies the star formation rate is very high. Large amounts of gas and dust make it difficult to observe the central regions of the galaxy with optical telescopes. However, X-ray emissions from the central part of the galaxy can penetrate gas and dust.

Observations performed with the Chandra X-ray observatory (Komossa et al. 2003) reveal the presence of two accreting supermassive black holes (Figure 2.3-right). The projected separation between the two black holes is 700 pc (Max et al. 2007). Kinematic evidence suggest that the two supermassive black holes are not yet bound.

Spiral Galaxy NGC 3393

A dual SMBH system has been reported in the central regions of NGC 3393 after the observation of X-ray emission from the two AGNs (see Figure 2.4) using NASA's Chandra X-ray Observatory (Fabbiano et al. 2011). Two SMBHs are separated by ~ 135 pc and are estimated to have masses $\sim 10^6 M\odot$. NGC 3393 hosts the nearest known pair of supermassive black holes (at a distance of 160 million light years). It also happens to be the first time that a pair of SMBHs has been reported in a spiral galaxy like our Milky Way.

Radio (Elliptical) Galaxy 0402+379

Using multi-frequency Very Long Baseline Array (VLBA) observations, Maness et al. (2004) reported the presence of two central, compact, flat-spectrum components (possibly active galactic nuclei) in the radio galaxy 0402+379 (Figure 2.5). Further VLBA observations of the same galaxy were performed by Rodriguez et al. (2006) who concluded that the two components are

Figure 2.4: Observational evidence for SMBH pair in a spiral galaxy NGC 3393 from the data obtained by NASA's Chandra X-ray Observatory. The figure shows composite image of X-rays from Chandra (blue) and optical data from the Hubble Space Telescope (gold) of the galaxy. The box (inset) shows the central region of NGC 3993 as observed by Chandra only. Credits: X-ray: NASA/CXC/SAO/G. Fabbiano et al; Optical: NASA/STScI
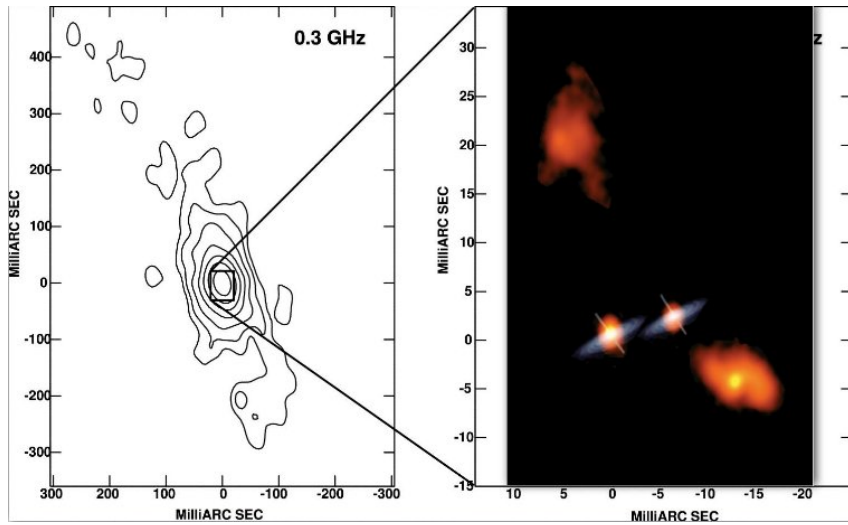
Figure 2.5: VLBA image of 0404+379 at 0.3 GHz. Contours are drawn at 3 σ and increase by factor of 2 thereafter (Figure taken from Rodriguez et al. (2006)). Right panel of the figure shows sketch of two SMBHs.

supermassive black holes in a single galaxy. The projected separation of the two SMBHs is 7 pc which makes this pair of SMBHs the closest binary SMBH system yet discovered. The estimated total mass of the SMBHs system is $1.5 \times 10^8 M\odot$.

2.1.2 Indirect Evidence for BBHs: Spatially Unresolved Binary Systems

The inspiral of a binary SMBH is expected to leave a characteristic imprint in the morphological and dynamical properties of the newly formed galactic nucleus following the merger of two galaxies. This section describes several observed phenomena in galaxy centers that could be explained by different models of SMBH binary evolution prior to or after the coalescence of the two black holes.

Radio Galaxies with X-shaped Jet Patterns

Large scale radio jets have been observed in several hundreds of radio sources (Liu & Zhang 2002). Among these, there is a class of so called "X-shaped" or "winged" radio sources characterized by two low surface brightness radio lobes oriented at an angle to high brightness lobes. The coalescence of the binary SMBHs preceded by gravitational waves can alter the spin axis of the larger SMBH. If one of the the two merging galaxies harbor a radio jet then a likely consequence of SMBH merger is the sudden change in the direction of the radio jet at some angle with respect to the original lobe (Merritt & Ekers 2002, Zier 2005).

Double-Double Radio Galaxies

These radio galaxy sources consist of a pair of symmetric double-lobed radio structures having a common center and aligned along same axis. Schoenmakers et al. (2000) proposed several ideas to explain this phenomenon. These structures are most likely caused by the interruption and restarting of the jet formation and are suggested to be the remnants of a coalesced SMBH binary system (Liu et al. 2003). Jet formation is interrupted as the inspiraling secondary black hole opens a gap in the accretion disc around the primary supermassive black hole. Once the SMBHs coalesce, the gap is refilled by disk material and jet formation restarts. Liu et al. (2003) showed that the observed time for the interruption of jet activity is the time required for the accreted
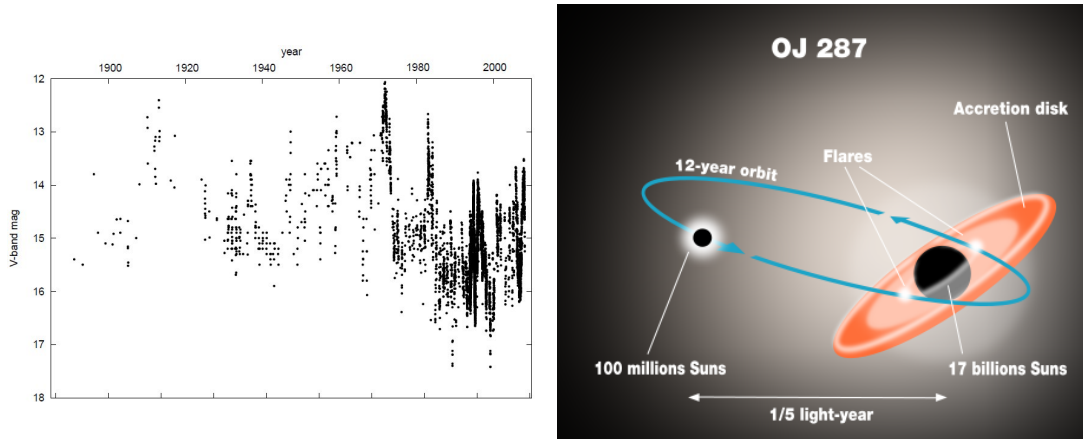
Figure 2.6: Left: Optical light curve of OJ 287 (Figure from Valtonen et al. (2008)). The light curve shows periodicity with approximately 12 years period. Right: Model for the SMBH binary in OJ 287.

plasma to refill the inner disc.

OJ 287

OJ 287, one of the brightest quasars, shows a quasi periodic pattern of prominent outbursts in its light curve (Figure 2.6). This object has been observed since the late nineteenth century. The interval between two outbursts peaks is 12 years and shows two peaks per interval (Sillanpaa et al. 1988, Valtaoja et al. 2000, Valtonen et al. 2008). Sillanpaa et al. (1988) proposed a scenario in which the secondary SMBH tidally perturbs the accretion disk of the primary SMBH on a close passage that leads to an increased activity resulting in a peak in the optical light curve. Another model which invokes a SMBH binary to explain the light curve variation of OJ 287 was proposed by Katz (1997). In this model the jet sweeps periodically across the line of sight as gravitational torque exerted by the secondary SMBH causes precession of the accretion disk around primary SMBH. Lehto & Valtonen (1996) proposed that the observed sharp flashes are caused by the impact of the secondary SMBH as it pierces the accretion disk of the primary SMBH. Valtonen (2008) constructed the orbit of the SMBH binary with eccentricity 0.663. The mass of the primary is $18 \times 10^9 M_\odot$ and that of secondary about $10^7 M_\odot$. Valtonen et al. (2008) predicted the next outburst using the post Newtonian corrections to the binary orbit and observed the outburst to be in good agreement to their predictions.

Sub-parsec SMBH Binary in Quasar SDSS J153636.22+044127.0

SMBH binaries at the center of active galaxies are expected to have observable effects on the profile of broad emission line due to the orbital motion of the two black holes. Recently a quasar SDSS J153636.22+044127.0 system which shows two broad-line emission system has been reported as a sub-parsec SMBH binary candidate (Boroson & Lauer 2009). The two SMBHs have masses $\sim 10^7 M\odot$ and $10^9 M\odot$ solar masses. The binary separation is ~ 0.1 pc with an orbital period of ~ 100 years. The subparsec separation of the binary suggests that gravitational wave emission can derive the binary to coalescence in approximately 1 Gyr (see Chapter 8).

A Close Binary Black Hole in the Giant Elliptical Galaxy 3C 66B

Several extragalactic sources show periodic variations in flux and outburst activity in γ-rays, X-rays, optical and radio. The periodicity in outburst variations can be associated with the presence of binary black hole system in numerous theoretical and observational studies (Rieger

& Mannheim 2000, De Paolis et al. 2002). The core of 3C 66B a nearby giant elliptical (radio) galaxy, is reported to have such periodic variations in its light curve that are associated with the presence of a very close SMBH binary system (Iguchi et al. 2010). The mass of the more massive of the two black holes is $1.2 \times 10^9 M\odot$ while for smaller black hole is $7.0 \times 10^8 M\odot$. The orbital separation of the binary is 6.1×10^{-3} pc with an orbital period of approximately one year. The binary with a separation $\sim$ milli parsec could already be in gravitational wave dominated regime and should be an interesting target for the GW detectors.

Core (missing light) Galaxies

Detailed surface photometry of ellipticals has revealed that their surface brightness is well described by a Sérsic profile, $\log I(r) \propto r^{1/n}$, over most of the body of a bulge or early-type galaxy (Kormendy et al. 2009). Bright ellipticals with total absolute magnitude less than -21 have cuspy cores–"missing light"– at small radii. Cores tend to be found in giant ellipticals and are loosely defined as the central region in a bulge or early-type galaxy where the surface brightness deviates and it is below the values that would result from the extrapolation of the Sérsic profile from the main body of the object down to its innermost region. In dry mergers, i.e. in the absence of a dynamically significant amount of gas, the slingshot ejection of stars by the central SMBH binary drives the binary inspiral. It has been proposed that inspiraling binaries could carve a core by throwing stellar mass of the order of the mass of the SMBH binary (Merritt 2006b).

2.2 Supermassive Black Hole Binary Evolution

Galaxy mergers, which are an essential part of galaxy evolution, are considered the prevalent path leading to the formation of SMBH binaries. An understanding of the formation and evolution of SMBH binaries is thus important to understand the galaxy formation and evolution.

The dynamical evolution of pair of supermassive black holes in galaxy mergers can be described broadly in three phases (Begelman et al. 1980):

1. Supermassive black holes are embedded in the central cores/cusps of their host galaxies. The galaxy cores/cusps sink to the center of the merger product due to the dynamical friction caused by background dark matter + stars + gas. The galaxy cores/cusps merge, undergo violent relaxation and form a new galaxy nucleus in a characteristic galactic dynamical time scale. The two SMBHs form a binary system once their separation shrinks below the influence radius.

2. The binary continues to decay under the combined effects of dynamical friction and the gravitational slingshot effect. As the binary's orbital time decreases the dynamical friction becomes inefficient and the binary's further evolution is governed by its interaction with stars on orbits intersecting the binary, carrying away energy and angular momentum from binary. These stars are then ejected at the velocities comparable to binary's orbital velocity.

3. For a sufficiently small separation the emission of the gravitational waves become dominant and carries efficiently the last remaining energy and angular momentum, resulting in a rapid coalescence of supermassive black holes.

Figure 2.7 show a sketch of the three distinct phases in evolution of SMBH binary and the underlying physical physical processes in each phase. Here we describe each phase in more detail:

Galaxy Mergers and Dynamical Friction

Galaxy mergers can be divided mainly in two classes: the first, in which the merging galaxies have almost equal masses, are termed as *major mergers* while the second, which involve mergers of galaxies with large mass ratio (typically 1:10 or larger), are referred to as *minor mergers*. In major mergers as the galaxies merge, the two SMBHs centered inside the individual cusps fall
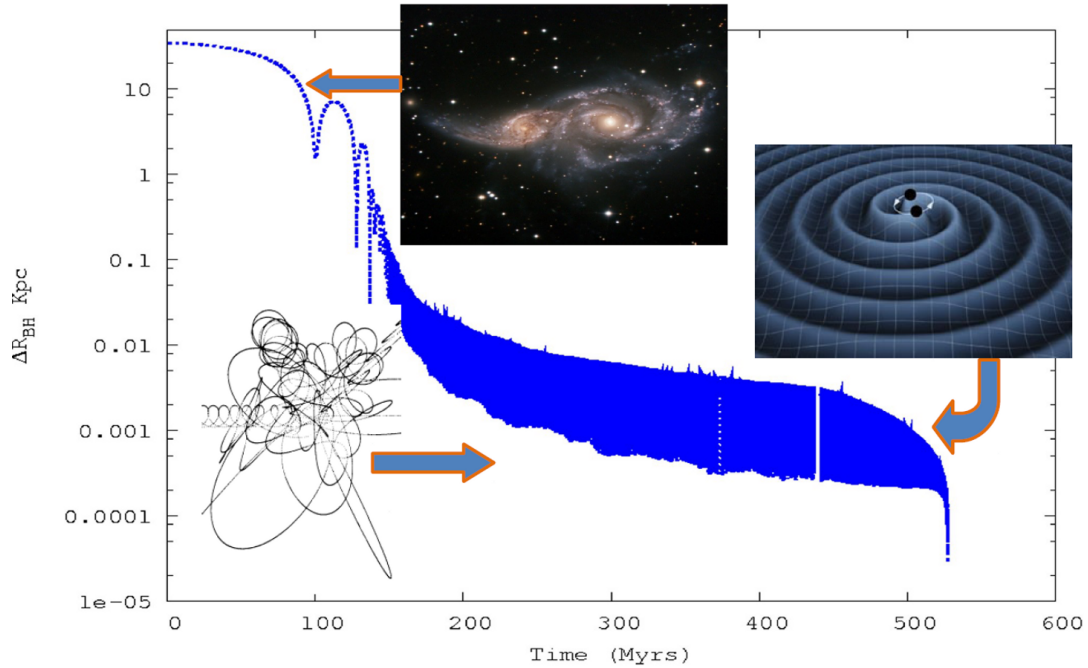
15

Figure 2.7: Different phases of SMBH binary evolution. Figure shows the relative separation of the two black holes during galaxy merger. As the galaxies merge the two SMBHs sink towards the center and form a binary system due to dynamical friction (phase I). The binary gets harder by flinging stars away on orbits intersecting the binary (phase II). At small separations ($\sim$ milli-parsec) SMBH binary shrink rapidly and SMBHs coalesce due to emission of gravitational waves (phase III).

towards the center of the merger remnant and form a close pair surrounded by individual cusps. Once the individual cusps are merged and a new galactic nucleus is formed the two SMBHs move as individual entities, loose angular momentum due to dynamical friction and form a bound pair. In the case of minor mergers, the less massive galaxy will be tidally disrupted. The black hole of the less massive galaxy looses its surrounding cusp and spirals in due to dynamical friction. The dynamical friction phase in minor mergers is shortened in the case of satellite galaxies which have compact center since these galaxies can survive against the tidal disruption for a longer period of time. If the merging galaxies (especially the less massive one) have a considerable fraction of the gas, the gas can be funneled towards the center and undergo a strong star-burst, making the central part of the galaxy more compact (Callegari et al. 2009). The orbital evolution of such an inspiraling SMBH due to dynamical friction is discussed in great detail in Chapter 5. Dynamical friction also plays a very important role in changing the shape of the binary's orbit. Near apo-center the orbital velocity is lowest while it is highest near peri-center. At peri-center SMBHs need to move faster than local circular velocity to climb up and at apo-center SMBHs need to move slower than local circular velocity to fall down. If dynamical friction is more efficient near peri-center then the orbit of the binary circularizes whereas if dynamical friction is stronger at apo-center it becomes eccentric.

Stellar Dynamical Hardening

Let us define the mass of the two black holes as $M_{1\bullet}$ and $M_{2\bullet}$ for larger and smaller black holes respectively. $M_{\bullet} = M_{1\bullet} + M_{2\bullet}$ and $q = M_{2\bullet}/M_{1\bullet}$ is the mass ratio of the two black holes. For equal mass binary $q = 1$ and for unequal mass binaries q is always less than 1. Also we define the reduced mass, $\mu = M_{1\bullet}M_{2\bullet}/M_{\bullet}$ and a is the semi-major axis of the SMBH binary. Following the dynamical friction phase the two black holes become bound and form a binary system. The separation at the time of formation of the SMBH binary is typically $\sim r_h$, the gravitational influence radius of the black holes, defined as (Merritt & Milosavljević 2005)

$$r_h = \frac{GM_{\bullet}}{\sigma^2} \approx 11\text{pc}(\frac{M_{\bullet}}{10^8 M_{\bullet}})(\frac{\sigma}{200\text{km } s^{-1}})^{-2}. \tag{2.4}$$

Here σ is the one dimensional velocity dispersion of the stellar bulge. An alternate definition of r_h is the radius which encloses the stellar mass around the SMBH equal to $2M_{\bullet}$,

$$r_h = M_{\star}(r) = 2M_{\bullet} \tag{2.5}$$

Here we define the binary's parameters according to approximate relative Keplarian orbit ignoring the force contribution from the stars. The binding energy is

$$E_b = -\frac{GM_{1\bullet}M_{2\bullet}}{2a} = -\frac{G\mu M_{\bullet}}{2a} \tag{2.6}$$

and the binding energy per unit mass of the SMBH binary is

$$\epsilon_b = -E_b/M_{\bullet} = G\mu/2a. \tag{2.7}$$

We define the semi-major axis a and eccentricity e via the standard relations:

$$\frac{1}{a} = \frac{2}{R} - \frac{v^2}{GM_{\bullet}}, \tag{2.8}$$

$$e = \sqrt{1 + \frac{2h^2}{GM_{\bullet}^2}\left[\frac{v^2}{2} - \frac{GM_{\bullet}}{R}\right]}. \tag{2.9}$$

where v is the relative speed, and h is the specific angular momentum of the relative motion. For a circular orbit, the relative velocity of two SMBHs and the orbital period is given by

$$v = \sqrt{\frac{GM_{\bullet}}{a}}, \tag{2.10}$$

and

$$P_{orb} = 2\pi\sqrt{\frac{a^3}{GM_{\bullet}}} \tag{2.11}$$

respectively.

The stars passing within a distance of a few times the semi-major axis of the SMBH binary are ejected by gravitational slingshot effect with velocities $V_{ej} \approx v$ (e.g. Hills & Fullerton (1980)). The stars carry energy and angular momentum away from the binary and the binary's binding energy increases. The rate at which E_b increases as a result of the encounter with field stars is given by

$$\frac{dE_b}{dt} = H\frac{G^2 M_{\bullet}^2 \rho}{8\sigma} \tag{2.12}$$

where ρ is the background stellar density, σ is 1D velocity dispersion of the stars and H is dimensionless hardening rate of the binary defined as

$$H = \frac{\sigma}{G\rho} \frac{d}{dt}(\frac{1}{a}). \tag{2.13}$$

Various studies (e.g. Mikkola & Valtonen (1992), Quinlan (1996), Sesana et al. (2006)) estimated the binary hardening rates by performing three-body scattering experiments with different mass ratios of circular binaries and provided fitting formulas for H. Sesana et al. (2006) derived fitting function for H,

$$H = A(1 + a/a_0)^\gamma. \tag{2.14}$$

The parameters A, a_0 and γ are given in Table 1 of Sesana et al. (2006) for various mass ratios of the binary. H has been found to be approximately constant in both N-body studies(e.g. Merritt (2006b), Khan et al. (2011)) and scattering experiments (e.g. Quinlan (1996), Sesana et al. (2006)) once $a \leq a_h$, where a_h is the semi-major axis of a "hard binary". SMBH binary is called hard when $\epsilon_b \geq \sigma^2$. Semi-major axis of a hard binary is defined as (e.g. Merritt (2006a))

$$a_h = \frac{G\mu}{4\sigma^2} \tag{2.15}$$

Using equation 2.4 for the influence radius, a_h can be written as

$$a_h = \frac{\mu}{4M_\bullet} r_h = \frac{r_h}{4} \frac{q}{(1+q)^2}. \tag{2.16}$$

For $q = 1$, $a_h \approx 0.06 r_h$ and for $q = 0.1$, $a_h \approx 0.02 r_h$. The eccentricity of the massive binary grows at a rate,

$$K = \frac{de}{d ln(a_0/a)}. \tag{2.17}$$

Sesana et al. (2006) found the following fitting relation for K from their scattering experiments

$$K = A(1 + a/a_0)^\gamma + B. \tag{2.18}$$

The parameters for fit can be found from Table 3 of Sesana et al. (2006). During this phase of SMBH binary hardening, the stars are deposited into large volume at large radii by gravitational slingshots. The mass ejection rate is

$$J = \frac{1}{M} \frac{dM_{ej}}{d ln(1/a)}. \tag{2.19}$$

where M_{ej} is the stellar mass ejected by the SMBH binary. Fitting formula for J is (Sesana et al. 2006)

$$J = A(a/a_0)^\alpha [1 + (a/a_0)^\beta]^\gamma, \tag{2.20}$$

with A, a_0, α, β and γ given in Table 2 of Sesana et al. (2006). The above mentioned formulas obtained from scattering experiments assume that the SMBH binary has always constant supply of stars to interact with. This may not be always the case as is discussed in the next section.

Gravitational Waves (Hardening)

Gravitational waves are generated by accelerated mass-energy distributions. If $M_\bullet$ is the mass of a system with size R at a luminosity distance D, the periodic motion of such a system generates gravitational waves having a strain amplitude:

$$h \sim (\frac{GM_\bullet}{Rc^2})^2 \frac{R}{D}, \tag{2.21}$$

and the frequency of the GWs is determined the frequency of motion of the system. The strongest gravitational field systems (GM/R), generate the most powerful GWs. SMBHs have large masses and small sizes $(GM/Rc^2) \approx 1$, and hence are very efficient at emitting gravitational waves.

If stellar dynamical processes or gas dynamics manage to reduce the binary separation sufficiently that gravitational waves emission become dominant mechanism in extracting energy and angular momentum then the two black holes coalesce in a time $T_{\rm gw}$ given by (Peters 1964),

$$T_{\rm GW} = \frac{5}{256} \frac{c^5 a^4}{G^3 \mu M_\bullet^2} F(e), \tag{2.22}$$

where

$$F(e) = (1 - e^2)^{-7/2} \left(1 + \frac{73}{24} e^2 + \frac{37}{96} e^4 \right)^{-1}.$$

Using equation 2.2,

$$T_{\rm GW} = 7.6 \times 10^{-5} \frac{G \mu^3 c^5}{\sigma^8 M_\bullet^2} (\frac{a}{a_h})^4 F(e). \tag{2.23}$$

2.3 The Final Parsec Problem

In the paradigm of a SMBH binary formation and evolution described in section 2.2, the transition from phase II to phase III is understood to be the bottleneck in binary's path to coalescence. As the SMBHs forms a binary system, the binary quickly ejects all stars on orbits that intersect the orbit of the SMBH binary - in stellar dynamical term the loss cone[1] is depleted. In a spherical, isotropic galaxy in equilibrium the loss cone can only be refilled by two-body relaxation. The relaxation time scales as N^{-1} and for real galaxies it is $\mathcal{O}(10^{11}$ years). Thus timescale of loss cone refilling is longer than Hubble time so once the loss cone is depleted, the supply of stars to the binary is cutoff and binary's further evolution stalls. The binary stalling happens at separations of around 1 parsec and this is the so called "Final Parsec Problem" (FPP) (Milosavljević & Merritt 2003b). Figure 2.8 shows a sketch of the final parsec problem.

2.3.1 Numerical Studies of Final Parsec Problem

Several theoretical and numerical studies have been performed to investigate the timescales of loss-cone depletion and refilling. Here we present a brief overview of some key numerical experiments which address this issue.

Makino (1997) performed N-body simulations with different number of particles to study the binary SMBH evolution by merging two (King profile) galaxies. He found that in the first (dynamical friction) phase the binary's evolution does not depend on number of particles used to construct the galaxy model. In second phase when the binary evolution is governed by three body interactions there is a clear N-dependence in the hardening timescale of SMBH binary ($\sim N^{1/3}$). This dependence, however, is weaker than what is expected if the hardening timescale is proportional to relaxation time, i.e. $\mathcal{O}(N)$.

Using a composite method (tree code and direct N-body code) Milosavljević & Merritt (2001) studied SMBH binary evolution in merging stellar cusps. Their initial spherical galaxy model consisted of steep power law density cusp ($\rho \propto r^{-2}$) similar to those observed in the center of spiral and faint elliptical galaxies. They employed a parallel tree code with individual time steps (Springel et al. 2001) in the first phase of the merging of the galaxy cusps. Just before the formation of SMBH binary they switched to a direct N-body code, NBODY6++ (Spurzem 1999). They performed three runs with 8,000, 16,000 and 32,000 particles. The hardening rates in their

---

[1]The loss cone is the region of phase space corresponding, roughly speaking, to orbits that cross the binary, i.e. with angular momentum $J \lesssim J_{\rm lc} = \sqrt{GM_\bullet f a_{\rm bin}}$, where $f = \mathcal{O}(1)$ (Lightman & Shapiro 1977).
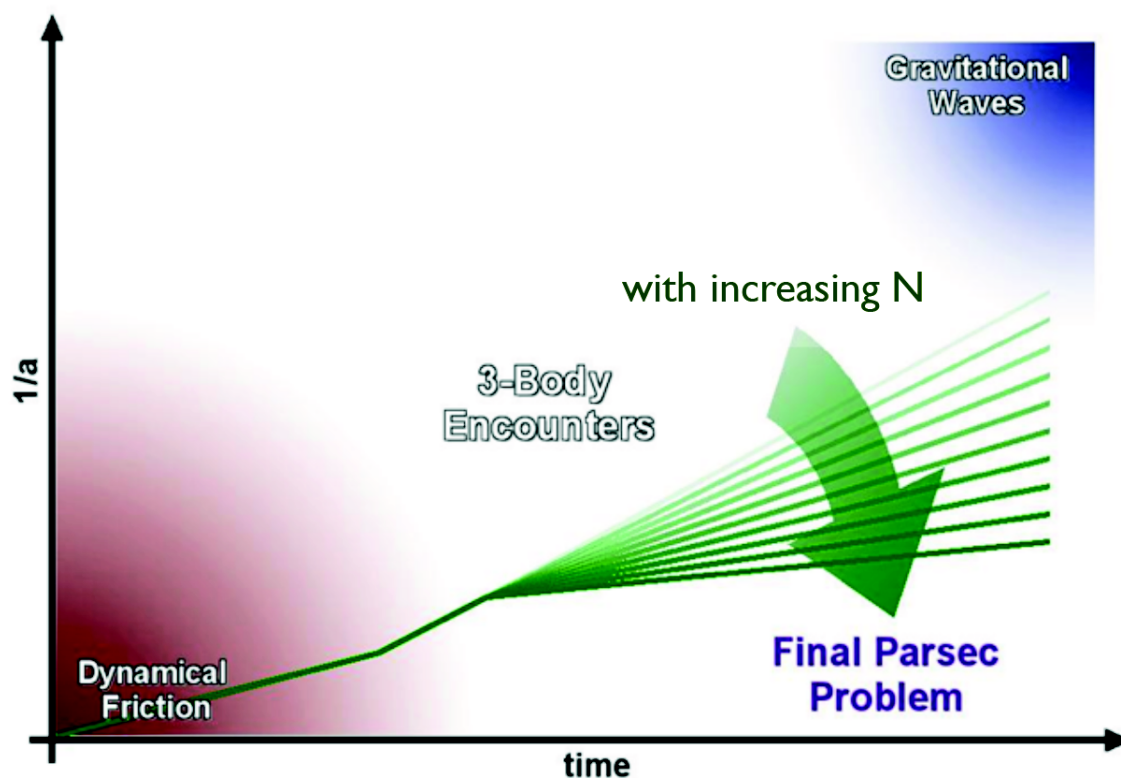
Figure 2.8: The figure shows a sketch of final parsec problem. The early phase of binary evolution is governed by dynamical friction. As mass is ejected from the central region and the separation shrinks dynamical friction becomes inefficient. Three body encounters take energy away from the binary. This phase is N-dependent; with an increasing number of particles in numerical experiments the rate at which binary semi-major axis evolves decreases. For realistic number of particles, which are several orders of magnitude larger than current state of the art simulation can accommodate, the binary semi-major axis should stop evolving and the two black holes should not enter the regime where gravitational waves become efficient in carrying energy away from the binary. Figure credit: Dr. Ingo Berentzen.
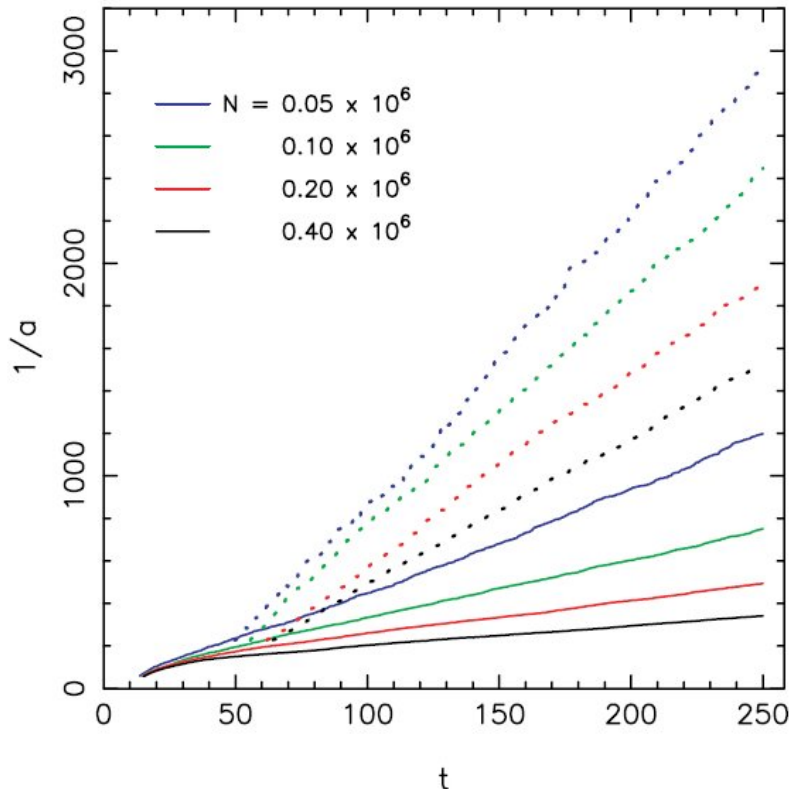
Figure 2.9: Evolution of inverse semi-major axis (1/a) for different particle numbers. Dashed lines show the evolution for which the mass of SMBHs in the binary is $M_{1\bullet} = M_{2\bullet} = 0.005$ and solid lines indicate the evolution for $M_{1\bullet} = M_{2\bullet} = 0.02$ mass binary. The total mass of the galaxy in the model is 1. Figure taken from Berczik et al. (2005).

simulation did not show a clear N-dependence. The small number of particles used in this study was explained (Milosavljević & Merritt 2003a) to be a reason for the N-independent hardening of SMBH binary: stars repopulate the loss cone via collisions at a higher rate than they are scattered by the binary. Thus binary continue to harden at a constant rate. In order to achieve an empty loss cone in N-body simulations of spherical galaxies one requires either very large numbers of the particles or very low densities, so that star-star relaxation time is long.

The depletion of the loss cone was first reported by Makino & Funato (2004) who performed large N-body simulations of SMBH binary evolution at the center of a spherical galaxy represented by King profile. They used sufficiently large particle number N (up to 1 million) made possible by a parallel GRAPE cluster. When the binary was evolved for a sufficiently long time, it was found that hardening rates depended directly on N. This result agrees with the simple theoretical prediction that hardening rate is proportional to two body relaxation timescale. Berczik et al. (2005) performed similar simulations again using a parallel GRAPE cluster with up to half a million particles, and studied the evolution of SMBH binaries in a Plummer galaxy model. They again noticed N-dependent binary hardening rates (see Figure 2.9). The hardening rate in their study scales as $N^{-0.8}$, almost as steep as the N^{-1} dependence predicted for an empty loss cone.

If the binary hardening rate is proportional to the relaxation time, as suggested by the above N-body experiments, then the binary evolution should stop at separation ~ 1 pc. On the other hand there is circumstantial evidence that binary coalescence is normal. Few observational phenomena discussed in section 2.1.2 such as X-shaped radio sources, are probably caused by coalescing
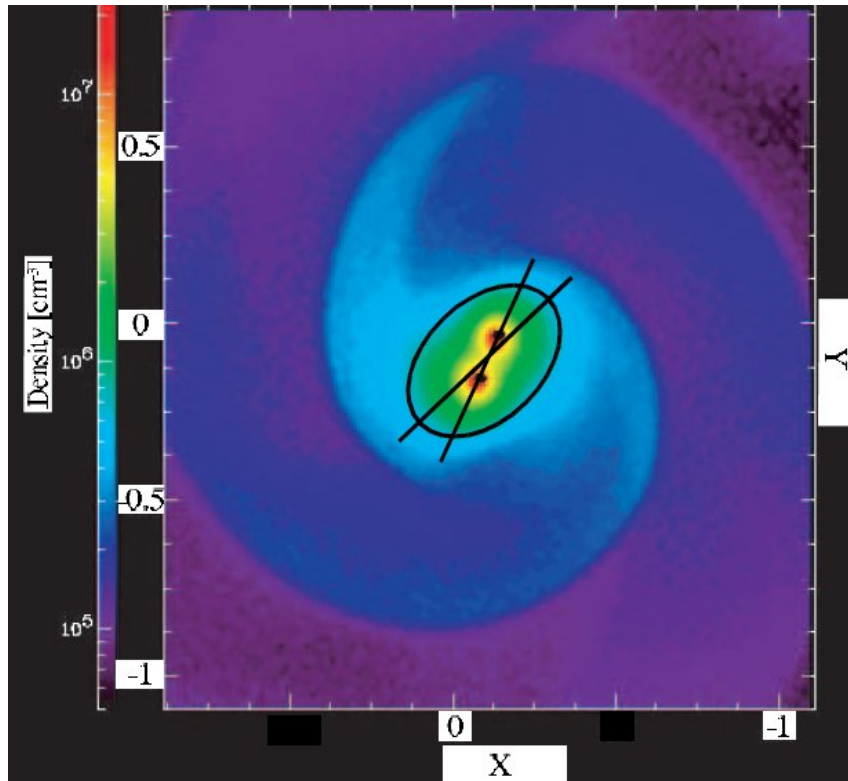
Figure 2.10: Ellipsoidal density enhancement of the gas trailing the massive binary that is responsible for the rapid decay in the binary separation by exerting torques on it. Figure taken from Escala et al. (2005).

SMBHs. If the binary stalls at some separation then a subsequent merger with another galaxy will add another SMBH or a SMBH binary and result in a 3-body or 4-body gravitational slingshot. These off centered SMBHs would not be able to accrete at high rates and we would observe much larger scatter in the $M_{\bullet}$ - σ relation. Also the number of observed parsec or sub-parsec scale binaries is small (Rodriguez et al. 2006, Boroson & Lauer 2009), which favors the prompt merger scenario of SMBHs. If the binaries had survived a Hubble time, such detections should be common (Volonteri et al. 2009). In the next section we present some physical mechanisms that can potentially assist the binary to bridge the gap between the stellar dynamical regime and gravitational wave dominated regime, thus avoiding the final parsec problem.

2.3.2 Avoiding Final Parsec Problem

Here we briefly mention mechanisms discussed in the literature that can help overcoming the final parsec problem:

Evolution in Gaseous Environment

Gas could certainly assist the inspiral if it is cold enough to settle into a circumbinary thin disk. Escala et al. (2005) investigated the effects of gas on an inspiraling SMBH binary. They found that in the late stage of binary evolution an ellipsoidal density enhancement is created whose axis lags behind the binary axis (see Figure 2.10). This offset between the two axis causes a gravitational torque on to the massive binary. Which results in the binary losing angular momentum and shrinking. Similar evolution of SMBH binary in gaseous and stellar disks was

reported by Dotti et al. (2007). In their study the binary separation shrinks to 0.1 pc, the resolution of their simulations. But the mass in Keplarian disk around the SMBH is only about few percent of the SMBH binary mass, which might not be enough to carry the the binary inspiral to the point where gravitational waves become important. Cuadra et al. (2009) studied the evolution of SMBH binaries in small-scale gas disks. Their simulations directly resolved the angular momentum transport within the gas disc. For the binary masses in the range $10^5 \lesssim M_\bullet \lesssim 10^8 M_\odot$, the decay rate of SMBH binary due to gas disc dominates the stellar dynamical hardening rates for $a \sim 0.01 - 0.1$ pc . According to their estimates the minimum merger time-scale is shorter than Hubble time for massive binary with mass $M_\bullet \lesssim 10^7 M_\odot$. For more massive binaries the gas dynamics could not attend black hole mergers.

To summarize, a gas disc can assist the binary's journey towards coalescence but the uncertainties associated with its long-term dynamical behavior are potentially more severe than those related to stellar dynamics. For instance, gaseous disks are susceptible to fragmenting and forming stars. In order for the disk to be marginally stable against fragmentation at every radius, its total mass is constrained to be $M_{\text{disk}} \sim (0.1 - 0.2)M_\bullet$ (Cuadra et al. 2009, Lodato et al. 2009). This is not likely to be enough to drive the binary to coalescence. More simulations involving the gas dynamics with high resolution and more physics are required to show a clear picture of influence of gas on SMBH binary evolution.

Massive Perturbers / Minor Mergers

Perets & Alexander (2008) suggested that massive perturbers such as giant molecular clouds or clusters can accelerate relaxation by orders of magnitude compared to two-body stellar relaxation alone. The perturbations caused by massive perturbers efficiently refill the loss cone. The perturbation caused by the inspiral of a merging dwarf galaxy in particular affects the stellar orbits in the galactic central region of the host galaxy and increases the supply of stars into the loss cone (Matsui & Habe 2009).

Triaxial Galaxies

Imaging of the centers of galaxies shows, a wealth of feature in the stellar distribution. These features include bars, bars-within-bars and nuclear spirals (Shaw et al. 1995, Peng et al. 2002, Erwin & Sparke 2002, e.g.). The orbits in triaxial potential do not conserve any component of angular momentum and possess a rich families like boxes, tubes and pyramids (Schwarzschild 1979, Ostriker et al. 1989, Holley-Bockelmann et al. 2001, 2002) and can pass very close to the centers. These orbits can potentially increase interaction rates with SMBHs in the center of galaxy (Norman & Silk 1983).

In a triaxial galaxy nucleus harboring a SMBH the orbit families have different characteristics depending on distance from the center. Inside the influence radius of SMBH, nearly circular orbits in axisymmetric potential become tubes, nearly radial orbits are converted to pyramids and Keplarian ellipses have one focus lying near the SMBH (Sridhar & Touma 1999, Poon & Merritt 2001). Gerhard & Binney (1985) suggested that SMBH will disrupt most box orbits with apocenters interior to about 1 kpc and boxlike orbits become chaotic . The mass enclosed in this zone of chaos could be as large as 100 time the SMBH mass (Valluri & Merritt 1998). Merritt & Poon (2004) built self-consistent cuspy, triaxial models with a single SMBH at the center and showed that such models posses significant fraction of centrophilic orbits that would efficiently drive the hardening rate of a binary if it were present at the center. The rotation in triaxial galaxies can increase the fraction of chaotic orbits (Deibel et al. 2011) which can also boost the supply of stars to the loss cone.

Berczik et al. (2006) performed direct N-body simulations and studied the evolution of supermassive black hole binaries in rotating and triaxial galaxy model. The rotating galaxy (King) models in their study become unstable leading to the formation of a bar, yielding a slowly tumbling, triaxial spheroid (see Figure 2.11 right). The steep N-dependence in the evolution of SMBH binary's semi-major axis reported in spherical galaxy models was absent (see Figure 2.11 left).
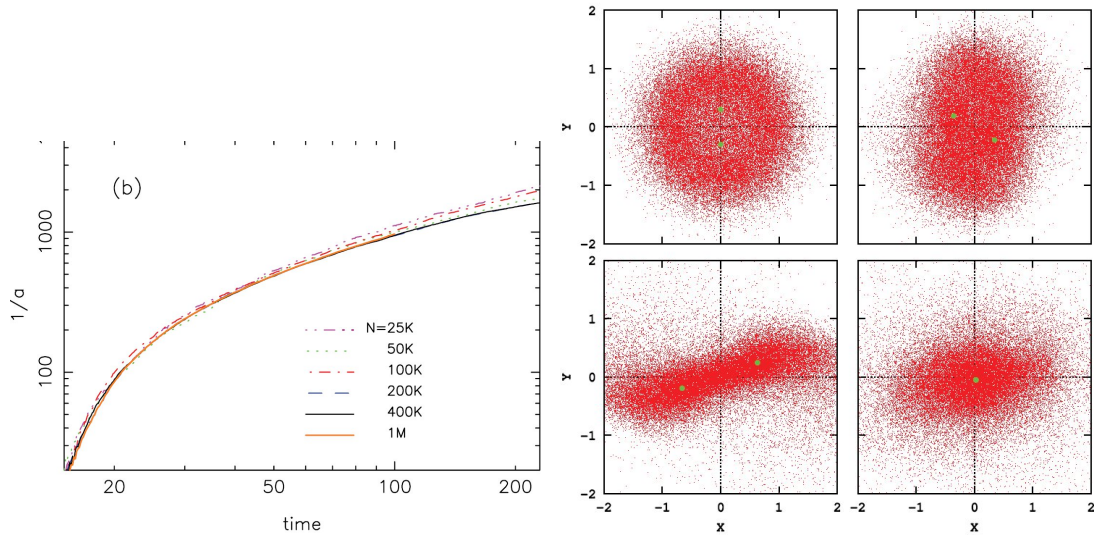
Figure 2.11: *Left:* Evolution of the inverse semi-major axis in rotating galaxy models for different number of particles N. *Right:* Particle positions projected on (x,y) plane for various time steps during the evolution of SMBH binary in rotating galaxy models. Figure is taken from Berczik et al. (2006)

This provided a potential solution to final parsec problem. Berentzen et al. (2009) showed, using simulations of SMBH binary evolution in rotating galaxy models of Berczik et al. (2006), but this time including post-Newtonian corrections to the binary's equation of motion up to order 2.5, that SMBH coalescence can be achieved for these models within a Hubble time.

However the question which remains unclear is whether these models of strong bar-mode instability are representative of more realistic models of galaxy mergers. Therefore more realistic simulations that follow the merger of two galaxies from an early stage prior to the formation of a galactic nuclei are hence necessary.

We studied the evolution of SMBH binaries by carrying out direct N-body simulations of mergers of galaxies having SMBHs at their centers. We used different density profiles and mass ratios of the merging galaxies and studied SMBH binary hardening rates, shapes of the merger remnants and estimated the mass ejected by the binary due to the gravitational slingshot effect. We also estimated the full time to the coalescence for the SMBHs in binaries.

Chapter 7 explains the methods and results of our study of SMBH binaries in equal mass galaxy mergers. We studied the N- dependence in the binary hardening rates and used these hardening rates to estimate the coalescence time of SMBH binaries. We also analyze the shapes of merger remnants.

In Chapter 8, we extended the study to galaxy mergers with different mass ratios. We also used different density profiles for merging galaxies and studied the hardening rates, merger induced triaxiality and mass deficits created by inspiraling black holes.

Chapter 9 presents the result of our study of binary SMBH evolution from the late stage of the realistic galaxy merger simulations of Milky Way type galaxies . The early phase of this study included star formation and accretion onto the black holes.

Key points in this review

- Supermassive black holes are correlated to their host galaxies through various relations.

- There is direct observational evidence of two well separated ($\sim$ 1 pc - 1 kpc) accreting SMBHs in a single galaxy nucleus.

- Several phenomena observed at the centers of galaxies can be explained by models of SMBH binary in the processes of coalescing or already coalesced.

- In spherical galaxy models, the separation of SMBH binary stalls at an approximate separation of one parsec referred to as "Final Parsec Problem".

Chapter 3

Galaxy Models and N-body Simulations

<div style="background-color: yellow;">

This Chapter reviews the following aspects of numerical modeling

1. Analytical models that we use to create galaxies in equilibrium for numerical investigations of SMBH evolution.

2. How to set up a galaxy in equilibrium (set up of Bahcall-Wolf cusp)

3. A brief summary of the numerical codes that we use to evolve our galaxy models and investigate the orbital decay of SMBHs towards the centers of the galaxies and the evolution of the SMBH binaries.

</div>

Despite the fact that gravity is the weakest force by far of the four fundamental forces (strong nuclear force, weak nuclear force, electromagnetic force and gravitational force), it dominates all other forces at large distances. Gravitational systems from planetary systems to star clusters to galaxies and the large scale structure of the universe can be described by an ensemble of point masses interacting gravitationally with each. In order to study the dynamical evolution of such systems, one needs to solve a large number of coupled differential equations. Numerical modeling has become a basic method, alongside observations and pure theory, to study the dynamical evolution of astrophysical objects. It allows astrophysicists to provide theoretical insights into physical processes at work in these objects. Gravitational systems can be classified in two classes "collisional systems" and "collision-less systems" – determined by whether or not the "two-body relaxation" timescale $T_{\rm r}$ is shorter than lifetime of the system (Spitzer 1987):

$$T_{\rm r} = \frac{0.13\sigma^3}{G^2 m_\star \rho \ln\Lambda}, \tag{3.1}$$

where G is the universal gravitational constant, $m_\star$ is the mean mass of the stellar population, σ is the velocity dispersion, ρ is the density and $\ln\Lambda$ is the Coulomb logarithm. Examples of collisional systems are dense objects like globular star clusters and galactic centers. Systems such as dark matter halos and galaxies have relaxation times much longer than the age of the Universe and hence can be treated as collision-less systems.

The dynamical modeling of stellar system dates back to the very first light bulb experiment of Holmberg (1941) who followed the evolution of a 37 particle system. The computer simulations

started with the first such calculation performed by von Hoerner (1960) at Astronomisches Rechen-Institut (ARI) in Heidelberg with 16 particles. Aarseth (1963) studied the dynamical evolution of galaxy clusters using up to 100 particles. For collision-less system fast and efficient algorithms such as particle-mesh (PM) codes and tree codes (Barnes & Hut 1986) were developed in 1980's. For tree codes and PM codes the computational cost increases roughly as $N\ln N$. With recent advances in computer power and massive parallelization on thousands of cores collision-less N-body codes can handle very large particle number simulations (Springel et al. 2008). On the other hand the key algorithms for collisional N-body (direct N-body) simulations were developed early on (Aarseth 1963, Ahmad & Cohen 1973, Aarseth & Zare 1974, Heggie 1974) and made public. Special purpose hardware boards, called GRAPEs, were developed to achieve high performance in the gravity calculations for direct N-body codes. For these codes the computational cost scales as $\mathcal{O}(N^2)$. Using several GRAPE-6A cards in parallel, Harfst et al. (2007) studied the evolution of a star cluster using up to 4 million particles. Recently direct N-body codes have been used on parallel supercomputer clusters accelerated by many-core graphical processing units (GPU) with the help of dedicated N-body libraries (Gaburov et al. 2009) to study the dynamics of supermassive black holes in galaxy mergers using up to a million particles (Khan et al. 2011, Preto et al. 2011).

3.1   Models for Spherical System

In order to setup a galaxy for numerical investigations, a smooth equilibrium model is needed for the probability distribution to have a system in dynamical equilibrium. In isotropic spherical systems, the gravitational potential, Φ, and the density, ρ, depend only on one dimension, the distance r from the center of the system. Spherical symmetry leads to $\rho(\vec{r}) \to \rho(r)$ and $\Phi(\vec{r}) \to \Phi(r)$. The gravitational potential and density are related through Poisson's equation:

$$\Delta\Phi(r) = 4\pi G\rho(r). \tag{3.2}$$

The amount of mass enclosed by a sphere of radius r is called the *cumulative mass distribution*, $M(r)$

$$M(r) = \int_0^r 4\pi(r')^2\rho(r')dr'. \tag{3.3}$$

The phase space distribution function depends only on the energy per unit mass $E = \frac{1}{2}v^2 + \Phi(r)$ and can be calculated from the Eddington formula (Binney & Tremaine 1987),

$$f(E) = \frac{1}{\sqrt{8}\pi^2}\frac{d}{dE}\left[\int d\Phi \frac{1}{\sqrt{\phi - E}}\frac{d\rho}{d\Phi}\right]. \tag{3.4}$$

Here we describe commonly used analytical models for star clusters, elliptical galaxies and the bulges of spiral galaxies.

3.1.1   The Plummer Model

The Plummer (1911) model is widely used to generate initial conditions for star cluster simulations. This model is an analytic solution of the Lane-Emden equation corresponding to stellar polytrope of index 5. In this chapter and others to follow we shall use gravitational constant $G = 1$, total mass of the system $M = 1$ and scale radius (plummer radius) $a = 1$ for convenience, unless otherwise is mentioned. The density distribution, cumulative mass profile and potential of the Plummer model are :

$$\rho(r) = \frac{3}{4\pi} \cdot \frac{1}{(1 + r^2)^{5/2}}, \tag{3.5}$$

$$M(r) = r^3(1+r^2)^{-3/2}, \tag{3.6}$$

$$\Phi(r) = -(1+r^2)^{-1/2}. \tag{3.7}$$

respectively.

3.1.2 The Hernquist Model

One of the most successful model for elliptical galaxies and bulges of disk galaxies is the Hernquist model (Hernquist 1990). The density profile, mass profile and potential are

$$\rho(r) = \frac{1}{2\pi} \frac{1}{r \cdot (1+r)^3}, \tag{3.8}$$

$$M(r) = r^2(1+r)^{-2}, \tag{3.9}$$

$$\Phi(r) = -(1+r)^{-1}. \tag{3.10}$$

respectively. Well inside the scale radius the Hernquist profile has a stellar density proportional to r^{-1} and well outside the scale radius its density drops as r^{-4}.

3.1.3 The Dehnen/Tremaine Model

Dehnen (1993) and Tremaine et al. (1994) presented a one-parameter family of isotropic spherical models for stellar systems. Here we describe the η- models of Tremaine et al. (1994) in more detail.

The density distribution of the "η-model" is given by

$$\rho(r) = \frac{\eta}{4\pi} \cdot \frac{1}{r^{3-\eta} \cdot (1+r)^{1+\eta}}, \tag{3.11}$$

Well outside scale radius (1 in our model units), all η-models have $\rho \propto r^{-4}$ and well inside scale radius density goes with $r^{3-\eta}$. Hernquist model corresponds to $\eta = 2$.

The cumulative mass profile for the η-models is given below

$$M(r) = \frac{r^\eta}{(1+r)^\eta}, \tag{3.12}$$

and the gravitational potential is

$$\Phi(r) = \frac{1}{\eta - 1} \left[\frac{r^{\eta-1}}{(1+r)^{\eta-1}} - 1 \right] \quad , \quad \eta \neq 1 \tag{3.13}$$

and for $\eta = 1$, the potential is -$\ln(1 + 1/r)$.

Some of the η-models ($\eta = 0.5, 1, 1.5, 2, 3$) have analytic expressions for the distribution functions (DF).

3.1.4 η-Models With a Central Black Hole

Here we describe the η-model modified to contain a central supermassive black hole of mass $M_\bullet$. The total mass in stars is still unity and the stellar density profile is still described by equation 3.11. The main effect of the black hole is to modify the potential:

$$\Phi_{\bullet\star}(r) = \Phi(r) - \frac{M_\bullet}{r} \tag{3.14}$$

We used a numerically computed distribution function in order to reproduce $\rho(r)$ (equation 3.11) in the combined potential of the SMBH and the stars in dynamical equilibrium. These models are used to set up initial conditions for galaxy models used in Chapters 7 and 8 to study SMBH binary evolution in galaxy mergers. Matsubayashi et al. (2007) modified the η- model with a central SMBH. The stellar density distribution of their model is given as

$$\rho(r) = \frac{\eta}{4\pi} \cdot \frac{1}{r^{3-\eta}(1+r^2)^{1+\eta/2}}, \tag{3.15}$$

One main difference of this model with original η- model is that it has an outer slope of -5 instead of -4. This sharp cutoff guarantees high particle resolution inside core radius as compared with the models having outer slope of -4. Thus this model is useful for studying the dynamics of black holes at the center of single a galaxy. We use it to study the orbital decay of a less massive SMBH inside the sphere of influence of a more massive black hole due to dynamical friction (Chapter 6). The mass profile and distribution function of the model (equation 3.15) are

$$M_\eta(r) = M_\eta \frac{r^\eta}{(1+r^2)^{\eta/2}} \tag{3.16}$$

and

$$f(\epsilon) = f_0(\epsilon)^{7/2}(\epsilon_0^s + \epsilon^s)^{-(\eta+2/\eta)} \tag{3.17}$$

respectively.

Here $\epsilon = -E$,

$$\epsilon_0 = (f_1/f_0)^{-1/(\eta+2)} \tag{3.18}$$

$$f_0 = \frac{\eta M_\eta \Gamma(4-\eta)}{2^{7/2}\pi^{5/2}M_\bullet^{3-\eta}\Gamma(5/2-\eta)} \tag{3.19}$$

$$f_1 = \frac{8\sqrt{2}}{7\pi^3}\eta M_\eta \tag{3.20}$$

Here with $s = 5$ and $\eta = 5/4$, these equations can be used to construct BW cusp in approximate equilibrium. The constant f_0 represents the BW cusp, f_1 the Plummer model and ϵ_0 is the transition threshold in energy.

Figure 3.1 shows the density profile and mass profile of various galaxy models that we use to study the evolution of SMBHs in single galaxy or galaxy mergers. They include Plummer model which has a constant density core in the center, shallow cusps with $\eta = 2.5$ and $\eta = 2.0$ (Hernquist profile) that we use to model the centers of bright elliptical galaxies and steep power law density cusps with $\eta = 1.5$ (Dehnen models) and $\eta = 1.25$ (Bahcall-Wolf cusp) representing density distribution around supermassive black holes at the centers of faint ellipticals and the bulges of spiral galaxies. As η decreases more and more mass is added to the central part of the cusp. Also one can observe from the figure that that the extended η-model of Matsubayashi et al. (2007) has significantly more mass inside the scale radius than the η-model of Tremaine et al. (1994).

Figure 3.1: **Top:** Figure shows the density profile for Plummer model, shallow cusp ($\eta = 2.5$), Hernquist model, Dehnen model ($\eta = 1.5$), Bahcall-Wolf cusp (equation 3.15 with $\eta = 1.25$) and Bahcall-Wolf cusp (equation 3.11 with $\eta = 1.25$) respectively.
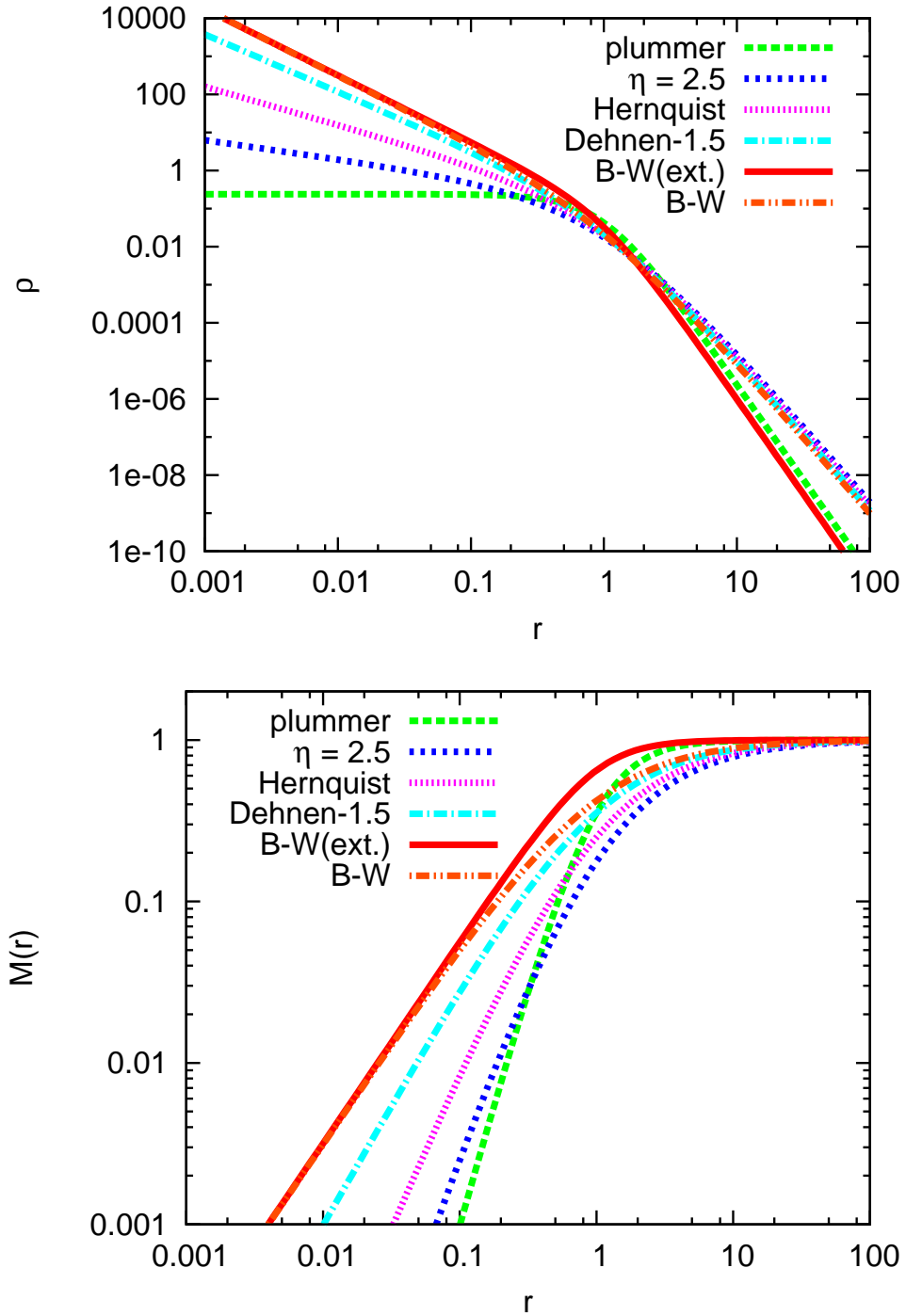**Bottom:** Figure shows the mass interior to radius r for Plummer model, shallow cusp ($\eta = 2.5$), Hernquist model, Dehnen model ($\eta = 1.5$), Bahcall-Wolf cusp (equation 3.15 with $\eta = 1.25$) and Bahcall-Wolf cusp (equation 3.11 with $\eta = 1.25$) respectively.

3.2   Initial Setup

In this section we shall describe how to generate initial positions and velocities for the particles representing a model galaxy. We shall present the procedure only for model described by equation 3.15. Following same steps one can generate initial conditions for all the models described above. In order to generate positions for the particles one needs the cumulative mass profile of the model while in order to assign the velocities of the particles, the energy distribution function is required. We choose $\eta = 5/4$ in equation (3.16) which corresponds to a Bahcall-Wolf cusp. The cumulative mass profile $M(r)$ is essentially a probability distribution function (PDF). The PDF can be realized using Monte Carlo sampling. We invert the function $M(r)$,

$$M(r) = \frac{r^{1.25}}{(1+r^2)^{.625}}, \tag{3.21}$$

into $r(M)$

$$r = \frac{1}{(M^{-1.6}(r) - 1)^{0.5}} \tag{3.22}$$

In order to give a distance r to the star, we generate a random number X_1 and equate $M(r)$ to this random number X_1. So the distance is selected as

$$r = \frac{1}{(X_1^{-1.6} - 1)^{0.5}} \tag{3.23}$$

Three dimensional positions (x, y, z) of the star are selected on the sphere of radius r. Again two random numbers X_2 and X_3 are generated and the coordinates x, y, z are computed as follow:

$z = z(1 - 2X_2)r$, $x = (r^2 - z^2)^{1/2}\cos(2\pi X_3)$, $y = (r^2 - z^2)^{1/2}\sin(2\pi X_3)$.

We compute the potential for the star at distance r due to SMBH and stellar distribution

$$\Phi_{\bullet\star} = -\left[\frac{M_\bullet}{r} + [4 - \frac{4}{(1+\frac{1}{r})^{1/4}}] \right]. \tag{3.24}$$

The escape velocity at distance r from the center is

$$V_e = \left[\frac{2M_\bullet}{r} + 2[4 - \frac{4}{(1+\frac{1}{r})^{1/4}}] \right]^{1/2} \tag{3.25}$$

and the energy distribution function 3.17 is proportional to

$$f(q) \propto \frac{q^2(1-q^2)^{3.5}}{\left[0.58 + \frac{V_e^{10}}{32}(1-q^2)^5 \right]^{13/20}} \tag{3.26}$$

Here $q = V/V_e$. The maximum value of $f(q)$ is $f_{\max} = 0.14$ and q has a range between 0 and 1. We use Neumann's acceptance-rejection method to assign velocities to the particles. We generate two more normalized random numbers X_4 and X_5. If $f_{\max} \times X_5$ is less than $f(X_4)$, we adopt $q = X_4$. Otherwise we generate a new pair of random numbers until the condition is fulfilled. The absolute velocity of the particle is then obtained by $V = q \times V_e$. Two new random numbers X_6 and X_7 are generated to assign the velocity components V_x, V_y and V_z.

$V_z = (1 - 2X_6)V$, $V_x = (V^2 - V_z^2)^{1/2}\cos(2\pi X_7)$ and $V_y = (V^2 - V_z^2)^{1/2}\sin(2\pi X_7)$

The procedure is repeated until positions and velocities are assigned to all N stars in galaxy model.

3.3 Numerical Codes

In this section we briefly describe the numerical codes that we use to study the dynamics and evolution of SMBHs in single galaxies or in galaxy mergers. SMBHs reside in the galactic nuclei, which are collisional systems, so we used direct N-body codes ϕ-GRAPE and Φ-GPU to carry out our simulations. For the orbital decay of SMBHs due to dynamical friction in outskirts of galaxies the system is collision-less and furthermore, the density drops rapidly (r^{-4} or r^{-5}) as we move far away from scale radius in all our models and in order to gain sufficient resolution higher particle numbers are necessary. The particle mesh code, SUPERBOX, which can accommodate a much higher number of particles when compared to direct N-body code such as ϕ-GRAPE or Φ-GPU, is used.

3.3.1 ϕ-GRAPE

ϕ-GRAPE (Harfst et al. 2007) is a parallel, direct-summation N-body code that uses special-purpose hardware to compute the pairwise gravitational forces between all particles:

$$\mathbf{F}_i = -m_i \sum_{j=1,j\neq i}^{N} \frac{m_j(\mathbf{r}_i - \mathbf{r}_j)}{(|\mathbf{r}_i - \mathbf{r}_j|^2 + \epsilon^2)^{3/2}}. \tag{3.27}$$

Here m_i and r_i are the mass and position of the ith particle and ϵ is a force softening parameter. ϕ-GRAPE integrates the equations of motion using a fourth-order Hermite integrator with individual block time steps .

Hermite Scheme

Let us assume that $\vec{x}_0$ and $\vec{v}_0$ are the position and velocity of the particle at time $t = t_0$. Then position and velocity of the particle can be predicted for time $t = t_1$ using

$$\vec{x}_p(t_1) = \vec{x}_0 + \vec{v}_0\Delta t + \frac{1}{2}\vec{a}_0\Delta t^2 + \frac{1}{6}\dot{\vec{a}}_0\Delta t^3 \tag{3.28}$$

$$\vec{v}_p(t_1) = \vec{v}_0 + \vec{a}_0\Delta t + \frac{1}{2}\dot{\vec{a}}_0\Delta t^2 \tag{3.29}$$

Where $\Delta t = t_1 - t_0$. The acceleration, $\vec{a}_0$, and jerk, $\dot{\vec{a}}_0$, can be calculated directly without need for differentiation:

$$\vec{a}_0 = \sum_{j=1,j\neq i}^{N} Gm_j \frac{\vec{r}_{ij}}{(r_{ij}^2 + \epsilon^2)^{3/2}} \tag{3.30}$$

$$\dot{\vec{a}}_0 = \sum_{j=1,j\neq i}^{N} Gm_j \left[\frac{\vec{v}_{ij}}{(r_{ij}^2 + \epsilon^2)^{3/2}} + \frac{3.(\vec{v}_{ij}.\vec{r}_{ij})\vec{r}_{ij}}{(r_{ij}^2 + \epsilon^2)^{5/2}}\right] \tag{3.31}$$

Using the predicted position and velocity, the acceleration (Eq. 3.30) and jerk (Eq. 3.31) can be updated. The corrected positions and velocities are then calculated from updated acceleration and jerk:

$$\vec{x}(t_1) = \vec{x}_p + \frac{\Delta t^4}{24}\vec{a}_0^{(2)} + \frac{\Delta t^5}{120}\vec{a}_0^{(3)} \tag{3.32}$$

and

$$\vec{v}(t_1) = \vec{v}_p + \frac{\Delta t^3}{6}\vec{a}_0^{(2)} + \frac{\Delta t^4}{24}\vec{a}_0^{(3)} \tag{3.33}$$

where $\vec{a}_0^{(2)}$ and $\vec{a}_0^{(3)}$ are second and third time derivatives of acceleration.

The large dynamic range in time involved in collisional systems makes it necessary to use individual time steps for each particle. The time step of particle i at time t is computed using the formula (Makino & Aarseth 1992):

$$\Delta t_i = \sqrt{\eta \frac{|\vec{a}(t)||\vec{a}^{(2)}(t)| + |\dot{\vec{a}}(t)|^2}{|\dot{\vec{a}}(t)||\vec{a}^{(3)}(t)| + |\vec{a}^{(2)}(t)|^2}} \tag{3.34}$$

where $\vec{a}$ is the acceleration of ith particle and the superscript (k) indicates the order of the time derivative. The time-step parameter η is set typically set to 0.02 but we also use 0.01 in some cases to achieve higher accuracy.

The acceleration and its time derivative are calculated using several GRAPE6A cards in parallel. In order to minimize communication among different nodes an MPI parallelization strategy is employed. For the simulations in a dense cusp around a massive central SMBH, we use a specially modified version of the ϕ-GRAPE code. We include the central SMBH as an external potential in order to avoid the relatively large random motion of a live SMBH due to the small particle number. The time step criterion is also modified: we add a reduction factor for the BH time step, which compensates the effect of its relatively small acceleration compared to the field particles.

3.3.2 Φ-GPU

The Φ-GPU code is also used for direct N-body simulations, and has a higher order Hermite integration scheme and individual block time steps (the code supports time integration of particle orbits with 4th, 6th and even 8th order schemes).

The code is fully parallelized with the use of MPI library. On each node, the code uses many cores of the GPU hardware. The code is based on an earlier `C` code version[1] for `GRAPE6a` clusters (Harfst et al. 2007). The new code is written from scratch in `C++` and based on (Nitadori & Makino 2008) earlier CPU serial N-body code (YEBISU). The MPI parallelization was done in the same "j" particle parallelization mode as in the earlier Φ-GRAPE code (Harfst et al. 2007). All the particles are divided equally between the working nodes (using the `MPI_Bcast()` commands) and in each node fractional forces are calculated only for the, so called, "active" – "i" particles at the current time step. The full forces from all the particles acting on the active particles we get after using the global `MPI_Allreduce()` communication routines.

The current version of ΦGPU code uses native GPU support and direct code access to the GPU using only the NVIDIA native CUDA library[2]. The multi GPU support is achieved through MPI parallelization. Each MPI process uses only a single GPU, but usually two or more MPI processes per node are started (to use effectively the multi core CPU's and the multi GPU's on our clusters) are.

This code uses different softening parameter ϵ (if required) for different components like SMBHs, dark matter and stars. More details and also the ΦGPU code public version will be published in an upcoming publication (Berczik et al.).

3.3.3 SUPERBOX

The particle mesh (PM) code Superbox (Bien et al. 1991, Fellhauer et al. 2000) is a highly efficient code with fixed time step for galaxy dynamics, where more than 10 million particles per galaxy

---

[1] `ftp://ftp.ari.uni-heidelberg.de/staff/berczik/phi-GRAPE/`
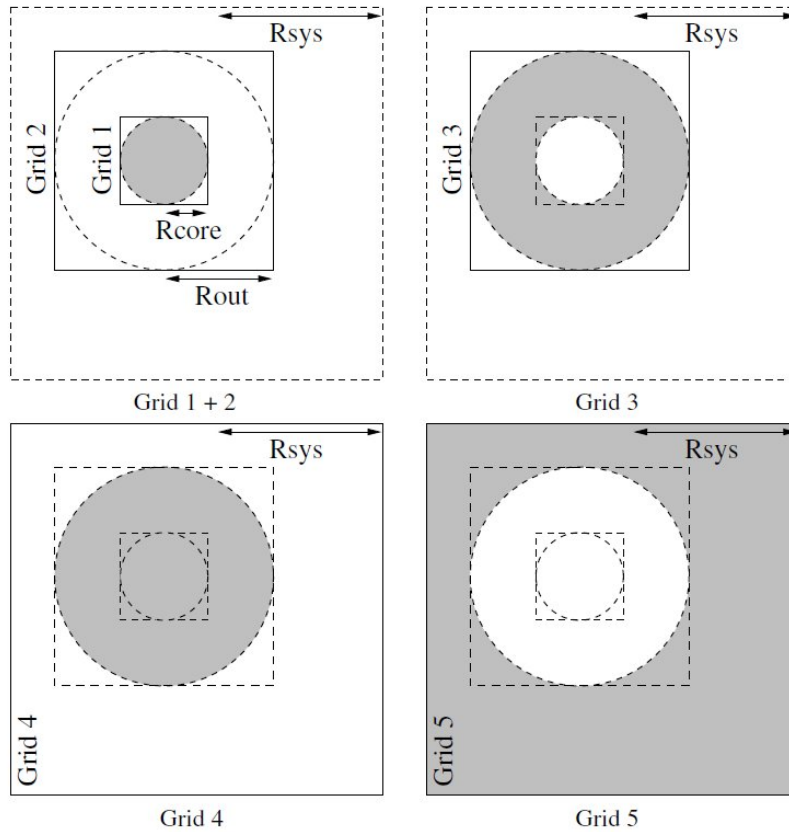[2] `http://www.nvidia.com/object/cuda_home_new.html`

Figure 3.2: The five grids that are used in SUPERBOX. Gray section in each grid shows the region filled with particles in respective grid. Figure taken from Bien et al. (2008).

in co-moving nested grids for high spatial resolution at the galaxy centers can be simulated. The code is intrinsically collision-less, which is necessary for long-term simulations of galaxies. Another advantage of a PM code is the large particle number which can be simulated in a reasonable computing time (up to a few days or a week per simulation). Three grid levels with different resolutions are used which resolve the core of each component/galaxy, the major part of the component/galaxy and the whole simulation area. The spatial resolution is determined by the number of grid cells per dimension $N_c = 2^m$ and the size of the grids. The SMBH is included as a moving particle with own sub-grids for high spatial resolution in its vicinity. The grid sizes are chosen such that the full orbit of the secondary BH falls into the middle grid. All Superbox runs were performed using the Astronomisches Rechen-Institut (ARI) fast computer facilities with no special hardware. We also tried to use SUPERBOX to study the orbital decay of SMBH due to dynamical friction in Bahcall Wolf cusp around a primary SMBH. We noticed that the cusp was not stable and the Lagrange radii (radius enclosing fraction of cusp mass) were expanding soon after the start of the run. The reason could be the use of fixed time steps for each particle. In the center, close to primary SMBH, one needs very small time steps to integrate the orbits of stars correctly.

3.3.4 Semi-analytic Code - INTGC

The program INTGC developed by Andreas Ernst is an integrator for orbits in an analytic background potential of a galactic center including the Chandrasekhar formula for dynamical fric-

tion. Different analytic models with their χ functions and a variable Coulomb logarithm Just & Peñarrubia (2005) are implemented. An 8th-order composition scheme is used for the orbit integration Yoshida (1990); for the coefficients see McLachlan & Scovel (1995). Since the symplectic composition schemes are by construction suited for Hamiltonian systems, the dissipative friction force requires special consideration. It is implemented in INTGC with an implicit midpoint method Mikkola & Aarseth (2002). Four iterations turned out to guarantee an excellent accuracy of the scheme. The gravitational potential and density are given analytically.

Chapter 4

Dynamical Friction Force

Contents of this Chapter

1. Chandrasekhar dynamical friction formula; we consider this formula as the working ansatz for our study.

2. Power law density profiles, calculation of their distribution functions and simplification of physical models to approximate power law cusps in the outskirts.

3. Introduction to position and velocity dependent Coulomb logarithm.

4. Self consistent cumulative distribution functions to calculate dynamical friction force and their comparison with the standard Maxwellian.

5. Brief discussion of dynamical friction force in a gaseous medium.

   Note: The contents of this Chapter are based on paper by Just, A., Khan, F. M., Berczik, P., Ernst, A., & Spurzem, R. 2011, MNRAS, 411, 653

When a massive object moves in a sea of background stars, it interacts gravitationally with them. The two body encounters between perturber and stars sum up and result in deceleration of the perturber, known as dynamical friction. The deflected particles form a wake behind the massive object. The important consequences of dynamical friction in collision-less astronomical systems show up as the orbital decay of the SMBH in galaxy mergers, sinking of satellite galaxies in the dark matter halo of host galaxies, mass segregation in star clusters, etc. Many researchers think it is sufficiently well understood and studied since the classical work of Chandrasekhar (1942) and the many follow-ups. There is a duality between a collective gas-dynamic approach, studying responses in a continuum through which a test body moves, and a kinetic or particles approach where a test body moves through a sea of light particles. As is known since long Bondi & Hoyle (1944), Rephaeli & Salpeter (1980) under certain limits both approaches can yield similar results.

Dynamical friction is quantified by the famous Chandrasekhar formula which considers the motion of a massive object M moving with velocity V in a uniform background with homogeneous density ρ of noninteracting light particles each having mass m (Binney & Tremaine 1987)

$$\dot{V} = \frac{-4\pi G^2 \rho M}{V^2} \chi \ln \Lambda \quad \text{with} \quad \chi = \frac{\rho(< V)}{\rho} \tag{4.1}$$

Here Λ is called Coulomb logarithm and χ the fraction of background particles with velocity smaller than V. The Coulomb logarithm is given by the ratio of maximum to minimum impact parameter. For maximum impact parameter, Chandrasekhar & von Neumann (1942) suggested cut off at roughly inter-particle distance. Later, researchers used a radial distance of the object and also the size of the host system for the upper cutoff. For χ, it is standard practice to use Maxwellian distribution for the velocities of the background stars. In general the functions χ and Λ depend on the velocity of the massive object and on the properties of the background system.

In this chapter, improvements in dynamical friction formula are presented by suggesting a varying Coulomb logarithm with the choice of self consistent distribution functions for the calculation of the χ value for variety of power law and physical models.

4.1 Power Law Profiles

For analytic estimations it is usually a first approach to use idealized power law distributions for the background distribution of stars. For both cases (self-gravitating and Kepler potential) the density profile of the cusp and the cumulative mass profile can be approximated by the functions

$$M(y) \;=\; M_{\mathrm{c}} + M_{\mathrm{t}} y^{\eta} \quad \text{with} \quad y = \frac{R}{R_0} \tag{4.2}$$

$$\rho(y) \;=\; \rho_0 y^{3-\eta} \quad \text{with} \quad \rho_0 = \frac{(\eta)M_{\mathrm{t}}}{4\pi R_0^3}. \tag{4.3}$$

It is comfortable to normalize all quantities to the initial values of the orbit. The initial position of the object is $R_0 = R(t=0)$ leading to $y_0 = 1$, the enclosed mass is $M_0 = M(y_0)$, and the circular velocity at R_0 is

$$V_{\mathrm{c},0} = V_{\mathrm{c}}(R_0) = \sqrt{GM_0/R_0}. \tag{4.4}$$

For the self-gravitating case one simply sets $M_{\mathrm{c}} = 0$ leading to $M_0 = M_{\mathrm{t}}$ via Eq. 4.3. In the Kepler case one must set $M(y) \approx M_{\mathrm{c}} = const.$ leading to the circular velocity with

$$V_{\mathrm{c}}^2 = GM_{\mathrm{c}}/R_0 \, y^{-1} \tag{4.5}$$

and the local density determined by M_{t}.

All velocities are normalized to the local circular velocity V_{c} instead of the velocity dispersion σ by

$$u = v/V_{\mathrm{c}} \quad \text{and} \quad U = V/V_{\mathrm{c}} \tag{4.6}$$

U can be converted to X with the normalized circular velocity X_{c} by

$$X = X_{\mathrm{c}} U \quad \text{with} \quad X_{\mathrm{c}}^2 \equiv \frac{V_{\mathrm{c}}^2}{2\sigma^2} \tag{4.7}$$

The velocity dispersion can be obtained by integrating the Jeans equation involving the second moment of the velocity distribution function (Binney & Tremaine 1987)

$$\sigma^2(y) = \frac{-G}{\rho(y)R_0} \left[\int \frac{\rho(y')M(y')}{y'^2} dy' + C'' \right] \tag{4.8}$$

where the integration constant C'' depends on the inner and outer boundary conditions.

Substituting $M(y)$ and $\rho(y)$ from Eq. 4.2 and Eq. 4.3 yields

$$\sigma^2(y) \;=\; \begin{cases} \dfrac{GM_0}{2R_0(2-\eta)} y^{\eta-1} = \dfrac{V_{\mathrm{c}}^2}{2(2-\eta)} & 0 < \eta < 2 \\[2ex] \dfrac{GM_0}{R_0} y\left(-\ln y + C\right) & \eta = 2 \\[2ex] C''' y^{3-\eta} & 2 < \eta < 3 \end{cases} \tag{4.9}$$

Inserting Eq. 4.9 into Eq. 4.7 we find

$$
X_c^2 = \begin{cases}
2 - \frac{\eta}{2} & \eta < 2.5 & \text{Kepler} \\
2 - \eta & \eta < 2 & \text{self-grav.} \\
[2(C - \ln y)]^{-1} & \eta = 2 & \text{self-grav.} \\
C' \, y^{(2\eta - 4)} & 2 < \eta \leq 3 & \text{self-grav.}
\end{cases}
\tag{4.10}
$$

which is independent of position y for the Kepler potential and the self-gravitating cusp with $\eta < 2$. For a shallow self-gravitating cusp with $\eta > 2$ the integration constant C' depends on the outer boundary conditions of the realization of the cusp.

The velocity dispersion in self-gravitating cusps behaves quite different for different η (Tremaine et al. 1994). For $\eta > 2$ the kinetic pressure $\rho\sigma^2$ converges to a finite value at the center, which depends on the outer boundary conditions. The transition case with $\eta = 2$ is of special interest, because it corresponds to the $\rho \propto y^{-1}$ cusp as in the standard NFW cusp and in the Hernquist model. In this case the kinetic pressure $\rho\sigma^2 \propto (C - \ln y)$, where the constant C is also determined by the outer boundary conditions. In a Kepler potential the isotropic distribution function degenerates for $\eta = 5/2$, because it is completely dominated by particles with low binding energy. Dependent on the outer boundary conditions the distribution function can vary between a δ-function at the escape velocity (i.e. at $E = 0$) and a power law $\propto |E|^{-1}$ with some cutoff at $E \approx 0$.

4.1.1 Distribution Functions

The distribution function of a power law cusp (eqs. 4.2 and 4.3) is given by

$$
f(E) = \begin{cases}
K|E|^p & \eta < 2.5 & \text{Kepler} \\
K|E|^p & 0 \leq \eta < 3 & \text{self-grav.} \\
K \exp(-E/\sigma^2) & \eta = 1 & \text{self-grav.}
\end{cases}
\tag{4.11}
$$

with normalization constant K and energy $E = \Phi + v^2/2$, where the zero point of the potential is at the center for self-gravitating cusps with $\eta > 1$ and at infinity for the Kepler case and self-gravitating cusps with $\eta < 1$. The dependence of the power law index p on η is different for the Kepler and the self-gravitating case (see below). Lets consider the two cases where Φ is given by the self-gravitating potential of the cusp or the Kepler case with Φ dominated by the central mass M_c. The natural normalization of the velocity is $\sqrt{|2\Phi|}$, which corresponds to the escape velocity for vanishing potential at infinity. For practical use it is more comfortable to normalize the velocities to the circular velocity (u from Eq. 4.6). Let us introduce the normalized 1-dimensional distribution function $F(u)$ by

$$
4\pi v^2 f(E)dv = \rho F(u)du.
\tag{4.12}
$$

which can be written in the form

$$
F(u) = \begin{cases}
K'u^2 \left(1 + \xi u^2\right)^p & \eta < 2.5 & \text{Kepler} \\
K'u^2 \left(1 + \xi u^2\right)^p & 0 < \eta < 3 & \text{self-grav.} \\
K'u^2 \exp\left(-u^2\right) & \eta = 1 & \text{self-grav.}
\end{cases}
\tag{4.13}
$$

$$
\text{with} \quad \xi = \frac{V_c^2}{2\Phi}
$$

Self-Gravitating Cusps

The constants in Eqs. 4.11 and 4.13 are given by

$$
\xi = \frac{\eta - 1}{2} \quad ; \quad p = \frac{3 + \eta}{2(1 - \eta)}
\tag{4.14}
$$

and

$$
K = \begin{cases}
\frac{\rho_0}{4\pi\sqrt{2}B\left(\frac{3}{2},1+p\right)} \left(\frac{V_{c0}^2}{1-\eta}\right)^{-p-\frac{3}{2}} & \eta < 1 \\[3ex]
\frac{\rho_0}{\pi\sqrt{\pi}} V_{c0}^{-3} & \eta = 1 \\[3ex]
\frac{\rho_0}{4\pi\sqrt{2}B\left(\frac{3}{2},-p-\frac{3}{2}\right)} \left(\frac{V_{c0}^2}{\eta-1}\right)^{-p-\frac{3}{2}} & 1 < \eta < 3
\end{cases}
\tag{4.15}
$$

$$
K' = \begin{cases}
\frac{2|\xi|^{3/2}}{B\left(\frac{3}{2},1+p\right)} & \eta < 1 \\[3ex]
\frac{4}{\sqrt{\pi}} & \eta = 1 \\[3ex]
\frac{2|\xi|^{3/2}}{B\left(\frac{3}{2},-p-\frac{3}{2}\right)} & 1 < \eta < 3
\end{cases}
\tag{4.16}
$$

Here the beta function $B(x,y) = \Gamma(x)\Gamma(y)/\Gamma(x+y)$ (see Gradshteyn I.S. (1980) (8.38)).

Kepler Potential

In the Kepler potential of a central SMBH (without the mean field contribution of the stellar cusp) one finds for the constants

$$
\xi = -\frac{1}{2} \quad ; \quad p = \frac{3}{2} - \eta \, .
\tag{4.17}
$$

and

$$
K = \frac{\rho_0}{4\pi\sqrt{2}B(3/2,1+p)} \left(V_{c0}^2\right)^{-p-3/2}
\tag{4.18}
$$

$$
K' = \frac{2\,|\xi|^{3/2}}{B\left(3/2,1+p\right)}
\tag{4.19}
$$

In a pioneering work Peebles (1972) analyzed the structure of a stellar cusp in a Kepler potential of a central SMBH, which is stationary for times large compared to the relaxation time. Unfortunately he derived incorrect values for p and thus η. The correct derivation can be found in Shapiro & Lightman (1976) using scaling arguments and in Bahcall & Wolf (1976) using a Fokker-Planck analysis. The resulting so-called Bahcall-Wolf (BW) cusp is given by $p = 1/4$ leading to $\eta = 5/4$ and the well-known density profile $\rho \propto y^{-7/4}$. In a Hernquist cusp (HE) with $\eta = 2$ we have a shallow density profile $\rho \propto y^{-1}$ and find $p = -1/2$ leading to a diverging 1-D distribution function at the escape velocity. The outskirts of Dehnen (DE) and Plummer (PL) distributions with densities $\rho \propto y^{-4}$ and $\rho \propto y^{-5}$ correspond to $\eta = -1$ and $\eta = -2$ with $p = 5/2$ and $p = 7/2$, respectively.

In Fig. 4.1 the distribution functions $F(u)$ are shown for different values of $\eta = 0.5, 1.0, 1.25, 1.95$ (with decreasing maximum). The thick line is the standard Maxwellian. For $\eta < 1$ the energy range is finite with $u^2 < |\xi|^{-1}$, whereas for $\eta \geq 1$ the potential is infinitely deep allowing for all velocities.

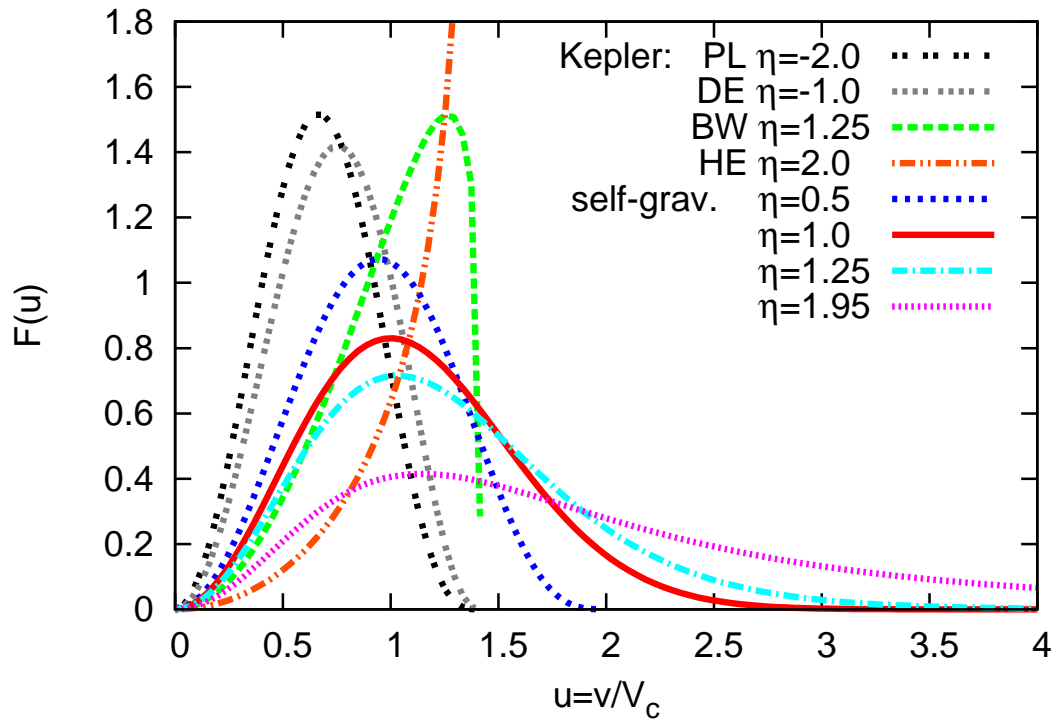Figure 4.1: Normalized 1-dim distribution function $F(u)$ for different cases as a function of normalized velocity $u = v/V_c$ (see Eq. 4.13). The sequence with $\eta = 0.5, 1.0, 1.25, 1.95$ shows a decreasing maximum. The full line is the Maxwellian ($\eta = 1$). The Kepler potential cases are labeled by PL for Plummer, DE for Dehnen outskirts, BW for the Bahcall-Wolf cusp, HE for Hernquist cusp.

4.2 Physical Models

In many simulations of stellar cusps it turned out that the setup of an initial cusp distribution in dynamical equilibrium with an unphysical outer cutoff is not stationary. The density profile evolves deep into the inner cusp region. Therefore it is necessary to set up initial particle distributions and velocities with a well-defined outer cutoff of the cusp distribution.

For the self-gravitating cusps we consider Dehnen (1993) models with an outer power law slope of -4 for the density. These models are identical to the η-models of Tremaine et al. (1994) and are already described in section 3.1.3. Here we rewrite density and cumulative mass using different normalization:

$$
\begin{aligned}
M(y) &= M_{\mathrm{t}} \left(\frac{y}{y_{\mathrm{a}} + y} \right)^{\eta} \quad y_{\mathrm{a}} = \frac{a}{R_0} \\
\rho(y) &= \frac{\rho_0}{y^{3-\eta}(y_{\mathrm{a}} + y)^{1+\eta}}, \quad \rho_0 = \frac{\eta M_{\mathrm{t}} y_{\mathrm{a}}}{4\pi R_0^3}
\end{aligned}
\tag{4.20}
$$

with Eq. 4.3 for the conversion for ρ_0. a is scale radius. Well inside the scale radius density profile of these models have slope of $-(3 - \eta)$ and well outside the scale radius all Dehnen models converge to a density slope of -4. The Jaffe and Hernquist models correspond to $\eta = 1$ and $\eta = 2$, respectively. Well inside the scale radius a the particles behave asymptotically like in the idealized power law distributions.

The Plummer model corresponding to stellar polytrope of index $n = 5$ is well known potential density pair for star cluster model. Density and cumulative mass for Plummer model (already described in section 3.1.1) are given by

$$
\begin{aligned}
M(y) &= M_{\mathrm{c}} \left(\frac{y^2}{y_{\mathrm{a}}^2 + y^2} \right)^{3/2} \quad y_{\mathrm{a}} = \frac{a}{r_p l} \\
\rho(y) &= \rho_0 \left(y_{\mathrm{a}}^2 + y^2 \right)^{-5/2}, \quad \rho_0 = \frac{3 M_{\mathrm{c}} y_{\mathrm{a}}^2}{4\pi R_0^3}
\end{aligned}
\tag{4.21}
$$

Here y_a is the Plummer radius.

For the Kepler potential case we investigate two different scenarios. In the first case we investigate power law cusps in the vicinity of a central SMBH with mass M_{c}, i.e. the BW cusp and a shallower Hernquist (He) cusp. There are no exact distribution functions known describing the Kepler potential part inside the influence radius of the SMBH and the transition to a self-gravitating outer regime. Tremaine et al. (1994) generalized their η models by including the gravitational potential of a central SMBH and derived the power law distribution function (Eqs. 4.11 and 4.17) well inside the influence radius, which is comparable to the scale radius a. In Matsubayashi et al. (2007) this approximation was adapted to a Plummer model instead of a η-model. This model has two advantages. Firstly the steeper slope in the outer part saves particles and computation time for simulations of BW cusps. Secondly the power law distribution function of the Plummer sphere is exact also in the inner part. Therefore realizations with smaller SMBH masses relative to the cusp mass are closer to equilibrium. The cumulative mass and density distribution analogous to equations (3.16) and (3.15) are given by

$$
M(y) = M_t \left(\frac{y^2}{y_{\mathrm{a}}^2 + y^2} \right)^{\eta/2}, \quad 0 < \eta \leq 3
\tag{4.22}
$$

$$
\rho(y) = \frac{\rho_0}{y^{3-\eta}(y_{\mathrm{a}}^2 + y^2)^{\eta/2+1}},
\tag{4.23}
$$

where M_t is the total mass of stars in the cusp.

The outskirts of Dehnen models (DE) and the Plummer model (PL) can also be approximated by cusps in a Kepler potential using asymptotic expansions in y. From an identification of the

density slopes for Dehnen and Plummer of -4 and -5, respectively, with $\eta_0 - 3$ in Eq. 4.3, one finds $\eta_0 = -1$ and $\eta_0 = -2$ for the outskirts (here the index 0 is used in order to distinguish it from the parameter η in the core). This leads with Eq. 4.17 to the correct distribution functions in Eq. 4.11 for the Dehnen models and the Plummer sphere in the limit of small energies. If we now identify M_t in Eq. 4.2 with the mass deficiency compared to the total mass M_c, then Eqs. 4.2 and 4.3 also hold for these cases. For the Dehnen models

$$
\begin{aligned}
M(y) &\approx M_c \left(1 - \eta y_a y^{-1}\right) = M_c + M_t y^{\eta_0} \\
\rho(y) &\approx \rho_0 y^{-4} = \rho_0 y^{\eta_0 - 3} \\
\eta_0 &= -1, \qquad M_t = -\eta M_c y_a \\
\rho_0 &= \frac{\eta M_c y_a}{4\pi R_0^3} = \frac{\eta_0 M_t}{4\pi R_0^3}
\end{aligned}
\tag{4.24}
$$

and similarly for the Plummer sphere

$$
\begin{aligned}
M(y) &= M_c \left(\frac{y^2}{y_a^2 + y^2}\right)^{3/2} \approx M_c \left(1 - \frac{3}{2} y_a^2 y^{-2}\right) \\
&= M_c + M_t y^{\eta_0} \\
\rho(y) &= \rho_0 \left(y_a^2 + y^2\right)^{-5/2} \approx \rho_0 y^{-5} = \rho_0 y^{\eta_0 - 3} \\
\eta_0 &= -2, \qquad M_t = -\frac{3}{2} M_c y_a^2 \\
\rho_0 &= \frac{3 M_c y_a^2}{4\pi R_0^3} = \frac{\eta_0 M_t}{4\pi R_0^3}
\end{aligned}
\tag{4.25}
$$

completely consistent with the power law cusp description.

4.3 Coulomb Logarithm

In derivation of Eq. 4.1, an integration over impact parameters is performed which diverges at the upper limit. So an upper cut-off must be used. Some researchers use the size of the host system, while others use the distance of spiraling perturber from the center as maximum impact parameter. Yet another group of researchers use the distance where the density drops significantly. Since this formula is applied to wide ranges of parameters, it is very useful to have the explicit parameter dependence of $\ln \Lambda$ instead of fitting a constant value for each single orbit. In Just & Peñarrubia (2005) the effect of the inhomogeneity of the background distribution on the dynamical friction force with Chandrasekhar's approach was discussed. The authors derived the approximation

$$
\ln \Lambda = \ln \frac{b_{\max}}{\sqrt{b_{\min}^2 + a_{90}^2}} \approx
\begin{cases}
\ln \left(\frac{D_r}{b_{\min}}\right) & \text{unres. or ext.} \\[2mm]
\ln \left(\frac{D_r}{a_{90}}\right) & \text{point-like.}
\end{cases}
\tag{4.26}
$$

The Coulomb logarithm depends on the maximum and minimum impact parameter $b_{\max}$ and $b_{\min}$, respectively, and for point-like objects on a_{90}, the typical impact parameter for a 90°-deflection in the 2-body encounters. Just & Peñarrubia (2005) found that the maximum impact parameter is given by the local scale-length D_r determined by the density gradient, i.e.

$$
b_{\max} = D_r \equiv \frac{\rho}{|\nabla \rho|} = \frac{R}{3 - \eta} \quad \eta \le 2.
\tag{4.27}
$$

In an isothermal sphere $b_{\max}$ is a factor of 2 smaller than the distance R to the center. In shallow cusps with $\eta > 2$ the local scale length D_r exceeds the distance to the center. In that case, the local scale-length may be substituted by R.

For point-like objects like BHs the effective minimum impact parameter a_{90} is given by the value for a 90°- deflection using a typical velocity v_{typ} for the 2-body encounters

$$a_{90} = \frac{GM_{\text{bh}}}{v_{\text{typ}}^2} \approx \frac{GM_{\text{bh}}}{2\sigma^2 + V_{\text{bh}}^2} = \frac{X_c^2}{1+X^2} \frac{M_{\text{bh}}}{M(y)} R = \frac{3\,r_g}{2(1+X^2)}\,. \tag{4.28}$$

Where $r_g = GM_\bullet/3\sigma^2$. If the motion of a point-mass is numerically derived by a code, where a_{90} is not resolved, the minimum impact parameter is determined by the effective spatial resolution of the code.

The parameter dependence of b_{max} and a_{90} leads to a position dependence of $\ln \Lambda$, which affects the decay time τ_{dec} and which also reduces the circularization of the orbits resolving a long-standing discrepancy between numerical and analytical results. Using the distance to the center as maximum impact parameter was proposed by different authors (Tremaine 1976, Hashimoto et al. 2003), but the effect on orbital evolution was never investigated in greater detail or for larger parameter sets.

On circular orbits the local scale-length D_r and the deflection parameter a_{90} are position dependent. On eccentric orbits a_{90} depends additionally on the velocity. Therefore $\ln \Lambda$ varies systematically during orbital decay and for eccentric orbits along each revolution. This has consequences on the decay time and on the evolution of orbital shape. In eccentric orbits the dynamical friction force varies strongly between apo-and peri-galacticon mainly due to the density variation along the orbit. The variation due to higher peri-center velocity and to the position dependent Coulomb logarithm weakens the differences. All these factors depend on the slope of the cusp density. That means that the effective Coulomb logarithm averaged over an orbit depends differently on the eccentricity for different values of η.

In the case of circular orbits with constant X_c the position dependence of the Coulomb logarithm (Eq. 4.26) can be parametrized by

$$\ln \Lambda = \ln(\Lambda_0 y^\beta)\,. \tag{4.29}$$

Deep in shallow self-gravitating cusps with $\eta > 2$ the contribution from the circular velocity vanishes and Λ is also described by Eq. 4.29. With Eq. 4.28 the Coulomb logarithm is

$$\beta = 1 \quad \Lambda_0 = \frac{1}{(3-\eta)} \frac{R_0}{b_{\text{min}}} \quad \text{extended or unresolved} \tag{4.30}$$

for extended objects and for point-like objects we find

$$\begin{aligned} \beta = 0 \qquad & \Lambda_0 = \frac{(6-\eta)}{(3-\eta)(4-\eta)} \frac{M_c}{M_{\text{bh}}} \quad \text{Kepler} \\ \beta = \eta \qquad & \Lambda_0 = \frac{1}{(2-\eta)} \frac{M_0}{M_{\text{bh}}} \qquad \text{self-grav., } \eta < 2 \\ \beta = 4-\eta \quad & \Lambda_0 = \frac{1}{C'} \frac{M_0}{M_{\text{bh}}} \qquad \text{self-grav., } 2 < \eta < 3 \end{aligned} \tag{4.31}$$

We see that the motion of a point-like object in a Kepler potential is also described by a constant Coulomb logarithm, because the linear dependence of D_r and a_{90} cancel. The standard case corresponds to $\beta = 0$ with R_0 instead of D_r and r_g instead of a_{90} in Eq. 4.26 leading to

$$\ln \Lambda_s = \begin{cases} \ln\left(\frac{R_0}{b_{\text{min}}}\right) & \text{unres. or ext.} \\[2ex] \ln\left(\frac{3}{2X_c^2} \frac{M_0}{M_{\text{bh}}}\right) & \text{point-like.} \end{cases} \tag{4.32}$$

4.4 Cumulative Distribution Functions

Another interesting actor in the play of dynamical friction is the χ-function: The integral over the velocity distribution of background particles. The cumulative distribution function $\chi(U)$ of the

normalized 1-dimensional distribution function $F(u)$ measures the fraction of background particles with velocities smaller than $U = V_{\mathrm{bh}}/V_{\mathrm{c}}$. The cumulative function $\chi(U)$ is related to distribution functions (Eq. 4.13) by

$$\chi(U) \quad = \quad \int_0^U F(u)du\,. \tag{4.33}$$

These self consistent distribution functions are significantly different to $\chi_{\mathrm{s}}(U)$ of the standard Maxwellian which is usually adopted for Chandrasekhar's formula. In most applications of the standard formula the local velocity dispersion is not known. Instead $X_{\mathrm{c}} = 1$ as in the singular isothermal sphere is adopted leading to the identification of $X = U$. In Fig. 4.3 the correction factors $\chi(U)/\chi_{\mathrm{s}}(U)$ entering the friction force formula Eq. 4.1 are shown. The different lines give the results for the self-gravitating cusps as a function of η. The values for the circular velocity $U = 1$ (full line) and for $U = 0.7, 1.4$ (dotted and dot-dashed line), typical values for apo- and peri-center velocities, are shown respectively. In shallow self-gravitating cusps (with $\eta \geq 1$) the efficiency of dynamical friction is reduced roughly by a factor of η due to the larger fraction of high velocity particles. In steep cusps dynamical friction is larger compared to the isothermal case, but with systematic deviations from the simple scaling for higher velocities U during peri-center passage due to the finite escape velocity. The circles in Fig. 4.3 show $\chi(U)/\chi_{\mathrm{s}}(U)$ for the BW and HE cusp (open symbols) and the outskirts of the Plummer (PL) and Dehnen (DE) spheres (full symbols) at the corresponding values for $\eta = 5/4, 2, -2, -1$, respectively. For the HE case numerically realized values are used.

For circular orbits the orbital decay time varies up to factor larger than two compared to the standard formula due to the self-consistent χ functions. For the evolution of the orbital shape, the relative variation of the friction force between apo- and peri-center is also important .

In Fig. 4.2 $\chi(U)$ is shown for the same set of η-values as in Fig. 4.1. In order to see more clearly the difference to the Maxwellian distribution function the ratios $\chi(U)/\chi_{\mathrm{s}}(U)$ are plotted in bottom panel. For $\eta < 1$ the χ-values are larger and for shallower cusps with $\eta > 1$ the values are smaller.

In Fig. 4.4 we show $\chi(U)$ as a function of η for fixed U. $U = 1$ corresponds to the circular velocity, and $U = 0.7, 1.4$ are typical values for peri- and apo-center velocities with moderate eccentricities.
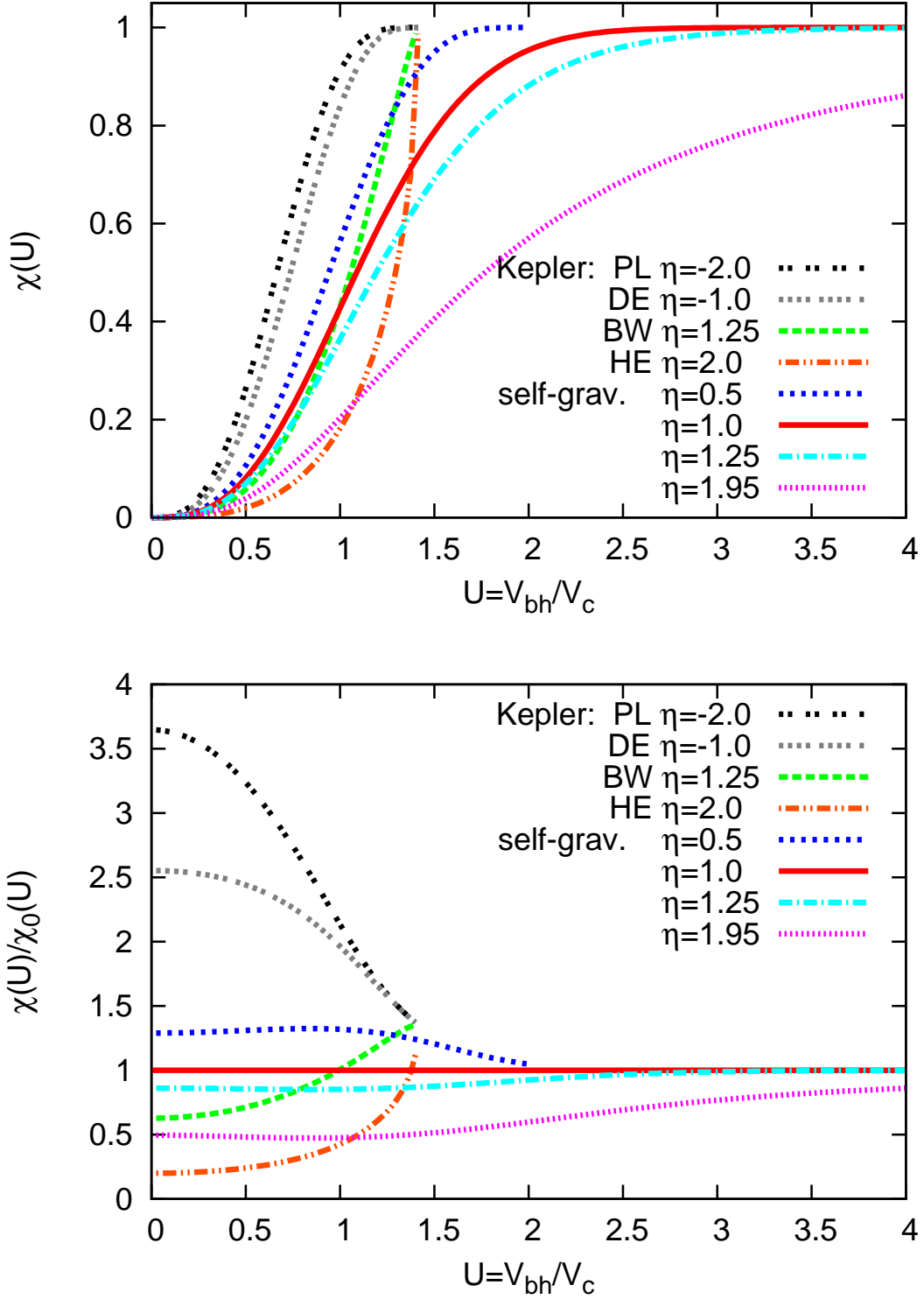
Figure 4.2: Top: $\chi(U)$ for the same values of η as in Fig. 4.1. Bottom: Same functions as in top panel, but here normalized to the Maxwellian: $\chi(U)/\chi_s(U)$ (increasing η from top to bottom).
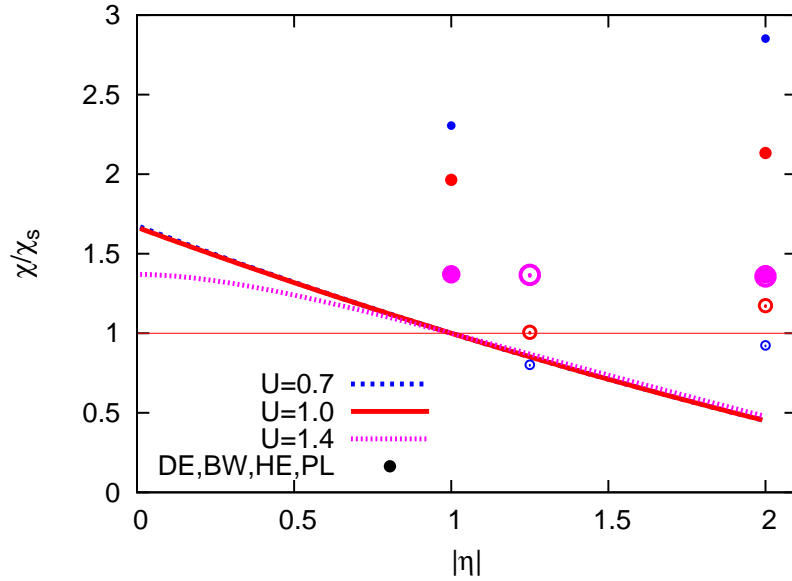
Figure 4.3: The plot shows the relative variation $\chi(U)/\chi_\mathrm{s}(U)$ as a function of η for for different values of U, where χ_s corresponds to the standard Maxwellian distribution function (i.e. $\eta = 1$). For self-gravitating cusps the full line is for the circular velocity $U = 1$, dotted and dot-dashed lines are for $U = 0.7$ and $U = 1.4$, respectively. The circles give the corresponding values for the Kepler potential cases with increasing size for increasing U (open symbols are for positive η and full symbols for negative η).

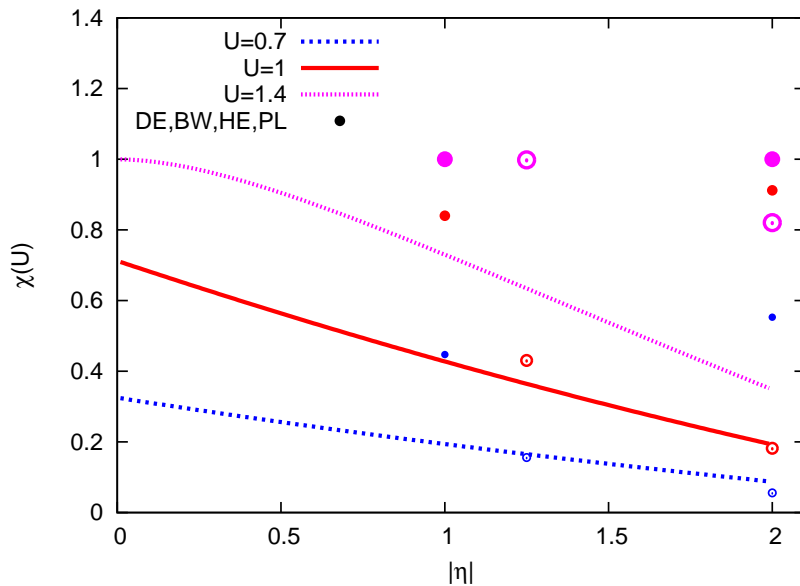Figure 4.4: The functions $\chi(U)$ as a function of η are shown for fixed $U = 0.7, 1.0, 1.4$ (Dashed blue, full red, dotted pink line, respectively). The circles give the corresponding values for the Kepler potential cases with increasing size for increasing U ($\eta = -1$ for DE, $\eta = -2$ for PL, $\eta = 1.25$ for BW, $\eta = 2.0$ for HE). Open circles are for positive η and full circles for negative η.
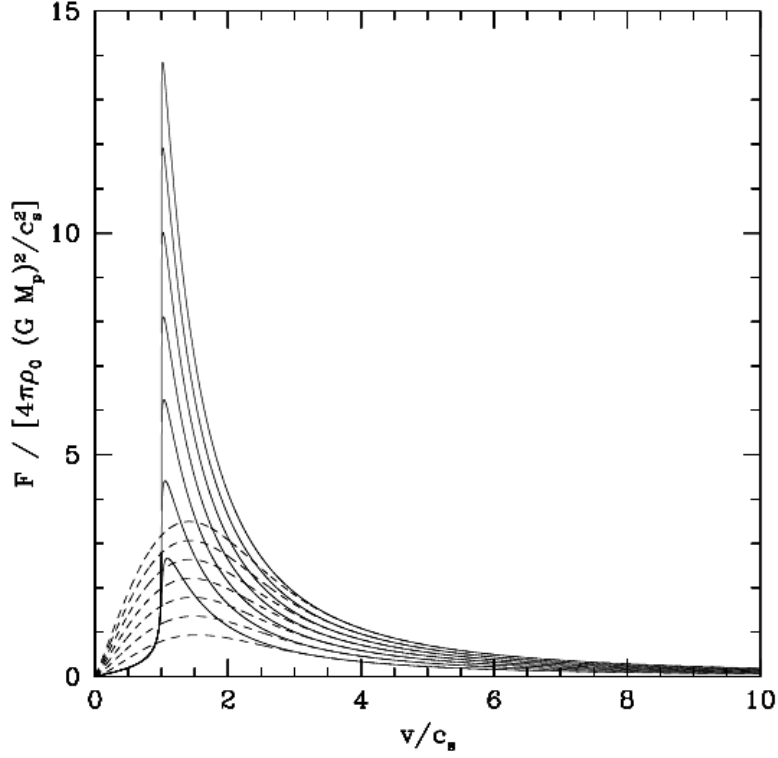
Figure 4.5: *Solid lines:* Dynamical friction force in gaseous medium as a function of Mach number $\mathcal{M} = V/c_s$. Curves correspond to $\ln(c_s t/r_{min}) = 4, 6, 8, ..., 16$. *Dashed lines:* Corresponding dynamical friction force in a collision-less medium with particle velocity dispersion $\sigma = c_s$ and $r_{max} = Vt = \mathcal{M}c_s t$. Figure from Ostriker (1999).

4.5   Dynamical Friction in Gaseous Medium

In collisional fluids dynamical friction arises from the gravitational pull between the perturber and its density wake in the background medium. The dynamical friction formula in a gaseous medium depends on the velocity V of the perturber which giving rise to two possibilities: (1) when the velocity V is greater than speed of sound v_c, i.e, supersonic case. (2) and the case in which it is less than speed of sound, the subsonic case.

In the steady state limit and for the supersonic motion (Ostriker 1999),

$$F_{DF} = -4\pi \left(\frac{GM_p}{V}\right)^2 \rho_0 \ln \left[\frac{b_{max}}{b_{min}} \frac{(\mathcal{M}^2 - 1)1/2}{\mathcal{M}}\right] \quad \mathcal{M} > 1 \tag{4.34}$$

where $\mathcal{M} = V/c_s$ is the Mach number. If perturber triggering disturbance moves subsonically then in this case dynamical friction force is given by formula

$$F_{DF} = -(4/3)\pi \left(\frac{GM_p}{V}\right)^2 \rho_0 \left[\frac{1}{2}\ln\left(\frac{1+\mathcal{M}}{1-\mathcal{M}}\right) - \mathcal{M}\right] \quad \mathcal{M} < 1 \tag{4.35}$$

In the the limit of a very slow perturber, $\mathcal{M} << 1$, dynamical friction force becomes proportional to perturber speed V. Figure 4.5 show the comparison for gravitational drag on a particle of

mass M_p in collisional and collision-less medium with the same density ρ_0 for both mediums. For collision-less medium Eq. 4.1 is used with a Maxwellian distribution of particle velocities. We can notice from the figure that for $\mathcal{M} >> 1$, dynamical friction forces are identical for collisional and collision-less medium. For $\mathcal{M} < 1$, the dynamical friction force is larger in collision-less medium in general. At $\mathcal{M} \sim 1$, the dynamical friction force in collisional medium is up to factor 4 larger than the drag force in collision-less medium.

Key results of the study

- The outskirts of Dehnen models and a Plummer model can be approximated by cusps in a Kepler potential.

- In the Coulomb logarithm, the minimum impact parameter is defined by a_{90} and the maximum parameter is defined by the local scale length.

- The motion of a point like object in a Kepler potential is described by a constant Coulomb logarithm.

- The orbital decay time for circular orbits when using self consistent distribution functions can be different up to a factor 2 when compared with those obtained with a standard Maxwellian.

Chapter 5

Orbital Decay of SMBHs in Galactic Centers

<div style="background-color:yellow">

Key scientific investigations addressed in this Chapter

1. Derivation of theoretical estimates for the orbital decay of supermassive black hole due to dynamical friction in self gravitating cusps and Kepler potential.

2. Estimates of orbital decay for the special cases in Kepler potential include Bahcall-Wolf cusp, Hernquist cusp, outskirts of Plummer and Dehnen models.

3. Applications of analytical estimates to the decay of IMBH in Galactic center and also for a minor mergers.

   Note: The contents of this Chapter are based on paper by Just, A., Khan, F. M., Berczik, P., Ernst, A., & Spurzem, R. 2011, MNRAS, 411, 653

</div>

The generalized formula for dynamical friction described in Chapter 4 is valid for extended objects like satellite galaxies or star cluster and for point-like objects like SMBHs. For extended objects the Coulomb logarithm is small and corrections to the relevant impact parameter regime are more significant than for SMBHs. Additionally the mass loss and the determination of the effective mass for dynamical friction must be taken into account Fujii et al. (2006, 2008). The present investigation is restricted to the orbital evolution of SMBHs.

Super-massive black holes, most likely to be present in merging galaxies from the early universe onwards Kormendy & Richstone (1995), Ferrarese et al. (2006), will sink to the centers of galactic merger remnants by dynamical friction and ultimately coalesce themselves Berentzen et al. (2009), Khan et al. (2011). Numerical simulations to follow this process in a particle-by-particle approach are still too computationally expensive for realistic particle numbers, and so this situation requires another careful look at dynamical friction.

Here the orbital decay of a massive object on a circular orbit in a cuspy density distribution is explicitly derived with a position dependent Coulomb logarithm. All values are normalized to the values at the initial distance R_0. The distance to the center is $y = R/R_0$.

The initial decay timescale for angular momentum loss is given by

$$\tau_0 \quad = \quad -\frac{V_{c0}}{\dot{V}_{df,0}} = \frac{1}{2\pi\eta\chi_0 \ln\Lambda_0} \frac{M_0^2}{M_{bh}M_t} \, T_0 \tag{5.1}$$

$$= \quad \frac{14.9}{\eta\chi_0 \ln\Lambda_0} \left[\frac{R_0}{pc}\frac{M_0}{M_\odot}\right]^{3/2} \left[\frac{M_t}{M_\odot}\frac{M_{bh}}{M_\odot}\right]^{-1} \, \text{Myr.}$$

The first expression is in units of the orbital time $T_0 = 2\pi R_0/V_{c0}$ and the second expression is in physical units. In the case of a self-gravitating cusp the enclosed cusp mass M_0 equals M_t and τ_0 is proportional to $M_t^{1/2}$. In the Kepler case M_0 equals M_c and τ_0 is proportional to $M_c^{3/2}$.

The orbital decay can be computed by identifying the angular momentum loss due to the dynamical friction force (Eq. 4.1)

$$\frac{d(yV_c)}{dy}\dot{y} = \dot{L} = y\dot{V}_{df} = -\frac{V_{c0}}{\tau_0}y^{\eta-1}\frac{M_0}{M(y)}\frac{\ln\left(\Lambda_0 y^\beta\right)}{\ln\Lambda_0} \tag{5.2}$$

where we have used the definition of the decay timescale τ_0 (Eq. 5.1), the position dependence of the density (Eq. 4.3), replaced the square of the circular velocity by $GM(y)/R_0 y$ with initial value GM_0/R_0, and the parametrization of the Coulomb logarithm (Eq. 4.29). The enclosed mass $M(y)$ on the right hand side and the circular velocity $V_c(y)$ on the left hand side are different for the Kepler case and the self-gravitating case.

In the Kepler potential with constant enclosed mass $M(y) = M_0 = M_c$ and

$$V_c^2 = V_{c0}^2 y^{-1} \tag{5.3}$$

we write Eq. 5.2 in the form

$$\dot{y} = -\frac{2}{\tau_0}\frac{\ln\left(\Lambda_0 y^\beta\right)}{\ln\Lambda_0} y^{(\eta-\frac{1}{2})} \tag{5.4}$$

We define for $\eta \neq 3/2$

$$z = \Lambda^{\frac{\kappa}{\beta}} = \Lambda_0^{\frac{\kappa}{\beta}} y^\kappa, \qquad \kappa = \frac{3}{2} - \eta \tag{5.5}$$

and find after a little mathematical manipulation

$$\frac{dz}{dt} = -\frac{2\kappa}{\tau_0}\frac{z_0}{\ln z_0}\ln z \tag{5.6}$$

or

$$t \quad = \quad -\frac{\tau_0}{2\kappa}\frac{\ln z_0}{z_0}\int\frac{1}{\ln z}dz$$

$$= \quad \tau_{df}\frac{\ln z_0}{z_0}\left[Ei(\ln z_0) - Ei(\ln z(y))\right] \qquad \beta,\kappa \neq 0 \tag{5.7}$$

and

$$\tau_{df} \quad = \quad \tau_0 \times \begin{cases} \frac{1}{3-2\eta} & \kappa \neq 0 & \text{Kepler} \\[2mm] \frac{\ln\Lambda_0}{2\beta} & \kappa = 0, \beta \neq 0 & \text{Kepler} \\[2mm] \frac{1}{2} & \kappa = \beta = 0 & \text{Kepler} \end{cases} \tag{5.8}$$

where τ_{df} measures the decay timescales and is given by Eq. 5.8 and the exponential-integral function $Ei(x)$ (see 2.2724.2 and 8.211.2 of Gradshteyn I.S. (1980)). For the special case of $\eta = 3/2$ we can use Λ as variable and find with

$$\frac{d}{dt} \ln(\ln \Lambda) = \frac{\beta}{\ln \Lambda} \frac{\dot{y}}{y} \tag{5.9}$$

the implicit solution

$$t = \tau_{\mathrm{df}} \ln \left(\frac{\ln \Lambda_0}{\ln \Lambda(y)} \right) \qquad \beta \neq 0,\, \kappa = 0 \tag{5.10}$$

For a point-like body the maximum and the minimum impact parameter D_{r} and a_{90} are both linear in y leading to a constant Coulomb logarithm (i.e. $\beta = 0$). For this case direct integration of Eq. 5.4 leads to the explicit solutions given by:

$$y(t) = \begin{cases} \left[1 - \frac{t}{\tau_{\mathrm{df}}} \right]^{1/\kappa} & \kappa \neq 0, \beta = 0 \\[2mm] \Lambda_0^{(\exp(-t/\tau_{\mathrm{df}})-1)/\beta} & \kappa = 0, \beta \neq 0 \quad \text{Kepler} \\[2mm] \exp\left(-\frac{t}{\tau_{\mathrm{df}}} \right) & \kappa = \beta = 0 \quad \text{Kepler} \end{cases} \tag{5.11}$$

For the Kepler potential the results can be easily generalized to expanding or contracting cusps. If the density varies proportional to a power of time, i.e. $\rho(y) = \rho(y, t = 0)(1 + t/t_{\mathrm{a}})^\nu$, then the differential equation 5.4 with time dependent τ_0 can be converted back to the original form with initial ρ_0 in τ_0 by

$$\frac{dy}{ds} = \dot{y} \frac{dt}{ds} = -\frac{2}{\tau_0} \frac{\ln\left(\Lambda_0 y^\beta \right)}{\ln \Lambda_0} y^{(\eta - \frac{1}{2})} \tag{5.12}$$

$$s = \left[(1 + t/t_{\mathrm{a}})^{1+\nu} - 1 \right] \frac{t_{\mathrm{a}}}{1 + \nu} \tag{5.13}$$

The implicit solution of the differential equation 5.4 is still given by Eq. 5.7 with the substitution $t \to s$. For a Plummer sphere with linear increasing Plummer radius $y_{\mathrm{a}} = y_{\mathrm{a}0}(1 + t/t_{\mathrm{a}})$ we find for the outskirts $\nu = 2$ (Eq. 4.25).

For shallow cusps with $\eta > 3/2$ in a Kepler potential κ becomes negative leading to a negative τ_{df}. In that case $\ln z_0$ is also negative and there is formally a stalling of the orbital decay for $\beta > 0$ when Λ approaches unity. In case of $\beta = 0$ equation 5.11 yields an infinite decay time to the center.

Also for positive κ the total decay time with varying $\ln \Lambda$ is not well-defined, because the approximations in Eq. 4.26 breaks down for $\ln \Lambda < 1$. In order to get an analytical estimate of the effective decay time τ_{dec}, let's choose the time needed to decrease $\ln \Lambda$ from the initial value $\ln \Lambda_0$ to $\ln \Lambda = 0.3725\beta/\kappa$, where $Ei(\ln z) = 0$. For $\ln z_0 \gg 1$ it can be estimated from Eq. 5.8 with the help of the asymptotic expansion $Ei(x) \sim e^x (1/x + 1/x^2)$ (8.216) Gradshteyn I.S. (1980)

$$\tau_{\mathrm{dec}} = \left[1 + \frac{\beta}{\kappa \ln \Lambda_0} \right] \tau_{\mathrm{df}} \quad \text{for} \quad \frac{\kappa}{\beta} \ln \Lambda_0 \gg 1. \tag{5.14}$$

The correction factor quantifies the effect due to the position dependence of the Coulomb logarithm, if $\beta \neq 0$. For a negative κ (as realized in the Hernquist cusp HE) the last term in Eq. 5.7 dominates and diverges as Λ approaches unity. Therefore we define a decay timescale for a fixed minimum value y_{dec} (e.g. three times the stalling radius) by

$$\tau_{\mathrm{dec}} = -\frac{\ln z_0}{z_0} \ln |\ln z| \, \tau_{\mathrm{df}} \quad \text{for} \quad |\ln z| = \frac{-\kappa}{\beta} \ln \Lambda \ll 1. \tag{5.15}$$

For $\kappa = 0$ and $\beta \neq 0$ the orbital decay of the BH would also stall at $\ln \Lambda = 0$. Only for $\kappa > 0$ and $\beta = 0$ there is a finite time $\tau_{\rm df}$ to reach the center. For completeness it is mentioned that for a negative β the total decay time to the center would be finite due to the enhanced friction force by an increasing Coulomb logarithm. But for all realistic cases one finds $\beta \geq 0$.

In a self-gravitating cusp we have $\beta = \eta,\ 1,\ 0$ for a point-like object, an extended object, and a constant Coulomb logarithm, respectively (Eq. 4.29). For the self-gravitating case we insert $M(y) = M_0 y^\eta$ and

$$V_c^2 = V_{c0}^2 y^{\eta-1} \tag{5.16}$$

into equation 5.2. The resulting differential equation takes the form

$$\dot{y} = -\frac{2}{(1+\eta)\tau_0} \frac{\ln\left(\Lambda_0 y^\beta\right)}{\ln \Lambda_0} y^{-\frac{1+\eta}{2}} \tag{5.17}$$

With the definition

$$\kappa = \frac{3+\eta}{2} \tag{5.18}$$

which is positive for all realistic cases, we find the same implicit solution for $\beta \neq 0$ and explicit solution for $\beta = 0$ as in the Kepler case but with a different $\tau_{\rm df}$:

$$\tau_{\rm df} \;=\; \tau_0 \times \frac{1+\eta}{3+\eta} \quad \kappa \neq 0 \quad \text{self-grav.} \tag{5.19}$$

The angular momentum evolution can be easily calculated by

$$L(t) = \sqrt{GM(y)R} = L_0 \times \begin{cases} y^{(1+\eta)/2} & \text{self-grav.} \\ y^{1/2} & \text{Kepler} \end{cases} \tag{5.20}$$

with $L_0 = \sqrt{GM_0 R_0}$.

The standard case of dynamical friction corresponds to the isothermal sphere and a constant Coulomb logarithm, i.e. initial enclosed mass M_0 at radius R_0 with $\eta = 1$ and $\beta = 0$ in Eq. 5.8. Here the decay time of the standard case

$$\tau_{\rm df0} = \frac{1}{\chi_{\rm s} \ln \Lambda_{\rm s}} \frac{M_0}{M_{\rm bh}} \frac{R_0}{V_{\rm c0}} \times \begin{cases} \frac{1}{2} & \text{self-grav.} \\[2mm] \frac{M_0}{M_{\rm t}} & \text{Kepler} \end{cases} \tag{5.21}$$

as given also in Binney & Tremaine (1987) (7-26) is used as normalization.

In Fig. 5.1 the orbital decay $y(t)$ of circular orbits is presented. The differences in the orbital evolution are caused by the combination of using self-consistent density profiles and distribution functions and by the position dependence of the Coulomb logarithm. The standard case is given by $\ln \Lambda = \text{const.}$ ($\beta = 0$, $\eta = 1$). For point-like objects $y(t)$ is given in the top panel. Orbits for different power law indices η with varying $\ln \Lambda$ are plotted. The full red line shows in an isothermal core the delay due to the position dependence of $\ln \Lambda$ and the slightly smaller initial value of $\ln \Lambda_0 = 4.6$ instead of 5.0. In the bottom panel the evolution for the same values of η are shown for extended bodies. The parameters are chosen to give the same Coulomb logarithm $\ln \Lambda_0 = 5.0$ in the standard case.

In Fig. 5.2 the variation of the effective decay time as a function of η is shown for point-like and extended bodies. Some care should be taken to use these numbers, because the innermost radius reached at time $\tau_{\rm dec}$ depends on η. But the general parameter dependence of $\tau_{\rm dec}$ gives some insight in the physics of the orbital decay in cusps. The effective decay time of circular orbits in self-gravitating cusps is affected by the following aspects:

In the case of eccentric orbits there is an additional effect of the variation of $\ln \Lambda$, because along these orbits the relative strength of the friction force at apo- and peri-center is changed.
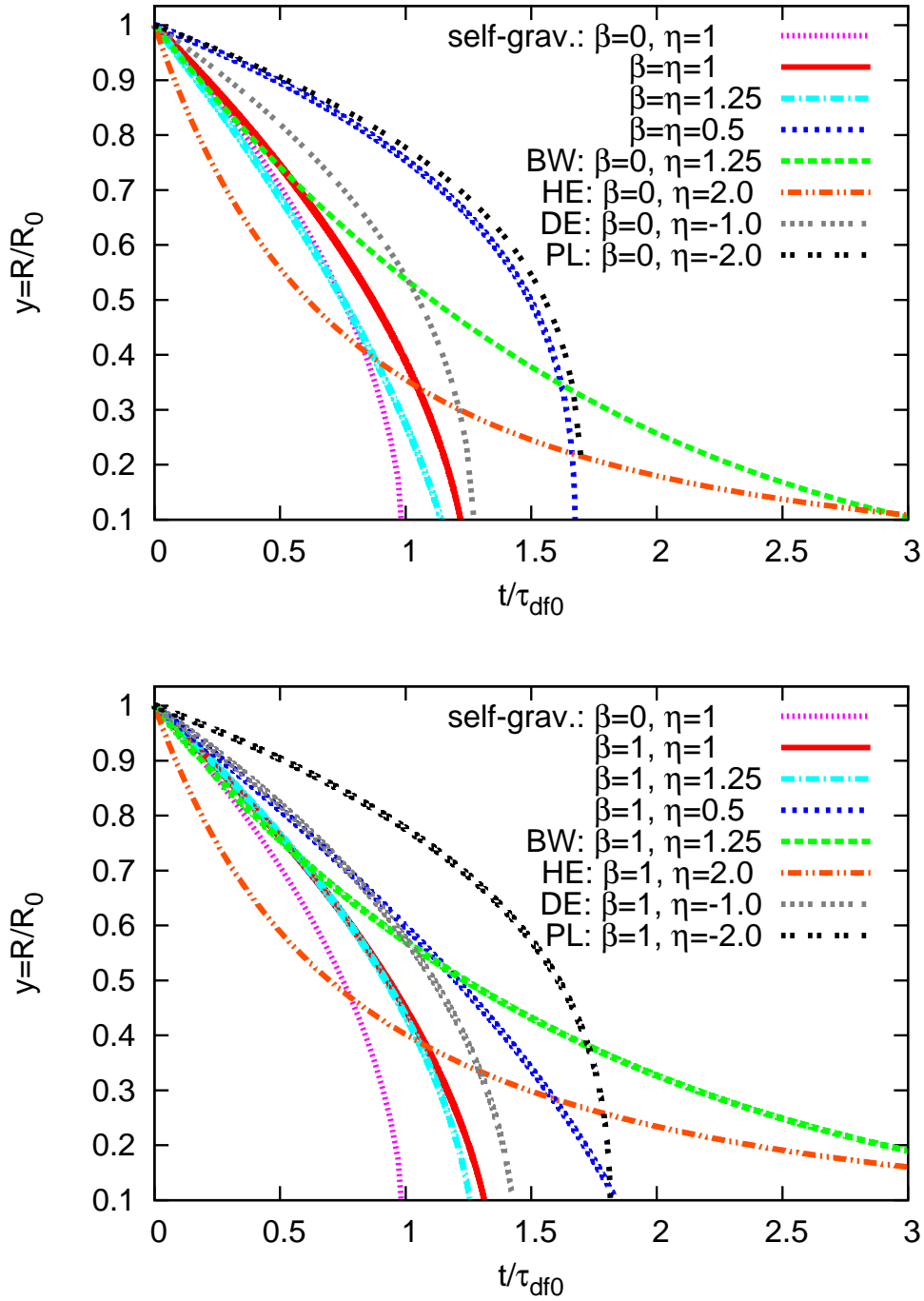
Figure 5.1: Radial evolution of circular orbits in cusps. Here $M_{\rm bh} = 10^{-2}M_0$ and $r_{\rm h} = 6.7\times10^{-3}R_0$ leading to the same $\ln\Lambda_0 = 5.0$ for the standard case with $\beta = 0, \eta = 1$. For the four Kepler cases Bahcall-Wolf cusp (BW), Hernquist cusp (HE), Dehnen (DE) and Plummer (PL) outskirts with $\eta = 1.25, 2.0, -1.0, -2.0$ the initial cusp masses are $M_{\rm t}/M_{\rm c} = 0.5, 0.5, -0.225, -0.06$, respectively. The top panel is for point-like objects and the lower panel for extended objects.

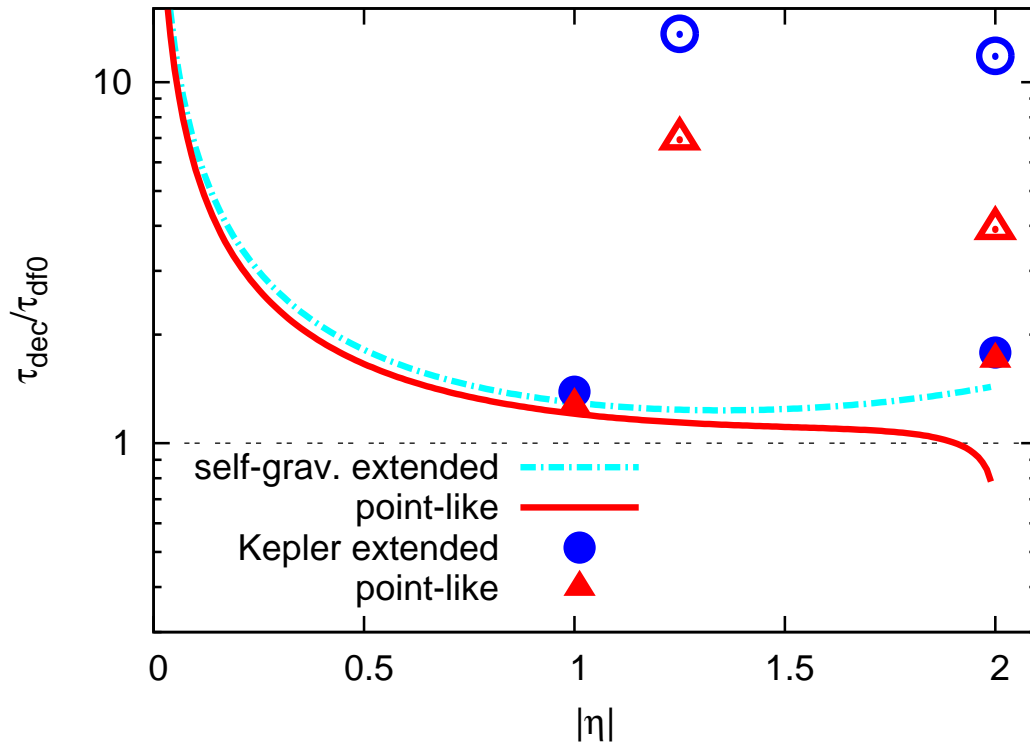Figure 5.2: Relative variation of total decay times (Eq. 5.14) normalized to the standard case of constant Coulomb logarithm. We used the same parameters as in Fig. 5.1. Open symbols are for positive η and full symbols for negative η.

5.1 Kepler Potential

In case of a Kepler potential the cusp mass distribution is decoupled from the potential and the enclosed cusp mass M_t is an additional free parameter. We discuss the explicit solutions for four cases. Well inside the influence radius of a central SMBH the stellar distribution can be described by a cusp in a Kepler potential. We present the orbital decay in the Bahcall-Wolf cusp and the shallow cusp of a Hernquist profile. In the outskirts of self-gravitating systems the density distribution may be approximated by a power law and the potential by a point-mass potential, if the density profile is steep enough. We investigate two cases with steep power law distributions to test the maximum impact parameter dependence of the Coulomb logarithm. The Plummer sphere with an outer density slope of -5 and the Dehnen models with a slope of -4 are the ideal cases.

5.1.1 Bahcall-Wolf cusp

Here we look to the orbital decay inside the gravitational influence radius, where the enclosed mass of the stellar component M_t is smaller than the mass M_c of the central SMBH. We neglect in this region the contribution of the stellar component to the mean gravitational field.

The general equations are already given in the previous sections, but we evaluate the terms explicitly for the Bahcall-Wolf cusp with

$$\eta = 5/4 \quad \rho \propto y^{-7/4}, \tag{5.22}$$

leading to

$$\kappa = \frac{1}{4} \qquad X_c^2 = \frac{11}{8}. \tag{5.23}$$

For circular orbits the minimum impact parameter for a point-like object becomes

$$a_{90} = \frac{11}{19} \frac{M_{bh}}{M_c} R, \tag{5.24}$$

leading to the initial Coulomb logarithm

$$\Lambda_0 = \begin{cases} \frac{76}{77} \frac{M_c}{M_{bh}} & \beta = 0 \quad \text{point-like} \\[2ex] \frac{4}{7} \frac{R_0}{b_{min}} & \beta = 1 \quad \text{unres. or ext.} \end{cases}. \tag{5.25}$$

The distribution function $F(u)$ and the corresponding $\chi(U)$ are shown in Figs. 4.1 - 4.2. The decay time-scale τ_{df} from Eq. 5.8 reads

$$\tau_{df} = \frac{55}{\ln \Lambda_0} \left[\frac{R_0}{\text{pc}} \frac{M_c}{\text{M}_\odot} \right]^{3/2} \left[\frac{M_t}{\text{M}_\odot} \frac{M_{bh}}{\text{M}_\odot} \right]^{-1} \text{Myr}, \tag{5.26}$$

For point-like objects the total decay time τ_{dec} equals τ_{df} and for extended bodies the corresponding equation is (using Eq. 5.14)

$$\tau_{dec} = \frac{\ln \Lambda_0 + 4}{(\ln \Lambda_0)} \tau_{df} \qquad \text{unres. or ext.} \tag{5.27}$$

The orbital decay of circular orbits is given by Eqs. 5.11,

$$y = \left[1 - \frac{t}{\tau_{df}} \right]^4, \tag{5.28}$$

which is very different to the standard case.

In Fig. 5.1 the orbit evolution in a Kepler potential is plotted for $M_t = 0.5 M_c$. It shows the strong slow-down in the inner part leading to long total decay times τ_{dec} (see Fig. 5.2).

5.1.2   Hernquist Cusp

For the Hernquist cusp the corresponding equations are

$$\eta_0 = 2 \qquad \rho \propto y^{-1} \tag{5.29}$$

$$\kappa = -\frac{1}{2} \qquad X_c^2 = 1\,. \tag{5.30}$$

$$a_{90} = \frac{1}{2}\frac{M_{\mathrm{bh}}}{M_{\mathrm{c}}}R\,, \tag{5.31}$$

$$\Lambda_0 = \begin{cases} 2\frac{M_{\mathrm{c}}}{M_{\mathrm{bh}}} & \beta = 0 \quad \text{point-like} \\[2ex] \frac{R_0}{b_{\min}} & \beta = 1 \quad \text{unres. or ext.} \end{cases} \tag{5.32}$$

The decay timescales are

$$-\tau_{\mathrm{df}} = \frac{15}{\ln \Lambda_0}\left[\frac{R_0}{\mathrm{pc}}\frac{M_{\mathrm{c}}}{\mathrm{M_\odot}}\right]^{3/2}\left[\frac{M_{\mathrm{t}}}{\mathrm{M_\odot}}\frac{M_{\mathrm{bh}}}{\mathrm{M_\odot}}\right]^{-1}\mathrm{Myr}\,, \tag{5.33}$$

$$\tau_{\mathrm{dec}} = -\frac{1}{2}\sqrt{\Lambda_0}\ln \Lambda_0 \ln\left(\frac{\ln \Lambda}{2}\right)\tau_{\mathrm{df}} \qquad \text{unres. or ext.} \tag{5.34}$$

and the orbital decay of circular orbits is for point-like objects

$$y = \left[1 + \frac{t}{|\tau_{\mathrm{df}}|}\right]^{-2}. \tag{5.34}$$

In Fig. 5.1 we have chosen the same y_{h} as for the BW case. We find an initially faster decay than in the BW cusp and a stronger slow-down in the late phase leading to a comparable τ_{dec} adopting a final Coulomb logarithm $\ln \Lambda = 1.1$ (see Figure 5.2). The comparison of the analytic and the numerically realized cumulative distribution function $\chi(U)$ is shown in Fig. 5.3. The Figure demonstrates the influence of the outer boundary conditions deep into the cusp.

5.1.3   The Outskirts of a Plummer Sphere

In the outskirts of a Plummer sphere with total mass M_{c} the corresponding equations are

$$\eta_0 = -2 \qquad \rho \propto y^{-5} \tag{5.35}$$

$$\kappa = \frac{7}{2} \qquad X_c^2 = 3\,. \tag{5.36}$$

$$a_{90} = \frac{3}{4}\frac{M_{\mathrm{bh}}}{M_{\mathrm{c}}}R\,, \tag{5.37}$$

$$\Lambda_0 = \begin{cases} \frac{4}{15}\frac{M_{\mathrm{c}}}{M_{\mathrm{bh}}} & \beta = 0 \quad \text{point-like} \\[2ex] \frac{1}{5}\frac{R_0}{b_{\min}} & \beta = 1 \quad \text{unres. or ext.} \end{cases} \tag{5.38}$$

$$\tau_{\mathrm{df}} = \frac{0.78}{y_{\mathrm{a}}^2 \ln \Lambda_0}\left[\frac{R_0}{\mathrm{pc}}\right]^{3/2}\left[\frac{M_{\mathrm{c}}}{\mathrm{M_\odot}}\right]^{1/2}\left[\frac{M_{\mathrm{bh}}}{\mathrm{M_\odot}}\right]^{-1}\mathrm{Myr}\,, \tag{5.39}$$

$$\tau_{\mathrm{dec}} = \frac{\ln \Lambda_0 + 2/7}{(\ln \Lambda_0)}\tau_{\mathrm{df}} \qquad \text{unres. or ext.} \tag{5.40}$$

We have used Eq. 4.25 for M_{t}. The orbital decay of circular orbits is for point-like objects

$$y = \left[1 - \frac{t}{\tau_{\mathrm{df}}}\right]^{2/7}. \tag{5.41}$$

and the distribution function $F(u)$ and the corresponding $\chi(U)$ are shown in Figs. 4.1 - 4.2. In Figs. 5.1 and 5.2 we have chosen $y_{\mathrm{a}} = 0.2$ for the Plummer radius in units of R_0.
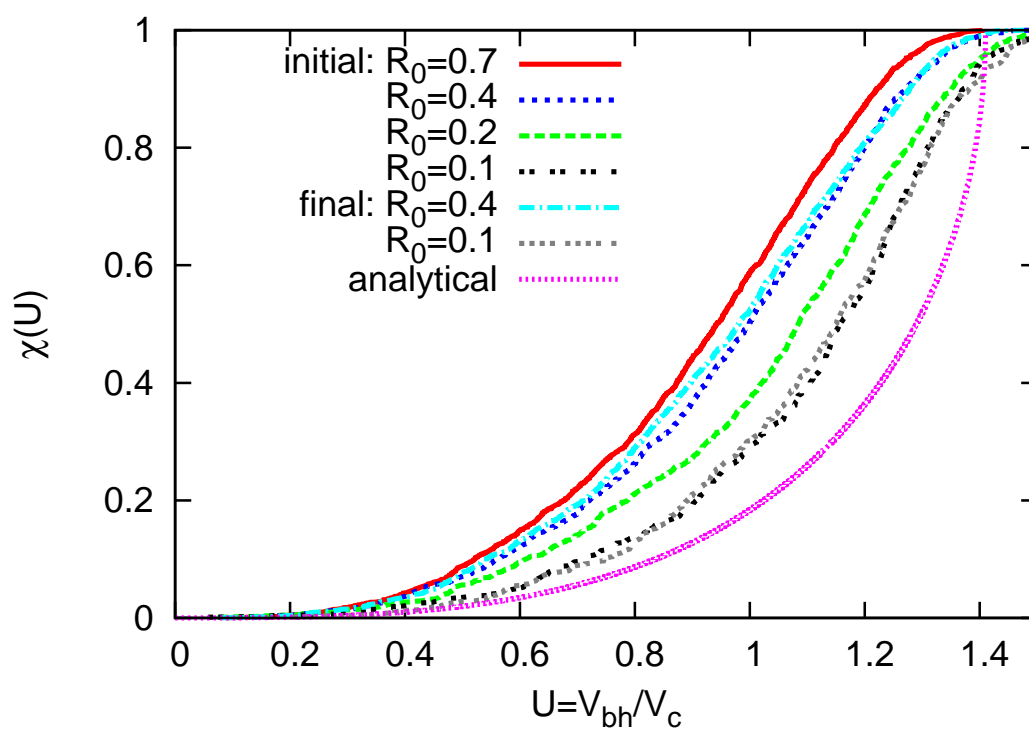
Figure 5.3: Initial and final cumulative distribution functions for the Hernquist cusp at different radii of runs E1 and E2. For comparison the analytic limit for $r \to 0$ is included.

5.1.4 The Outskirts of Dehnen Models

In the outskirts of Dehnen models with total mass M_c and inner cusp slope η the corresponding equations are

$$\eta_0 = -1 \qquad \rho \propto y^{-4} \tag{5.42}$$

$$\kappa = \frac{5}{2} \qquad X_c^2 = \frac{5}{2} \, . \tag{5.43}$$

$$a_{90} = \frac{5}{7} \frac{M_{bh}}{M_c} R \, , \tag{5.44}$$

$$\Lambda_0 = \begin{cases} \frac{7}{20} \frac{M_c}{M_{bh}} & \beta = 0 \quad \text{point-like} \\[2mm] \frac{1}{4} \frac{R_0}{b_{min}} & \beta = 1 \quad \text{unres. or ext.} \end{cases} \, . \tag{5.45}$$

$$\tau_{df} = \frac{2.36}{y_a \ln \Lambda_0} \left[\frac{R_0}{pc} \right]^{3/2} \left[\frac{M_c}{M_\odot} \right]^{1/2} \left[\frac{M_{bh}}{M_\odot} \right]^{-1} \text{Myr} \, , \tag{5.46}$$

$$\tau_{dec} = \frac{\ln \Lambda_0 + 0.4}{(\ln \Lambda_0)} \tau_{df} \qquad \text{unres. or ext.} \tag{5.47}$$

We have used Eq. 4.24 for M_t with $\eta = 1.5$. The orbital decay of circular orbits is for point-like objects

$$y = \left[1 - \frac{t}{\tau_{df}} \right]^{2/5} \, . \tag{5.48}$$

and the distribution function $F(u)$ and the corresponding $\chi(U)$ are shown in Figs. 4.1 - 4.2. In Figs. 5.1 and 5.2 we have chosen $y_a = 0.15$ for the scale radius in units of R_0.

5.2 Applications

5.2.1 The Galactic Center

The central region of the Galactic Center can be modeled by a cusp with $\eta = 1.2$ and enclosed mass $M_0 = M(R_0) = 1 \cdot 10^9 M_\odot$ at $R_0 = 200 \, pc$, and a central BH with mass $M_c = 2.6 \cdot 10^6 M_\odot$ Genzel & Townes (1987). The gravitational influence radius is at $R = 1.4 \, pc$, where we may assume a slightly shallower cusp with $\eta = 1.25$. If the central BH would have entered the cusp on a circular orbit at some later time, the decay time from $R_0 = 200 \, pc$ to the center would be $110 \, Myr$ (Eq. 5.14 with $\beta = \eta$). An intermediate mass BH with $M_{bh} = 1 \cdot 10^4 M_\odot$ can reach the center from $R_0 = 60 \, pc$ in $2.5 \, Gyr$. For the final decay inside the influence radius of $R = 1.4 \, pc$ the decay time is $15 \, Myr$.

In the central cusp of the Galaxy there are young star clusters like the Arches and the Quintuplet cluster with a projected distance from the Galactic center of about 30 pc and an age of a few Myr. The stellar mass is $\approx 1 \cdot 10^4 M_\odot$ with a half-mass radius of $r_h \approx 0.2 \, pc$ Cotera et al. (1996). Assuming that the initial distance is $R_0 = 30 pc$ we find with Eq. 4.31 for the initial Coulomb logarithm $\ln \Lambda_0 = 4.4$ leading to the decay time $\tau_{dec} = 720 \, Myr$. If we assume that the star clusters are still embedded in their parent molecular cloud with mass $1 \cdot 10^6 M_\odot$ and initial half-mass radius $r_{h0} \approx 3 \, pc$, the decay time becomes considerably smaller. Adopting cluster mass loss linear in time we get $\tau_{dec} \approx 30 \, Myr$, which is still large compared to the actual age of the clusters. This is in contrast to Gerhard (2001), who investigated the in-fall of massive clusters, also embedded in giant molecular clouds, to the Galactic center. He found much shorter time-scales, because he used unrealistically high values for the Coulomb logarithm $\ln \Lambda \approx 10 - 20$.

5.2.2 Minor Merger

One important application is the orbital decay of the SMBHs after the merger process of two galaxies. Let us assume a 10:1 merger with primary BH of mass $M_c = 1 \cdot 10^8 M_\odot$ and the secondary BH with $M_{bh} = 1 \cdot 10^7 M_\odot$. After violent relaxation of the stellar components and settling of the primary BH to the center we adopt a shallow new central cusp with $\eta = 1.75$ at radii large compared to the gravitational influence radius of the central SMBH. With an enclosed mass $M_0 = M(R_0) = 1 \cdot 10^{10} M_\odot$ at $R_0 = 1 \, \text{kpc}$ the circular velocity is $V_{c0} = 207 \, \text{km/s}$ corresponding to a velocity dispersion of $\sigma_0 = 293 \, \text{km/s}$ (Eq. 4.10). For the secondary BH we find with Eq. 5.14 a decay time of 830 Myr. For the inner 500 pc with enclosed mass of $M(500\text{pc}) = 3 \cdot 10^9 M_\odot$ the BH needs 190 Myr. After reaching the gravitational influence radius of the central SMBH at $R = 72 \, \text{pc}$, the final decay takes 15 Myr (with Eq. 5.26). If we compare these decay times with an isothermal model with the same enclosed mass at $R_0 = 1 \, \text{kpc}$ and adopting a constant Coulomb logarithm of $\ln \Lambda = 6.9$, we find the corresponding times 792; 200; 4.1 Myr, respectively. The total decay time is comparable, but in the final phase the decay is significantly slower in the Kepler potential compared to the standard isothermal approximation.

Key findings of this Chapter

- **Density profile** With decreasing η the mass M_0 is more and more concentrated to the center leading to a smaller density in the outer regions. This results in a smaller dynamical friction force and prolonged τ_{dec}.

- **Distribution function** With decreasing η the fraction of slow particles χ_0 increases considerably from 0.2 to 0.7, reducing the effect of the smaller density in the outer parts.

- **Coulomb logarithm** The position dependence of $\ln \Lambda$ leads to a moderate delay in orbital decay in the later phase. The effect is strongest for large values of η.

- **Extended bodies** For extended bodies like star clusters $\ln \Lambda$ is generally smaller compared to point-like bodies, because the minimum impact parameter is larger. Compared to the standard case, the prolongation factor is only weakly dependent on η.

Chapter 6

Numerical Tests of Dynamical Friction Formula

<div style="background-color: yellow;">

Contents of this Chapter

1. Large set of numerical simulations to study the orbital decay of SMBHs on circular and eccentric orbits in power-law cusps.

2. Comparison of orbital decay in N-body simulations with analytic/semi-analytic estimates using improved and standard dynamical friction formula.

3. Study of the effect of the new Coulomb logarithm and correct distribution function separately.

4. Numerical resolution of the particle particle code ϕ-GRAPE and the particle mesh code SUPERBOX.

   Note: The contents of this Chapter are based on paper by Just, A., Khan, F. M., Berczik, P., Ernst, A., & Spurzem, R. 2011, MNRAS, 411, 653

</div>

The contributions to the dynamical friction force covers a large range of parameters for the 2-body encounters, which must be fully covered by the numerical simulations in order to reach a quantitative measure of the Coulomb logarithm. The numerical representation is mainly restricted by the resolution of small impact parameters determined by the spatial resolution, the time resolution and the number statistics. For PP codes the number statistics is the main limitation. Therefore we can use the ϕGRAPE code for the BW cusp only with a very high local density in the inner cusp. We reach a few encounters per decay timescale τ_0 with impact parameters below twice the minimum value. For the SUPERBOX runs the spatial resolution is limited, which we can take into account by a correct choice of the minimum impact parameter. But even in that case it turns out that due to the fixed time step the time resolution is still a bottleneck, which limits the total time of some simulations.

Table 6.1: Parameters of the runs for the BW cusp.

Run	$N/10^3$	$\epsilon/10^{-4}$	M_{bh}	R_0	$V_{\mathrm{c},0}$	$V_0/V_{\mathrm{c},0}$	$a_{90}/10^{-4}$	$\ln \Lambda_0$
A0	64	1.0	–	–	–	–	–	–
A1	64	0.1	.005	0.2	2.25	1.0	5.79	5.28
A2	64	0.1	.005	0.1	3.17	1.0	2.89	5.29
A3	64	0.1	.01	0.2	2.25	1.0	11.6	4.59
B1	64	0.1	.005	0.2	2.25	0.7	7.01	5.09
B2	64	0.1	.005	0.1	3.17	0.5	4.07	4.94
C1	64	1.0	.005	0.2	2.25	1.0	5.79	5.25
C2	64	5.0	.005	0.2	2.25	1.0	5.79	4.79
C3	64	10.0	.005	0.2	2.25	1.0	5.79	4.26
E1	64	0.1	.005	0.7	1.20	1.0	17.5	5.33
E2	128	0.1	.002	0.2	2.27	1.0	2.0	6.91

Note. For all runs the gravitational constant G, the SMBH mass M_{c} and the scale radius a are normalized to unity. N is the total number of particles in the cusp, ϵ the softening length of the particles, M_{bh} the mass of the secondary black hole with initial distance R_0 in units of a, the circular velocity $V_{\mathrm{c},0}$ at R_0 in units of $\sqrt{GM_{\mathrm{c}}/a}$ and the initial velocity V_0 in units of the circular velocity, the initial value of a_{90} from Eq. 4.28 is in units of a.

6.1 Bahcall-Wolf Cusp

We used the extended η-model of Matsubayashi et al. (2007) to generate the initial particle distributions in phase space. In all our runs we are using $N = 64,000$ particles (see section 3.2 for setup of Bahcall-Wolf cusp). The particle positions are generated so that their spatial distribution satisfy Eq. 4.23 and the velocities were assigned to these particles according to Eq. 3.17. In all our simulations we are using the normalization $G = M_{\mathrm{c}} = a = 1$ leading to $y_{\mathrm{a}} = R_0^{-1}$ in N-body units. The mass of the central black hole is M_{c} and the total cusp mass $M_t = 0.1$. For the setup we used a radius range of $10^{-4} - 20$ in all our runs. Inside one unit length our cusp follows density profile $-7/4$ and then turns over to a Plummer density profile with slope -5 for far out distances. Table 6.1 shows the list of parameters for the series of runs.

6.1.1 Cusp Stability Analysis

Since we are using an approximate DF, we first performed a run (run A0 in the table) without a secondary BH to test whether or not the cusp is stationary around the central SMBH. We run this model up till 50 time units. Figure 6.1 shows the evolution of Lagrange radii and also the cumulative mass profile at various time steps. We can see that the cusp is very stable. So the problem how to get a stationary cusp in a Kepler potential was solved by this kind of a compromise distribution between Bahcall-Wolf cusp in the inner (high binding energy) regime and a Plummer distribution in the outskirts.

6.1.2 Circular Runs

We performed two series of circular runs (see table 6.1). The runs A1–A3 with different BH masses and initial radii are all resolved, i.e. the softening parameter $\epsilon = 10^{-5}$ is much smaller than the initial value of a_{90}. Since a_{90} decreases linearly in y Eq. 5.24, the minimum impact parameter is fully resolved to very small radii and we can use Eq. 5.28 for analytic estimates. In figures 6.2 and 6.3 we show the distance and the angular momentum evolution, because already small deviations from circularity smear out the appearance of the orbits due to the very short orbital time compared to the decay time. The top panel of figure 6.2 shows the distance evolution for runs A1, A2, and A3. Run A2 corresponds to a restart of A1 after time $T = 155$ but using the initial
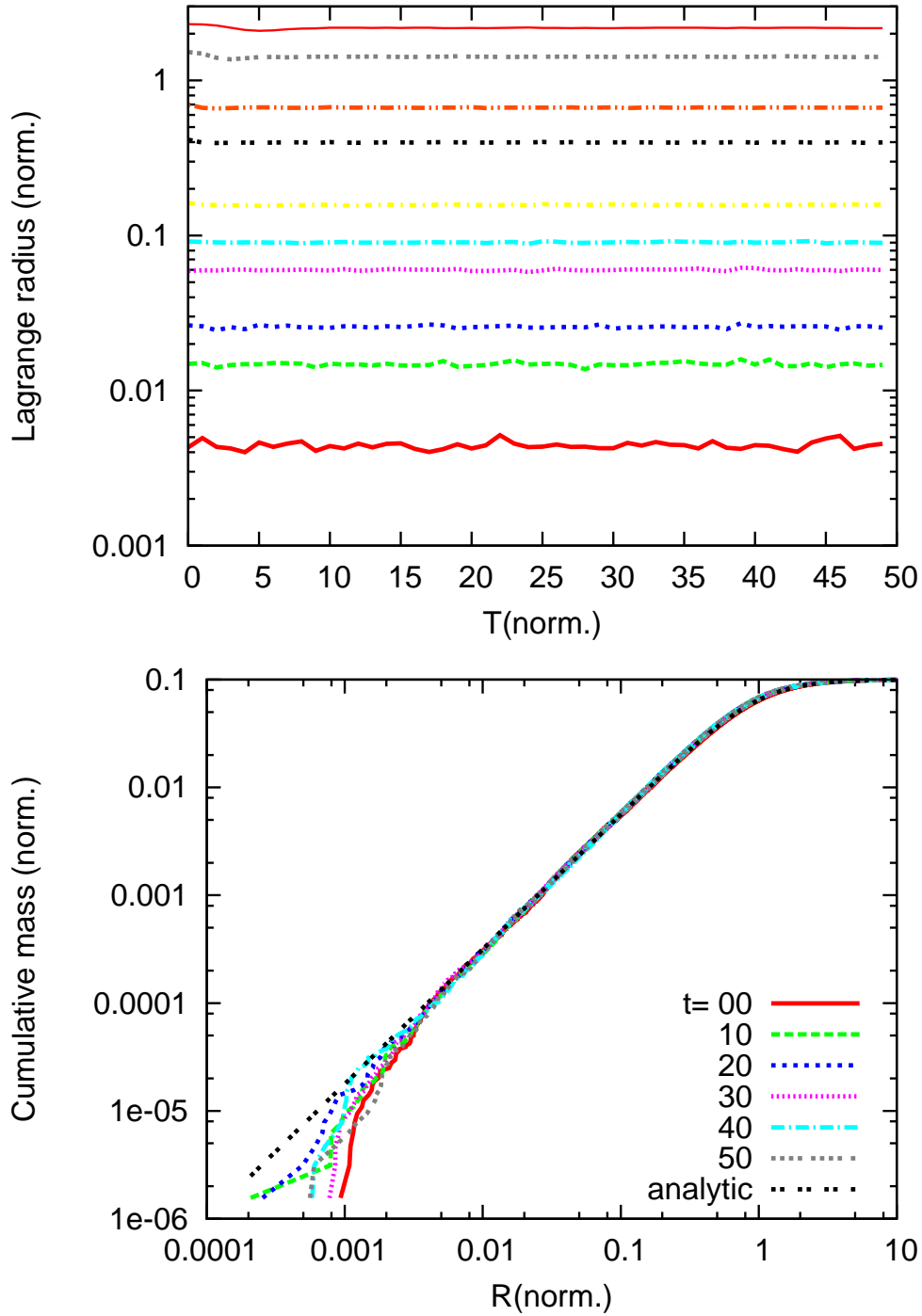
Figure 6.1: **Top:** Figure shows the evolution of Lagrange radii of 0.1, 0.5, 1, 3, 5, 10, 30, 50, 80, 90% enclosed mass (from bottom to top) for the BW cusp. The Lagrange radii do not show any systematic evolution with time.
Bottom: Cumulative mass profile at various time steps. The cumulative mass profile is practically indistinguishable from the theoretical one except the inner few dozen particles, where deviations due to the inner cutoff and noise are expected.

particle distribution of the cusp. We see that there is no significant long-term evolution of the cusp, which influences the orbital decay, until the end of run A1. The dashed (green) lines show the analytic predictions of the orbital evolution from Eq. 5.28. There is an excellent agreement in the first phase with a small delay in the later phase of run A1, which occurs much earlier in A2. The reason for the reduced friction is investigated in run A3 further. In run A3 we increased the mass of the BH and put it back at $R_0 = 0.2$ such that in case A3 the radius, where the enclosed cusp mass M_t equals M_{bh} (horizontal lines in figures 6.2 and 6.3), is twice that of run A2. In run A3 the delay starts also very early. In the bottom panel of figure 6.2 and in figure 6.3 the same evolution is shown much clearer in angular momentum L using Eq. 5.20 for the analytic predictions. The horizontal lines show the distance, where $M_{bh} = M_t$ in all figures. This radius coincides with the distance, where the BH mass exceeds the mass in a shell centered at the orbit. An inspection of the cumulative mass profiles shows that the back-reaction of the scattering events to the cusp distribution becomes significant (see figure 6.4). The cumulative mass profile becomes shallower, which means that the local density is reduced leading to a smaller dynamical friction force.

For a circular orbit in a Bahcall-Wolf cusp the new friction formula is very close to the standard formula: the Coulomb logarithm is also constant, the value deviates only by $\Delta \ln \Lambda = -0.1$ from $\ln \Lambda_s$, the χ value is 0.430 instead of $\chi_s = 0.428$. This leads to an indistinguishably faster decay when applying the standard formula. The picture changes slightly for the eccentric orbits (see below).

In all simulations the eccentricity of the orbits vary slightly. The increasing eccentricities in the later phases of the runs may correlate to the decreasing mean density, i.e. may be connected to the feedback of the BH on the cusp. The eccentricity evolution will be investigated in more detail in future work.

In a second series of runs C1–C3, we study the impact of the minimum impact parameter by increasing the softening parameter until it is much larger than a_{90}. In figure 6.5 we can see that for the largest softening length ϵ (greater than a_{90}) the decay is slower as expected from the smaller Coulomb logarithm (Eq. 5.25). We can use the variation to measure the effective resolution of the code. The best simultaneous fit of all curves lead to $b_{min} = 1.5\epsilon$ in Eq. 4.26 for the PP code ϕ-GRAPE. The random variations of the orbital decay on time-scales of $10 \ldots 100$ time units are expected from a rough estimate of the close encounter rate and the corresponding velocity changes.

6.1.3   Eccentric Runs

In eccentric runs the additional effect of the velocity dependence of $\chi(U)$ and also a_{90} (Eq. 4.28) along the orbit occurs. We performed two runs B1 and B2 with different initial radii and velocities at apo-center corresponding to eccentricities of $e = 0.5, 0.75$, respectively. The effective minimum impact parameter a_{90} is well resolved along the orbits. In the left panel of figure 6.6 the orbit of B1 is shown in two short time intervals of length $\Delta T = 1$ in order to resolve individual revolutions. Since the orbital phase is very sensitive to the exact enclosed mass and apo- peri-center positions, the cumulative phase shift after hundreds of orbits is expected. In the right panel the evolution in L is shown for runs B1 and B2 for the full evolution time. The comparison with the semi-analytic results show very good agreement for run B1. The delay in the orbital evolution as in runs A1 –A3 does not occur. In run B2 there is a delay in the later phase. In contrast to run B1 the peri-center passages of B2 suffer from low number statistics. The peri-center distance decays from 0.015 at $T = 0$ to 0.01 at $T = 150$, where only 200 cusp particles are enclosed inside the orbit.

In the right panel of figure 6.6 we show also the orbital evolution using the standard parameters. In the standard case with constant $\ln \Lambda_s$ (equation 4.32) and χ_s from a Gaussian velocity distribution are applied. The decay is slightly faster. In order to separate the effect of the new Coulomb logarithm and the correct distribution function we show also the orbital decay substituting only χ by χ_s (dotted blue line) and only $\ln \Lambda$ by $\ln \Lambda_s$ (dashed-dotted cyan line), respectively. The effect of the new Coulomb logarithm is larger, but still not significant in the Bahcall-Wolf cusp.
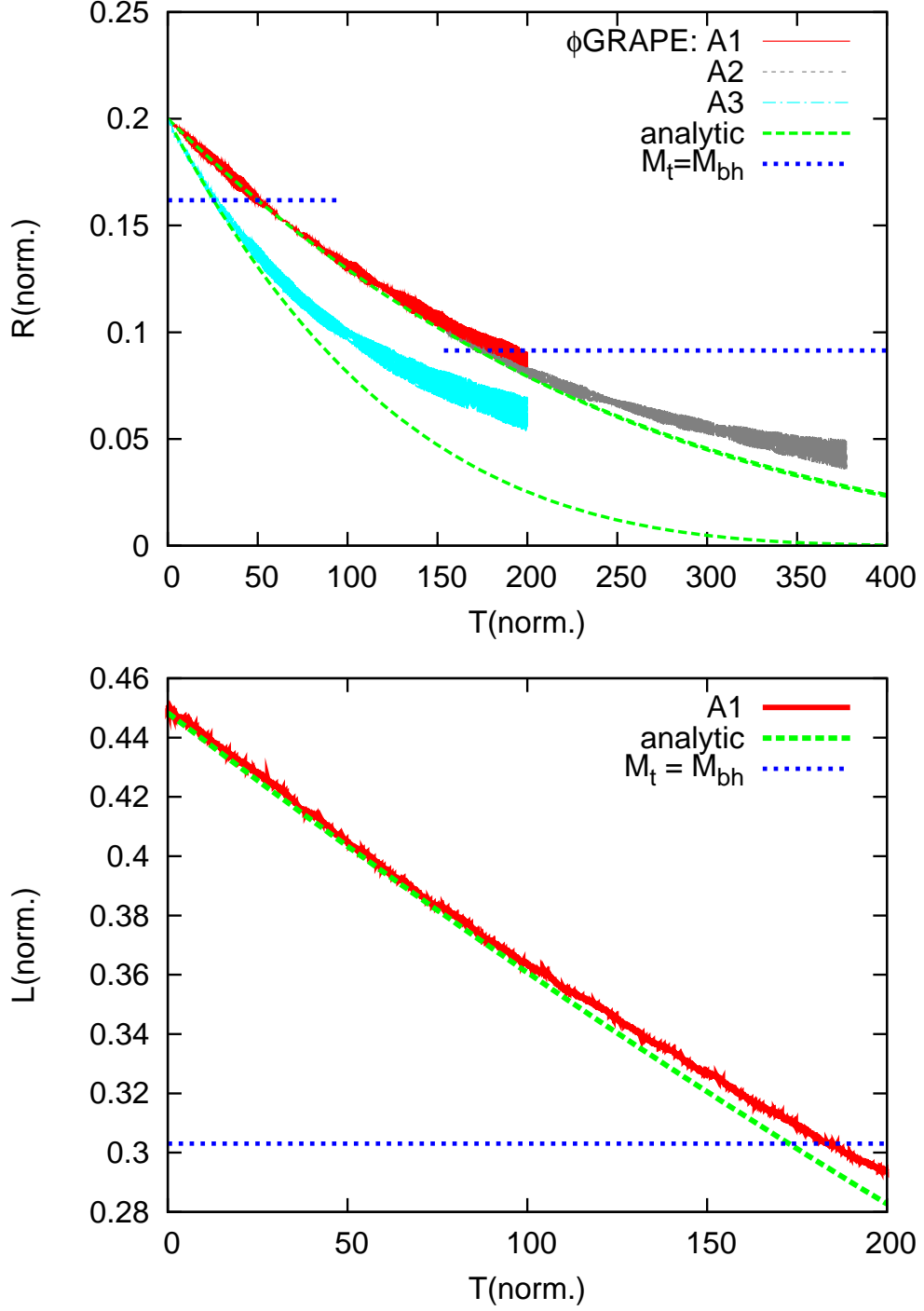
Figure 6.2: Top panel: Comparison of the orbit evolution of the ϕ-GRAPE data and the analytic estimates (Eq. 5.28) for the circular orbits A1, A2, A3. The run A2 is shifted by $T_0 = 155$ in order to continue the theoretical line of A1. The horizontal lines shows the radii, where the enclosed cusp mass equals M_{bh} (for A1, A2 at $T > 150$ and for A3 at $T < 100$). Bottom panel: Comparison of the angular momentum evolution of the ϕ-GRAPE data and the analytic estimates (Eq. 5.20) for the circular orbit A1. The horizontal line shows L_c at the radius, where the enclosed cusp mass equals M_{bh}.
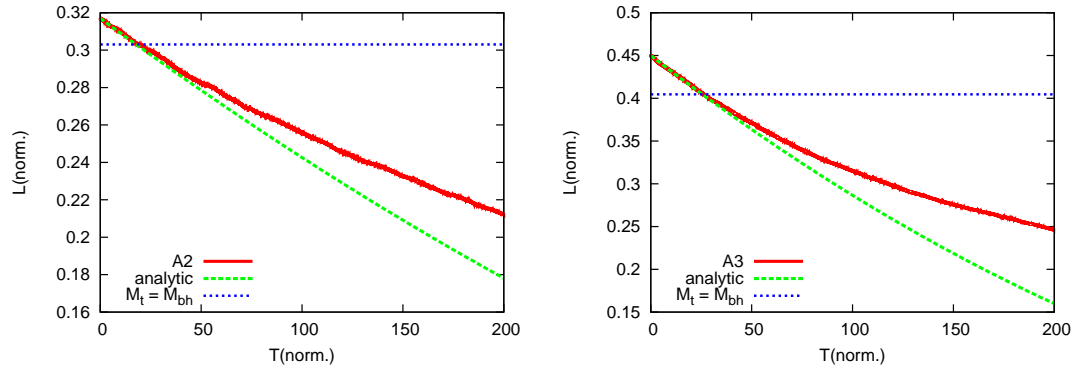
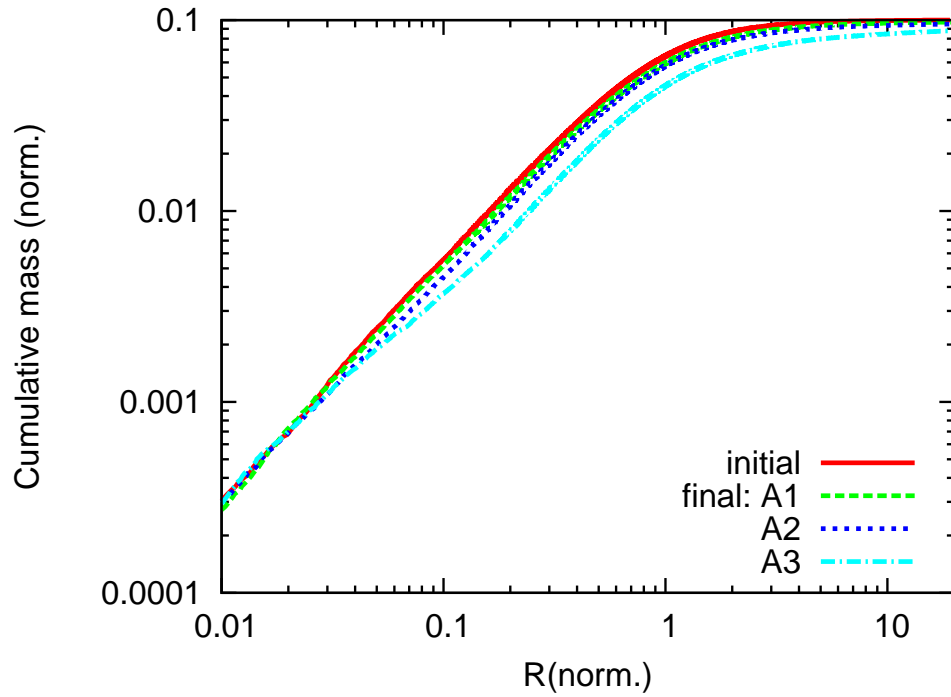Figure 6.3: Same as in the bottom panel of figure 6.2 for runs A2 and A3.

Figure 6.4: Cumulative mass profiles for the runs A1–A3 demonstrating the reduced local density in runs A2 and A3 at the position of the BH.
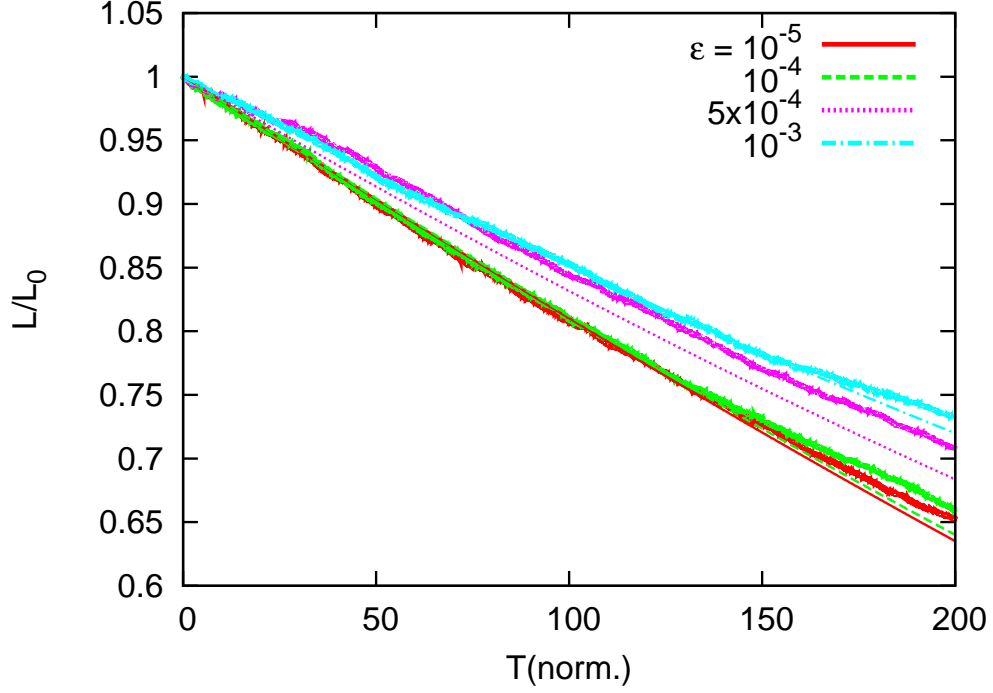
Figure 6.5: Evolution of a circular orbit in Bahcall-Wolf cusp for with different softening lengths ϵ (runs A1, C1–C3). Thin lines show the semi-analytic calculations with INTGC with Eq. 4.26 for the Coulomb logarithm with the best fit minimum impact parameter $b_{\min} = 1.5\epsilon$.
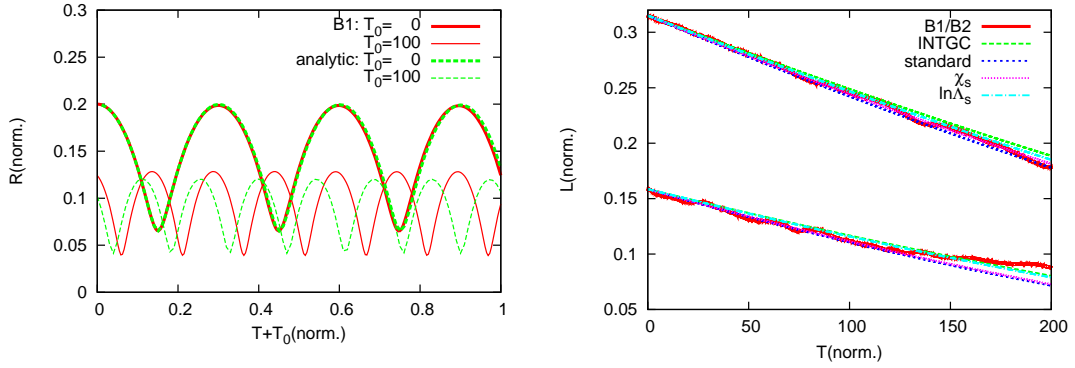
Figure 6.6: Left Panel: Orbit evolution of run B1 in two time intervals (0,1) and and (100,101) compared to the semi-analytic predictions from INTGC. Right panel: Angular momentum decay for runs B1 (top) and B2 (bottom) for the full simulated time compared to the semi-analytic predictions. Label INTGC stands for the new $\ln \Lambda$ and χ, 'standard' for $\ln \Lambda_s$ and χ_s, the other two for substituting only one parameter by the standard value.
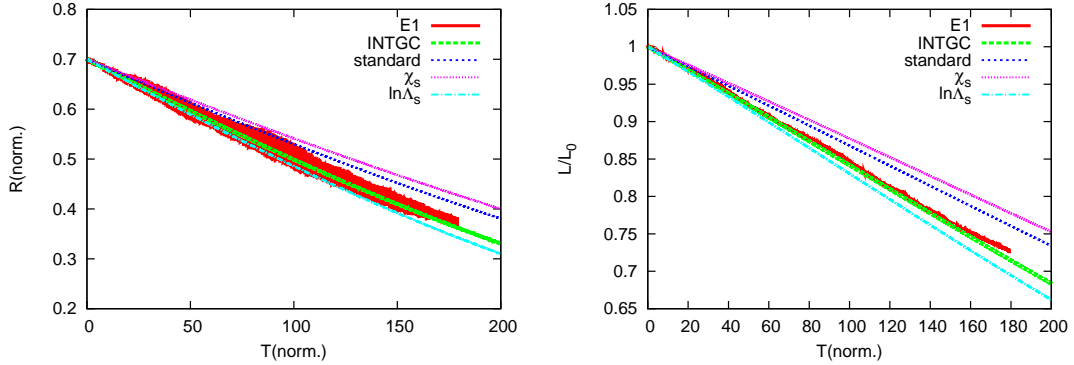
Figure 6.7: Orbital decay of a BH in the Hernquist cusp of the circular orbit E1 in $r(t)$ (left panel) and $L(t)/L_0$ (right panel). The ϕGRAPE simulation is compared to the semi-analytic results with INTGC. Same notation as in figure 6.6.
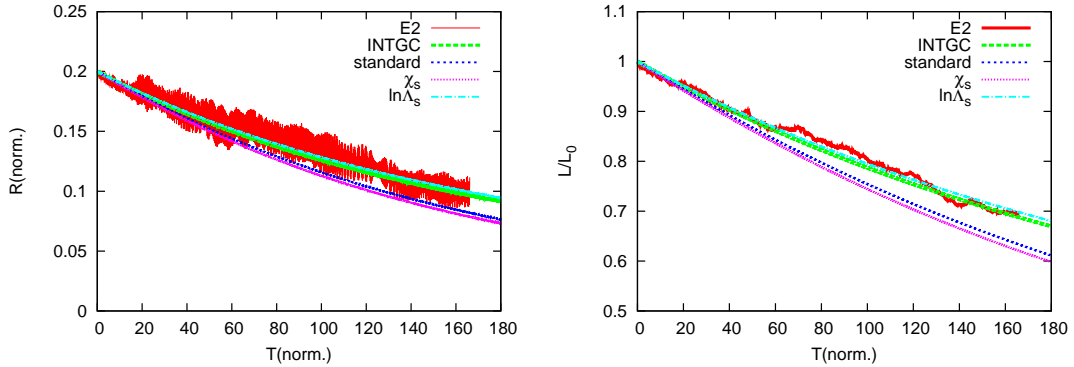

Figure 6.8: Same as in figure 6.7 but for run E2 with higher resolution and closer in.

6.2 Hernquist Cusp

We performed two circular runs E1 and E2 in the shallow Hernquist cusp to test the limit of our friction formula using the ϕGRAPE code. Run E1 is performed on the GRAPE cluster at ARI and E2 with larger N on the GPU cluster of NAOC/CAS. The orbital decay is shown in figures 6.7 and 6.8. The velocity distribution function deviates significantly from the analytic limiting case of an idealized cusp (see figure 5.3). The χ function is stable over the simulation time and depends only weakly on the distance to the central SMBH. Therefore we used for the semi-analytic simulations with INTGC constant mean values for the circular orbits. The local scale length of run E1 entering the Coulomb logarithm is smaller than the distance to the center, which is the limiting value, because $R_0 = 0.7$ is close to the scale radius. The orbital decays are very well reproduced in R and in L. A comparison with the standard values $\ln \Lambda_s$ and χ_s show a significant deviation mainly due to the different χ function.

6.3 Outskirts of the Plummer Sphere

The background distribution is a self-gravitating Plummer sphere and the outskirts are described by eq. 4.25. We place the orbits of the circular run P1 and eccentric run P2 far outside the

Table 6.2: Parameters of the SUPERBOX runs.

Run	M_0	a	r_{cut}	N	m	dt	d_{c}	R_0	$V_{\text{c},0}$	$V_0/V_{\text{c},0}$	a_{90}	$\ln \Lambda_0$
	$10^9\,\mathrm{M_\odot}$	kpc	kpc	10^7		Myr	pc	kpc	km/s		pc	
P1	0.970	0.1	10	1	7	0.3	16.1	0.7	77.2	1.0	0.538	2.87
P2	0.970	0.1	10	1	7	0.3	16.1	0.7	77.2	0.7	0.869	2.87
D1	0.826	0.1	1	1	6	0.1	16.7	0.4	94.2	1.0	0.186	2.48
D2	0.826	0.1	1	1	6	0.1	16.7	0.4	94.2	0.7	0.207	2.48
D3	0.128	1.0	10	1	8	0.1	2.78	0.3	42.8	1.0	1.24	4.75
D4	0.128	1.0	10	1	8	0.3	2.78	0.3	42.8	0.7	1.70	4.44
H1	0.197	1.0	10	1	7	1.0	16.1	0.7	34.8	1.0	6.0	3.68
H2	0.197	1.0	10	1	7	0.3	16.1	0.7	34.8	0.56	9.7	3.46
H3	0.052	1.0	10	1	8	0.1	4.76	0.3	30.3	1.0	2.13	3.64
H4	0.052	1.0	10	1	8	0.1	4.76	0.3	30.3	0.9	2.39	3.53

Note. All quantities are given in physical units. For all cases, the total mass M_{tot} inside the cutoff radius r_{cut} is $10^9\,M_\odot$ and mass of the supermassive black hole is $10^6\,M_\odot$, M_0 is the enclosed mass at the initial distance R_0, a is the scale radius, N is the particle number, 2^m is the number of cells per dimension in each grid, and d_{c} is the cell size of the middle grid. The initial value of a_{90} from Eq. 4.28 is calculated for the exact model.

Plummer radius in order to be very close to the power law density with $\eta_0 - 3 = -5$ and a Kepler potential according to eqs. 4.25. Since the number density is very small, we cannot use a PP code. Instead we use SUPERBOX with ten million particles. The parameters of all SUPERBOX runs are listed in table 6.2.

Due to the very long orbital decay time the density distribution evolves slowly. In steep cusps the representation of the local density in the semi-analytic calculations is the most critical parameter. This affects the decay time scale via the local density and also the enclosed mass (Eq. 5.1). In the Kepler limit the enclosed mass is given by the constant central mass M_{c}. In lowest order the density evolution can be modeled by a linear expansion of the Plummer radius. The analytic solution of circular orbits is still given by equation 5.11 with the substitution $t \to s(t)$ with $\nu = 2$ (see Eq. 5.13). By fitting the density profiles at different times we find $t_{\text{a}} = 11.3$ Gyr.

The numerical results of the circular run P1 are compared in figure 6.9 to the analytic solution of Eq. 5.6 in the Kepler limit using an expanding Plummer profile. For the calculations with INTGC we correct additionally for the decreasing enclosed mass. Since in these simulations a_{90} is not resolved by the grid cell size d_{c}, we determined the best value for the minimum impact parameter to be $b_{\text{min}} = d_{\text{c}}/2$. The same factor $1/2$ is used for all other SUPERBOX runs. In the lower panel of figure 6.9 the orbits with standard Coulomb logarithm $\ln \Lambda_{\text{s}}$ and standard χ_{s} as in figure 6.6 are shown for comparison. In figure 6.10 the orbital evolution is shown for the eccentric run P2.

In both cases we find a satisfying agreement of the numerical results and our analytic predictions. With the standard formula the decay is significantly delayed (figures 6.9 and 6.10). Here the corrections due to the correct χ function and the new Coulomb logarithm have a different sign and cancel each other partly. In the circular run both corrections are equally important. In the eccentric run the correction by the χ function dominates, but the additional correction due to the new $\ln \Lambda$ is also significant.

6.4 Outskirts of Dehnen Models

The background distribution is a self-gravitating Dehnen model with $\eta = 1.5$ in the inner cusp. We place the orbits of the circular run D1 and the eccentric run D2 (table 6.2) far outside the
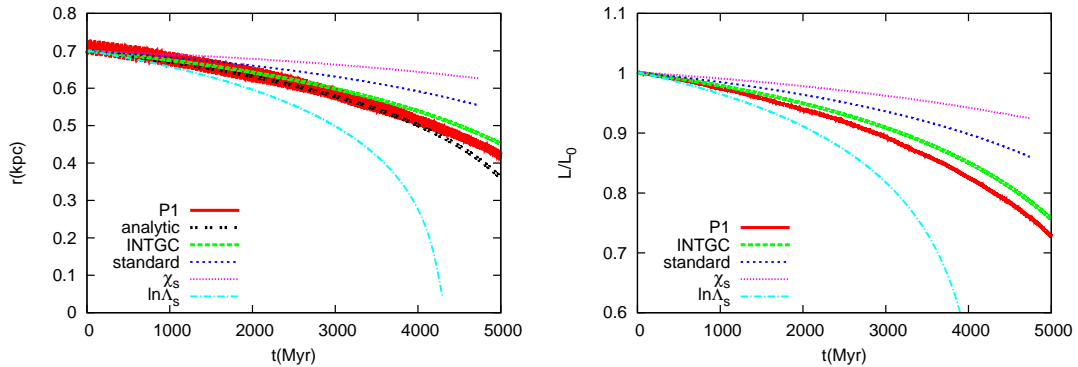
Figure 6.9: Orbital decay of a BH in the outskirts of a self-gravitating Plummer sphere for the SUPERBOX runs of the circular orbit P1 in $r(t)$ (left panel) and in $L(t)/L_0$ (right panel). The SUPERBOX run is compared to the semi-analytic results with INTGC. Same notation as in figure 6.6. The left panel shows additionally the analytic approximation from equation 5.7.

scale radius in order to be very close to the power law density with $\eta_0 - 3 = -4$ and a Kepler potential according to Eqs. 4.24.

The numerical results are compared in figures 6.11 and 6.12 with the semi-analytic calculations using INTGC. In the numerical simulations the inner cusp becomes shallower and shrinks considerably leading to a decreasing enclosed mass and increasing density in the outer parts. We correct for that in INTGC. In these simulations a_{90} is not resolved as in the Plummer case. The numerical results are in good agreement with the analytic predictions using the same minimum impact parameter $b_{\min} = d_c/2$. The orbital resonances seen in figure 6.11 are connected to a motion of the density center of the cusp, which is used as the origin of the coordinate system. Therefore the angular momentum of the orbit oscillates due to the accelerated zero point.

6.5 Self Gravitating Cusps

Here we study the orbital decay of a BH in self-gravitating cusps of Dehnen models using SU-PERBOX without a central SMBH. We performed two runs (one circular and one eccentric) for a Hernquist ($\eta = 2$) and a Dehnen-1.5 ($\eta = 1.5$) model each. For the semi-analytic calculations we use again the same minimum impact parameter $b_{\min} = d_c/2$ in Eq. 4.26.

6.5.1 Dehnen-1.5 Model

We studied the decay of a circular and an eccentric orbit in the inner cusp of a Dehnen model with $\eta = 1.5$ (D3 and D4 in table 6.2). A comparison of $d_c/2$ and a_{90} shows that the close encounters are marginally resolved. For this reason and because the transition of the inner and outer power law regimes is very wide, the analytic approximation of a self-gravitating cusp shows systematic deviations. With INTGC we find nevertheless a very good match to the SUPERBOX results of the circular run D3 (see Fig. 6.11) and for the eccentric run D4 (see Fig. 6.12). In the upper panel of Fig. 6.11 we show also the circular run with a larger time-step in SUPERBOX, where for the close encounters with impact parameter comparable to the cell length d_c the motion of the perturber are not resolved in time. This leads to a larger effective minimum impact parameter and a slower orbital decay.
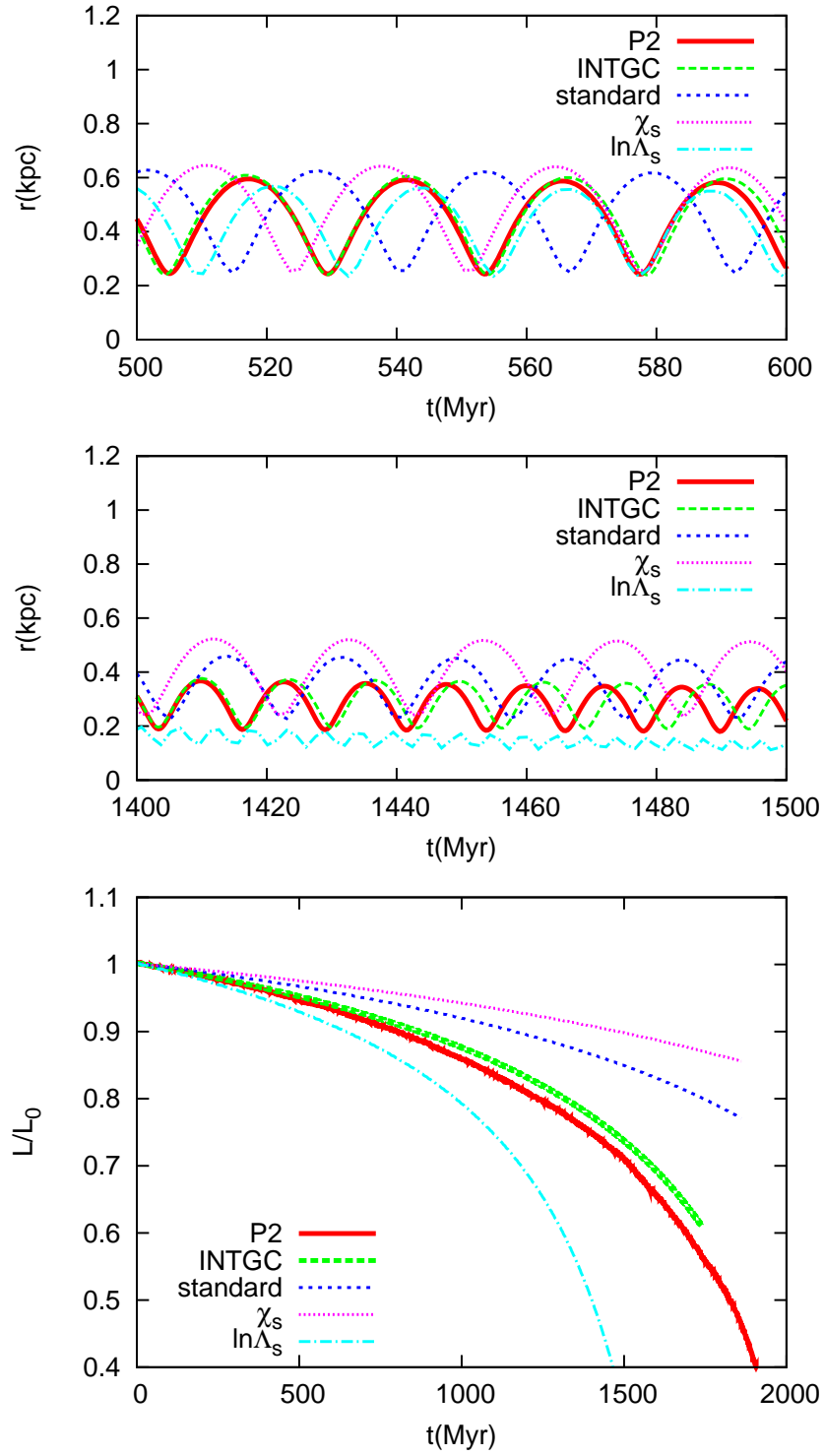
Figure 6.10: Same as in figure 6.9 but for the eccentric orbit P2. The top panels show $r(t)$ for two time intervals with higher resolution and the bottom panel shows $L_z(t)$ for the full calculation. Same notation as in figure 6.6.
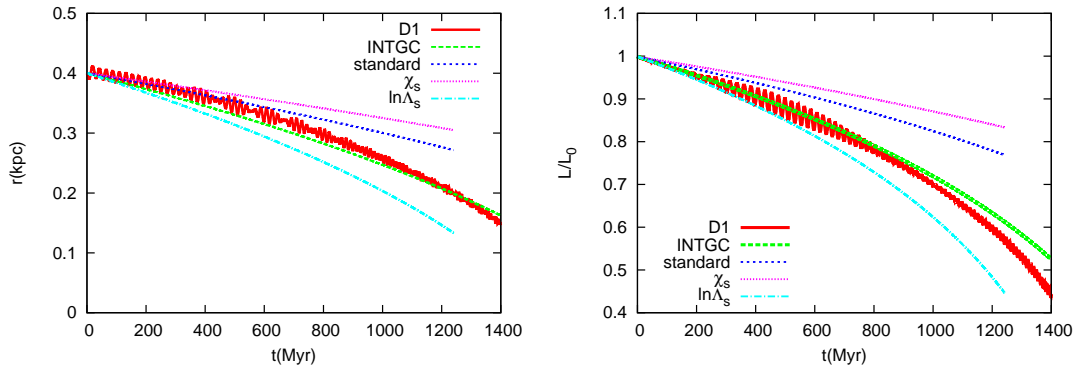
Figure 6.11: Same as in figure 6.9 but for the orbit D1 in the outskirts of a Dehnen model. Same notation as in figure 6.6.

6.5.2 Hernquist Model

The Hernquist model with shallower cusp ($\eta = 2$) is even more complicated, because X_c^2 (see equation 4.10) is not constant and the χ function depends on the outer boundary conditions. For the two runs H1 (circular) and H2 (eccentric) the parameter range is similar to the Dehnen-1.5 case with marginally resolved a_{90}. The orbits of H3 (circular) and H4 (eccentric) are further in and the grid resolution is higher leading to a fully resolved a_{90}. All orbits are reproduced reasonably well by INTGC using the correct χ function and taking the correct velocity dispersion in a_{90} Tremaine et al. (1994) into account (see figures 6.15 – 6.18).

6.6 Velocity Distribution Functions

The local velocity distribution functions are crucial for the dynamical friction force. Therefore we check here the numerical realization of the distribution functions. The best way to measure the distribution function is to determine the χ function in a spherical shell at the distance of the BH for different times. In figure 6.19 the χ functions are shown for a few examples. The top panel shows the Kepler cases and the bottom panel the self-gravitating cusps.

In the Kepler case we present the circular runs in the Bahcall-Wolf cusp (BW, A1, A3), the Plummer case P1, and the Dehnen case D1. In the Bahcall-Wolf cusp the final distribution function of A1 is very close to the theoretical line. The χ functions of the eccentric runs B1, B2 are very similar and therefore not plotted here. In the runs A2 and A3, where the density profile flattens slightly, a bump in the χ function at velocities below the circular velocity can be observed. It is more pronounced in run A3. The χ value at the circular speed is not influenced dramatically showing that the orbital delay is caused entirely by the reduced local density. The distribution functions in the outskirts of the Plummer and Dehnen cases are very stable and well represented by the theoretical expectations.

The lower panel of figure 6.19 shows the χ functions of the self-gravitating cusps for the circular runs H1 and D3. Here we added the case of the eccentric run D4 to demonstrate the stability of the velocity distribution functions independent of the shape of the orbit.

Overall the velocity distribution functions are very robust and well reproduced in the numerical simulations.
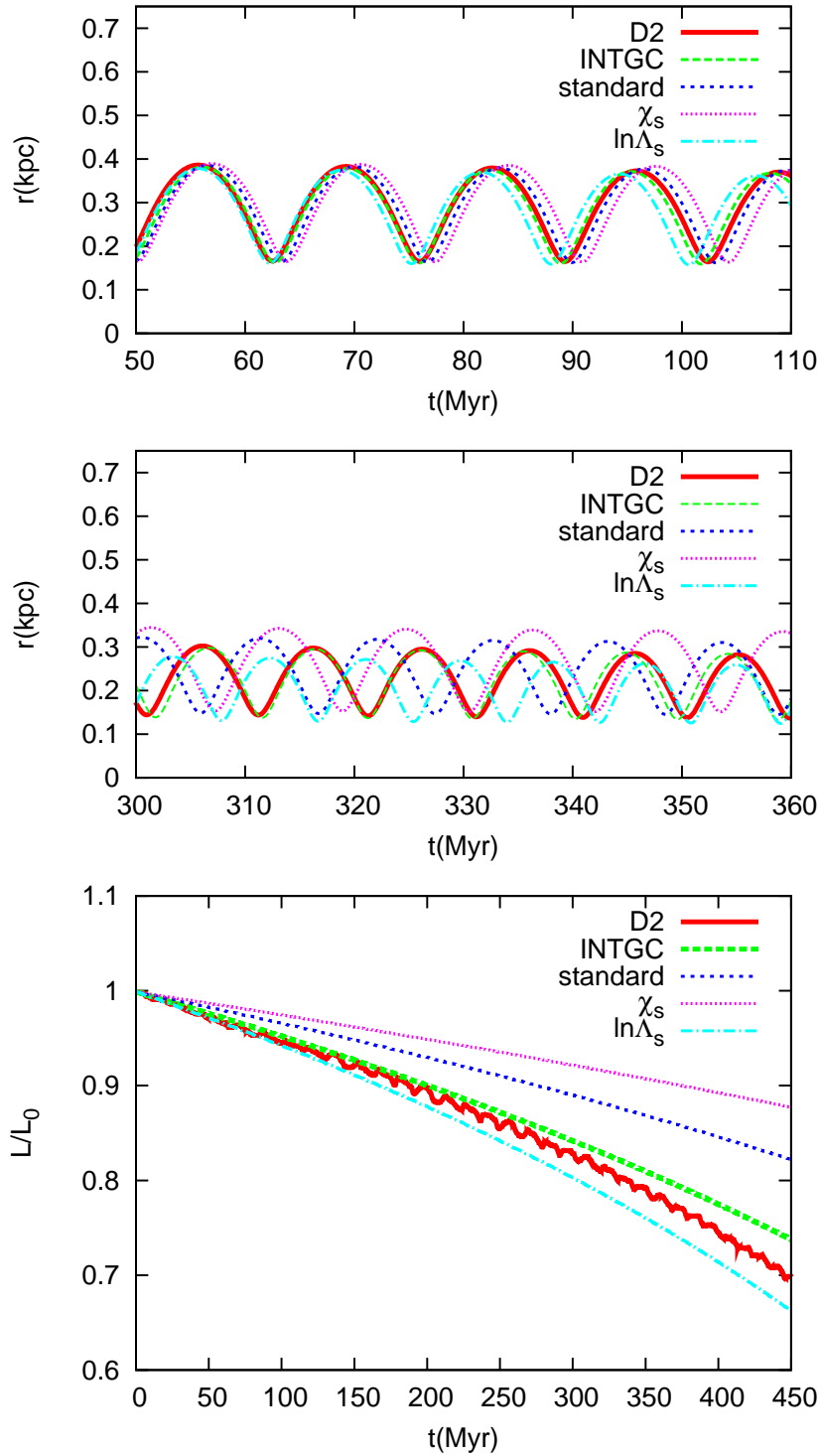
Figure 6.12: Same as in figure 6.11 but for the eccentric orbit D2. Same notation as in figure 6.6.
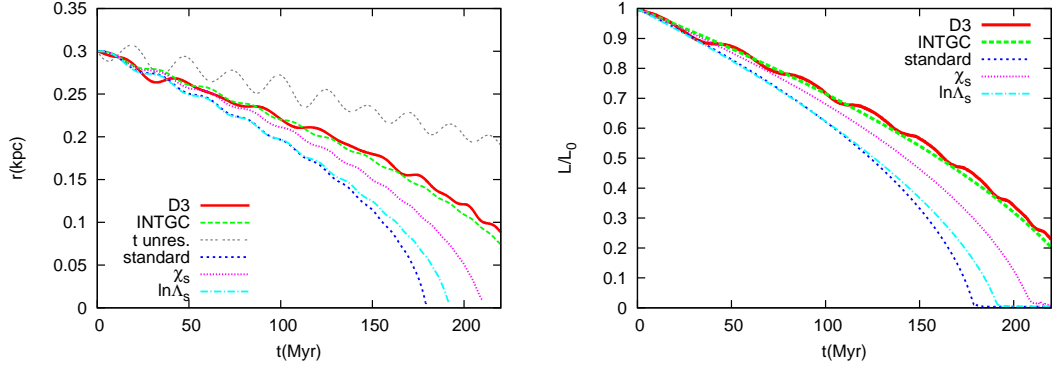
Figure 6.13: Orbital decay in distance (left panel) and angular momentum (right panel) for the circular orbit D3 in the self-gravitating inner cusp of the Dehnen-1.5 model. Same notation as in figure 6.6. In the left panel there is additionally the orbit with insufficient time resolution shown.
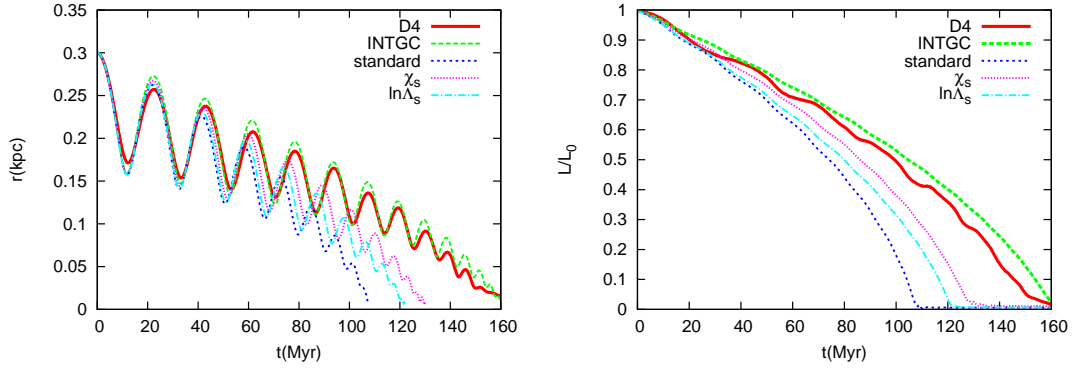
Figure 6.14: Same as in figure 6.13 but for the eccentric orbit D4.
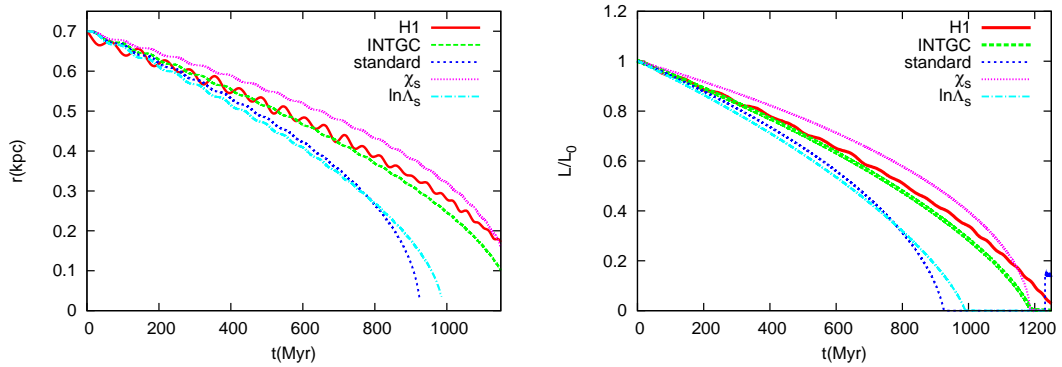
Figure 6.15: Same as in Fig. 6.13 for the circular orbit H1 in the self-gravitating inner cusp of the Hernquist model.
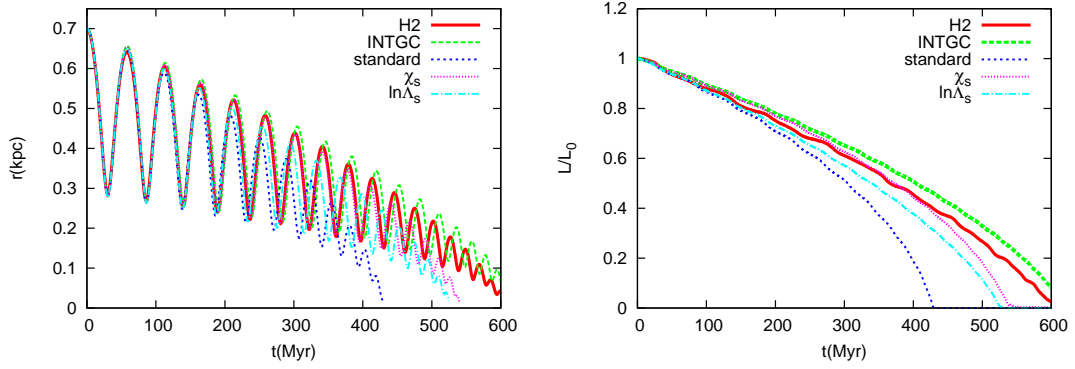
Figure 6.16: Same as in Fig. 6.15 for the eccentric orbit H2.
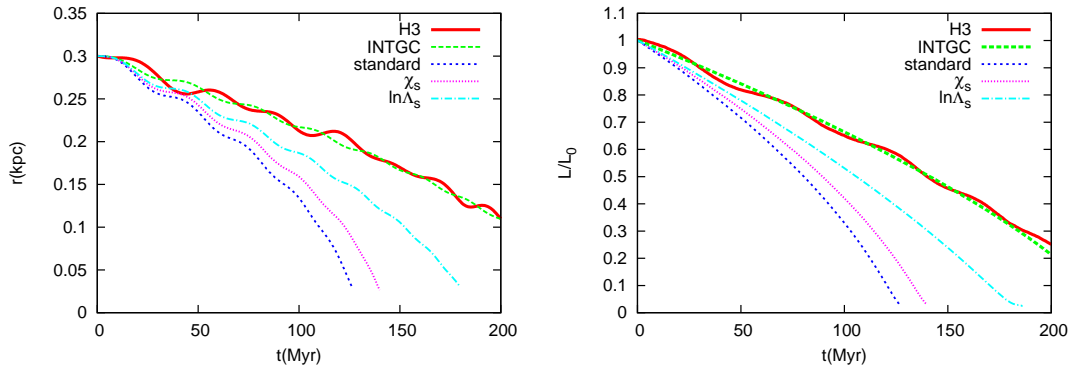
Figure 6.17: Same as in Fig. 6.15 for the circular orbit H3 with resolved a_{90}.
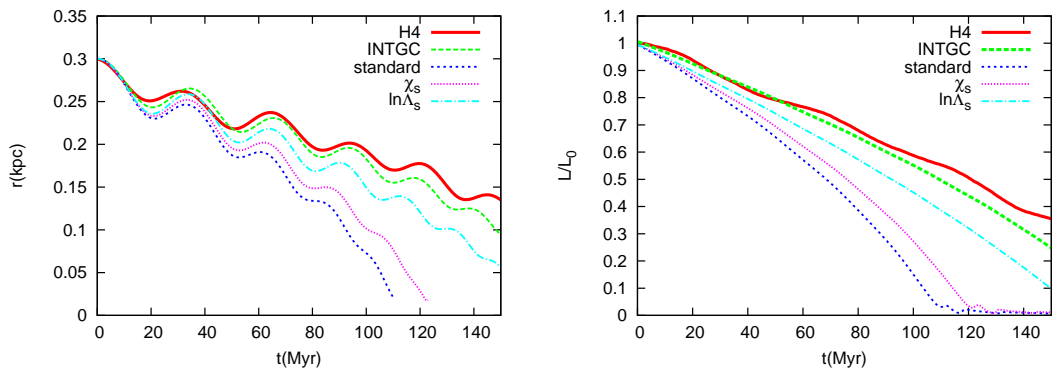
Figure 6.18: Same as in Fig. 6.17 for the eccentric orbit H4.
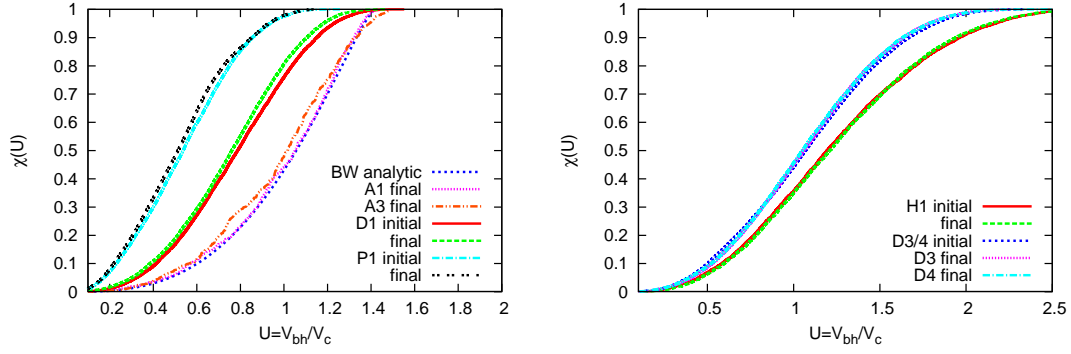
Figure 6.19: Left:Initial and final χ functions for the circular runs in the Bahcall-Wolf cusp (BW, A1, A3), the Dehnen case D1, and the Plummer case P1. Right:Same for the self-gravitating cusps with Dehnen-1.5 (D3, D4) and Hernquist profiles (H1).

Key findings of the study

1. The new Coulomb logarithm combined with self-consistent velocity distribution functions in the Chandrasekhar formula fits very well for wide range of power law indices (-1 ... -5).

2. The orbital decay of SMBH caused by dynamical friction is delayed when compared to theoretical predictions once the mass enclosed by the SMBH orbit becomes less than the mass of SMBH.

3. In the phase where the delay in orbital decay is noticed, eccentricity of the SMBH orbit tends to increase. The cause of this increase in eccentricity is not known and needs to be investigated further.

4. For the cases, where the minimum impact parameter a_{90} is not resolved, fits to the numerical study suggest that one should use 1.5 times the softening length for PP code and half the cell size for PM code as minimum impact parameter.

Chapter 7

Evolution of SMBH Binaries in Equal Mass Galaxy Mergers

<div style="background: yellow;">

Contents of this Chapter

1. Evolution of the SMBHs at the center of isolated spherical galaxy models and study of the N-dependence of the SMBH binary hardening rates.

2. Equal mass galaxy mergers and evolution of supermassive black holes in stellar dynamical regime.

3. Study of the N-dependence of the binary hardening rates in galaxy merger study and comparison with evolution in spherical galaxy models.

4. Analysis of the shapes of the merger remnant and its relation to the SMBH binary hardening rates.

5. The estimate of the coalescence time of the SMBH binary for each of our galaxy merger simulations.

   Note: The contents of this Chapter are based on paper by Khan, F. M., Just, A., & Merritt, D. 2011, ApJ, 732, 89

</div>

In this chapter we present the results of the two sets of N-body experiments performed to study the evolution of supermassive black holes. In first study we introduce two SMBHs in the center of a single spherical galaxy on almost circular orbit and study the evolution of the binary in late hard binary phase. In the second case we follow the evolution of two SMBHs in the merger of two spherical galaxies. In both cases we study the effect of different particle number N used to represent the galaxy model and measure the binary's hardening rates for each model. In the case of galaxy mergers we also analyze the shapes of the merger remnant and estimate the time it takes the SMBHs to coalesce in each of our models.

7.1   Numerical Methods and Initial Conditions

Our initial conditions are based on spherical galaxy models following Dehnen's (1993) density law already described in section 3.1.3. Here we use the power law index γ for density profile and it is

related to η through $\gamma = 3 - \eta$.

$$\rho(r) = \frac{(3-\gamma)M_{\text{gal}}}{4\pi} \frac{r_0}{r^\gamma(r+r_0)^{4-\gamma}}, \tag{7.1}$$

and with cumulative mass profile

$$M(r) = M_{\text{gal}} \left(\frac{r}{r+r_0} \right)^{3-\gamma}, \tag{7.2}$$

where M_{gal} is the total mass of the galaxy, r_0 is a scale radius, and γ defines the slope of inner (inside r_0) density profile. We adopted $\gamma = 1$, corresponding to a Hernquist model (Hernquist 1990), for all initial models. A massive particle representing a SMBH was placed at the center of each galaxy model. The isotropic distribution function reproducing $\rho(r)$ in the combined potential of the stars and the SMBH in dynamical equilibrium was computed numerically and used to generate Monte-Carlo positions and velocities for the stars. In what follows, we adopt "model units" such that $M_{\text{gal}} = G = r_0 = 1$.

The models can be scaled to physical units by fixing galaxy mass M_{gal} and scale radius r_0 combined with the relations

$$
\begin{aligned}
[T] &= \left(\frac{GM_{\text{gal}}}{r_0^3} \right)^{-1/2} \\
&= 1.5\text{Myr} \left(\frac{M_{\text{gal}}}{10^{11}M_\odot} \right)^{-1/2} \left(\frac{r_0}{\text{kpc}} \right)^{3/2}, \tag{7.3} \\
[V] &= \left(\frac{GM_{\text{gal}}}{r_0} \right)^{1/2} \\
&= 655\text{km}\,\text{s}^{-1} \left(\frac{M_{\text{gal}}}{10^{11}M_\odot} \right)^{1/2} \left(\frac{r_0}{\text{kpc}} \right)^{-1/2} \tag{7.4}
\end{aligned}
$$

We use following relation (Gualandris & Merritt 2008) to scale our models to the physical systems:

$$R_{eff} \approx 1.2\text{kpc}(\frac{M_{\text{gal}}}{10^{11}M_\odot})^{0.075} \tag{7.5}$$

In a Hernquist model the effective (projected half-mass) radius R_{eff} is $\sim 1.81 r_0$. For a typical, luminous ($M_{\text{B}} \approx -20$) elliptical galaxy or bulge, $R_{\text{eff}} \approx 1.5$ kpc, $M_{\text{gal}} \approx 10^{11}M_\odot$ and $[T] \approx 1.1$ Myr. Effective radii scale very weakly with galaxy luminosity (though with considerable scatter; e.g. Ferrarese et al. (2006)) and in the case of $10^9 M_\odot$ galaxy, whose SMBH would have a mass more suited to detection by LISA, the physical unit of time would be closer to 6 Myr. In the latter case, the length of our longest integrations amounts to ~ 1.5 Gyr.

Two sets of simulations were carried out. In the first set, a single spherical galaxy was created, with a central SMBH of mass $M_{\bullet 1} = 0.001$ (Model A) or 0.01 (Model B). A second SMBH, of the same mass ($M_{\bullet 2} = M_{\bullet 1}$), was then placed at a distance of 0.5 from the center on a circular orbit. Integrations were continued until a time $t_{\max} = 100$.

In the second set, two identical spherical models were created, each containing a single central SMBH, and the two galaxies were merged. Here again, two values for SMBH mass were used: $M_{\bullet 1} = 0.001$ (Model C) or 0.01 (Model D) and the integrations were continued until a time $t_{\max} = 250$.

In order to test the dependence of the results on particle number N, all simulations were carried out with $N = (32, 64, 128, 256, 512) \times 10^3$. Tables 7.1 and 7.2 summarize the parameters of the two sets of runs.

The N-body integrations were carried out using ϕ-GRAPE (see section 3.3.1 for details). The time-step parameter η was set to 0.01 for all our runs. The choice of parameters was motivated by

Table 7.1: Parameters of the single-galaxy integrations

Run	N	$M_{\bullet 1}$	Run	N	$M_{\bullet 1}$
A1	32k	0.001	B1	32k	0.01
A2	64k	0.001	B2	64k	0.01
A3	128k	0.001	B3	128k	0.01
A4	256k	0.001	B4	256k	0.01
A5	512k	0.001	B5	512k	0.01

Note. Columns from left to right read: the galaxy model; number of particles used in galaxy model; The mass of the supermassive black hole used in the model; galaxy model; particle number N; SMBH mass.

Berczik et al. (2005) who found that integration accuracy is more sensitive to η than to softening length ϵ. Those authors adopted $\eta = 0.01$ and $\epsilon = 1 \times 10^{-4}$ for their study of SMBH binary evolution. In order to resolve the orbit of the massive binary in our simulations down to a semi-major axis $a \approx 10^{-4}$ we adopted the smaller softening length $\epsilon = 10^{-5}$. With these choices of η and ϵ, the relative energy error in our simulations was $\sim 10^{-8}$. For a more detailed discussion of these issues we refer the reader to section 2 of Merritt et al. (2007) .

The N-body integrations were carried out on three, special-purpose computer clusters. `Titan`, at the Astronomisches Rechen-Institut in Heidelberg, and `gravitySimulator`, at the Rochester Institute of Technology are both 32-node clusters employing GRAPE accelerator boards. Some calculations were also carried out on the GPU-enhanced cluster "Kolob" at the University of Heidelberg. For the latter runs we used the modified version of the ϕ-GRAPE code including the SAPPORO library (Gaburov et al. 2009).

7.2   Isolated Models

Evolution of a binary SMBH in a gas-free galaxy can be divided into three phases (Begelman et al. 1980) and is described in detail in section 2.2. In first phase, the SMBHs are unbound to each other and move independently in the galaxy potential. The evolution of the individual SMBH orbits during this phase is governed by dynamical friction against the background stars. The second phase begins when the two SMBHs are close enough together to form a bound pair. In this phase, the separation between the SMBHs decreases very rapidly due to the combined effects of dynamical friction and ejection of stars by the gravitational slingshot. (For a detailed discussion of this phase, we refer the reader to the careful analysis in Milosavljević & Merritt (2001).) At the end of the second phase, the two SMBHs form a hard binary, defined as a binary that ejects passing stars with positive (unbound) energies. Phase three consists of slow evolution of the binary as depleted orbits are repopulated, via two-body scattering or some other process. In a spherical galaxy with large N, the timescale for orbital re-population is essentially the two-body relaxation time which scales as $\sim N/\ln N$.

Figure 7.1 plots the separation R between the two SMBH particles versus time in the isolated galaxies, Models A and B. Here we can see the three phases of binary evolution described above.

(1) In the first phase, the separation between the two SMBHs decreases due to dynamical friction. This phase ends when $R \approx r_h$, the gravitational influence radius. r_h can be defined as the radius of a sphere around the binary SMBH that encloses a stellar mass equal to twice the binary mass. For Models A, $M_{\bullet 1} = 0.001$ and $r_h \approx 0.07$. From Figure 7.1, we can see that the first phase ends indeed when $R \approx 0.07$. Here we want to emphasize that this estimate does not take into account the changes in the galaxy that are induced by the presence of the second SMBH.

For Models B, the radius of influence is ~ 0.25. From the right panel of Figure 7.1, it is clear that the first phase ends when $R \approx 0.25$. Here the dynamical friction phase is very short-lived
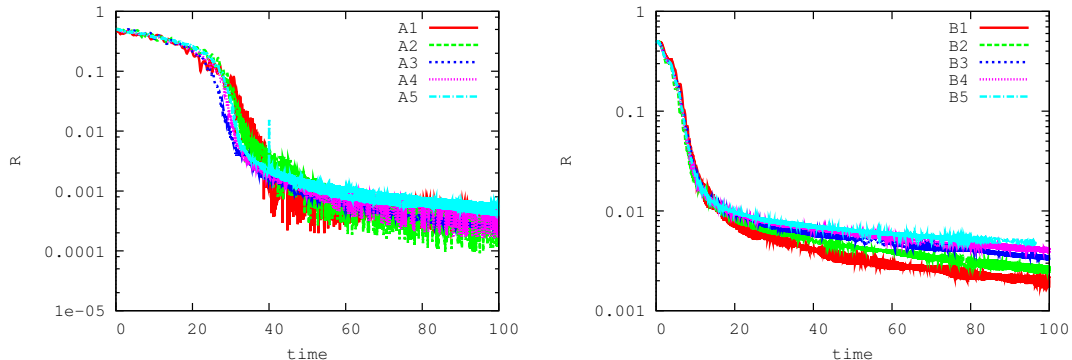
Figure 7.1: Evolution of the relative separation between the SMBHs, in ten N-body integrations of isolated spherical galaxies with different particle numbers according to Table 7.1. Models A (left) have $M_{\bullet 1} = M_{\bullet 2} = 0.001$ and models B (right) have $M_{\bullet 1} = M_{\bullet 2} = 0.01$.

because the initial separation of the two SMBHs is only $\sim 2r_h$.

(2) In the second phase, the separation between the two SMBHs decreases very rapidly. Dynamical friction, and the ejection of stars by the gravitational slingshot, act together to efficiently extract angular momentum from the massive binary. These processes are not well defined in the regime where the massive binary is neither very hard nor very soft; equations (13) and (14) of Milosavljević & Merritt (2001) give approximate expressions for the rate at which energy is transferred to stars by the two mechanisms. For Models A this process continues until $t \approx 40$ while for Models B, this phase ends at $t \approx 20$. The motion of two SMBHs in this phase is approximately Keplerian. We define the semi-major axis a and eccentricity e via the standard relations:

$$\frac{1}{a} = \frac{2}{R} - \frac{v^2}{\mu}, \tag{7.6}$$

$$e = \sqrt{1 + \frac{2h^2}{\mu^2}\left[\frac{v^2}{2} - \frac{\mu}{R}\right]}. \tag{7.7}$$

where $\mu = G(M_{\bullet 1} + M_{\bullet 2})$, v is the relative speed, and h is the specific angular momentum of the relative motion.

(3) The rapid phase of binary hardening comes to an end when $a \approx a_h$, where a_h is the semi-major axis of a "hard binary":

$$a_h = \frac{q}{(1+q)^2}\frac{r_h}{4} \tag{7.8}$$

(e.g. Merritt et al. 2007). Here $q = M_{\bullet 2}/M_{\bullet 1}$) is the mass ratio of two SMBHs; for both Models A and B, $q = 1$. For Models A, $a_h \approx 0.004$ with $a_h^{-1} \approx 250$ and for Models B, $a_h \approx 0.016$ with $a_h^{-1} \approx 65$.

From Figure 7.2, we see that there is no clear dependence of the binary hardening rate on N until the binary becomes hard, $a < a_h$. For Models A this happens around $t = 25$ and for Models B around $t = 30$. Beyond these times the binary hardening rate exhibits a clear N dependence in the sense that hardening is slower for larger N. Similar N-dependence has been seen in other studies of binary evolution in spherical galaxies (e.g. Makino & Funato 2004, Berczik et al. 2005, Merritt et al. 2007). For real spherical galaxies, with much larger N, the binary would stop evolving beyond this point. This is the origin of final parsec problem (see section 2.3 for details).

We estimated the hardening rate s in the N-body integrations, where

$$s \equiv \frac{d}{dt}\left(\frac{1}{a}\right), \tag{7.9}$$
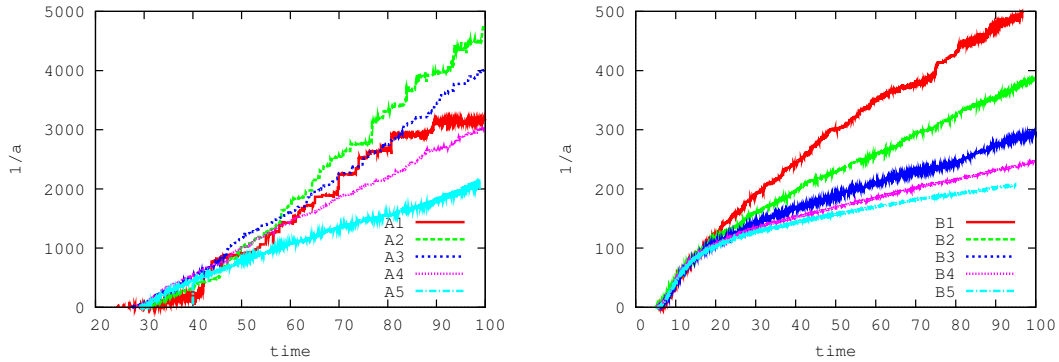
Figure 7.2: Evolution of the inverse semi-major axis of the massive binary in the isolated models for models A and B.
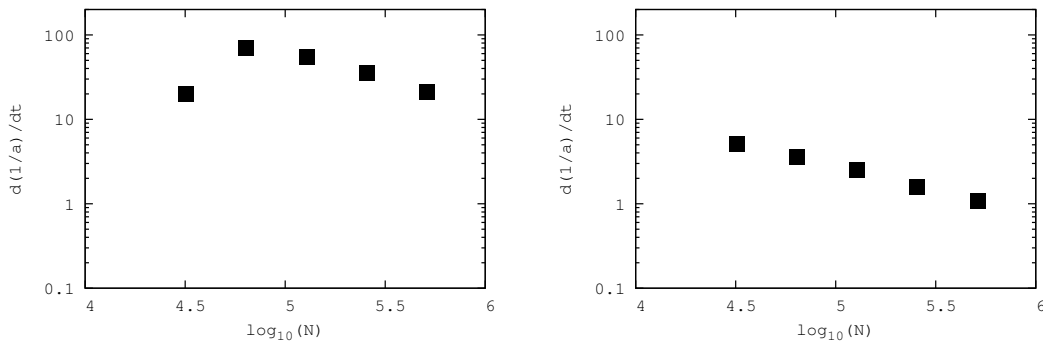
Figure 7.3: N-dependence of the binary hardening rate in the isolated galaxy models. *Left:* Models A; *Right:* Models B.

by fitting straight lines to $a^{-1}(t)$ in an interval $\Delta t = 50$ from $t = 50$ to $t = 100$. Figure 7.3 shows the N-dependence of s. We see that for $N > 50k$, the hardening rate is a decreasing function of N; scaling as $\propto N^{-0.6}$; this is consistent with the scalings found by other authors in the same N-range, e.g. Berczik et al. (2005), Merritt et al. (2007). The Figure 7.3 also shows lower hardening rates for Model B (right panel) when compared with Model A (right panel), by roughly an order of magnitude. For large N, the two-body relaxation time is long compared with orbital periods of stars near the massive binary, and the loss cone around the binary is nearly empty. In this regime, and in the asymptotic (large-N) limit, the rate of binary evolution is predicted to scale as $\sim [(M_{\bullet 1} + M_{\bullet 2})]^{-1}$ (e.g. equation (32) of Merritt et al. (2007)). Given that a is roughly a factor ten smaller, at a given time, in Models A as compared with Models B, there is an additional delay in the early phase of the hard binary evolution. However this delay is negligible for the decay time t_0 until which the semimajor axis reaches a_0, when energy loss by GWs start to dominate.

7.3 Galaxy Mergers

We studied the evolution of binary SMBHs in merging galaxies by creating two identical galaxy models, each with a central SMBH, and placing the two galaxies on bound relative orbits. Table 7.2 summarizes the parameters of the galaxy merger models. The initial separation of the two

Table 7.2: Parameters of the galaxy merger simulations

Run	$2 \times N$	$M_{\bullet 1}$
C1	64k	0.001
C2	128k	0.001
C3	256k	0.001
C4	512k	0.001
D1	64k	0.01
D2	128k	0.01
D3	256k	0.01
D4	512k	0.01

Note. Columns from left to right read: the galaxy merger model; Total number of particles used in galaxy merger; The mass of the supermassive black hole used in each of the merging galaxies.

galaxy centers was $20r_0$. The initial relative velocity of the two galaxies was chosen such that the SMBH separation at first peri-center passage was $\sim r_0$; in other words, the initial orbit of the binary galaxy was substantially eccentric. This was done in order to reduce the computational time required to bring the two SMBHs close together; in fact, a galaxy merger from such nearly "head-on" initial conditions is unlikely.

Figure 7.4 illustrates the merging of two galaxies. The two galaxies merge due to violent relaxation. In the initial phase (top panels) the two SMBH particles remain strongly associated with their respective density cusps. As a consequence dynamical friction is much more efficient in bringing the two black holes together than if they were naked. This is because the effective mass that goes into the dynamical friction is higher. Dynamical friction cannot be distinguished from violent relaxation due to the deformation of the galaxies. The two cusps merge and form a new galactic center. The density profile of the newly formed galaxy as a result of the merger is identical to those of initial merging systems (both merging galaxies have Hernquist profile). Homology following a merger of galaxies with SMBHs at their centers was already found by Milosavljević & Merritt (2001). The homology is short lived and the profile changes drastically in the sphere of influence of SMBHs after they form the binary. This change is attributed to the transfer of energy from the SMBH binary to surrounding stars.

Fig. 7.5 shows the density profile for model A5 where core scouring is done by the binary in individual galaxy and model C4 where we notice same effect for the cusp which is formed by the galaxy merger. This depleted cusp is already reported by (e.g. Makino & Funato 2004, Merritt et al. 2007) studying the evolution of binary in a single spherical galaxy model and by Milosavljević & Merritt (2001) while studying binary SMBH evolution in merger of steep cusps ($\rho \propto r^{-2}$). The central logarithmic slope of the density profile has dropped from -1 to ~ -0.3 (model C4). This drop in the central density is caused by the transfer of SMBH binary's energy to stars that interact with it, hence providing an explanation of mass deficiency in the centers of giant elliptical galaxies. In the next Chapter (section 8.3), we present the estimates of the mass ejected from the center of galaxies by the SMBH binaries using a large set of N-body simulations.

7.4   SMBH Binary Evolution in Galaxy Mergers

Figure 7.6 shows the separation between the two SMBHs in the merger models. The first peri-center passage occurs around $t \approx 80$. As the galaxies merge, the two SMBHs remain centrally located in their respective density cusps, until coming close enough together that a binary SMBH forms, at $t \approx 100$, or slightly earlier in the case of Model D (phase one). The separation between the two SMBHs then decreases very rapidly due to the combined effects of dynamical friction and slingshot ejection of stars (phase two). Once the hard binary is formed, the hardening rate of
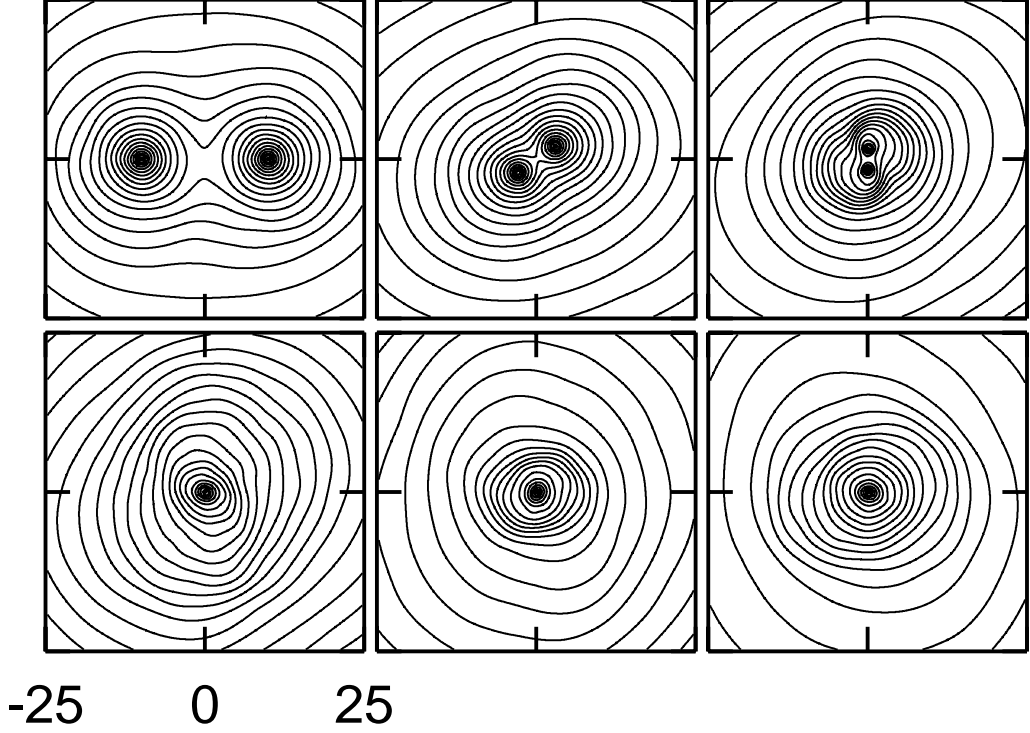
Figure 7.4: Density contours projected onto the initial orbital plane for Model C3 ($M_\bullet = 0.01$). First row: $t = (0, 70, 90)$. The two black holes spiral in centered at their respective cusps. Second row: $t = (110, 150, 200)$. The two cusps undergo violent relaxation and merge into one. The density of the newly-formed cusp drops rapidly as the stars in the central region gain energy from SMBH binary.
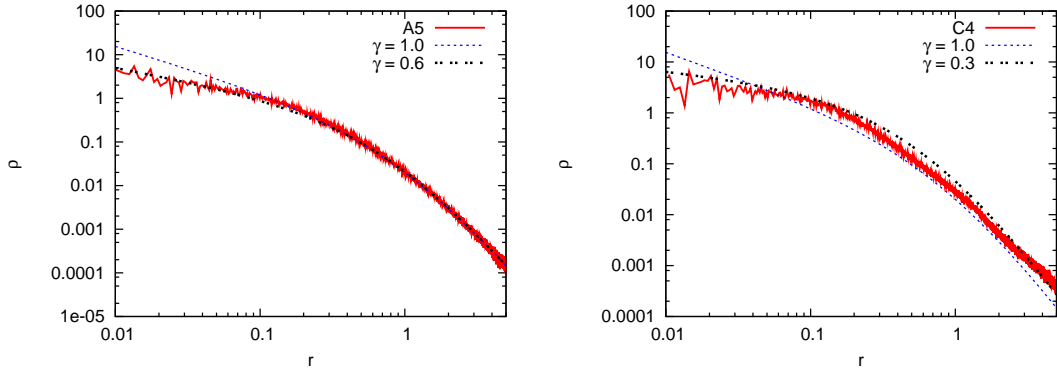
Figure 7.5: *Left:* Spatial density profile for model A5 averaged over five different time steps ($t = 60, 68, 76, 84, 92$). The figure also shows the initial density profile ($\gamma = 1$) and a fit to the data using Eq. 7.1 with $\gamma = 0.6$ and $r_0 = 0.8$. The central density drops as the binary ejects mass from the core. *Right:* Spatial density profile for model C4 averaged over five different time steps ($t = 140, 160, 180, 200, 220$). The figure also shows the initial density profile ($\gamma = 1$) and a fit to the data using equation 7.1 with $\gamma = 0.3$ and $r_0 = 0.6$.
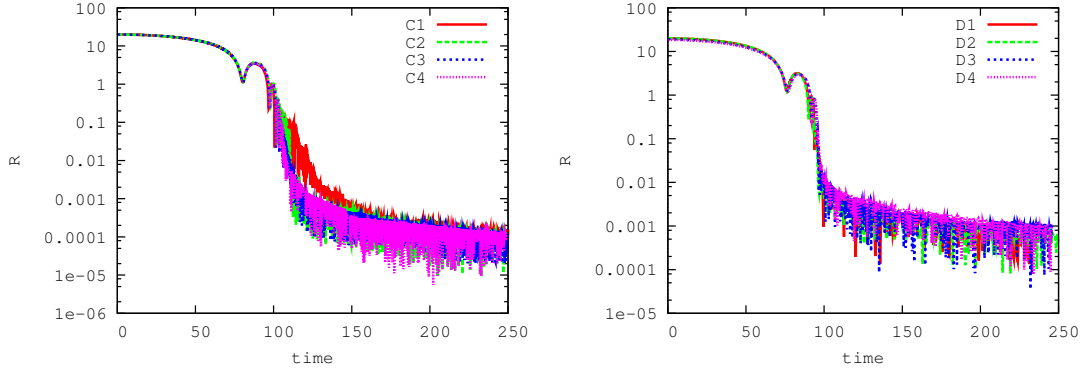
Figure 7.6: Evolution of the relative separation between the two SMBHs in the galaxy merger simulations. For models C the peri-center of the bound SMBH orbit is just above 10^{-5} which is the softening used in the code. For models D the peri-center is well above 10^{-5}.
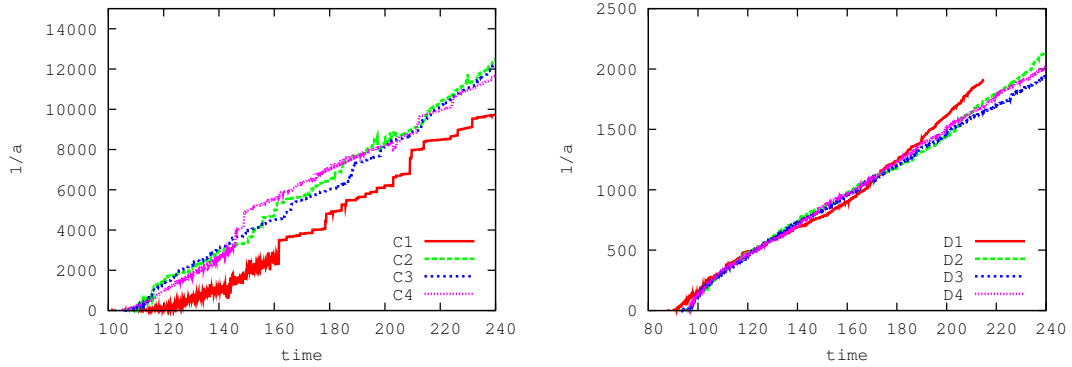
Figure 7.7: Evolution of the inverse semi-major axis of the binary SMBH during the galaxy merger simulations. Clearly the binary evolution does not depend on the number of particles used in both model C and model D.

the binary decreases (phase three). This behavior is qualitatively similar to what was seen in the isolated galaxy models.

However there is one important difference between the binary evolution in the isolated and merging galaxies. Figure 7.7 shows the evolution of the inverse binary semi-major axis. One can notice a striking difference in the long term evolution of SMBH binary evolution in galaxy merger runs when compared with the evolution in those of single galaxy models, i.e **SMBH binary evolution does not depend on the number of particles N used in galaxy mergers**. All the models C with different particle numbers produce same evolution of the SMBH binary's semi-major axis except model C1 which has very small number of particles (N = 64 K). Same is true for models D.

Figure 7.8 shows the binary hardening rates in the galaxy merger simulations; the latter were computed in the same way as in the isolated galaxy models, by linear fit of $1/a$ in the range $150 \leq t \leq 200$. **In the galaxy merger models, there is essentially no dependence of the binary hardening rate on particle number.** Furthermore, in Models C and D, the hardening rates are much higher – more than five times higher than in the Models A and B, respectively, when N = 512k. Also the $(M_{\bullet 1} + M_{\bullet 2})^{-1}$ dependence of binary hardening rates noticed in the spherical galaxy models is still present for the galaxy mergers. The N-independent hardening in galaxy mergers simulations imply that our results can be extrapolated to the much larger N of real
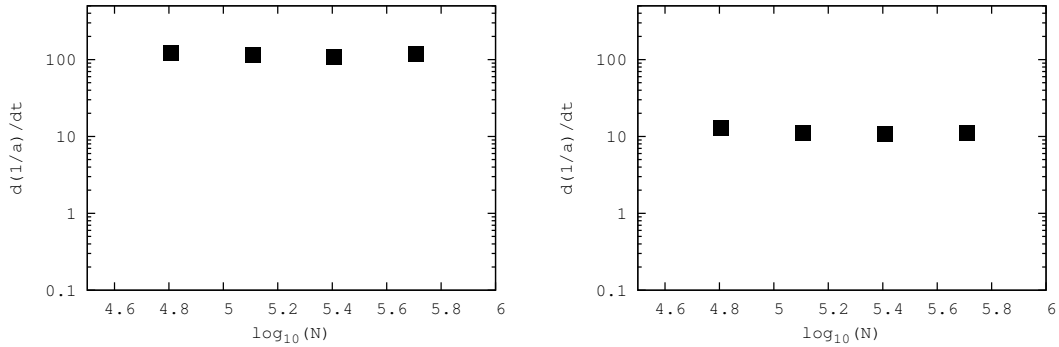
Figure 7.8: Binary hardening rates in the galaxy merger simulations (left panel: Model C, right panel: Model D). The binary hardening rates are calculated by fitting straight lines to the inverse semi-major axis in final phase of the binary evolution. For both models C and D the hardening rates are N-independent. Also the hardening rates are approximately 10 times smaller for models D which has 10 times more massive SMBH binary than for models C.

galaxies. The SMBH binary can efficiently harden through stellar dynamical interactions alone in the centers of merged galaxies, hence providing a plausible solution to the final parsec problem.

A likely explanation for this difference is that the non-spherical shapes of the merger remnants provide an additional source of torque on the stellar orbits, allowing them to interact with the central binary on a timescale shorter than the two-body relaxation time. It has been argued (Merritt & Poon 2004, Berczik et al. 2006) that allocating even a small fraction of the stellar orbits to a "centrophilic" family could lead to binary hardening rates that are much larger than those that result from two-body relaxation alone. In galaxies with non spherical shapes the angular momentum of the stars is not conserved. This produces a whole wealth of stellar orbits including the orbits that can pass very close to the center.

We evaluated the shapes of the merged galaxies in a number of ways. The central density contours for Model C3 are shown in Figure 7.9. Departures from axisymmetry are evident. Figure 7.10 shows the principle axis ratios of the merger remnant in Model C3 as a function of time; these were defined as the axis ratios of a homogeneous ellipsoid with the same inertia tensor. The departures from spherical symmetry are modest, but definite, and they appear to be nearly independent of time toward the end of the simulation. Presumably, the non-spherical shapes of merger remnants reported in this study result in a large population of stars on centrophilic orbits. Inside the influence radius of SMBH, the centrophilic orbit family includes saucer or cone orbits in the axisymmetric potentials (Sridhar & Touma 1999) and pyramids orbits (angular momentum close to zero) in triaxial potentials (Merritt & Vasiliev 2011). Outside the influence radius, most of the centrophilic orbits are chaotic in a triaxial potential (Poon & Merritt 2001).

The evolution of binary eccentricity in the merger models is presented in Figure 7.11. We notice high eccentricities for both models as soon as the SMBHs become bound, approaching unity for models D. The high eccentricities are due in part to the high eccentricity ($e = 0.95$) of the galaxies relative orbit prior to the merger, and, in some runs, to post-merger evolution. The high values of eccentricity in these models have potential implications for the SMBH binary evolution. The rate of orbital energy loss due to gravitational wave emission increases very steeply for the value of eccentricity approaching unity (see equation 7.10). As a consequence the eccentric binary will coalesce much faster than a circular binary.

87
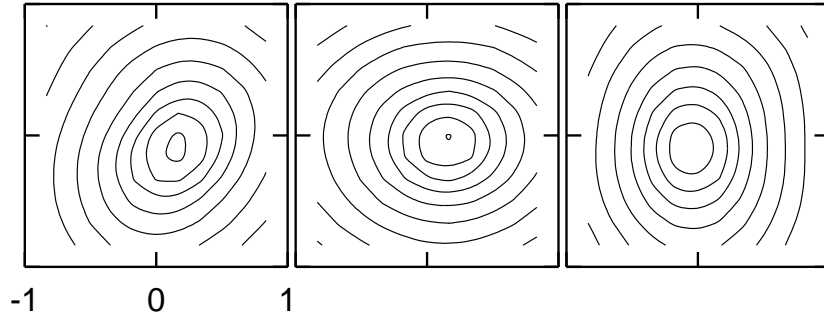
Figure 7.9: Density contours of the central region for galaxy merger model C3 at t = 150, projected on xy plane(left), xz plane(center), yz plane(right). Departures from spherical symmetry are clearly evident.
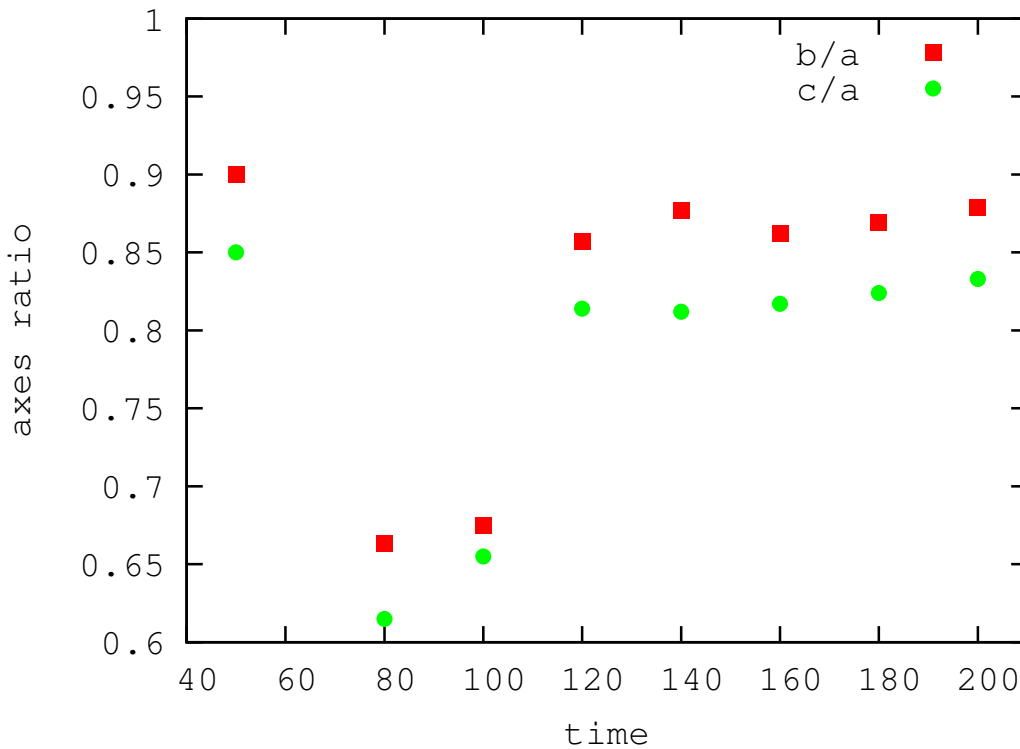
Figure 7.10: Ratio of intermediate to major (b/a) and minor to major (c/a) axes for Run C3, calculated at a distance of 1 (in model units) from the center of mass of the SMBH binary. As the two individual cusps merge at time around 110 (see figure 7.4), the axes ratio of the newly formed galactic nuclei remain constant with time.
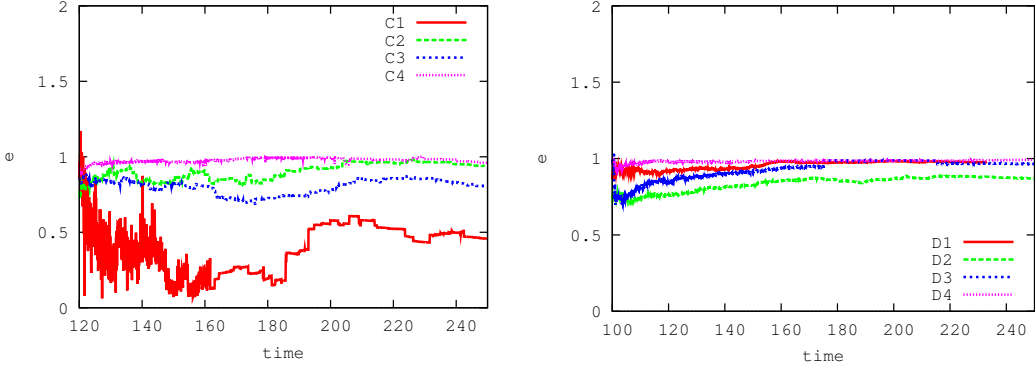
Figure 7.11: Evolution of binary eccentricity for models C (left) and models D (right). The SMBH binary has very eccentric orbit for both models. For models D the value of eccentricity approaches unity.

7.5   Estimates of Coalescence Time for SMBHs

SMBH binaries are a potentially important source of gravitational wave (GW) emission. Gravitational waves extract energy and angular momentum from the binary, hence changing its orbital elements. Peters (1964) gives approximate, orbit-averaged expressions for the rates of change of a binary's semi-major axis and eccentricity due to GW emission:

$$
\begin{aligned}
\left(\frac{da}{dt}\right)_{\mathrm{GW}} &= -\frac{64}{5}\frac{G^3 M_{\bullet 1} M_{\bullet 2}(M_{\bullet 1}+M_{\bullet 2})}{a^3 c^5 (1-e^2)^{7/2}} \times \\
&\qquad \left(1+\frac{73}{24}e^2+\frac{37}{96}e^4\right), \quad (7.10)\\
\left(\frac{de}{dt}\right)_{\mathrm{GW}} &= -\frac{304}{15}e\frac{G^3 M_{\bullet 1} M_{\bullet 2}(M_{\bullet 1}+M_{\bullet 2})}{a^4 c^5 (1-e^2)^{5/2}} \times \\
&\qquad \left(1+\frac{121}{304}e^2\right). \quad (7.11)
\end{aligned}
$$

We define $t_{\mathrm{GW}}(a_0, e_0)$ as the time required, according to the coupled equations (7.10, 7.11), for the binary semi-major axis to shrink to zero under the influence of GW emission, starting from the initial values (a_0, e_0). This time is a strong function of e_0 for $e_0 \approx 1$, as it is in some of our simulations.

The full time to coalescence, t_{coal}, includes also the time from the start of the simulation until the GW regime is entered. We estimated t_{coal} as follows. In the N-body merger models, the post-merger hardening rate of the binary, s, is essentially independent of a and N (Figures 7.7, 7.8). The rate of change of the binary semi-major axis in this regime is approximately

$$
\left(\frac{da}{dt}\right)_{\mathrm{NB}} \approx -sa^2, \quad s \approx \mathrm{const.} \quad (7.12)
$$

Given values for M_{gal} and r_0, this dimensionless rate can be converted into physical units. At some time in the simulation, a will have fallen to such a small value that $(da/dt)_{\mathrm{NB}}$ as given by equation (7.12) will equal $(da/dt)_{\mathrm{GW}}$, where the latter quantity is computed from *both* a and e. We define t_0 as the time at which these two rates are equal. The full time to coalescence, t_{coal}, is the time from the start of the simulation until t_0, plus $t_{\mathrm{GW}}(a_0, e_0)$, where $a_0 \equiv a(t=t_0)$, $e_0 \equiv e(t=t_0)$.

Table 7.3: Time to Gravitational Wave Coalescence

Run	a_{final}	s_{final}	e_0	a_0 (pc)	t_0 (Gyr)	t_{coal} (Gyr)
C1	1.2×10^{-4}	120.3	0.51	$(2.6 \times 10^{-3}, 1.2 \times 10^{-2})$	$(11.5, 0.54)$	$(15.9, 0.94)$
C2	7.2×10^{-5}	115.2	0.96	$(1.2 \times 10^{-2}, 8.5 \times 10^{-2})$	$(2.6, 0.21)$	$(5.1, 0.29)$
C3	7.3×10^{-5}	108.3	0.80	$(4.9 \times 10^{-3}, 3.3 \times 10^{-2})$	$(7.5, 0.35)$	$(10.8, 0.41)$
C4	6.8×10^{-5}	118.2	0.95	$(1.0 \times 10^{-2}, 8.3 \times 10^{-2})$	$(2.8, 0.22)$	$(5.7, 0.30)$
D1	5.2×10^{-4}	13.0	0.97	$(9.0 \times 10^{-2}, 6.7 \times 10^{-1})$	$(2.7, 0.21)$	$(5.5, 0.35)$
D2	4.0×10^{-4}	11.2	0.88	$(4.4 \times 10^{-2}, 3.0 \times 10^{-1})$	$(6.7, 0.26)$	$(10.8, 0.47)$
D3	5.1×10^{-4}	10.7	0.95	$(7.2 \times 10^{-2}, 5.4 \times 10^{-1})$	$(4.0, 0.22)$	$(7.6, 0.38)$
D4	4.7×10^{-4}	11.0	0.98	$(9.0 \times 10^{-2}, 9.1 \times 10^{-1})$	$(2.2, 0.23)$	$(4.7, 0.26)$

Note. (col 1) galaxy merger model, (col 2) the value of semi-major axis of massive binary at the end of the simulation, (col 3) binary hardening rate, (col 4) The value of the eccentricity at the end of the run, (col 5) the estimated value of semi-major axis at which stellar dynamical hardening becomes equal to the hardening due to GW emission (given here for two galaxy models with masses $10^9 M_\odot$, $10^{11} M_\odot$ respectively), (col 6) time spend by the SMBH binary in classical hardening regime, (col 7) The total time to coalescence calculated from the time of formation of SMBH binary till the final merger of the two SMBHs.

Table 7.4: Time to Gravitational Wave Coalescence (Run C3)

e_0	a_0 (pc)	t_{coal} (Gyr)
0.5	$(2.6 \times 10^{-3}, 1.8 \times 10^{-2})$	$(14.96, 0.65)$
0.0	$(1.9 \times 10^{-3}, 1.3 \times 10^{-2})$	$(20.46, 0.86)$

Note. columns from left to right read: col(1) eccentricity e used to calculate GW hardening rates and estimate coalescence time for the SMBHs, col(2) the estimated value of semi-major axis at which stellar dynamical hardening becomes equal to the hardening due to GW emission (given here for two galaxy models with masses $10^9 M_\odot$, $10^{11} M_\odot$ respectively), col (3) SMBH binary's time to coalescence for the two galaxy models with masses $10^9 M_\odot$, $10^{11} M_\odot$ respectively.

In most cases, t_0 exceeded the final time t_{final} of the simulation. In these cases, the time Δt between t_{final} and t_0 was assumed to be

$$\Delta t = s(t_{\text{final}})^{-1} \left(\frac{1}{a_0} - \frac{1}{a_{\text{final}}} \right). \tag{7.13}$$

In such cases, we also assumed that $e(t)$ was constant, $e(t) = e(t_{\text{final}})$, for $t > t_{\text{final}}$ when computing t_{GW}.

Computation of the GW evolution rates required adoption of particular values for the physical units of length and time because speed of light c introduces a physical scale. We fix mass of the galaxy M_{gal} and effective radius R_{eff} by using equation 7.5. Table 7.3 gives results for two different assumed values of the galaxy mass: $M_{\text{gal}} = (10^9, 10^{11}) M_\odot$.

For low mass-galaxies ($10^9 M_\odot$), the total time to merge the SMBHs exceeds ~ 1 Gyr, whereas for high-mass galaxies ($10^{11} M_\odot$) the coalescence time is well below 0.5 Gyr. For Models D with higher SMBH masses, the total decay times are comparable to those in Models C, because the energy loss due to GWs increases with BH mass compensating for the delay due to the reduced hardening rate s. Both phases t_0 and t_{GW} scale with $M_\bullet^{1/5}$. Because of the strong dependence of t_{GW} on eccentricity, Table 7.4 gives a_{GW} and Δt, for run C3 only, under two different assumptions about e_0: $e_0 = 0.5$ and $e_0 = 0$. The total decay time increases by a factor of 2–3 if the orbit is assumed circular at the start of the GW phase.

Key Findings of The Study

- For the evolution of the SMBH binary in isolated spherical galaxy models, we rediscovered the N-dependence in the hardening rates.

- The N-dependence in SMBH binary hardening rates found in spherical galaxy models, disappears in galaxy mergers suggesting that stellar dynamics alone can solve final parsec problem.

- The SMBH binary hardening rates are approximately 5 times higher for galaxy mergers when compared to those of isolated spherical galaxy models.

- The hardening rates scales as $\sim M_\bullet^{-1}$ with the mass of the binary if the masses of the merging galaxies remain fixed.

- The newly formed galaxy as a result of the merger of two galaxies is mildly triaxial and ensures a constant supply of stars to interact with massive binary on timescales much shorter than relaxation time.

- The estimated coalescence time for billion solar mass SMBH binaries is less than 1 Gyr for all our models and for those with mass of a million solar mass it is few Gyr.

Chapter 8

Unequal Mass Galaxy Mergers and SMBH Binaries

<div style="border: 2px solid; padding: 1em; background: yellow;">

Contents of this Chapter

1. Direct N-body simulations of galaxy mergers having different mass ratios and density profiles of the merging galaxies.

2. The dependence of SMBH binary hardening rate on mass ratios of merging galaxies as well as on the density profiles.

3. Study of the shape of the merger remnant formed as a result of the merger of galaxies with different mass ratios and density profiles.

4. The density profiles of newly formed galaxies as a result of the merger and estimates of mass deficits obtained by comparing the cumulative mass profile at various times.

5. Estimate of the SMBH binary coalescence time for different masses of SMBHs and implications for GW detection by LISA.

6. Post Newtonian simulations to test the accuracy of the estimated coalescence times for few selected cases.

   Note: The contents of this Chapter are based on paper by Khan, F. M., Preto, M., Berczik, P., Berentzen, I., Just, A., & Spurzem, R. submitted to ApJ

</div>

In previous chapter we have shown that galaxies which form via equal mass mergers are mildly triaxial. We have also shown that hardening rates of SMBH binaries resulting from equal-mass mergers are substantially higher than those found in spherical nuclei, and are independent of the total number N of stars, thus allowing us to extrapolate our results to real galaxies. This scenario also needs to be investigated for unequal mass mergers of galaxies.

The slingshot ejection of stars by the central SMBH binary drives the binary inspiral. As a result the central density profile of the merger remnant becomes very shallow. On energetic grounds it can be shown that in order for the binary to reach coalescence, it needs to eject an amount of stellar mass of order of its own mass, $M_{\mathrm{ej}} \sim \alpha \times M_{\bullet}$, where $\alpha = O(1)$ and $M_{\bullet} = M_{\bullet 1} + M_{\bullet 2}$ (Merritt & Milosavljević 2005, Perets & Alexander 2008). Merritt (2006b) studied

the mass deficits created by SMBH inspirals evolving in spherical symmetric nuclei and found an average $\alpha \sim 0.5$. However, unless their mass $M_\bullet \lesssim$ few $\times 10^6 M_\odot$, the evolution of SMBH binaries in gas-poor *spherical* galaxies tends to stall due to depletion, on the (local) dynamical timescale, of the pool of stars whose orbits intersect the binary (e.g. Milosavljević & Merritt 2003a, Makino & Funato 2004, Berczik et al. 2005, Khan et al. 2011, Preto et al. 2011); as a consequence, the binaries studied by Merritt (2006b) did not reach coalescence, and therefore the analysis of mass deficits in that study was restricted to the early phases of the hard binary inspiral – thus compromising the interpretation of its final α. Merritt et al. (2007) extended the latter study by following the inspiral of binaries up to coalescence in the lower mass range using an approximate Fokker-Planck description for stellar scattering. They find substantially higher mass deficits than before, albeit restricting their calculations to spherical models and very shallow cusps (with initial $\gamma \sim 1/2$) in strong contrast with the larger γ typical of compact low-mass nuclei. More precise estimates of α from more realistic galaxy merger studies are therefore certainly needed; in particular, ones that do not rely on any of the following approximations: spherical symmetry, low γ, crude model for inferring the mass ejected from the increase in the binary's orbital energy, or those generally inherent to the Fokker-Planck formalism.

In this chapter, we present the results of detailed N-body simulations using a range of more realistic models of merging galactic nuclei with varying mass ratio q and central logarithmic slopes γ. We restrict the simulations to $q = M_{\rm gal,s}/M_{\rm gal,p} = M_{\bullet 2}/M_{\bullet 1}$. We study the shape of the merger remnant of galaxies having different density profiles and different mass ratios. For each of our models, the hardening rate of the SMBH binary, the axis ratios of the merger remnant and the resulting mass deficit are calculated. The coalescence timescales for binary SMBHs from the time of formation of binary till the full coalescence of SMBHs due to emission of gravitational waves are also estimated and for few cases confirmed by using simulations which include $\mathcal{PN}$ terms up to 3.5 orders.

8.1   Initial Conditions and Numerical Methods

Our aim is to study the dependence of the hardening rates with the mass ratios and central concentration of the nucleus – as well as the resulting imprint of the SMBH inspiral on the stellar distributions of post-coalescence nucleus. Here we describe setup for our galaxy models, numerical methods and hardware used for dynamical numerical modeling of SMBHs and their host galaxies.

8.1.1   The Host Galaxies and Their SMBHs

Following closely the initial set-up of our previous numerical experiments (see chapter 7), we represent the individual galaxies or galactic nuclei by spherically symmetric Dehnen (1993)N-body models (see equations 7.1 and 7.2) .

In addition, we represent the SMBHs by massive particles with zero velocity placed at the center of both the primary and the secondary galaxies. The masses of the SMBHs are set to be 0.5 percent of their host galaxy, a choice made to be consistent with the observed ratio of SMBH mass to bulge mass (Kormendy & Richstone 1995, Ferrarese & Ford 2005). Thus the two SMBHs in the simulations have the same mass ratio q as their host galaxies. The Dehnen models have an isotropic distribution function of velocities (no net rotation), are spherically symmetric and are initially set-up to be in dynamical equilibrium with a gravitational potential given by $\Phi(r) = -GM_\bullet/r + \Phi_*(r)$, where $\Phi_*(r)$ is the gravitational potential due to the stars alone.

The galaxies size ratio scales with the corresponding mass ratio as $R_2/R_1 \propto \sqrt{M_2/M_1}$. By choosing four different values of $\gamma = 0.5, 1.0, 1.5, 1.75$, the central part of our galaxy models represent the variety of observed density profiles in both early and late type galaxies.

For Dehnen models the ratio of the effective radius (projected half-mass radius) $R_{\rm eff}$ to the

Table 8.1: Model parameter and properties of the primary galaxy.

Model	N	γ	$r_{1/2}$	R_{eff}
A	128k	0.5	3.13	2.35
B	128k	1.0	2.41	1.81
C	128k	1.5	1.69	1.27
D	64k	1.75	1.35	1.01

NOTE — Columns from left to right show the model name, the particle number N, the half-mass radius $r_{1/2}$ and the effective radius R_{eff}, respectively, for our primary galaxy models.

half-mass radius $r_{1/2}$ is given approximately as

$$\frac{R_{eff}}{r_{1/2}} \approx 0.75, \tag{8.1}$$

and shows only a weak dependence on γ (Dehnen 1993). In the following we refer to the more massive galaxy as the *primary* galaxy and the lighter one as the *secondary*. In our model units we use for our primary galaxy a total mass and scale radius of $M_{\text{gal,p}} = r_{0,\text{p}} = 1$. We also set the gravitational constant to $G = 1$.

In the absence of relativistic effects on the binary's orbit, our models are scale-free and can be *a posteriori* scaled to galaxies of different total mass and size. However, the inclusion of radiation reaction effects on the binary due to GW emission introduces an absolute scale associated to the universal value of the speed of light. Such scalings are described in detail in section 8.4 when coalescence times are explicitly computed.

We have performed a series of N-body experiments where we vary the mass ratio of the galaxies and SMBHs q and the inner density slope γ. In Table 8.1 we summarize the model parameters and properties for the primary galaxies used in our simulations. The computational wall-clock time increases with increasing cuspiness (higher γ) of the density profile since particles in the center need very small numerical time steps in order to resolve accurately the (locally) strongly varying gradients of the gravitational potential. In order to keep the computational time within reasonable limits we built our model D (highest $\gamma = 7/4$) with only half as many particles as the other models.

The secondary galaxies used in our merger simulations have the same density profile, i.e., the same γ, as the primary galaxies, but have different masses $M_{\text{gal,s}}$ and scale radii $r_{0,\text{s}}$. Both primary and secondary galaxy models have equal number of particles N.

8.1.2 Galaxy Merger Setup

The initial center of mass positions and velocities for the two galaxies are calculated from the Keplerian orbit of the equivalent two-body problem, with given apo- and peri-centers, r_{a} and r_{p}, respectively. The two galaxies start at the apo-center of their relative orbit. The initial separation between the center of mass of the two galaxy is $\Delta r = 15 r_{0,\text{p}}$; and since the half-mass radius of each nucleus is $R_{1/2} \lesssim 2.5$, this choice ensures that the galaxies are initially well separated while, at the same time, we minimize computing time. The initial relative velocity of the two galaxies is chosen such that the SMBH separation at first peri-center passage is $\sim 2 r_{0,\text{p}}$; in other words, the initial orbit of the binary galaxy has eccentricity ~ 0.75, which corresponds to a circularity parameter value of $\epsilon = L/L_{\text{c}} \sim 0.66$.

Table 8.2: Parameters of the galaxy mergers study

Run	N_{tot}	γ	q	$r_{0,\text{s}}$
A1	256k	0.5	0.1	0.316
A2	256k	0.5	0.25	0.5
A3	256k	0.5	0.5	0.707
A4	256k	0.5	1.0	1.0
B1	256k	1.0	0.1	0.316
B2	256k	1.0	0.25	0.5
B3	256k	1.0	0.5	0.707
B4	256k	1.0	1.0	1.0
B5	256k	1.0	0.05	0.22
C1	256k	1.5	0.1	0.316
C2	256k	1.5	0.25	0.5
C3	256k	1.5	0.5	0.707
C4	256k	1.5	1.0	1.0
D1	128k	1.75	0.1	0.316
D2	128k	1.75	0.25	0.5
D3	128k	1.75	0.5	0.707
D4	128k	1.75	1.0	1.0

NOTE. — Col.(1) Galaxy merger model. Col.(2) Number of particles. Col.(3) Central density profile index γ. Col.(4) Mass ratio of merging galaxies and their black holes. Col.(5) Scale radius of secondary galaxy.

8.1.3   Numerical Methods and Hardware

We used ϕ-GRAPE (see section 3.3) to carry out N-body integrations. As ϕ-GRAPE does not include the regularization (Mikkola & Aarseth 1998) of close encounters or binaries, we have to use a gravitational (Plummer-)softening for all particles. The softening length is chosen to be sufficiently small (i.e. 5×10^{-5} in our model units) to keep the (dense) stellar system as collisional as possible/necessary. Only in the few runs in which we include the $\mathcal{PN}$ terms added to the equations of motion of the binary, the softening between the SMBH particles is equal to zero.

The N-body integrations were carried out on three computer clusters. "titan", at the Astronomisches Rechen-Institut in Heidelberg, the GPU-enhanced cluster "kolob" at the University of Heidelberg and "laohu" in Beijing.

8.2   Evolution of SMBH Binaries

Figure 8.1 shows the relative separation R between the two black holes during a galaxy merger. According to the equivalent two-body trajectory used to set up the initial galaxy orbital parameters, the galaxy centers, and hence the SMBHs, should reach a separation of $2r_{0,\text{p}}$ during the first peri-center passage. However, as figure 8.1 shows, in case $q \gtrsim 1/2$, the SMBH separation shrinks well below $2r_{0,\text{p}}$ during the galaxy merger phase. As q decreases, and hence the mass of the secondary galaxy decreases as well, the galaxies reach the first pericenter passage after following more closely the corresponding two-body orbit. In the same figure the color of the arrows signals the time T at which the two SMBHs in a particular model form a binary system. As q decreases, the arrows move from left to right signaling the longer interval of time between the start of merger and formation of the binary. Neither the time T nor R_{peri} are as sensitive to γ as they are to q.

When the SMBHs become bound their separation is $R \approx r_{\text{h}}$. Once a SMBH binary is formed, dynamical friction and the ejection of stars by the gravitational slingshot, act together to efficiently extract angular momentum from the massive binary and the binary separation shrinks rapidly.
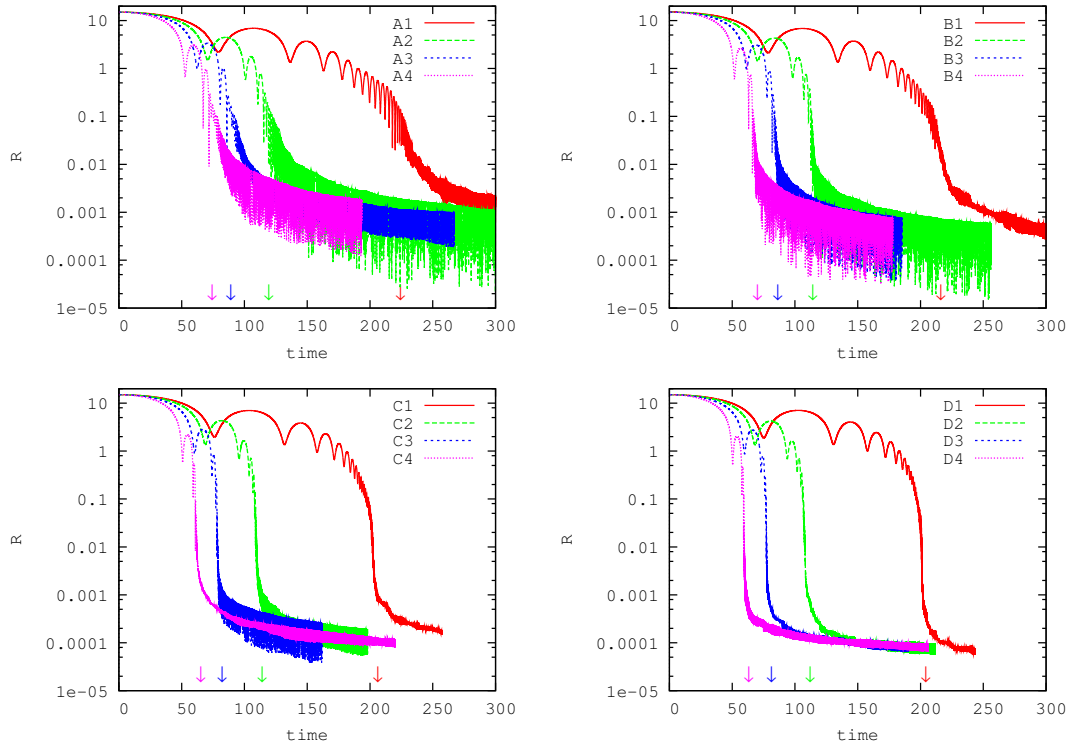
Figure 8.1: Evolution of the separation between the SMBHs, in N-body integrations of galaxy mergers for $\gamma = 0.5$ (top left), 1.0 (top right), 1.5 (bottom left) and 1.75 (bottom right) according to Table 8.2. The arrows represent the time ($T = 0$) at which the two black holes become gravitationally bound for each model. Time and R are measured in N-body units.
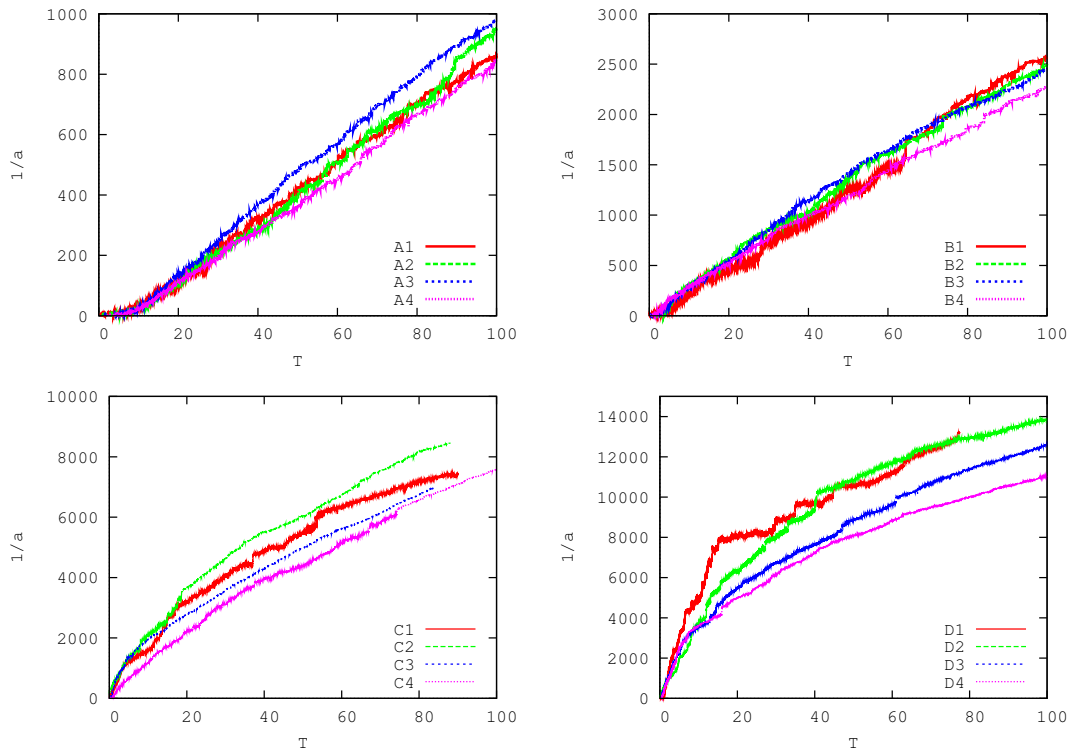
Figure 8.2: Evolution of the inverse semi-major axis of SMBH binary, in N-body integrations of galaxy mergers for $\gamma = 0.5$ (top left), 1.0 (top right), 1.5 (bottom left) and 1.75 (bottom right) according to Table 8.2.

When the semi-major axis $a \approx a_{\rm h}$, this initial rapid phase of binary hardening comes to an end as the pool of stars whose orbits cross the binary orbit gets depleted on the (local) dynamical timescale.[1]

The subsequent hardening of the binary occurs only if the loss cone orbits are replenished.[2] In a spherical galaxy with no gas, the only dynamical mechanism for replenishing loss cone orbits is two-body relaxation, with the corresponding timescale for repopulating the loss cone orbits scaling as $\sim N / \ln N$ (Binney & Tremaine 2008), and the inspiral rate thus becomes strongly N-dependent (Makino & Funato 2004, Berczik et al. 2005). In Chapter 7, it was shown that the hardening phase, in the case of a mildly triaxial remnant nuclei resulting from a galaxy merger, is essentially N-independent – which allows our results to be scaled to real galaxies whose typical number of stars, $N_{\rm star}$, is always several orders of magnitude larger than the maximum number reachable with state-of-the-art direct N-body simulations. Furthermore, it was also shown in Chapter that the flux of stars into the loss cone in a triaxial remnant is also consistently higher than in the spherical case, meaning the binary evolution and coalescence can occur much faster than in spherical models.

Figure 8.2 shows the time evolution of the binary's inverse semi-major axis $1/a$ from the time T when the two black holes become bound. An initial phase with faster binary hardening becomes more evident for steep inner density profiles ($\gamma = 1.5, 1.75$) – presumably corresponding to the clearing of the original loss cone (Yu 2002). The inverse semi-major axis increases very rapidly

---

[1]The semi-major axis a and eccentricity e of the binary are defined here via the standard Keplerian relations, i.e., neglecting effects of the field stars.

[2]The loss cone is the region of phase space corresponding, roughly speaking, to orbits that cross the binary, i.e. with angular momentum $J \lesssim J_{\rm lc} = \sqrt{GM_\bullet f a_{\rm bin}}$, where $f = \mathcal{O}(1)$ (Lightman & Shapiro 1977).

with increasing γ and seems to be more or less independent of q.

The binary hardening rates s are calculated by fitting straight lines to $a^{-1}(t)$ in the late phase of binary evolution from $T = 60 - 100$. The results are shown in Figure 8.3. The hardening rates depend very weakly on the mass ratio of the binary SMBHs, in contrast with the $\sim M_\bullet^{-1}$ dependence found in equal mass merger study (Chapter 7). By changing q from 0.1 - 1, $M_\bullet$ changes by almost a factor of 2, but we do not see a factor of 2 difference in the hardening rates for fix value of γ. On the other hand, the value of $s(t)$ increases significantly for higher values of γ. Note that for the single run with the smallest mass ratio in our sample, $q = 0.05$ and $\gamma = 1$, the hardening rates are significantly weaker than the remaining $\gamma = 1$ models.

The SMBH binary hardening rate, which is a measure for the energy loss of the binary, is given by

$$s(t) \equiv \frac{d}{dt}\left(\frac{1}{a}\right) \approx \frac{2m_*\langle C\rangle}{M_\bullet a}\int_0^{+\infty} dE \mathcal{F}_{lc}(E,t), \tag{8.2}$$

where $\mathcal{F}_{\rm lc}(E,t)$ is stellar flux into the loss cone, $\langle C\rangle = O(1)$ is a dimensionless quantity obtained from three-body scattering experiments (Quinlan 1996) and $E = GM_\bullet/r + \Phi_*(r) - 1/2\ v^2$ is the (specific) energy of each star ($E > 0$ for bound stars). The behavior of the hardening rates can thus be qualitatively understood as follows. The flux $\mathcal{F}_{\rm lc}(E,t)$, and its time evolution, depends on the degree of symmetry in the underlying gravitational potential (or, equivalently, the orbit families supported by it) – including the radial density distribution of stars around the binary. On the other hand, the flux of stars into the loss cone is expected to peak around $r_{\rm h}$ (Perets & Alexander 2008). For a given energy E and fixed $M_\bullet$, $\mathcal{F}_{\rm lc}(E,t) \propto n(E,t)/\tau(E,t)$ where $n(E,t)$ is the number of stars of energy E per unit (specific) energy, while $\tau(E,t)$ is equal, in the spherical case, to $\tau_{\rm rlx} \propto \sigma^3/\rho \propto r^{\gamma-3/2}$ (Binney & Tremaine 2008) or, in the triaxial case, to the star's orbital precession time $\tau_{\rm prec}(E,t) \propto M_*^{-1/2}(< r) \propto r^{(3-\gamma)/2}$, for $r \lesssim$ few $\times r_{\rm h}$ (Yu 2002). Note that, for typical nucleus parameters, $\tau_{\rm prec} \ll \tau_{\rm rlx}$. As a result, and since for more concentrated nuclei (higher γ) $n(E_{\rm h},t)$ is higher and $\tau(E,t)$ is shorter, so more concentrated nuclei experience higher $\mathcal{F}_{\rm lc}$ and higher $s(t)$.

The triaxiality also plays an important role in determining the hardening rate. This is because of its role in supporting centrophilic orbits; in fact, at fixed $n(E,t)$ only a fraction of the stars will be on centrophilic orbits, and this fraction is an increasing function of increasing triaxiality. As q decreases, the triaxiality of the remnant also decreases as shown in the bottom panel of Figure 8.3. This results presumably in a weaker hardening rate since the fraction of stars on centrophilic orbits is smaller. This effect partially explains why the dependence of the hardening rate on $M_\bullet$ is much weaker than expected based on the results obtained in Chapter 7 for equal-mass mergers.

We analyze the shape of the merger remnant by calculating principal axis ratios and density profiles for galaxy merger models. Figure 8.3 shows the principle axis ratios of the merger remnant; these were defined as the axis ratios of a homogeneous ellipsoid with the same inertia tensor. The departures from spherical symmetry become more apparent for mergers with larger q. For $q = 0.05$ and 0.1, the merger-induced triaxiality becomes residual and the remnant results only a slightly flattened system. The dynamical effect of this transition seems to be abrupt, as the hardening rates shown in top panel of Figure 8.3 are essentially independent of mass ratio down to $q \sim 0.1$. In such minor mergers, the secondary galaxy gets tidally disrupted within a few peri-center passages, and eventually the *naked* black hole of satellite spirals in due to dynamical friction. The evolution of SMBH binary in such a merger results very similar to those of binaries embedded in spherical galaxy models. Nevertheless in reality situations such as these are not very likely to happen as both galaxies would surely retain some triaxiality or flattening from a previous major merger.

The density profiles of the newly formed galaxies as the result of the merger are shown in figure 8.4. As a result of the galaxy merger and the ejection of stars from the central galaxy region by the inspiraling black holes, the merger remnant nuclei have significantly shallower inner slopes than those of its progenitors. The "damage" caused by in-falling black holes increases with their
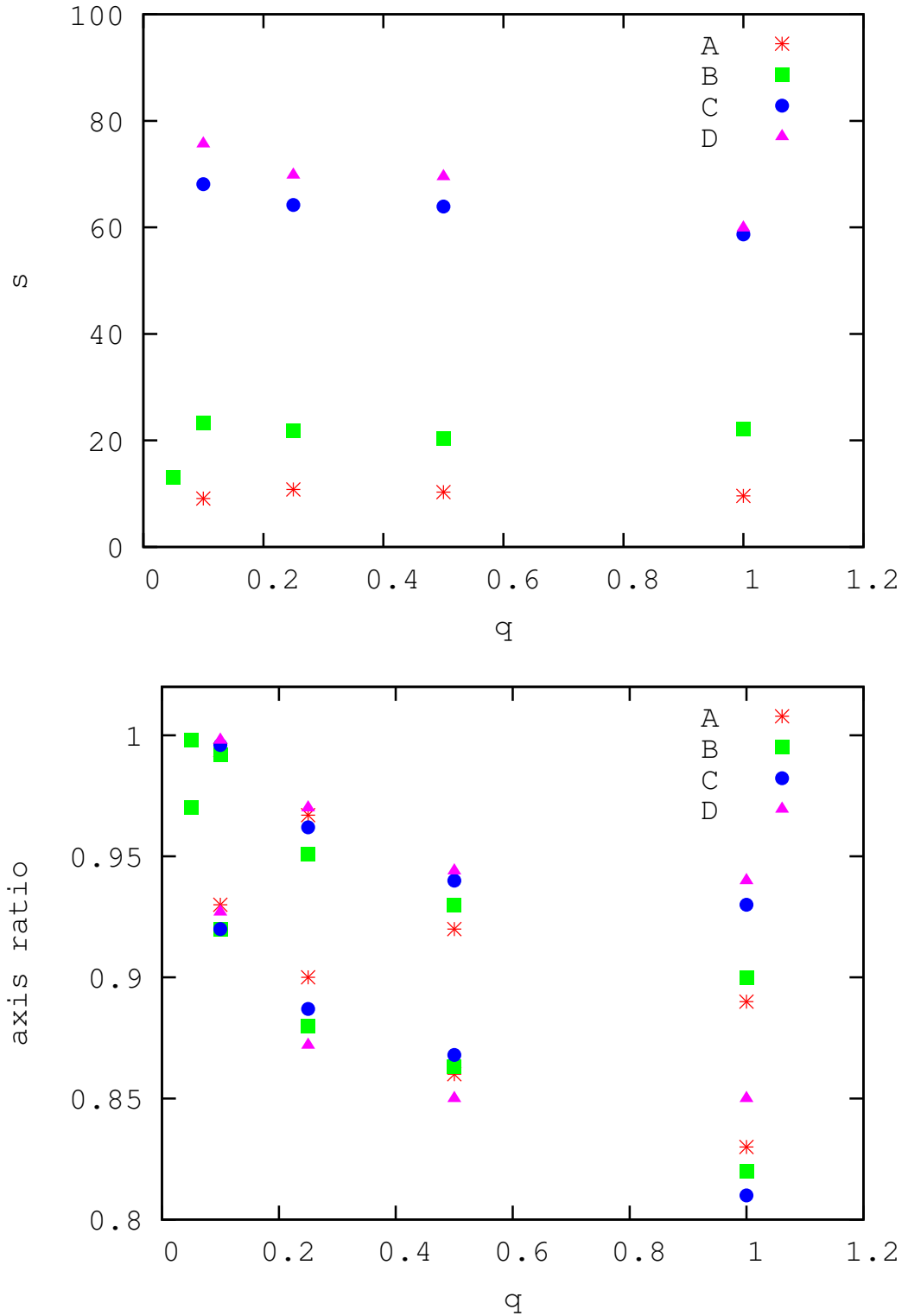
Figure 8.3: TOP — Average hardening rates for $\gamma = 0.5, 1.0, 1.5$ and 1.75 according to Table 8.2. The average is measured between $T = 60$ and $T = 100$ in N-body units. See text for details. BOTTOM — Ratio of intermediate to major (b/a, upper series of points) and minor to major (c/a, lower series of points) axes for $\gamma = 0.5, 1.0, 1.5$ and 1.75 according to Table 8.2.
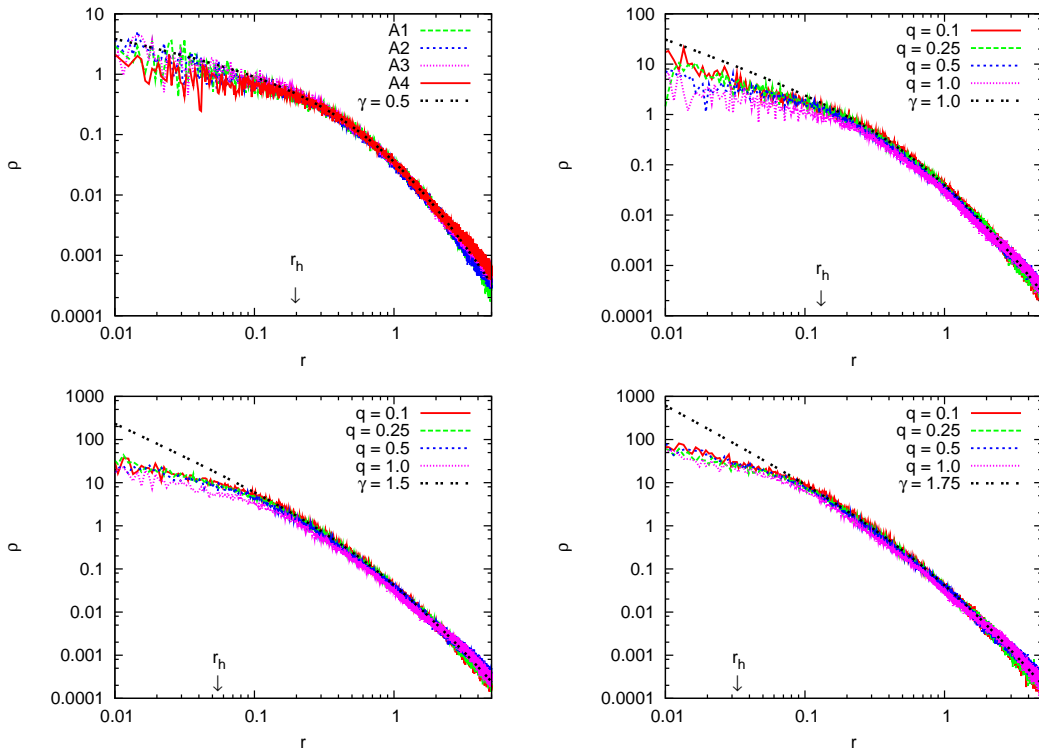
Figure 8.4: Density profiles of merger remnant for $\gamma = 0.5$ (top left), 1.0 (top right), 1.5 (bottom left) and 1.75 (bottom right) according to Table 8.2.

mass. The values of γ_f are calculated by fitting Dehnen's model to merger remnant right after the time when phase of rapid binary hardening ends. Table 8.3 presents the final inner slopes for merged galaxies.

8.3 Mass Deficits

Observations of nearby galaxies show that Sérsic functions provide remarkably accurate fits for the major axis brightness surface profiles over the main bodies of bulges and early-type galaxies. This has been confirmed with increased accuracy and dynamic range over the last decade or so (Kormendy et al. 2009). Moreover, detailed state-of-the-art simulations of merging galaxies also generate profiles which are consistent with Sérsic functions (Hopkins, Lauer, Cox, Hernquist & Kormendy 2009, Hopkins, Cox, Dutta, Hernquist, Kormendy & Lauer 2009). Even though there is not a complete theoretical understanding for the remarkable regularity of these profiles, their apparent generality and robustness led people to identify and interpret departures from Sérsic fits and use them as a probe of the physics underlying the co-evolution of galaxies and their massive black holes.

Cores tend to be found in giant ellipticals and are loosely defined as the central region in a bulge or early-type galaxy where the surface brightness deviates and it is below the values that would result from the extrapolation of the Sérsic profile from the main body of the object down to its innermost region. Typically they are associated to shallower cusps with $\gamma \lesssim 0.5 - 1$. One possible explanation of a central core in a gas poor galaxy can be attributed to the ejection of stars by a hard SMBH binary. The destruction caused by the inspiraling massive black hole in the center of galaxy can be measured in-terms of missing mass called "mass-deficit". Graham

(2004) and Ferrarese et al. (2006) measured the mass-deficits from the difference in flux between the observed galaxies light profiles at the center and the inward extrapolation from their outer Sérsic profiles. Estimated mass-deficits from these studies yield $M_{\mathrm{def}} \sim (1-2)M_\bullet$, and values as high as $\sim (4-5)M_\bullet$ were uncommon. More recent studies obtained larger values with an average value $\langle M_{\mathrm{def}}/M_\bullet \rangle \sim 11$ and an error in the mean of about 18% (Kormendy et al. 2009).

Top panel of figure 8.5 shows the cumulative mass profile for model C1 at different time of its evolution. The merger of a secondary galaxy with the primary causes some changes in the inner profile of the latter. This can be seen by comparing the profiles at times $t = 0$ and $t = 100$, between which there is a noticeable drop in the stellar density around r_{h} due to the merging of the two galaxies. Then, as the secondary is being tidally disrupted, after a few peri center passages, the profile of the resulting merger remnant remains stable. Once, at time $t \sim 202$, the two black holes become bound and form a binary, the stars inside the loss cone start to be cleared by the binary and a rapid evolution of the mass profile ensues till $t \sim 240$. This drop in the central density is due to the slingshot ejection of stars by the binary. As a result, the the mass inside $\sim$ few $\times r_{\mathrm{h}}$ drops rapidly hence changing the mass-profile there. Once this phase of rapid mass ejection ends, the density profile – notably inside r_{h} – remains almost constant as the binary continues its inspiral. This can be understood as follows. Inside r_h, the gravitational potential is approximately spherical and thus the stars residing there can enter the loss cone only by diffusing in energy and angular momentum space through two-body encounters. The corresponding timescale is the relaxation time which scales as $\tau_{\mathrm{rlx},J} \sim \sigma^3/\rho \sim r^{\gamma-3/2}$ (Spitzer 1987); since $\gamma \lesssim 3/2$ for all models at almost all times of interest, this implies that τ_{rlx} increases towards the center. The timescale for such stars to enter the loss cone is thus much longer than the typical precession time needed for centrophilic orbits of stars, resident at distances $\gtrsim r_{\mathrm{h}}$, to come sufficiently close to interact with the binary. As a result, the density profiles well inside r_{h} remain essentially constant during the remainder of the inspiral so the damage impinged on the cusp by the SMBH inspiral following a merger is less severe than naive spherical model scenarios might let expect. The conclusion is that it is not very likely that a hole in the stellar distribution will ever be created by such mergers.

We calculate the mass-deficits for each of our galaxy mergers as the difference between the stellar mass enclosed at a given radius at the time when the binary first becomes bound and at the end of the runs. The end of the run is *a priori* a somewhat arbitrary choice since not all runs end at exactly the same point in the binary's inspiral. However, when we compare the four cases (A2, A4, B3 and B4) for which we followed the binary up to final coalescence, we realize that most of the change in the density profiles happens at a relatively early stage in the evolution of the binary, and this is mostly covered in almost all of the runs. The conclusion is that the derived mass deficit is quite insensitive to the exact final time of the runs, provided this occurs at a time when the binary's semi-major axis already reached a separation which is orders of magnitude shorter than the influence radius r_{h}. It is also worth pointing out that the final density profile shown the top panel of Figure 8.5 has a central density slope $\gamma \sim 1$. This means that a single inspiral is not enough to turn a steep cusp ($\gamma \gtrsim 1.5$) into a core ($\gamma \lesssim 0.5$).

Ours and the (several) observational definitions of mass deficit are obviously not equivalent, but they are surely somehow related provided the assumption that the mass is ejected by the binary holds true. We will not attempt to dwell into the intricacies of a detailed comparison, but will instead use the mass deficits obtained from our simulations as qualitative indicators regarding the evolution of the galactic nuclei as they undergo minor/major dry mergers.

The bottom panel of the Figure 8.5 shows the resulting mass-deficits measured out to various radii for model C1. Mass-deficits have a maximum value at around $2-3r_{\mathrm{h}}$ for each model. We are showing the value of mass-deficit at different radii in table 8.3 for all the runs. First, we can see that the mass-deficits are clearly larger for more concentrated (higher γ) models. They are also increasing with the mass ratio q. Note that what we are directly measuring from the runs is the effect of the inspiraling binary on the stellar distribution, *not* the total amount of mass ejected by
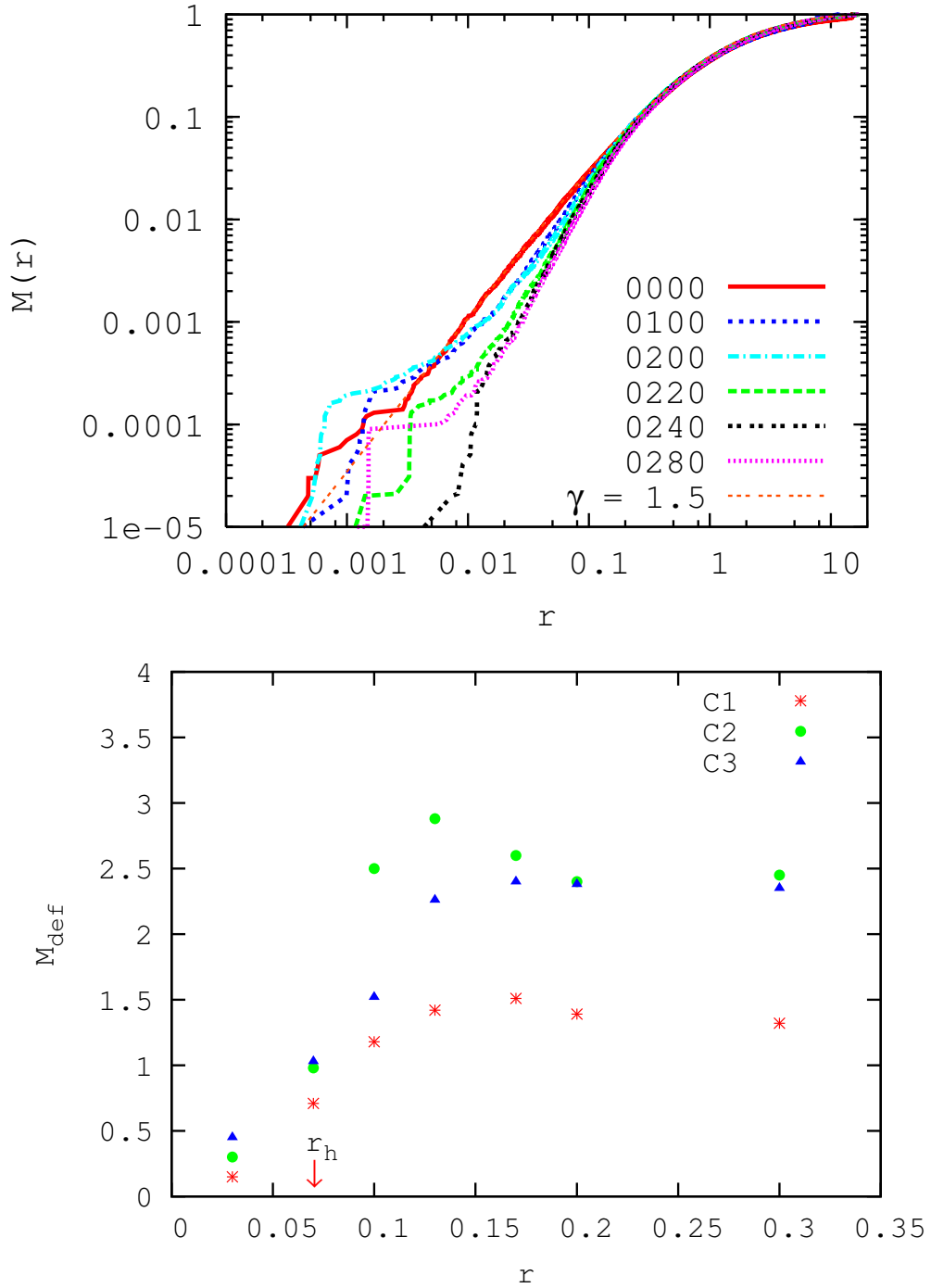
Figure 8.5: Cumulative mass profile for one of our merger models at different time steps (top) and mass deficits normalized to $M_\bullet$ for models C (bottom). The red arrow in the bottom panel of the figure shows the influence radius at the time of the formation of the SMBH binary.

Table 8.3: Mass Deficit Analysis

Run	r_{h}	γ_{f}	a_{final}	T_{final}	$M_{\mathrm{def},1}$	$M_{\mathrm{def},1.5}$	$M_{\mathrm{def},2}$	$M_{\mathrm{def},2.5}$	$M_{\mathrm{def},3}$
A1	0.19	0.34	6.4×10^{-4}	180	0.51	0.76	0.84	0.93	0.72
A2	0.19	0.26	5.5×10^{-4}	180	0.50	0.94	1.20	1.20	1.05
A2($\mathcal{PN}$)	0.19	0.23	$merged$	160	0.48	0.91	1.11	1.14	1.01
A3	0.19	0.22	5.9×10^{-4}	210	0.68	1.21	1.49	1.40	1.34
A4	0.22	0.18	9.7×10^{-4}	220	0.58	0.76	1.05	1.50	1.86
A4($\mathcal{PN}$)	0.22	0.15	$merged$	204	0.59	0.74	1.06	1.47	1.81
B1	0.155	0.61	2.9×10^{-4}	140	0.50	1.18	1.31	1.38	1.64
B2	0.14	0.57	3.0×10^{-4}	110	0.83	1.19	1.35	1.12	1.35
B3	0.115	0.51	4.0×10^{-4}	115	1.33	1.73	2.0	2.13	1.87
B3($\mathcal{PN}$)	0.115	0.45	$merged$	168	1.69	1.75	2.10	2.30	1.91
B4	0.13	0.48	3.9×10^{-4}	230	0.80	2.0	2.9	3.50	3.26
B4($\mathcal{PN}$)	0.13	0.43	$merged$	189	1.05	2.05	2.80	3.34	3.21
C1	0.066	0.86	1.25×10^{-4}	090	0.71	1.18	1.42	1.51	1.29
C2	0.066	0.80	1.2×10^{-4}	090	0.96	2.50	2.88	2.60	2.40
C3	0.067	0.77	1.4×10^{-4}	080	1.03	1.52	2.26	2.40	2.26
C4	0.069	0.70	1.02×10^{-4}	140	1.10	2.3	3.9	4.80	5.30
D1	0.045	1.15	8.3×10^{-5}	080	0.91	1.27	1.82	2.01	1.89
D2	0.046	1.06	7.1×10^{-5}	100	1.15	1.85	2.56	3.04	3.28
D3	0.046	1.04	7.0×10^{-5}	112	1.39	2.36	3.14	3.81	3.97
D4	0.047	1.01	7.9×10^{-5}	130	1.50	2.84	3.88	4.96	5.62

NOTE. — In this table the columns from left to right represent: (1) Galaxy merger model, (2) the influence radius, (3)The inner density slope γ_{f} for merger remnant, (4) semi-major axis of SMBH binary at the end of the run, (5) time at the end of the run in N-body units, (6–10) mass deficits $M_{\mathrm{def},n}$ in units of the mass of the binary $M_{\bullet}$ measured within $n \times r_{\mathrm{h}}$; r_{h} is calculated at the time of the formation of the SMBH binary.

the binary. The latter value should, by simple energetic arguments and given a fixed total binary mass, be on average the same regardless of the detailed properties of the surrounding nucleus. The damage incurred by the stellar cusps in more concentrated nuclei, however, is expected to be greater as stars on loss cone orbits at small radii will represent a larger fraction of the (local) total stellar mass than those more outside. Major mergers ($q \gtrsim 0.25$) of galaxies with shallow cusps ($\gamma = 0.5, 1$) lead to mass deficits of order $M_{\mathrm{def}}/M_\bullet \sim 1-3$. Taking our results at face value would imply that at least a few major mergers are required to create the average value $\langle M_{\mathrm{def}}/M_\bullet \rangle \sim 11$ found in Kormendy et al. (2009)'s sample.

8.4 Coalescence Times for SMBH Binaries

In this section we want to derive an estimate for the coalescence times of the SMBH binaries in our simulations, similar to what has been done in previous chapter. Here we equate the stellar dynamical and GW hardening rates to find the value of a_0 because we measure s directly from our simulations. To test the accuracy of our estimates made here, we repeat four of our N-body simulations of merging galaxies – this time including the post-Newtonian equations of motion for the SMBHs up to order $3.5\mathcal{PN}$ (see Sec. 8.4.1).

In Fig. 8.2 one can see the rate of change of the binary's inverse semi-major axis during the hard binary phase is approximately independent of time, so we can write

$$s_{\mathrm{NB}} = -\frac{1}{a^2}\left(\frac{da}{dt}\right)_{\mathrm{NB}} \approx \mathrm{const.}, \tag{8.3}$$

a value which we can measure directly from each run.

The corresponding hardening rate due to GW emission alone is given as:

$$
\begin{aligned}
s_{GW} \quad = \quad & \frac{64}{5}\frac{G^3 M_{\bullet 1}M_{\bullet 2}M_\bullet}{a^5 c^5 (1-e^2)^{7/2}} \times \\
& \left(1 + \frac{73}{24}e^2 + \frac{37}{96}e^4\right),
\end{aligned}
\tag{8.4}
$$

To calculate the coalescence time in our simulations we divide the evolution into two distinct regimes: (1) the classical regime, in which the hardening is driven by stellar-dynamical effects and (2) the relativistic regime in which the GW emission is dominant. We define this latter regime, starting from a time t_0 when

$$s_{\mathrm{NB}} = s_{\mathrm{GW}} . \tag{8.5}$$

The semi-major axis a_0 at time t_0 can be calculated from Eq. 8.5 by assuming that both s_{NB} and eccentricity $e(t)$ remain roughly constant[3] during the stellar dynamical hardening phase, as supported by our simulations.

We find that a_0 is typically smaller than a_{final}, the semi-major axis at the time t_{final} at which our simulations end. Therefore, t_0 usually exceeds t_{final} and the time interval Δt between t_{final} and t_0 can be derived as

$$\Delta t = s_{NB}^{-1}\left(\frac{1}{a_0} - \frac{1}{a_{\mathrm{final}}}\right). \tag{8.6}$$

With this, the full time to coalescence, t_{coal}, in our (Newtonian) simulations takes into account (1) the time from when the two SMBHs become gravitationally bound (T) until they enter the GW regime t_0 and (2) the binary's lifetime t_{GW} until the final coalescence. The lifetime t_{GW} of an

---

[3]Note that if $e(t)$ (slightly) increases as suggested by scattering experiment by Quinlan (1996) then the full time to coalescence shall be smaller than our estimated t_{coal}. Therefore, our results here should be interpreted as upper bounds to the true coalescence times.

Table 8.4: Physical Scaling of our Models

Model	Galaxy	$M_\bullet(M_\odot)$	$r_{\rm h}$(pc)	T(Myr)	L(kpc)	$M(M_\odot)$	speed of light(c)
A	M87	3.6×10^9	460	1.9	2.3	7.2×10^{11}	257
B	N4486A	1.3×10^7	31	1.4	0.3	2.6×10^9	1550
D	M32	3.1×10^6	3	0.75	0.12	6.2×10^8	2011

NOTE. — Columns from left to right; (1) Primary galaxy model, (2) Observed galaxy used to scale our model, (3) Observed mass of SMBH in the galaxy in column 2, (4) observed influence radius, (5)time unit, (6) length unit, (7) mass unit and (8) speed of light in model unit.

isolated relativistic binary can be calculated from Equations 7.10 and 7.11 for a given semi-major axis a_0 and corresponding eccentricity e_0, respectively (see Eq. 5.14 in Peters 1964).

In order to compute the GW evolution rates one requires to adopt some physical units, e.g., of length and mass. In Chapter 7, we equated the effective radii of our models to the effective radii of observed galaxies to fix the mass ($M_{\rm gal}$) and the length (r_0) units. Here to compute the coalescence times, we select three different elliptical galaxies (M32, M87, NGC4486A) to scale our models to physical units (Table 8.4). We use the observed mass of the SMBH and its influence radius and compare it to the mass and influence radius of the primary galaxy in our models to fix $M_{\rm gal,p}$ and $r_{0,\rm p}$. Model A's which have a very shallow slope are scaled with M87, model B's with NGC4486A and model D's are scaled with M32. The choice of galaxies for our models scaling is consistent with the fact that bright ellipticals have very shallow inner slopes and faint ellipticals have steep cusps. The estimated coalescence times for SMBH binaries in our simulations obtained through the procedure described above are presented in Table 8.5. We find that the time interval spend in the Newtonian and in the relativistic regime, respectively, are always comparable in almost all our simulations (see column 7 in Tab. 8.5). This can be understood as follows: binaries with high eccentricities reach the relativistic regimes earlier than with low eccentricity and thus shortening the stellar dynamical phase. Also the higher eccentricities mean that the GW emission becomes more efficient which then shortens the relativistic inspiral phase. The black hole of M32 with a mass $\sim 3 \times 10^6 M_\odot$ corresponds to possible sources detectable by LISA. The coalescence timescales for low mass black hole binaries are less than a Gyr (see table 8.5) which suggests that prompt coalescence of binary SMBH detectable by LISA should be very common at high redshifts. Even at the high mass end our models suggest the coalescence timescales $\sim$ Gyr or even less depending on the eccentricity of the binary. These timescales are short enough that SMBH binaries in these galaxies should achieve full coalescence before a subsequent galaxy merger occurs. The coalescence times for SMBHs at low mass end are significantly ($\sim 10\times$) shorter than the ones presented in Chapter 7. The reason for this discrepancy is the weak dependence of effective radii with galaxy luminosity relation adopted there, which was optimized for nuclei with $\gtrsim 10^8 M_\odot$ black holes, but would lead to overestimate the influence radius of the Galactic center (or similarly compact nuclei) by an order of magnitude. Naturally, the coalescence times at high mass end of binary SMBHs are in nice agreement for both studies.

8.4.1 Post-Newtonian Simulations

In order to verify the accuracy of our estimate for the coalescence times given in Table 8.5, we select the two cases A2 and A4 from Table 8.5 (plus two other cases, $B3$ and $B4$, not shown) and re-started these runs with exactly same initial conditions. The choice of these runs is motivated by their relative short coalescence times compared to other runs.

We have implemented the relativistic effects to the MBH binary only by using the $\mathcal{PN}$ equations of motion written in the inertial frame of binary center of mass including all the terms up to 3.5$\mathcal{PN}$ order

Table 8.5: Time to Gravitational Wave Coalescence

Run	a_{final}	s_{final}	e_0	a_0 (pc)	t_0 (Gyr)	t_0/t_{GW}	t_{coal} (Gyr)
A1	6.4×10^{-4}	9.10	0.50	3.5×10^{-1}	1.30	2.1	1.89
A2	5.5×10^{-4}	10.8	0.98	3.9×10^{0}	0.12	1.1	0.23
A3	5.9×10^{-4}	10.3	0.70	6.9×10^{-1}	0.63	1.2	1.15
A4	9.7×10^{-4}	9.60	0.88	1.6×10^{0}	0.30	1.1	0.57
B1	2.9×10^{-4}	23.3	0.62	7.4×10^{-3}	2.10	1.3	3.70
B2	3.0×10^{-4}	21.9	0.98	7.1×10^{-2}	0.24	0.5	0.77
B3	4.0×10^{-4}	20.4	0.95	4.5×10^{-2}	0.39	1.4	0.66
B4	3.9×10^{-4}	22.2	0.96	6.3×10^{-2}	0.27	0.7	0.64
D1	9.2×10^{-5}	75.7	0.69	2.1×10^{-3}	0.48	1.0	0.98
D2	7.1×10^{-5}	69.8	0.66	2.4×10^{-3}	0.43	1.0	0.82
D3	7.6×10^{-5}	69.5	0.61	2.6×10^{-3}	0.41	1.4	0.70
D4	7.5×10^{-5}	59.9	0.60	3.3×10^{-3}	0.38	1.3	0.67

NOTE. — Columns from left to right; (1) Galaxy mergers model, (2) semi-major-axis (in model units) at the end of simulation t_{final}, (3) hardening rate (model units), (4) eccentricity at t_{final}, (5) semi-major axis of the binary at which the stellar dynamical hardening becomes equal to the hardening due to GWs, (6) Life time of binary in classical stellar dynamical hardening phase, (7) ratio between the time spend in classical regime and the time spend in GW regime and (8) Full time to coalescence of SMBHs.

$$\frac{d\mathbf{v}}{dt} = -\frac{GM_\bullet}{r^2} \left[(1 + \mathcal{A})\mathbf{n_{12}} + \mathcal{B}\mathbf{v_{12}} \right] + \mathcal{O}(1/c^8), \tag{8.7}$$

where $\mathbf{n} = \mathbf{r}/r$, the coefficients $\mathcal{A}$ and $\mathcal{B}$ are complicated expressions of the binary's relative separation and velocity (Blanchet 2006). The Post-Newtonian approximation is a power series expansion in $1/c$: the 0th order term corresponds to the dominant Newtonian acceleration. The $1\mathcal{PN}$, $2\mathcal{PN}$ and $3\mathcal{PN}$ order terms are conservative and proportional to c^{-2}, c^{-4} and c^{-6}. The dissipative $2.5\mathcal{PN}$ and $3.5\mathcal{PN}$ terms, which are proportional to c^{-5} and c^{-7}, cause the loss of orbital energy and of angular momentum due to the gravitational wave radiation reaction. We treat the SMBHs as point particles (no spin) and thus we neglect any spin-orbit or spin-spin coupling which in general is taken into account in the $1.5\mathcal{PN}$ (spin-orbit), $2\mathcal{PN}$ (spin-spin) and $2.5\mathcal{PN}$ (spin-orbit) terms in our common $\mathcal{PN}$ implementation.

Figure 8.6 shows the evolution of the inverse semi-major axis $1/a$ and eccentricity e of the SMBH binary for run A2 with and without $\mathcal{PN}$ corrections. Hardening of the binary due to GWs emission starts to dominate at $1/a \sim 1000$ which is slightly larger than the estimated $1/a_0$ (all in model units). This is due to the slightly higher value of eccentricity reached during the run without $\mathcal{PN}$ which is then used to estimate a_0. For the correct value of eccentricity obtained from run with $\mathcal{PN}$, the estimated $1/a_0$ matches accurately with the value where hardening due to GWs starts to dominate. The full coalescence time for the binary in our $\mathcal{PN}$ simulations is 0.25 Gyr which is very close to estimated $t_{\text{coal}} \sim 0.23$ Gyr. The inverse semi-major axis and eccentricity evolution for model A4 are shown in figure 8.7. If we look at the evolution of the inverse semi-major axis for this run then we see that hardening due to GW becomes important at estimated $1/a_0$, as the average eccentricity evolution matches almost perfectly between the $\mathcal{PN}$ and non-$\mathcal{PN}$ runs.

We find very good agreement between our estimated coalescence times and those found using full $\mathcal{PN}$ terms in our merger runs. We can see both from Figure 8.1 and Table 8.5 that the binary eccentricities tend to be lower ($e \sim 0.6 - 0.65$) for $\gamma = 7/4$, and indeed in equal mass merger study of Chapter 7, the binaries reached very often values $e \gtrsim 0.9$ (in accordance to values obtained in this Chapter for $\gamma = 1$). The dependence on eccentricity of the coalescence time under GW emission is $T_{\text{coal,GW}} \sim (1 - e^2)^{7/2}$ could easily account for a decrease of an order of magnitude or so when the binaries are very eccentric.
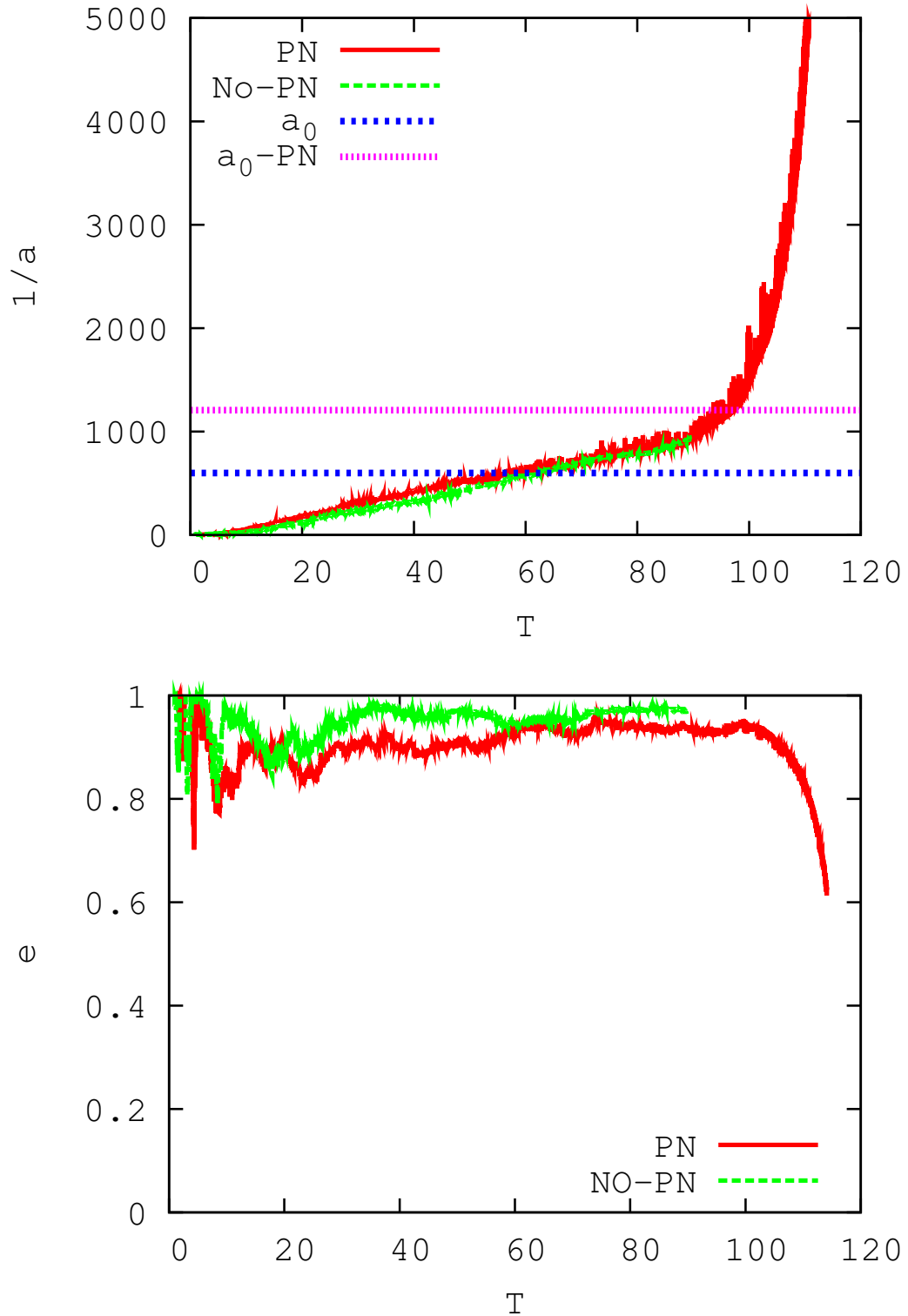
Figure 8.6: Evolution of the inverse semi-major axis $1/a$ (top) and eccentricity e (bottom) for model A2, with and without $\mathcal{PN}$ terms. The horizontal lines represent the estimated semi-major axis of the SMBH binary for which the stellar dynamical hardening becomes equal to the $\mathcal{PN}$ hardening derived from the run without $\mathcal{PN}$ (a_0) and with $\mathcal{PN}$ ($a_0 - \mathcal{PN}$). See main text for further details.
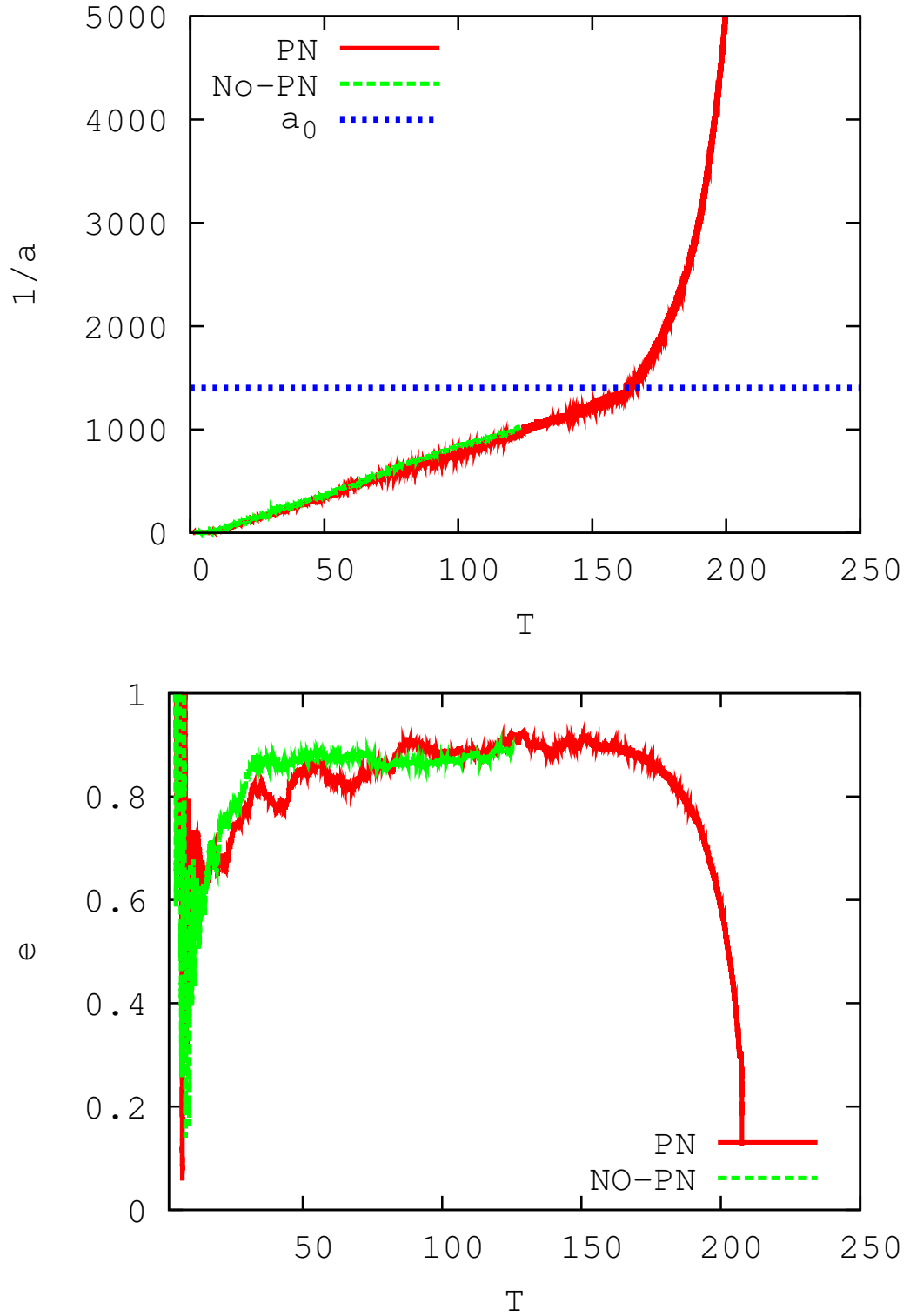
Figure 8.7: Evolution of inverse semi-major axis $1/a$ (top) and eccentricity e (bottom) for model A4 with and without $\mathcal{PN}$ terms. a_0 is the semi-major axis of the SMBH binary for which stellar dynamical hardening is equal to $\mathcal{PN}$ hardening.

Key Results of The Study

- The merger induced triaxiality fades away as the ratio of merging galaxies q become smaller and for $q = 0.05$, we have a spherical merger remnant.

- For galaxies having same γ, the hardening rates are independent of the mass ratios of SMBHs in binary.

- The hardening rates increase significantly with the steepness of the density profiles of the merging progenitors.

- The merger of galaxies always leads to shallower density profiles at the center and the merger of steep density profile galaxies still preserve a profile which is close to Hernquist profile.

- The eccentricity of SMBH binary in the merger of shallow density profile galaxies is always very high ($e \sim 0.8 - 0.99$) and approaches almost unity in some cases where as for the SMBH binaries evolving in the steep density profile galaxy mergers it is mild ($e \sim 0.5-0.7$).

- The estimated mass deficit increases both with the mass of the coalescing binaries and for the galaxies with steeper density profiles.

- The estimated coalescence time is less than 1 Gyr for all range of SMBHs masses ($M_\bullet = 10^6 M_\odot - 10^9 M_\odot$) suggesting that prompt coalescence of SMBH binaries in galaxy merger may be very common.

- The estimated coalescence times match very nicely with the coalescence times obtained from full $\mathcal{PN}$ simulations for all 4 of our selected cases.

Chapter 9

SMBH Binary Evolution in a Late Type Galaxy Merger

<div style="background:yellow">

Contents of this Chapter

1. Selection of initial conditions from the merger study of (Callegari et al. 2011) for direct N-body simulations of SMBH binary evolution in the merger remnant of a late type galaxy merger.

2. Numerical methods and choice of softening for different components (dark matter, stars, SMBHs).

3. Evolution of SMBH binary (semi-major axis and eccentricity), estimated hardening rate and shape of the merger remnant.

4. Estimate of the coalescence time for the SMBHs.

</div>

9.1 Initial Conditions

We study the evolution of binary Supermassive Black Holes using the final phase of galaxy mergers simulations of Callegari et al. (2011) as initial conditions. The reference galaxy model was a Milky Way type disk galaxy consisting of three components: i) a spherical and isotropic NFW profile dark matter halo, ii) an exponential disk of stars and gas and iii) a spherical Hernqusit bulge. Callegari et al. (2011) studied the pairing of binary SMBHs in a 1 : 10 merger of two Milky Way type disk galaxies using smooth particle hydrodynamics (SPH) simulations. They adopted a gravitational softening of 45 pc for both dark matter and baryonic particles in the larger galaxy and 20 pc in the smaller galaxy. The SMBH were represented by a point mass particle at the center of each galaxy. The adopted masses for the SMBHs were $6 \times 10^5 M\odot$ and $6 \times 10^4 M\odot$ for the larger and smaller galaxy respectively, consistent with $M_\bullet$-M_{bulge} relation (Häring & Rix 2004). The simulations also include the effects of both star formation and gas accretion by the SMBHs, as well as feedback from both processes. The final separation of the two SMBHs at the end of the simulations was ~ 30 pc, comparable to the softening used in the simulations. For more details of

construction of galaxy models and the set up for initial orbit of galaxy merger we refer reader to Callegari et al. (2011).

In this study we evolved the system from an earlier time, when the separation between the two black holes is 700 pc and the black holes are still embedded in separate cusps. We selected ~ 3 millions particles in the central 5 kpc region of the merger remnant. Our sample also includes all particles that have peri-center passage smaller than 3 kpc (Fig. 9.1). Most of the gas in the central region is already converted into the stars. The gas particles which have a order of magnitude less presence (Fig. 9.2) in mass in the central region are also treated as stars in our simulations .

Because of the fact that state of the art simulations can only use $\sim$ million particles to represent the galaxy, a number that is several orders of the magnitude smaller than number of stars in real galaxies, each particle in these simulations is much more massive than a real star. Because of the small number of particles the masses of individual dark matter particles in the primary galaxy were comparable to the mass of SMBH in less massive galaxy. This leads to unrealistic mass segregation of the dark matter and to unphysical scattering for the SMBH binary. To avoid such high mass particle encounters with the SMBH binary (when it forms in the final phase), we split each dark matter particle in the major galaxy into ten particles. The split particles have mass 1/10 of the parent particle. The split particles are distributed over a 10 pc (ϵ_d) sphere having same velocities as their parent particles. Numerical tests show that split particles do not form bound systems.

9.2 Numerical Methods

We use Φ-GPU to carry out the direct N-body simulations. The code itself is described in section 3.3. In order to achieve full coalescence of the SMBH binary it is important to have zero softening for SMBHs. But the use of zero softening for the stars and dark matter leads to the formation of binaries in the system which though is more realistic but causes the enormous slow down of simulations because of small time steps needed to resolve the orbits of these binaries. Φ-GPU supports the use of different softening lengths for different components. We use three different softenings (ϵ): $\epsilon_{bh} = 0$ when calculating the pairwise forces between the two SMBHs, $\epsilon_s = 0.01$ pc for star star interactions and $\epsilon_{dm} = 10$ pc for dark matter - dark matter interactions. For the interactions between two different components, we adopt the following criteria:

- To calculate the forces between dark matter particles and stars, the softening $\epsilon_{ds} = \sqrt{(\epsilon_d^2 + \epsilon_s^2)/2}$ is used.

- To calculate the forces between dark matter particles and the SMBHs, the softening $\epsilon_{db} = \sqrt{(\epsilon_d^2 + \epsilon_b^2)/2}$ is used.

- To calculate the forces between the SMBHs and star particles, the softening $\epsilon_{bs} = 0.1 \cdot \sqrt{(\epsilon_b^2 + \epsilon_s^2)/2}$ is used.

A softening of 0.001 pc is necessary to bring the SMBH binary separation to milli parsec regime where GW emission become efficient. The time step criteria for for individual particles is optimized for the case in which the total mass of the system is $\sim$ unity. So we change the units of system from physical unit to model units. In our model units, the total mass of the galaxy ($3.3 \times 10^{10} M_\odot$) $M_{\rm gal} = 1$, the length unit is 1 kpc, resulting in a time unit = 2.6 Myr and speed of light = 795.0 in model units.

9.3 SMBH Binary Evolution

We started our high resolution run at a time (T = 0), when the two SMBHs are still embedded in their respective cusps. Figure 9.1 shows the particle positions (top panel) and projected stellar
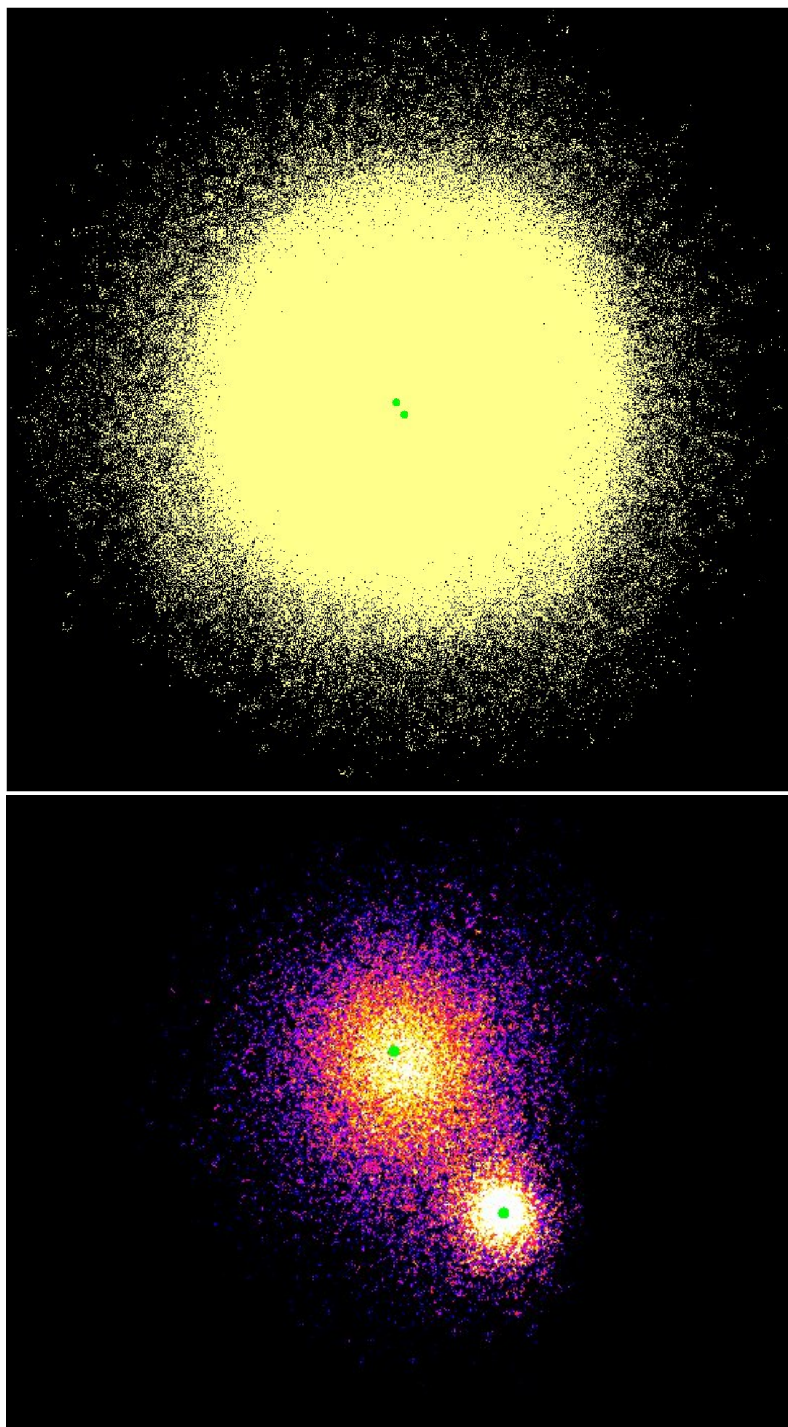
Figure 9.1: Particles positions (inner 5 kpc) projected on initial orbital plane (top) and projected stellar densities (bottom). The two high density regions are clearly visible around the two SMBHs (green points) in the center.
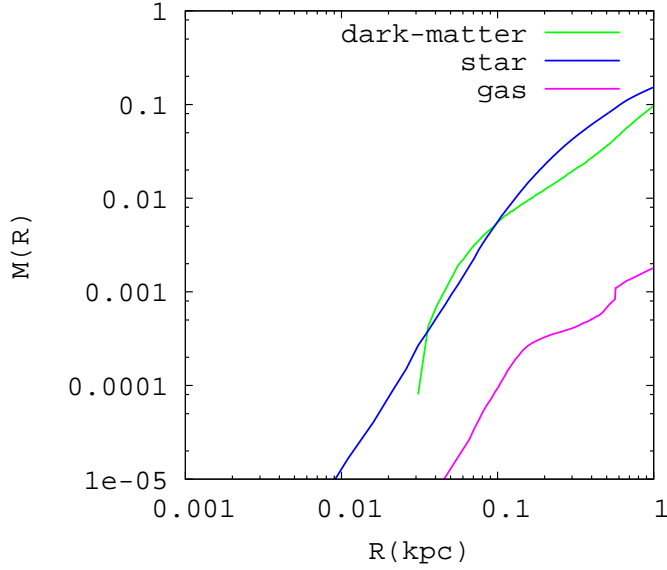
Figure 9.2: Comparison of mass in different components enclosed inside the inner 1 kpc at the start of our run.

densities (bottom panel) on initial orbital plane. The phases of evolution for the SMBH binary in our study are explained below:

- In the first phase, the two black holes centered in their respective galaxy's cusps are not bound to each other and move independently in the potential of galaxy. Dynamical friction against background dark matter and stars is very effective in bringing the two SMBHs closer. At about T = 40 Myr the individual cusps have merged and the two SMBHs are located in a single cusp (Fig. 9.3). Earlier studies show that the SMBHs form a binary when their relative separation, ΔR_{BH}, is $\sim r_h$, where r_h is the gravitational influence radius defined to be the radius of sphere around the two black holes enclosing a stellar mass equal to twice the SMBHs masses. Figure 9.4 shows the evolution of binary separation. At time about T = 40 the separation of the two SMBHs is roughly about r_h and a SMBH binary system is formed (Fig. 9.5 top).

  The SMBH binary separation shrinks very rapidly due to the combined effect of dynamical friction and the gravitational slingshot effect, which efficiently draws energy and angular momentum away from the SMBH binary. Judging from figure 9.4, this phase of rapid binary evolution ends somewhere around $T = 110 - 120$ Myr. The contribution from these two mechanisms (i.e. dynamical friction and gravitational slingshot effects) in this phase is difficult to disentangle however equations (13) and (14) of Milosavljević & Merritt (2001) give approximate estimates of energy transfer from the binary to the stars by these mechanisms. The motion of SMBH binary in this phase is approximately Keplarian.[1]

- Once the binary semi-major axis reaches $a \approx a_h$, where a_h is semi-major axis of a hard binary, the phase of rapid evolution of the SMBH binary comes to an end.

  In this case r_h is 15 pc, $a_h \approx 0.3$ pc and $a_h^{-1} \approx 3.5$ pc^{-1}. From figure 9.5, we see that indeed, the rapid hardening comes to an end when inverse semi-major axis of the massive binary is approximately 4 pc^{-1}.

---

[1]The semi-major axis a and eccentricity e of the binary are defined again via the standard Keplerian relations, i.e., neglecting effects of the field stars.
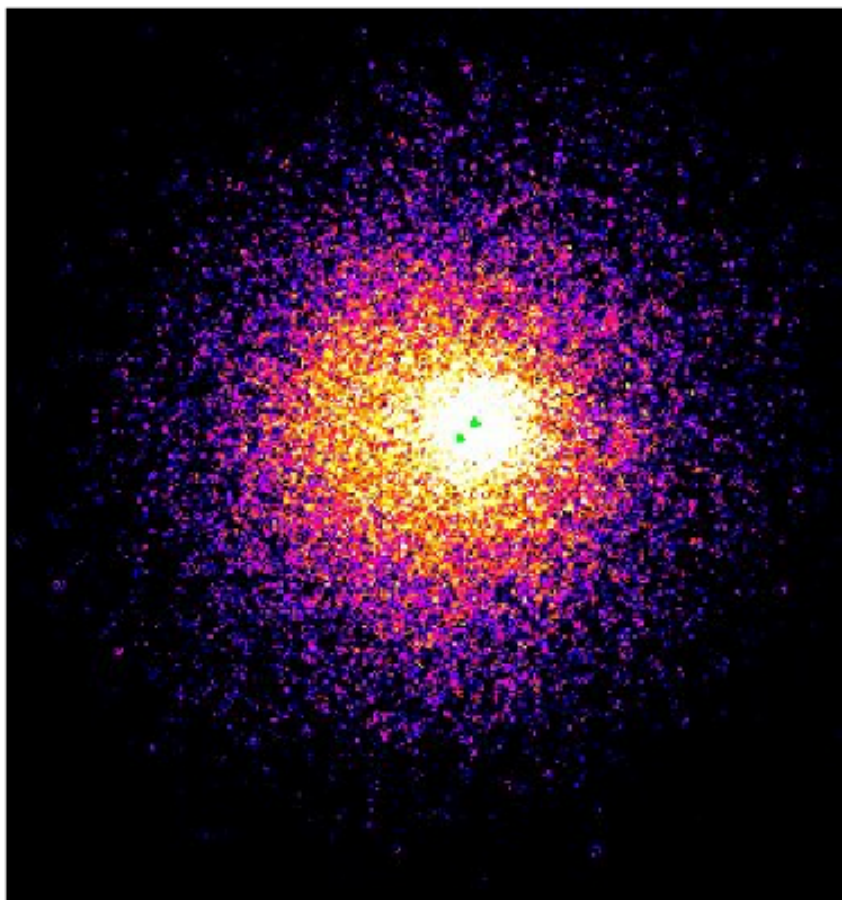
Figure 9.3: Projected density (inner 5kpc) on initial orbital plane at T = 40 Myr. Both SMBHs clearly are surrounded by single cusp around them.
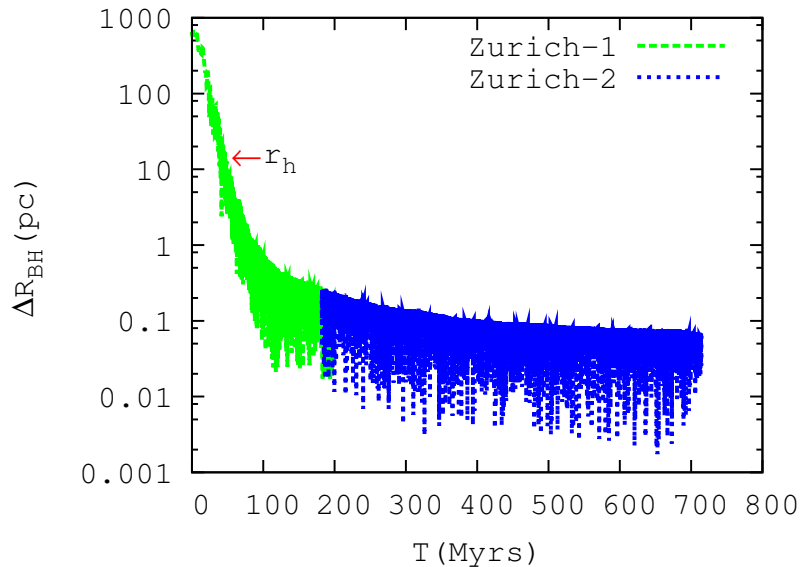
Figure 9.4: Relative separation between the two SMBHs as a function of time. The red arrow shows the estimated value of influence radius r_h.

The subsequent evolution of the massive binary is governed by encounters of individual stars (three body encounters) with the binary. For spherical galaxy models this phase of binary hardening is reported to depend on particle number and for realistic particle numbers, the binary should stall at a separation where its semi-major axis $a \sim a_h$. However it has been shown in previous two Chapters that for galaxy merger simulations this N-dependence disappears, which suggests that results obtained in galaxy merger simulations can be extrapolated to real galaxies. At $T = 200$ we reduce the particle number from ~ 3 million to ~ 1.15 million by selecting the particles that have their peri-centers in the inner 1 kpc to increase the computational speed (Zurich-2). In order to determine whether our selection has introduced some changes in the mass distribution, we plot the cumulative mass distribution at various time steps after the new selection of particles sample (figure 9.6). The cumulative mass profile looks very stable in the inner parts. Only in the outer parts are there small deviations. Also we start the new run (zurich-2) 20 Myr earlier to see if we reproduce the evolution of the binary found in the earlier run (zurich-1). Figure 9.5 shows that both inverse semi-major axis and eccentricity evolution are well reproduced for the period where the two runs overlap.

The binary's inverse semi-major axis evolves at a constant rate, which is consistent with our earlier studies where we follow the evolution of SMBH binary by merging two spherical galaxies. We fit a straight line to calculate the binary's hardening rate $s = \frac{d}{dt}(1/a)$ in the late phase. The value of the hardening rate is 84.3 in model units and 32.42 kpc^{-1} Myr^{-1} in physical units.

This value of hardening rate when compared to the value for similar mass of SMBHs in spherical galaxy model having mass M_{gal} of unity is approximately 8 times higher. We attribute the higher hardening rate to the non spherical shape of the merger remnant. The departure from spherical symmetry (as discussed in previous Chapters) supports a large fraction of stars on centrophilic orbits. For this merger of two late type galaxies, we again analyzed the shape of merger remnant by calculating axes ratios defined for a homogeneous ellipsoid with the same inertia tensor. Figure 9.7 shows the intermediate to major (b/a) and minor to major (c/a) axes ratio at various distances from the center (top panel) and also at
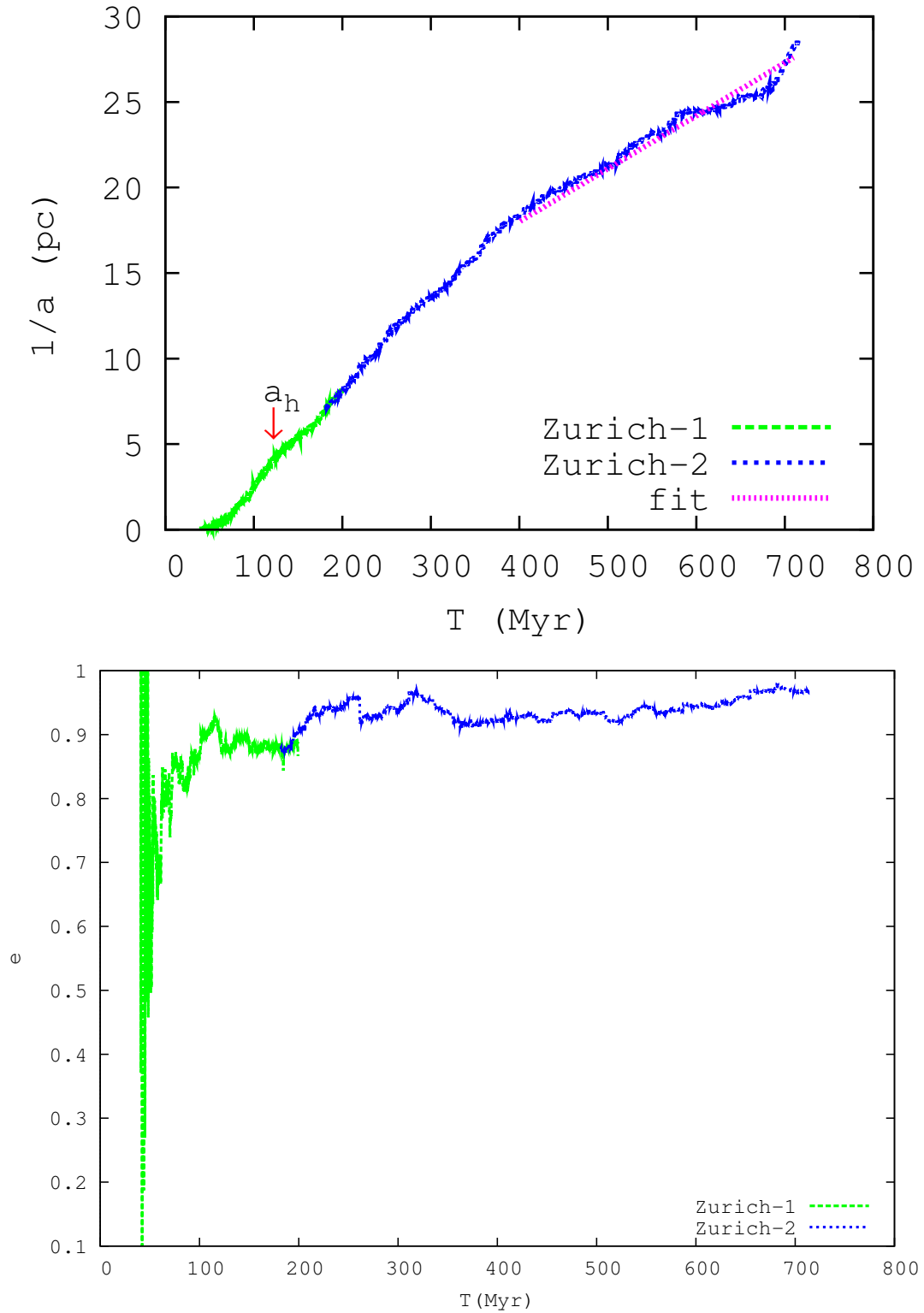
Figure 9.5: The evolution of the binary's inverse semi-major axis (top) and eccentricity (bottom). The red arrow in the upper panel of the figure points to value of $1/a$ which corresponds to the estimated semi-major axis a_h of the hard binary.
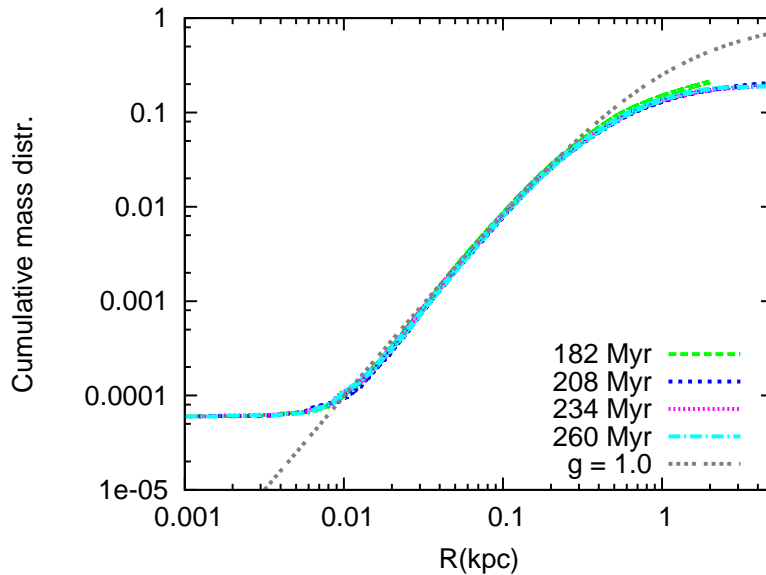
Figure 9.6: Stability of the mass profile after the selection of new particle sample at T = 182 Myr. The black dotted line represents theoretical Hernquist model $\gamma = 1.0$. Clearly the cumulative mass profile is very stable in inner kpc.

different times (bottom panel). The merger remnant is considerably flattened compared to the remnants that result from the merger of the two spherical galaxy progenitors of Chapters 7 and 8. Hence we expect that the SMBH binary should evolve at a constant rate, driven by the centrophilic stellar orbits family rather than the relaxation effects alone. This means that it is safe to extrapolate our results for the merger of late type galaxies with realistic number of stars and hence can predict the coalescence time for the SMBHs using the estimated hardening rates in both the stellar dynamical phase and in GW regime.

- At small enough separation, the exact value of which depends on the mass of the SMBH binary and eccentricity of the binary, gravitational waves extract energy and angular momentum efficiently from the binary, and make its coalescence inevitable. It is worth mentioning that LISA will be most sensitive for SMBHs with masses comparable to those that are addressed in this Chapter. The SMBH with such masses ($10^5 - 10^6 M_\odot$) are found in centers of late type galaxies. Therefore in this study we follow the evolution of massive binary in an interesting mass regime starting from a consistent initial set up of merging galaxies.

9.4   Time for the Coalescence of SMBH Binary

To calculate the time to coalescence in our simulations we use a similar approach to that used in section 8.4. First we calculate a_0 - the value of the semi-major axis at which the stellar dynamical hardening of the SMBH binary becomes equal to the hardening caused by gravitational wave emission (see equation 8.5). Again in order to compute a_0, we assume that eccentricity and hardening rate remain almost constant during the phase of stellar dynamical hardening. In this case the eccentricity of the SMBH binary at the end of our simulation is $e_{\text{final}} = 0.97$ and the hardening rate is $32.42 \text{ kpc}^{-1} \text{ Myr}^{-1}$. The time at the end of simulation is $t_{\text{final}} = 710$ Myr. In our case, the predicted value of the semi-major axis where the stellar dynamical and GW hardening rates are equal, is $a_0 = 1.73 \times 10^{-5}$ kpc. This value is smaller than the semi-major axis of the
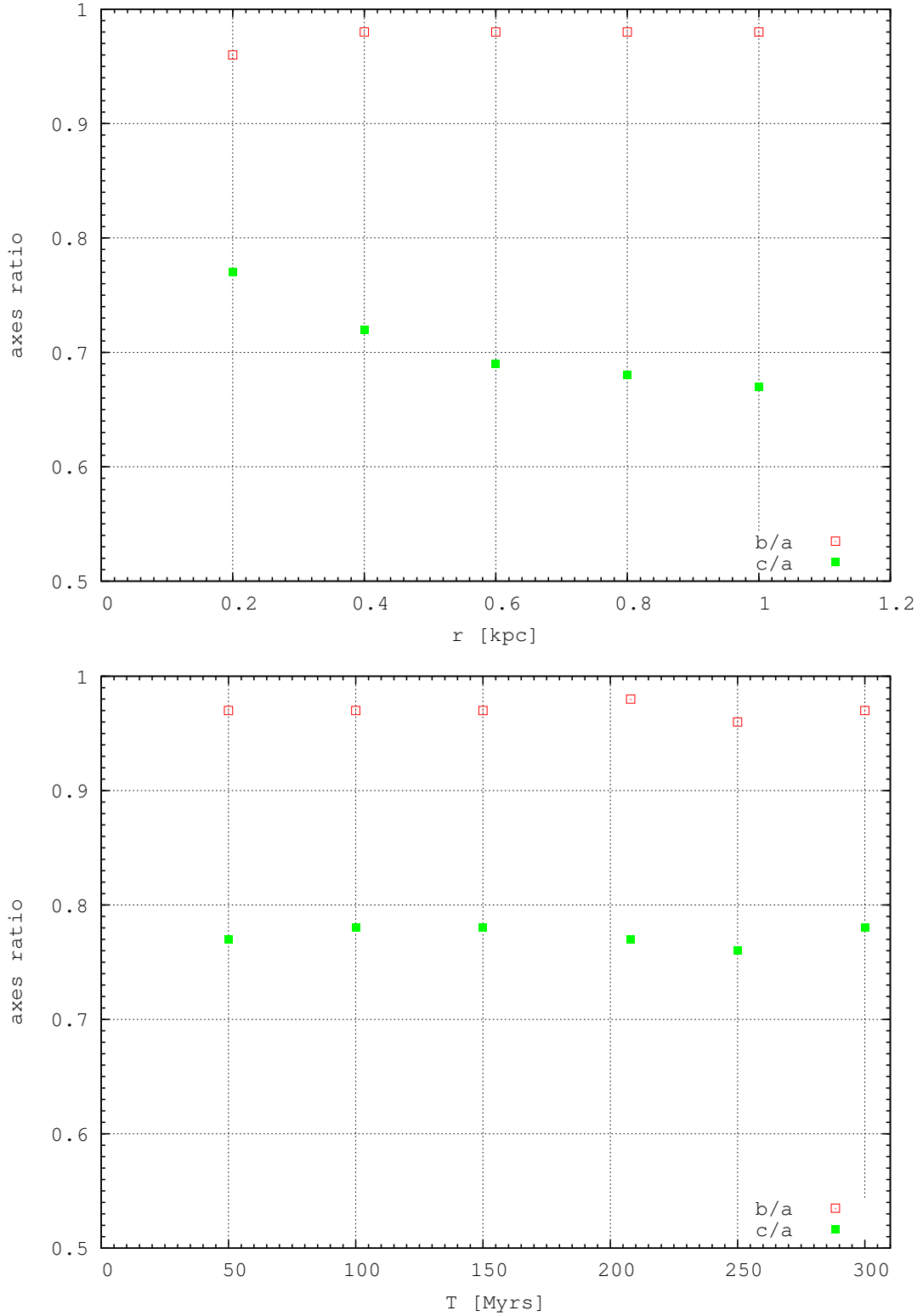
Figure 9.7: *Top*: Intermediate to major (b/a) and minor to major (c/a) axes ratio as a function of distance from the center of the SMBH binary at $T = 200$ Myr. *Bottom*: The time evolution of axes ratio calculated at a distance of 0.2 kpc from the center of the SMBH binary.

SMBH binary at the end of our simulation $a_{\text{final}} = 3.57 \times 10^{-5}$ kpc. The time t_0 to reach the semi-major axis value a_0 is the sum of the time t_{final} at the end of our simulation and the time Δt required by the binary to reach a_0. The time interval Δt can be calculated by using equation 7.13 and in this case is 860 Myr. This leads to a total time spent by the SMBH binary in the classical regime of 1.57 Gyr. The lifetime, t_{GW}, of an isolated relativistic binary can be calculated from Equations (7.10) and (7.11) for a given a_0 and corresponding eccentricity, e_0 (see Eq. 5.14 in Peters 1964). In our case the life time of SMBH binary in GW regime is $t_{\text{GW}} = 1.31$ Gyr and leads to the full coalescence time for the massive binary of $T_{\text{coal}} = 2.88$ Gyr.

9.5 Discussion

Starting from the results of Callegari et al. (2011), we studied the merger of two gas rich disk galaxies (gas fraction in disk 30 percent) on coplanar orbit having SMBHs at their centers from an initial separation of 60 kpc to a final separation of 0.01 pc. Initially the mass ratio between the galaxies and SMBHs is 0.1. During the merger the two SMBHs accrete gas and increase their masses in the process. The mass of the SMBH in the satellite galaxy increases almost 8 fold as the gas in the secondary galaxy is funneled towards the center due to the tidal force of the primary galaxy at each peri-center passage. The perturbations produced by the passages of secondary galaxy are not significant for the primary galaxy so the SMBH in the primary galaxy accretes gas steadily and the mass of SMBH here grows by a factor of 2. At the end of SPH simulations, the mass ratio between the two SMBHs is approximately 0.3 (see figure 1 of Callegari et al. (2011)).

At the start of our direct N-body simulations the separation between the two SMBHs is roughly 700 pc and a binary is not formed at this time. We use particle splitting to reduce the mass of dark matter particle to avoid both mass segregation and unphysical encounters of high mass dark matter particles with SMBHs. Dynamical friction is very efficient in bringing the two SMBHs to separation where they form a binary. The subsequent hardening at a constant rate is governed by individual stars interacting with the massive binary. We artificially suppress the contribution of dark matter to the hardening of the SMBH binary by introducing a large softening ($\epsilon_d = 10$ pc). Although we split the dark matter particles, the mass of a dark matter particle is only a factor 10 smaller than the mass of the SMBH in secondary galaxy. Thus the large softening is used to obtain a smooth evolution of the binary. The analysis of shape of merger product shows a flattened system at the center. The SMBH binary hardening rates are comparable to those obtained for our galaxy merger studies in Chapters 7 and 8 for similar density profiles. This suggests that the stalling of the SMBH binary should not be an issue for this more realistic scenario of the galaxy mergers. The eccentricity is very high as was observed for the shallow density profile ($\gamma \leq 1.0$) galaxy merger simulations performed in Chapters 7 and 8. The reason for this high eccentricity is not clear and needs further investigations.

The coalescence time of 2.88 Gyr, although longer when compared to the times obtained for similar mass binaries in previous Chapter, is still short enough to have a few 1:10 mergers of SMBHs in late type galaxy mergers in the range at which LISA is most sensitive. From previous Chapter we know that binary hardening rates depend strongly on the adopted density profile. For steep density cusps having an inner power law density index $\gamma = 1.75$, the study shows a factor of 4-5 higher value of s when compared to $\gamma = 1.0$. In the current study the adopted density profile at the start of the merger simulation was a Hernquist profile, which has $\gamma = 1.0$. This slope is observed in bright elliptical galaxies which host SMBHs having masses $\sim 10^8 - 10^9$ M⊙. The faint bulges/ellipticals which host smaller SMBHs with masses $\sim 10^6 - 10^7$ M⊙ typically have steep cusps ($\gamma \sim 1.5 - 1.75$). So for an appropriate density profile, we can expect the coalescence times to be much shorter, comparable to the ones that were obtained in the last Chapter for the merger of steep power law density profile galaxies.

Currently the simulation is still running and we plan to obtain a full coalescence of SMBHs including $\mathcal{PN}$ terms to the force calculations of SMBHs. This will be the first study where the

coalescence of SMBHs starting at separation of 60 kpc is followed in a realistic galaxy merger scenario.

Key Findings of the Study

- The idea of splitting the study of SMBH binary evolution into two parts (study of galaxy merger using SPH code followed by a study of the SMBH binary using direct N-body code), motivated by the fact that state of art simulations cannot cover the whole range of physical scales of interest, seems to work successfully.

- The splitting of dark matter particles and proper selection of a sub-sample of particles in the central region of merger remnant does not change the mass profile in the center.

- The hardening rates obtained for the SMBH binary are 8 times higher than found in a similar study of binary evolution in spherical galaxy model.

- The flattening found in the central region of merged galaxy system is significant and is perhaps responsible for high hardening rates.

- The estimated coalescence time is less than 3 Gyr and can be of the order of 1 Gyr if a proper density profile were to be adopted for progenitor galaxy bulges at the start of the simulation.

Chapter 10

Conclusion

This study uses N-body simulations to investigate different aspects of the dynamical evolution of supermassive black holes in galaxy mergers. This Chapter summarizes the study, discusses the astrophysical implications of our investigations and considers the outlook for future investigations.

Summary

In this study we quantitatively tested the effect of using the self-consistent velocity distribution function in χ and a general analytic formula for $\ln \Lambda$ derived by Just & Peñarrubia (2005). We performed high-resolution numerical simulations, using both particle-mesh and direct N-body codes, of the orbital evolution of a massive black hole in a variety of stellar distributions. We investigated circular and eccentric orbits in self-gravitating cusps (Dehnen models), in cusps in a central Kepler potential (so-called Bahcall-Wolf cusps) and in the Kepler limit of steep power law density profiles in the outskirts of stellar systems. The background distributions cover a large range of power law indices between $-1 \cdots -5$ of the density profile.

The application of the self-consistent χ functions leads to correction factors in the orbital decay times in the range between $0.5 \ldots 3$ (Fig. 4.3). The main new feature in the improved general form of the position and velocity dependent Coulomb logarithm (Eq. 4.26) is the use of the local scale length D_r of the density profile as maximum impact parameter. In most applications the effect of the new $\ln \Lambda$ is a significant delay in the orbital decay. A detailed comparison with orbital decay calculated using the standard values $\ln \Lambda_s$ and χ_s shows that the corrections are very different for the different cases and lead to a general improvement of the orbit approximation. In a few cases, such as circular orbits in a Bahcall-Wolf cusp with a resolved minimum impact parameter the standard formula can still be used. But even in this case a measurable difference already occurs for eccentric orbits. We like to point out the generality of the new formula such that a fit of individual orbits is no longer necessary. We find a general agreement between the orbital decay in the numerical simulations and the analytic predictions at the 10% level. This holds for circular as well as eccentric orbits in all background distributions in both self-gravitating and Kepler potentials.

Another more technical finding concerns the best choice of the minimum impact parameter, $b_{\min}$, measuring the numerical resolution. It should be remembered, that from the structure of $\ln \Lambda$ there is implicitly one common scaling factor for $b_{\max}$, $b_{\min}$, a_{90} that is free. Thus the normalization of one of these quantities must be fixed in order to determine the other two. Here we fixed $b_{\max} = D_r$ and proved that a_{90} is the correct effective minimum impact parameter in the numerically resolved cases. On that basis, we determined the numerical resolution for the different codes in terms of the softening length ϵ or grid cell size d_c. We find $b_{\min} = 1.5\epsilon$ for the PP code, consistent with the results of other authors, and $b_{\min} = d_c/2$ for the PM code SUPERBOX.

The new formula can be used for extensive parameter studies of orbital decay, where it is computationally impossible to use a high numerical resolution to resolve the dynamical friction force. Although we did not test the formula for extended objects like satellite galaxies or star clusters in this article, we expect it to work equally well in these cases. Since $\ln \Lambda$ is generally smaller in these applications, the correction due to the maximum impact parameter would be more significant. Additional effects like mass loss in the satellite galaxies must be taken into account (Fujii et al. 2006, 2008). The new Coulomb logarithm also works for non-isotropic background distributions.

We studied the evolution of SMBH binaries in spherical galaxies as well as in galaxy mergers using direct N-body simulations. We focused on the orbital decay of hard binaries. In the case of spherical galaxies we recover the N-dependent shrinking of the separation of the binary that shows the evolution is driven by relaxation effects. For real galaxies with a large number of stars, the evolution of the SMBH binary should stall and lead to the "final parsec problem". By contrast, the N-independence and higher hardening rates found in merger models suggest large pool of stars on centrophilic orbits. The stalling that occurs in the long-term evolution of massive binary black holes at the centers of spherical stellar systems, does not occur when the binary is created via a galaxy merger. The formation of a triaxial merger remnant is a generic outcome in our galaxy merger models. Apparently, even modest departures from axisymmetry in the merged galaxy are sufficient to drive stars into the center, overcoming the orbital depletion that occurs in the spherical geometry. This result provides a plausible solution to the "final parsec problem".

Direct N-body simulation of mergers of spherically symmetric galaxies with different mass ratios were performed to investigate the evolution of binary SMBHs from the onset of merger through the stellar hardening phase until the eventual relativistic coalescence. The merging galaxies have different initial density profiles varying from shallow ($\gamma = 1/2, 1$) to steep cusps ($\gamma = 3/2, 7/4$) – thus covering the range of stellar distribution typically observed in the centers of bulges or early-type galaxies. In Chapter 8, we have shown that merger-induced triaxiality could support a purely stellar dynamical solution to the FPP in the case of equal-mass mergers. In order to assess the prospects for such a solution in the more general unequal-mass case, we measured both the hardening rate and merger-induced triaxiality for mass ratios in the range $q \in [0.05, 1]$. The merger-induced triaxiality found for equal-mass mergers is still present in unequal ($q < 1$) mergers, albeit it becomes weaker as q decreases. Minor mergers with $q \lesssim 0.05$ of spherical progenitor galaxies leave the primary almost unperturbed, so the subsequent binary evolution follows suit in an almost spherical background nucleus. The classical FPP could well show up in such cases. This transition seems to be abrupt, as the measured hardening rates are essentially independent of the mass ratio q until it suddenly declines at a value somewhere between $q = 0.05$ and 0.1 – thus indicating that only a very modest triaxiality (or substantial flattening) is needed for driving the binary inspiral at rates consistently higher than in a spherical nucleus. It is also not surprising that we find that the hardening rate increases substantially for high γ, as more concentrated nuclei will have larger numbers of centrophilic orbits due to their higher central densities.

We have produced estimates of coalescence times using a simplified prescription for the late relativistic phase of the inspiral – *i.e.* adopting the Peter's (1964) equations for the evolution of an isolated binary and ignoring the late *stellar-driven* hardening and eccentricity evolution. We assessed the accuracy of these approximations by including Post-Newtonian terms (up to $3.5\mathcal{PN}$ order) to the equations of motion of the binary in a few representative cases of our sample. At least in these few selected cases, the agreement is remarkably good, and this is mainly due to the fact that the eccentricity evolution is almost identical in the $\mathcal{PN}$ and non-$\mathcal{PN}$ runs. One should add a little note of caution though. The eccentricity evolution may be a quite sensitive function of the properties of the surrounding stellar cluster (slope γ, mass ratio q, amount of net rotation, etc) and on the initial conditions of the binary. Previous studies indeed indicate that one could expect significant evolution of the eccentricity during the hardening phase (Sesana 2010,

Preto et al. 2011). The coalescence times resulting from our calculations are consistently shorter than a Hubble time at a given redshift (up to $z \sim 2-3$ for all masses and up to $z \sim 6-10$ for those in the LISA mass range). Coalescence times for binaries of $\sim 10^6 M_\odot$ are all shorter than 1 Gyr; for the most massive $\sim 10^9 M_\odot$ they range between hundreds of millions of years (highly eccentric ones) to $\sim 1-2$ Gyr (less eccentric ones). Therefore SMBH binaries are very promising sources of GWs for LISA both at low and high redshift. The coalescence times obtained here – especially those from models D – may be effectively an upper bound if the mild eccentricity growth observed in these runs is not generic (we have only four runs). The detailed properties of the distribution of coalescence times hinges in part on the dependence of the eccentricity evolution on the properties of the surrounding cluster. The question of whether eccentricity grows, decays or remains approximately constant during the hardening phase remains still uncertain and we are currently pursuing it. Interestingly, the duration of the stellar dynamical hardening phase of SMBH binaries and the relativistic one are roughly equal due an eccentricity regulated process. This means that SMBH binaries on highly eccentric orbits have a lower probability at detection in the classical regime but at the same time are sources of strong GW signals to be detected. On the other hand, binaries with low eccentricities remain longer in the Newtonian regime and therefore are more likely to be observed in this phase, but may only be luminous GW sources in the final phase of coalescence.

We study the evolution of SMBH binary in late type galaxy merger in two parts. First part uses SPH simulations including important physics, such as star formation and gas accretion on to the supermassive black holes (Callegari et al. 2011) while the second part uses direct N-body code combined with the particle splitting and no additional physics. This approach is adopted due to large distance scales (from 100 kpc to 10^{-6} pc), different physical processes (stellar dynamics, the gas dynamics, relativistic dynamics) involved and the fact that the current numerical codes that treat only few of these physical processes can handle only $10^6 - 10^7$ particles. In the first phase of galaxy merger the two SMBHs grow in mass due to the accretion of gas and the mass ratio of the two black holes changes from 0.1 to 0.3. The results obtained for the SMBH binary evolution in the merger remnant of the gas rich disk galaxies (Chapter 9) are qualitatively similar with those obtained for the mergers of spherical galaxies. The hardening rates are higher compared to the ones reported for the binary evolution in the center of spherical galaxies. The merger remnant is more flattened when compared to those of 1:10 mergers of spherical galaxies. The eccentricity of the binary is also very high (approximately 0.97) consistent with those observed in the spherical galaxy mergers described in Chapters 7 and 8. The estimated SMBH binary coalescence time is about 3 Gyr, which can be a factor 3-4 smaller if a steeper central density profile (observed in late type galaxies) were to be adopted for the merging galaxies. Currently, we are continuing the simulation to the full coalescence of the SMBHs, thus producing a unique study where SMBHs coalescence is achieved in a realistic merger scenario starting at a separation of several tens of kilo-parsecs.

With our results we move one step closer to a consistent stellar dynamical solution to the FPP and providing a solid dynamical support for cosmological scenarios where prompt coalescences are the norm during SMBH-galaxy co-evolution. If our results hold true in real galaxies, the bottleneck to SMBH coalescences – if any – is likely to be associated with the long timescales needed for SMBHs to become a bound pair in galaxy mergers of unequal-mass – especially in case where $q \lesssim 0.1$ and gas fractions are low (Callegari et al. 2011). These results are promising for SMBH binaries being abundant LISA sources at high redshift.

In our study "mass deficits" induced in the centers of gas-free galaxies by inspiraling SMBH binaries are found to be of order $\sim (1-5) M_\bullet$, depending on the slope of central stellar distribution and on the mass ratio of SMBHs. This is consistent with the picture that cores in giant ellipticals are scoured by SMBH binary inspirals during successive merger events – assuming only that relaxation times are long enough in those systems for the results from different mergers to be

cumulative. For galaxies in the mass range of the Milky Way the picture is different. Since the amount of mass depletion in a single merger event only partially destroys a steep inner cusp, even if a major merger were to have happened in the Galactic center at redshift $z = 1$ or larger, it would have had enough time to regrow a mass segregated Bahcall & Wolf cusp since then (Preto & Amaro-Seoane 2010).

Astrophysical Implications

The evolution of SMBHs over the cosmic history is one of the most fascinating puzzles among the many of large scale structure formation in the universe. SMBHs profoundly effect the galaxy formation and evolution by feedback processes. The formation of supermassive black holes is thought to be associated with multistage mergers together with accretion. However early theoretical and numerical studies of SMBH binary evolution suggested that following the merger of two galaxies, the SMBHs may stall at a separation of 1 pc (FPP). If the SMBH binaries do not coalesce faster than the rate at which galaxies merge, the next galaxy merger would bring another SMBH or SMBH binary to the center. This would lead in a 3-body or 4-body gravitational slingshot. Thus non efficient merger of SMBH binaries would result in a much larger scatter in the observed $M_\bullet$ - M_σ and $M_\bullet$ - M_{bulge} relations. In this study we show that stellar dynamics alone can bring the SMBH binaries (over all observed mass range of SMBHs) to coalescence in the centers of merged galaxies, hence solving final parsec problem. Our results support a cosmological scenario where prompt coalescence is the norm during SMBH-galaxy co-evolution.

Another very interesting aspect of the SMBH coalescence is the emission of gravitational radiation. The coalescing SMBH binaries are very promising sources of GWs for pulsar timing arrays (PTA) and future space borne gravitational wave detectors. Recent interests in the study of SMBH binary evolution is also motivated by the fact that gravitational waves shall be detected by LISA. Binary SMBH mergers constitute highest signal to noise ratio among the possible LISA sources. Assuming the prompt coalescence of SMBH binaries Sesana et al. (2004) estimated the SMBH merger rate from the galaxy merger rate (from $z = 20$ to present) in the Λ CDM cosmology. Gravitational wave events, integrated over observable universe, can be as frequent as 10^2 per year. The coalescence time for SMBH binaries in Chapters 8 and 9 suggest that these estimates are reliable. LISA will provide strong constraints on the mechanisms by which SMBH masses evolve over time in the centers of galaxies by observing the masses of SMBHs experiencing binary SMBH coalescences as a function of the redshift. This will help to trace the early merger history of galaxies. At the moment of coalescence, a SMBH binary represents the most extreme transfer of mass into energy produced by any process in the universe. The two SMBHs, in the last few orbits before coalescence, have velocities close to velocity of the light and will provide exceptionally strong tests of the prediction of general relativity.

The inspiral of SMBHs following galaxy merger leaves characteristic imprints on the morphology of the galaxy. The brightness profiles of elliptical galaxies fit remarkably well by Sérsic function (Ferrarese et al. 2006, Kormendy et al. 2009). Although there is no astrophysical explanation for this fit, the fact that Sérsic function fits well all the elliptical galaxies led to identification and interpretation of departures from the function as diagnostic of galaxy formation and evolution (Graham 2004, Kormendy et al. 2009). At small radii two kind of deviations from Sérsic function are observed. The bright elliptical galaxies ($M_{VT} \leq -22$) have cores while faint elliptical galaxies ($M_{VT} \geq -21$) have cuspy profiles. A power law cusp in spatial density ($\rho \propto r^{-\gamma}$) with $\gamma = 1$ projects to core in surface brightness (Dehnen 1993). While power law cusps with $\gamma > 1$ retain power laws in projection as well.

The numerical simulations of dry galaxy mergers performed in Chapter 8 demonstrate that steep power law cusps in density ($\gamma = 1.75$) transform into shallow cusps ($\gamma \simeq 1.0$). The merger of two galaxies with shallow cusps ($\gamma \leq 1.0$) in density results in cores ($\gamma < 0.5$). Early numerical simulations of the galaxy mergers without SMBHs at the center found homology (the merger

product preserves the profile of its progenitors) following the merger (Barnes 1999, Milosavljević & Merritt 2001). The shallow cusps reported in Chapters 7 and 8 are caused by the energy input from inspiraling SMBHs in the center of merger remnant - flinging stars away. Similar destruction of the cusps at the center is earlier reported in the simulations of SMBH binary evolution in a single spherical galaxy and is thought to responsible for appearance of core in giant elliptical galaxies (Milosavljević & Merritt 2001, Makino & Funato 2004, Merritt 2006b). The removal of the stars causes a decrease in surface brightness at the center of the galaxy experiencing a SMBH merger. The galaxies preserve this profile because of the very long relaxation time, which exceeds a Hubble time by orders of magnitudes for giant elliptical galaxies (Merritt & Milosavljević 2005).

The missing light in the centers of galaxies is measured in terms of the mass deficits. The most recent estimates of mass deficits are $\langle M_{\mathrm{def}}/M_{\bullet}\rangle \sim 11$ found in Kormendy et al. (2009)'s sample. In our simulations of the dry galaxy mergers, we found $M_{\mathrm{def}}/M_{\bullet} \sim 1-5$ depending on the initial density profile of the merging galaxies. If galaxies undergo a series of mergers as suggested by the hierarchical galaxy formation scenario, then the mass deficits should add up because the time required to fill in the gap (removal of stars by inspiraling SMBH binary) is essentially of the order of relaxation time. The mass deficit following $\mathcal{N}$ dry mergers is $\mathcal{N} \cdot (M_{\mathrm{def}}/M_{\bullet})$ so the estimated mass deficits obtained from our simulations imply that at least few ($\mathcal{N} = 2-3$) major mergers are required to create $\langle M_{\mathrm{def}}/M_{\bullet}\rangle \sim 11$ reported by Kormendy et al. (2009). Asymmetric emission of gravitational waves by a coalescing SMBH binary leads to a recoil of the merged SMBH. The sinking of the displaced SMBH back to the center caused by dynamical friction displaces additional stellar mass during repeated central passages (Gualandris & Merritt 2008). The cores at the center of bright elliptical galaxies can be attributed to the combined effect of these two mechanisms discussed.

Both core and power law galaxies satisfy $M_{\bullet} - \sigma$ relation so the power law galaxies are also believed to be formed by galaxy mergers. The results of our numerical simulations suggest that mergers of steep power law galaxies result in relatively shallower power law cusps, which is in contradiction to the steep density profiles observed at the centers of these galaxies. Faint elliptical galaxies are believed to be the end product of wet galaxy mergers (Kormendy et al. 2009) and it is proposed that core scouring by the SMBH inspiral is swamped by the starburst resulting from the gas funneled to the center by the mergers (Mihos & Hernquist 1994, Mayer et al. 2010, Callegari et al. 2011). This idea can be tested by N-body simulations that include gas dynamics and can resolve both stellar and gas dynamics to the scales where a hard SMBH binary is formed. Our simulations show that the profile does not change considerably after the formation of a hard binary.

The same mechanism that creates cores in the stellar profile may also be responsible for cores observed in the dark matter profile at the centers of galaxies. This can provide a potential solution to famous "core-cusp" problem.

Outlook

- Currently we are running the simulation which we started from the merger product of an earlier high-resolution smoothed particle hydrodynamics simulation that included star formation and gas accretion onto the SMBHs (Chapter 9). Using the direct N-body code Φ-GPU, we evolved the binary to separation of about 0.01 pc. Our aim here is to achieve full coalescence using post-Newtonian ($\mathcal{PN}$) corrections to the gravitational force between the binary black holes.

- We are also studying the evolution of SMBH binaries by carrying out a large set of simulations of merger of galaxies that have initial mass function (IMF) of stars. We are studying the impact of the IMF on SMBH binary hardening rates and dynamical cusp regeneration after the binary coalescence.

- The eccentricity evolution of SMBH binaries seems to be very sensitive to the density profile of the stellar system hosting SMBH binary evolution. The merger of two galaxies with shal-

low density cusps leads to very high eccentricities of SMBH binaries while steep cusp mergers produce only mild values of binary eccentricities. The SMBH binary coalescence time depends sensitively on the value of eccentricity, particularly for high e. Therefore the exact eccentricity distribution as a function of merger parameters requires further investigation.

- The solution of final parsec problem hinges on the triaxiality and flattening of the merger product in which the SMBH binary evolves. It is worthwhile carrying out galaxy merger simulations starting from the triaxial galaxy progenitors and investigating the shapes and hardening rates in this more realistic scenario. Also the investigations of the phase space distribution of stars interacting with SMBH binaries in galaxy mergers is still missing and a goal of our further studies.

- A big step forward in the study of evolution of SMBH binaries in galaxy mergers would be N-body simulations that resolve both stellar and gas dynamics to milli parsec regime where the emission of GWs dominate the binary evolution.

List of Publications

List of publications during doctoral studies:

[1] **Khan, F. M.**, Preto, M., Berczik, P., Berentzen, I., Just, A., & Spurzem, R. submitted to ApJ

[2] **Khan, F. M.**, Just, A., & Merritt, D. 2011, ApJ, 732, 89

[3] Just, A., **Khan, F. M.**, Berczik, P., Ernst, A., & Spurzem, R. 2011, MNRAS, 411, 653

Bibliography

Aarseth, S. J. (1963), 'Dynamical evolution of clusters of galaxies, I', *Month. Not. Roy. Astr. Soc.* **126**, 223–+.

Aarseth, S. J. & Zare, K. (1974), 'A regularization of the three-body problem', *Celestial Mechanics* **10**, 185–205.

Ahmad, A. & Cohen, L. (1973), 'A numerical integration scheme for the N-body gravitational problem.', *Journal of Computational Physics* **12**, 389–402.

Antonini, F. & Merritt, D. (2011), 'Dynamical Friction around Supermassive Black Holes', *ArXiv e-prints* .

Bahcall, J. N. & Wolf, R. A. (1976), 'Star distribution around a massive black hole in a globular cluster', *Astrophys. J.* **209**, 214–232.

Barack, L. & Cutler, C. (2004), 'LISA capture sources: Approximate waveforms, signal-to-noise ratios, and parameter estimation accuracy', *Physical Review D* **69**(8), 082005–+.

Barnes, J. E. (1999), Dynamics of Mergers Remnants, *in* J. E. Barnes & D. B. Sanders, ed., 'Galaxy Interactions at Low and High Redshift', Vol. 186 of *IAU Symposium*, p. 137.

Barnes, J. & Hut, P. (1986), 'A hierarchical O(N log N) force-calculation algorithm', *Nature* **324**, 446–449.

Begelman, M. C., Blandford, R. D. & Rees, M. J. (1980), 'Massive black hole binaries in active galactic nuclei', *Nature* **287**, 307–309.

Begelman, M. C., Volonteri, M. & Rees, M. J. (2006), 'Formation of supermassive black holes by direct collapse in pre-galactic haloes', *Month. Not. Roy. Astr. Soc.* **370**, 289–298.

Berczik, P., Merritt, D. & Spurzem, R. (2005), 'Long-Term Evolution of Massive Black Hole Binaries. II. Binary Evolution in Low-Density Galaxies', *Astrophys. J.* **633**, 680–687.

Berczik, P., Merritt, D., Spurzem, R. & Bischof, H.-P. (2006), 'Efficient Merger of Binary Supermassive Black Holes in Nonaxisymmetric Galaxies', *Astrophys. J. Let.* **642**, L21–L24.

Berentzen, I., Preto, M., Berczik, P., Merritt, D. & Spurzem, R. (2009), 'Binary Black Hole Merger in Galactic Nuclei: Post-Newtonian Simulations', *Astrophys. J.* **695**, 455–468.

Bien, R., Fuchs, B. & Wielen, R. (1991), 'High spatial resolution using the conventional particle-mesh technique', *International Journal of Modern Physics C* **2**, 3–13.

Bien, R., Just, A., Berczik, P. & Berentzen, I. (2008), 'High resolution in z-direction: The simulation of disc-bulge-halo galaxies using the particle-mesh code SUPERBOX', *Astronomische Nachrichten* **329**, 1029–+.

BIBLIOGRAPHY

Binney, J. & Tremaine, S. (1987), *Galactic Dynamics*, Princeton Univ.Press, New Jersey, USA.

Binney, J. & Tremaine, S. (2008), *Galactic Dynamics: Second Edition*, Princeton University Press.

Blanchet, L. (2006), 'Gravitational Radiation from Post-Newtonian Sources and Inspiralling Compact Binaries', *Living Reviews in Relativity* **9**, 4–+.

Bondi, H. & Hoyle, F. (1944), 'On the mechanism of accretion by stars', *Month. Not. Roy. Astr. Soc.* **104**, 273–+.

Boroson, T. A. & Lauer, T. R. (2009), 'A candidate sub-parsec supermassive binary black hole system', *Nature* **458**, 53–55.

Callegari, S., Kazantzidis, S., Mayer, L., Colpi, M., Bellovary, J. M., Quinn, T. & Wadsley, J. (2011), 'Growing Massive Black Hole Pairs in Minor Mergers of Disk Galaxies', *Astrophys. J.* **729**, 85–+.

Callegari, S., Mayer, L., Kazantzidis, S., Colpi, M., Governato, F., Quinn, T. & Wadsley, J. (2009), 'Pairing of Supermassive Black Holes in Unequal-Mass Galaxy Mergers', *Astrophys. J. Let.* **696**, L89–L92.

Chandrasekhar, S. (1942), *Principles of Stellar Dynamics*, University of Chicago Press.

Chandrasekhar, S. & von Neumann, J. (1942), 'The Statistics of the Gravitational Field Arising from a Random Distribution of Stars. I. The Speed of Fluctuations.', *Astrophys. J.* **95**, 489–+.

Cotera, A. S., Erickson, E. F., Colgan, S. W. J., Simpson, J. P., Allen, D. A. & Burton, M. G. (1996), 'The Discovery of Hot Stars near the Galactic Center Thermal Radio Filaments', *Astrophys. J.* **461**, 750–+.

Cuadra, J., Armitage, P. J., Alexander, R. D. & Begelman, M. C. (2009), 'Massive black hole binary mergers within subparsec scale gas discs', *Month. Not. Roy. Astr. Soc.* **393**, 1423–1432.

De Paolis, F., Ingrosso, G. & Nucita, A. A. (2002), 'Astrophysical implications of binary black holes in BL Lacertae objects', *Astron. & Astrophys.* **388**, 470–476.

Dehnen, W. (1993), 'A Family of Potential-Density Pairs for Spherical Galaxies and Bulges', *Month. Not. Roy. Astr. Soc.* **265**, 250–+.

Deibel, A. T., Valluri, M. & Merritt, D. (2011), 'The Orbital Structure of Triaxial Galaxies with Figure Rotation', *Astrophys. J.* **728**, 128–+.

Dotti, M., Colpi, M., Haardt, F. & Mayer, L. (2007), 'Supermassive black hole binaries in gaseous and stellar circumnuclear discs: orbital dynamics and gas accretion', *Month. Not. Roy. Astr. Soc.* **379**, 956–962.

Eckart, A. & Genzel, R. (1997), The Galactic Center Black Hole, *in* 'American Astronomical Society Meeting Abstracts'.

Erwin, P. & Sparke, L. S. (2002), 'Double Bars, Inner Disks, and Nuclear Rings in Early-Type Disk Galaxies', *Astron. J.* **124**, 65–77.

Escala, A., Larson, R. B., Coppi, P. S. & Mardones, D. (2005), 'The Role of Gas in the Merging of Massive Black Holes in Galactic Nuclei. II. Black Hole Merging in a Nuclear Gas Disk', *Astrophys. J.* **630**, 152–166.

Fabbiano, G., Junfeng, W., Elvis, M. & Risaliti, G. (2011), 'A Close Nuclear Black Hole Pair in the Spiral Galaxy NGC 3393', *ArXiv Astrophysics e-prints* .

Fan, X. (2006), 'Evolution of high-redshift quasars', *New Astronomy* **50**, 665–671.

Fellhauer, M., Kroupa, P., Baumgardt, H., Bien, R., Boily, C. M., Spurzem, R. & Wassmer, N. (2000), 'SUPERBOX - an efficient code for collisionless galactic dynamics', *New Astronomy* **5**, 305–326.

Ferrarese, L., Côté, P., Jordán, A., Peng, E. W., Blakeslee, J. P., Piatek, S., Mei, S., Merritt, D., Milosavljević, M., Tonry, J. L. & West, M. J. (2006), 'The ACS Virgo Cluster Survey. VI. Isophotal Analysis and the Structure of Early-Type Galaxies', *Astrophys. J. Sup. S.* **164**, 334–434.

Ferrarese, L. & Ford, H. (2005), 'Supermassive Black Holes in Galactic Nuclei: Past, Present and Future Research', **116**, 523–624.

Ferrarese, L. & Merritt, D. (2000), 'A Fundamental Relation between Supermassive Black Holes and Their Host Galaxies', *Astrophys. J. Let.* **539**, L9–L12.

Fujii, M., Funato, Y. & Makino, J. (2006), 'Dynamical Friction on Satellite Galaxies', **58**, 743–752.

Fujii, M., Iwasawa, M., Funato, Y. & Makino, J. (2008), 'Evolution of Star Clusters near the Galactic Center: Fully Self-Consistent N-Body Simulations', *Astrophys. J.* **686**, 1082–1093.

Gaburov, E., Harfst, S. & Portegies Zwart, S. (2009), 'SAPPORO: A way to turn your graphics cards into a GRAPE-6', *New Astronomy* **14**, 630–637.

Gebhardt, K., Bender, R., Bower, G., Dressler, A., Faber, S. M., Filippenko, A. V., Green, R., Grillmair, C., Ho, L. C., Kormendy, J., Lauer, T. R., Magorrian, J., Pinkney, J., Richstone, D. & Tremaine, S. (2000), 'A Relationship between Nuclear Black Hole Mass and Galaxy Velocity Dispersion', *Astrophys. J. Let.* **539**, L13–L16.

Genzel, R. & Townes, C. H. (1987), 'Physical conditions, dynamics, and mass distribution in the center of the Galaxy', *Ann. Rev. Astron. Astrophys.* **25**, 377–423.

Gerhard, O. (2001), 'The Galactic Center HE I Stars: Remains of a Dissolved Young Cluster?', *Astrophys. J. Let.* **546**, L39–L42.

Gerhard, O. E. & Binney, J. (1985), 'Triaxial galaxies containing massive black holes or central density cusps', *Month. Not. Roy. Astr. Soc.* **216**, 467–502.

Ghez, A. M., Klein, B. L., Morris, M. & Becklin, E. E. (1998), 'High Proper-Motion Stars in the Vicinity of Sagittarius A*: Evidence for a Supermassive Black Hole at the Center of Our Galaxy', *Astrophys. J.* **509**, 678–686.

Ghez, A. M., Salim, S., Weinberg, N. N., Lu, J. R., Do, T., Dunn, J. K., Matthews, K., Morris, M. R., Yelda, S., Becklin, E. E., Kremenek, T., Milosavljevic, M. & Naiman, J. (2008), 'Measuring Distance and Properties of the Milky Way's Central Supermassive Black Hole with Stellar Orbits', *Astrophys. J.* **689**, 1044–1062.

Gradshteyn I.S., R. I. (1980), *Table of integrals, series, and products*, Academic Press.

Graham, A. W. (2004), 'Core Depletion from Coalescing Supermassive Black Holes', *Astrophys. J. Let.* **613**, L33–L36.

Gualandris, A. & Merritt, D. (2008), 'Ejection of Supermassive Black Holes from Galaxy Cores', *Astrophys. J.* **678**, 780–797.

Gültekin, K., Richstone, D. O., Gebhardt, K., Lauer, T. R., Tremaine, S., Aller, M. C., Bender, R., Dressler, A., Faber, S. M., Filippenko, A. V., Green, R., Ho, L. C., Kormendy, J., Magorrian, J., Pinkney, J. & Siopis, C. (2009), 'The M-σ and M-L Relations in Galactic Bulges, and Determinations of Their Intrinsic Scatter', *Astrophys. J.* **698**, 198–221.

Gürkan, M. A., Freitag, M. & Rasio, F. A. (2004), 'Formation of Massive Black Holes in Dense Star Clusters. I. Mass Segregation and Core Collapse', *Astrophys. J.* **604**, 632–652.

Haehnelt, M. G. (1994), 'Low-Frequency Gravitational Waves from Supermassive Black-Holes', *Month. Not. Roy. Astr. Soc.* **269**, 199–+.

Haiman, Z. (2004), 'Constraints from Gravitational Recoil on the Growth of Supermassive Black Holes at High Redshift', *Astrophys. J.* **613**, 36–40.

Harfst, S. et al. (2007), 'Performance analysis of direct N-body algorithms on special-purpose supercomputers', *New Astronomy* **12**, 357–377.

Häring, N. & Rix, H.-W. (2004), 'On the Black Hole Mass-Bulge Mass Relation', *Astrophys. J. Let.* **604**, L89–L92.

Hashimoto, Y., Funato, Y. & Makino, J. (2003), 'To Circularize or Not To Circularize?-Orbital Evolution of Satellite Galaxies', *Astrophys. J.* **582**, 196–201.

Heggie, D. C. (1974), 'A global regularisation of the gravitational N-body problem', *Celestial Mechanics* **10**, 217–241.

Hernandez, X. & Gilmore, G. (1998), 'Dynamical friction in dwarf galaxies', *Month. Not. Roy. Astr. Soc.* **297**, 517–525.

Hernquist, L. (1990), 'An analytical model for spherical galaxies and bulges', *Astrophys. J.* **356**, 359–364.

Hills, J. G. & Fullerton, L. W. (1980), 'Computer simulations of close encounters between single stars and hard binaries', *Astron. J.* **85**, 1281–1291.

Holley-Bockelmann, K., Mihos, J. C., Sigurdsson, S. & Hernquist, L. (2001), 'Models of Cuspy Triaxial Galaxies', *Astrophys. J.* **549**, 862–870.

Holley-Bockelmann, K., Mihos, J. C., Sigurdsson, S., Hernquist, L. & Norman, C. (2002), 'The Evolution of Cuspy Triaxial Galaxies Harboring Central Black Holes', *Astrophys. J.* **567**, 817–827.

Holmberg, E. (1941), 'On the Clustering Tendencies among the Nebulae. II. a Study of Encounters Between Laboratory Models of Stellar Systems by a New Integration Procedure.', *Astrophys. J.* **94**, 385–+.

Hopkins, P. F., Cox, T. J., Dutta, S. N., Hernquist, L., Kormendy, J. & Lauer, T. R. (2009), 'Dissipation and Extra Light in Galactic Nuclei. II. "Cusp" Ellipticals', *Astrophys. J. Sup. S.* **181**, 135–182.

Hopkins, P. F., Lauer, T. R., Cox, T. J., Hernquist, L. & Kormendy, J. (2009), 'Dissipation and Extra Light in Galactic Nuclei. III. "Core" Ellipticals and "Missing" Light', *Astrophys. J. Sup. S.* **181**, 486–532.

Hughes, S. A. (2003), 'Listening to the universe with gravitational-wave astronomy', *Annals of Physics* **303**, 142–178.

Hulse, R. A. & Taylor, H. J. (1974), Discovery of a Pulsar in a Close Binary System., *in* 'Bulletin of the American Astronomical Society', Vol. 6 of *Bulletin of the American Astronomical Society*, pp. 453–+.

Iguchi, S., Okuda, T. & Sudou, H. (2010), 'A Very Close Binary Black Hole in a Giant Elliptical Galaxy 3C 66B and its Black Hole Merger', *Astrophys. J. Let.* **724**, L166–L170.

Inoue, S. (2009), 'The test for suppressed dynamical friction in a constant density core of dwarf galaxies', *Month. Not. Roy. Astr. Soc.* **397**, 709–716.

Jaffe, A. H. & Backer, D. C. (2003), 'Gravitational Waves Probe the Coalescence Rate of Massive Black Hole Binaries', *Astrophys. J.* **583**, 616–631.

Johnson, J. L., Greif, T. H. & Bromm, V. (2007), Radiative Feedback in the Formation of the First Protogalaxies, *in* 'American Astronomical Society Meeting Abstracts', Vol. 38 of *Bulletin of the American Astronomical Society*, pp. 886–+.

Just, A., Khan, F. M., Berczik, P., Ernst, A. & Spurzem, R. (2011), 'Dynamical friction of massive objects in galactic centres', *Month. Not. Roy. Astr. Soc.* **411**, 653–674.

Just, A. & Peñarrubia, J. (2005), 'Large scale inhomogeneity and local dynamical friction', *Astron. & Astrophys.* **431**, 861–877.

Katz, J. I. (1997), 'A Precessing Disk in OJ 287?', *Astrophys. J.* **478**, 527–+.

Kauffmann, G. & Haehnelt, M. (2000), 'A unified model for the evolution of galaxies and quasars', *Month. Not. Roy. Astr. Soc.* **311**, 576–588.

Khan, F. M., Just, A. & Merritt, D. (2011), 'Efficient Merger of Binary Supermassive Black Holes in Merging Galaxies', *Astrophys. J.* **732**, 89–+.

Komossa, S. (2006), 'Observational evidence for binary black holes and active double nuclei', *Memorie della Societ Astronomica Italiana* **77**, 733–+.

Komossa, S., Burwitz, V., Hasinger, G., Predehl, P., Kaastra, J. S. & Ikebe, Y. (2003), 'Discovery of a Binary Active Galactic Nucleus in the Ultraluminous Infrared Galaxy NGC 6240 Using Chandra', *Astrophys. J. Let.* **582**, L15–L19.

Kormendy, J., Fisher, D. B., Cornell, M. E. & Bender, R. (2009), 'Structure and Formation of Elliptical and Spheroidal Galaxies', *Astrophys. J. Sup. S.* **182**, 216–309.

Kormendy, J. & Richstone, D. (1995), 'Inward Bound—The Search For Supermassive Black Holes In Galactic Nuclei', *Ann. Rev. Astron. Astrophys.* **33**, 581–+.

Koushiappas, S. M., Bullock, J. S. & Dekel, A. (2004), 'Massive black hole seeds from low angular momentum material', *Month. Not. Roy. Astr. Soc.* **354**, 292–304.

Lauer, T. R., Ajhar, E. A., Byun, Y.-I., Dressler, A., Faber, S. M., Grillmair, C., Kormendy, J., Richstone, D. & Tremaine, S. (1995), 'The Centers of Early-Type Galaxies with HST.I.An Observational Survey', *Astron. J.* **110**, 2622–+.

Lehto, H. J. & Valtonen, M. J. (1996), 'OJ 287 Outburst Structure and a Binary Black Hole Model', *Astrophys. J.* **460**, 207–+.

Lightman, A. P. & Shapiro, S. L. (1977), 'The distribution and consumption rate of stars around a massive, collapsed object', *Astrophys. J.* **211**, 244–262.

Liu, F. K., Wu, X.-B. & Cao, S. L. (2003), 'Double-double radio galaxies: remnants of merged supermassive binary black holes', *Month. Not. Roy. Astr. Soc.* **340**, 411–416.

Liu, F. K. & Zhang, Y. H. (2002), 'A new list of extra-galactic radio jets', *Astron. & Astrophys.* **381**, 757–760.

Lodato, G., Nayakshin, S., King, A. R. & Pringle, J. E. (2009), 'Black hole mergers: can gas discs solve the 'final parsec' problem?', *Month. Not. Roy. Astr. Soc.* **398**, 1392–1402.

Madau, P. & Rees, M. J. (2001), 'Massive Black Holes as Population III Remnants', *Astrophys. J. Let.* **551**, L27–L30.

Makino, J. (1997), 'Merging of Galaxies with Central Black Holes. II. Evolution of the Black Hole Binary and the Structure of the Core', *Astrophys. J.* **478**, 58–+.

Makino, J. & Aarseth, S. J. (1992), 'On a Hermite integrator with Ahmad-Cohen scheme for gravitational many-body problems', **44**, 141–151.

Makino, J. & Funato, Y. (2004), 'Evolution of Massive Black Hole Binaries', *Astrophys. J.* **602**, 93–102.

Maness, H. L., Taylor, G. B., Zavala, R. T., Peck, A. B. & Pollack, L. K. (2004), 'Breaking All the Rules: The Compact Symmetric Object 0402+379', *Astrophys. J.* **602**, 123–134.

Matsubayashi, T. et al. (2007), 'Orbital Evolution of an IMBH in the Galactic Nucleus with a Massive Central Black Hole', *Astrophys. J.* **656**, 879–896.

Matsui, H. & Habe, A. (2009), 'Effects of Minor Mergers on the Coalescence of a Supermassive Black Hole Binary', *Publications of the Astronomical Society of Japan* **61**, 421–.

Max, C. E., Canalizo, G. & de Vries, W. H. (2007), 'Locating the Two Black Holes in NGC 6240', *Science* **316**, 1877–.

Mayer, L., Kazantzidis, S., Escala, A. & Callegari, S. (2010), 'Direct formation of supermassive black holes via multi-scale gas inflows in galaxy mergers', **466**, 1082–1084.

McLachlan, R. I. & Scovel, C. (1995), 'Equivariant constrained symplectic integration', *Journal of NonLinear Science* **5**, 233–256.

Menou, K., Haiman, Z. & Narayanan, V. K. (2001), 'The Merger History of Supermassive Black Holes in Galaxies', *Astrophys. J.* **558**, 535–542.

Merritt, D. (2006a), 'Dynamics of galaxy cores and supermassive black holes', *Reports on Progress in Physics* **69**, 2513–2579.

Merritt, D. (2006b), 'Mass Deficits, Stalling Radii, and the Merger Histories of Elliptical Galaxies', *Astrophys. J.* **648**, 976–986.

Merritt, D. & Ekers, R. D. (2002), 'Tracing Black Hole Mergers Through Radio Lobe Morphology', *Science* **297**, 1310–1313.

Merritt, D. & Ferrarese, L. (2001), 'The M-σ Relation for Supermassive Black Holes', *Astrophys. J.* **547**, 140–145.

Merritt, D., Mikkola, S. & Szell, A. (2007), 'Long-Term Evolution of Massive Black Hole Binaries. III. Binary Evolution in Collisional Nuclei', *Astrophys. J.* **671**, 53–72.

Merritt, D. & Milosavljević, M. (2005), 'Massive Black Hole Binary Evolution', *Living Reviews in Relativity* **8**, 8–+.

Merritt, D. & Poon, M. Y. (2004), 'Chaotic Loss Cones and Black Hole Fueling', *Astrophys. J.* **606**, 788–798.

Merritt, D. & Vasiliev, E. (2011), 'Orbits Around Black Holes in Triaxial Nuclei', *Astrophys. J.* **726**, 61–+.

Mihos, J. C. & Hernquist, L. (1994), 'Dense stellar cores in merger remnants', *Astrophys. J. Let.* **437**, L47–L50.

Mikkola, S. & Aarseth, S. (2002), 'A Time-Transformed Leapfrog Scheme', *Celestial Mechanics and Dynamical Astronomy* **84**, 343–354.

Mikkola, S. & Aarseth, S. J. (1998), 'An efficient integration method for binaries in N-body simulations', *New Astronomy* **3**, 309–320.

Mikkola, S. & Valtonen, M. J. (1992), 'Evolution of binaries in the field of light particles and the problem of two black holes', *Month. Not. Roy. Astr. Soc.* **259**, 115–120.

Milosavljević, M., Couch, S. M. & Bromm, V. (2009), 'Accretion Onto Intermediate-Mass Black Holes in Dense Protogalactic Clouds', *Astrophys. J. Let.* **696**, L146–L149.

Milosavljević, M. & Merritt, D. (2001), 'Formation of Galactic Nuclei', *Astrophys. J.* **563**, 34–62.

Milosavljević, M. & Merritt, D. (2003*a*), 'Long-Term Evolution of Massive Black Hole Binaries', *Astrophys. J.* .

Milosavljević, M. & Merritt, D. (2003*b*), The Final Parsec Problem, *in* 'The Astrophysics of Gravitational Wave Sources'.

Navarro, J. F., Frenk, C. S. & White, S. D. M. (1997), 'A Universal Density Profile from Hierarchical Clustering', *Astrophys. J.* **490**, 493–+.

Nitadori, K. & Makino, J. (2008), 'Sixth- and eighth-order Hermite integrator for N-body simulations', *New Astronomy* **13**, 498–507.

Norman, C. & Silk, J. (1983), 'The dynamics and fueling of active nuclei', *Astrophys. J.* **266**, 502–515.

Ostriker, E. C. (1999), 'Dynamical Friction in a Gaseous Medium', *Astrophys. J.* **513**, 252–258.

Ostriker, J. P., Binney, J. & Saha, P. (1989), 'The effect of galaxy triaxiality on globular clusters', *Month. Not. Roy. Astr. Soc.* **241**, 849–871.

Peñarrubia, J., Just, A. & Kroupa, P. (2004), 'Dynamical friction in flattened systems: a numerical test of Binney's approach', *Month. Not. Roy. Astr. Soc.* **349**, 747–756.

Peebles, P. J. E. (1972), 'Star Distribution Near a Collapsed Object', **178**, 371–376.

Peng, C. Y., Ho, L. C., Impey, C. D. & Rix, H.-W. (2002), 'Detailed Structural Decomposition of Galaxy Images', *Astron. J.* **124**, 266–293.

Perets, H. B. & Alexander, T. (2008), 'Massive Perturbers and the Efficient Merger of Binary Massive Black Holes', *Astrophys. J.* **677**, 146–159.

Peters, P. C. (1964), 'Gravitational Radiation and the Motion of Two Point Masses', *Physical Review* **136**, 1224–1232.

Plummer, H. C. (1911), 'On the problem of distribution in globular star clusters', *Month. Not. Roy. Astr. Soc.* **71**, 460–470.

Poon, M. Y. & Merritt, D. (2001), 'Orbital Structure of Triaxial Black Hole Nuclei', *Astrophys. J.* **549**, 192–204.

Portegies Zwart, S. F., Dewi, J. & Maccarone, T. (2004), 'Intermediate mass black holes in accreting binaries: formation, evolution and observational appearance', *Month. Not. Roy. Astr. Soc.* **355**, 413–423.

Portegies Zwart, S. F. & McMillan, S. L. W. (2002), 'The Runaway Growth of Intermediate-Mass Black Holes in Dense Star Clusters', *Astrophys. J.* **576**, 899–907.

Preto, M. & Amaro-Seoane, P. (2010), 'On Strong Mass Segregation Around a Massive Black Hole: Implications for Lower-Frequency Gravitational-Wave Astrophysics', *Astrophys. J. Let.* **708**, L42–L46.

Preto, M., Berentzen, I., Berczik, P. & Spurzem, R. (2011), 'Fast Coalescence of Massive Black Hole Binaries from Mergers of Galactic Nuclei: Implications for Low-frequency Gravitational-wave Astrophysics', *Astrophys. J. Let.* **732**, L26+.

Preto, M., Merritt, D. & Spurzem, R. (2004), 'N-Body Growth of a Bahcall-Wolf Cusp around a Black Hole', *Astrophys. J. Let.* **613**, L109–L112.

Quinlan, G. D. (1996), 'The dynamical evolution of massive black hole binaries I. Hardening in a fixed stellar background', *New Astronomy* **1**, 35–56.

Read, J. I., Goerdt, T., Moore, B., Pontzen, A. P., Stadel, J. & Lake, G. (2006), 'Dynamical friction in constant density cores: a failure of the Chandrasekhar formula', *Month. Not. Roy. Astr. Soc.* **373**, 1451–1460.

Rees, M. J. (1984), 'Black Hole Models for Active Galactic Nuclei', *Ann. Rev. Astron. Astrophys.* **22**, 471–506.

Rephaeli, Y. & Salpeter, E. E. (1980), 'Flow past a massive object and the gravitational drag', *Astrophys. J.* **240**, 20–24.

Rhook, K. J. & Wyithe, J. S. B. (2005), 'Realistic event rates for detection of supermassive black hole coalescence by LISA', *Month. Not. Roy. Astr. Soc.* **361**, 1145–1152.

Rieger, F. M. & Mannheim, K. (2000), 'Implications of a possible 23 day periodicity for binary black hole models in Mkn 501', *Astron. & Astrophys.* **359**, 948–952.

Robinson, I., Schild, A. & Schucking, E. L., eds (1965), *Quasi-stellar sources and gravitational collapse.*

Rodriguez, C., Taylor, G. B., Zavala, R. T., Peck, A. B., Pollack, L. K. & Romani, R. W. (2006), 'A Compact Supermassive Binary Black Hole System', *Astrophys. J.* **646**, 49–60.

Rosenbluth, M. N., MacDonald, W. M. & Judd, D. L. (1957), 'Fokker-Planck Equation for an Inverse-Square Force', *Physical Review* **107**, 1–6.

Salpeter, E. E. (1964), 'Accretion of Interstellar Matter by Massive Objects.', *Astrophys. J.* **140**, 796–800.

Schoenmakers, A. P., de Bruyn, A. G., Röttgering, H. J. A., van der Laan, H. & Kaiser, C. R. (2000), 'Radio galaxies with a 'double-double morphology' - I. Analysis of the radio properties and evidence for interrupted activity in active galactic nuclei', *Month. Not. Roy. Astr. Soc.* **315**, 371–380.

Schwarzschild, M. (1979), 'A numerical model for a triaxial stellar system in dynamical equilibrium', *Astrophys. J.* **232**, 236–247.

Sesana, A. (2010), 'Self Consistent Model for the Evolution of Eccentric Massive Black Hole Binaries in Stellar Environments: Implications for Gravitational Wave Observations', *Astrophys. J.* **719**, 851–864.

Sesana, A., Haardt, F. & Madau, P. (2006), 'Interaction of Massive Black Hole Binaries with Their Stellar Environment. I. Ejection of Hypervelocity Stars', *Astrophys. J.* **651**, 392–400.

Sesana, A., Haardt, F., Madau, P. & Volonteri, M. (2004), 'Low-Frequency Gravitational Radiation from Coalescing Massive Black Hole Binaries in Hierarchical Cosmologies', *Astrophys. J.* **611**, 623–632.

Shapiro, S. L. & Lightman, A. P. (1976), 'The distribution of stars around a massive black hole', *Nature* **262**, 743–745.

Shaw, M., Axon, D., Probst, R. & Gatley, I. (1995), 'Nuclear bars and blue nuclei within barred spiral galaxies', *Month. Not. Roy. Astr. Soc.* **274**, 369–387.

Sillanpaa, A., Haarala, S., Valtonen, M. J., Sundelius, B. & Byrd, G. G. (1988), 'OJ 287 - Binary pair of supermassive black holes', *Astrophys. J.* **325**, 628–634.

Spinnato, P. F., Fellhauer, M. & Portegies Zwart, S. F. (2003), 'The efficiency of the spiral-in of a black hole to the Galactic Centre', *Month. Not. Roy. Astr. Soc.* **344**, 22–32.

Spitzer, L. (1987), *Dynamical Evolution of Globular Clusters*, Princeton Univ.Press, New Jersey, USA.

Springel, V., Wang, J., Vogelsberger, M., Ludlow, A., Jenkins, A., Helmi, A., Navarro, J. F., Frenk, C. S. & White, S. D. M. (2008), 'The Aquarius Project: the subhaloes of galactic haloes', *Month. Not. Roy. Astr. Soc.* **391**, 1685–1711.

Springel, V., Yoshida, N. & White, S. D. M. (2001), 'GADGET: a code for collisionless and gasdynamical cosmological simulations', *New Astronomy* **6**, 79–117.

Spurzem, R. (1999), 'Direct N-body Simulations', *Journal of Computational and Applied Mathematics* **109**, 407–432.

Sridhar, S. & Touma, J. (1999), 'Stellar dynamics around black holes in galactic nuclei', *Month. Not. Roy. Astr. Soc.* **303**, 483–494.

Tremaine, S. D. (1976), 'The effect of dynamical friction on the orbits of the Magellanic clouds', *Astrophys. J.* **203**, 72–74.

Tremaine, S., Gebhardt, K., Bender, R., Bower, G., Dressler, A., Faber, S. M., Filippenko, A. V., Green, R., Grillmair, C., Ho, L. C., Kormendy, J., Lauer, T. R., Magorrian, J., Pinkney, J. & Richstone, D. (2002), 'The Slope of the Black Hole Mass versus Velocity Dispersion Correlation', *Astrophys. J.* **574**, 740–753.

Tremaine, S. et al. (1994), 'A family of models for spherical stellar systems', *Astron. J.* **107**, 634–644.

Valluri, M. & Merritt, D. (1998), 'Regular and Chaotic Dynamics of Triaxial Stellar Systems', *Astrophys. J.* **506**, 686–711.

Valtaoja, E., Teräsranta, H., Tornikoski, M., Sillanpää, A., Aller, M. F., Aller, H. D. & Hughes, P. A. (2000), 'Radio Monitoring of OJ 287 and Binary Black Hole Models for Periodic Outbursts', *Astrophys. J.* **531**, 744–755.

Valtonen, M. J. (2008), OJ287: a binary black hole system, *in* 'Revista Mexicana de Astronomia y Astrofisica Conference Series', Vol. 32 of *Revista Mexicana de Astronomia y Astrofisica, vol. 27*, pp. 22–24.

Valtonen, M. J., Lehto, H. J., Nilsson, K., Heidt, J., Takalo, L. O., Sillanpää, A., Villforth, C., Kidger, M., Poyner, G., Pursimo, T., Zola, S., Wu, J.-H., Zhou, X., Sadakane, K., Drozdz, M., Koziel, D., Marchev, D., Ogloza, W., Porowski, C., Siwak, M., Stachowski, G., Winiarski, M., Hentunen, V.-P., Nissinen, M., Liakos, A. & Dogru, S. (2008), 'A massive binary black-hole system in OJ287 and a test of general relativity', *Nature* **452**, 851–853.

Volonteri, M. & Begelman, M. C. (2010), 'Quasi-stars and the cosmic evolution of massive black holes', *Month. Not. Roy. Astr. Soc.* **409**, 1022–1032.

Volonteri, M., Haardt, F. & Madau, P. (2003), 'The Assembly and Merging History of Supermassive Black Holes in Hierarchical Models of Galaxy Formation', *Astrophys. J.* **582**, 559–573.

Volonteri, M., Miller, J. M. & Dotti, M. (2009), 'Sub-Parsec Supermassive Binary Quasars: Expectations at z less than 1', *Astrophys. J. Let.* **703**, L86–L89.

Volonteri, M. & Rees, M. J. (2006), 'Quasars at z=6: The Survival of the Fittest', *Astrophys. J.* **650**, 669–678.

von Hoerner, S. (1960), 'Die numerische Integration des n-Körper-Problemes für Sternhaufen. I', *Zeitschrift für Astrophysik* **50**, 184–214.

Weinberg, M. D. (1985), 'Evolution of barred galaxies by dynamical friction', *Month. Not. Roy. Astr. Soc.* **213**, 451–471.

Weinberg, M. D. (1989), 'Self-gravitating response of a spherical galaxy to sinking satellites', *Month. Not. Roy. Astr. Soc.* **239**, 549–569.

Wyithe, J. S. B. & Loeb, A. (2003), 'Low-Frequency Gravitational Waves from Massive Black Hole Binaries: Predictions for LISA and Pulsar Timing Arrays', *Astrophys. J.* **590**, 691–706.

Yoshida, H. (1990), 'Construction of higher order symplectic integrators', *Physics Letters A* **150**, 262–268.

Yu, Q. (2002), 'Evolution of massive binary black holes', *Month. Not. Roy. Astr. Soc.* **331**, 935–958.

Zel'Dovich, Y. B. & Novikov, I. D. (1964), 'The Radiation of Gravity Waves by Bodies Moving in the Field of a Collapsing Star', *Soviet Physics Doklady* **9**, 246–+.

Zier, C. (2005), 'Orientation and size of the 'Z' in X-shaped radio galaxies', *Month. Not. Roy. Astr. Soc.* **364**, 583–592.

Acknowledgements

First and foremost I offer my sincerest gratitude to my thesis advisor, Priv. Doz. Dr. Andreas Just for his supervision, advice and guidance. He was always there to assist me and dedicated his time whenever I visited his office. He encouraged and supported me to participate in scientific conferences and to interact with different people to gain knowledge and ideas. This proved indeed very helpful for me. Before starting my thesis, somebody advised me that "there are two persons who can make or destroy your life; your PhD supervisor and your wife". I am extremely lucky to have Dr. Andreas Just as my supervisor and hope to be as much as (if not more) lucky to have Tooba as my wife.

I gratefully acknowledge Prof. Dr. Rainer Spurzem for his support and help to integrate me in his scientific group and for offering me his valuable guidance whenever I needed it. I am also thankful to him for offering generous access to all the computer clusters used in this work.

I am also indebted to Prof. Dr. David Merritt for valuable discussions during a summer school in Leiden which assisted me a lot to excel in the field of supermassive black hole binaries.

I gratefully thank Dr. Peter Berczik for his help and guidance in almost all of my projects. He always kindly granted me time to discuss issues with numerical simulations. I benefited a lot from his expertise in computational astrophysics. My special thanks also go to Dr. Ingo Berentzen for having all those valuable scientific discussions on our way to Mensa. I would also like to extend my sincere thanks to my other collaborators, Prof. Dr. Lucio Mayer, Dr. Miguel Preto, Dr. Andreas Ernst and Simone Callegari for their valuable contributions in my scientific projects.

It is a pleasure to thank my thesis committee members, Dr. Andreas Just, Prof. Dr. Rainer Spurzem, Prof. Dr. Jochen Heidt and Dr. Robi Banerjee for their useful scientific advices. Furthermore, I would like to thank Prof. Dr. Johanna Stachel and Prof. Dr. Volker Springel for joining my examination committee.

I gratefully appreciate Prof. Dr. Eva Grebel and Prof. Dr. Christian Fendt for supporting my participation in scientific conferences.

Special thanks go to Dr. Ingo Berentzen and Dr. Jonathan Downing for their valuable suggestions while thesis writing. I also extend my thanks to the other proof readers Dr. Andreas Ernst, Dr. Dominik Leier, Dr. Markus Hartmann, Raoul Haschke and Gabriel Stöckle. Without their suggestions and corrections my thesis would not be the way it is.

I am grateful to all our group members Oleksiy Golubov, Dr. Jose Fiestas, Tobias Brandt, Dr. Christoph Olczak, Dr. Isabel Franco, Patrick Brem for interesting discussions. I am also thankful to all the colleagues from the International Max Planck Research School (IMPRS) at Heidelberg for providing nice company during scientific sessions and traveling excursions.

It is indeed a great pleasure to share my office with Dr. Dominik Leier. I thank him for all those scientific, political and religious discussions, although in politics we never manage to converge to a single point of view.

I am thankful to all my friends in Heidelberg, especially Dr. Atif Shahbaz, Malik Majeed, Mateusz Dworaczek, Fabienne Texier and Louise Joksuizes, who made my stay memorable. I greatly appreciate the hospitality, helpfulness and cooperative nature of people here in Germany.

My parents and grandparents deserve special mentioning for their inseparable support and prayers. My Father, Mahmood Khan, in the first place is the person who developed my learning character, showing me the joy of intellectual pursuit ever since I was a child. My Mother, Hameeda Begum, is the one who sincerely raised me with her caring and love. Samia, thanks for being such a supportive and caring sister. Tooba, I am looking forward for your love and company for rest of my life.

Statement of Authorship - Selbständigkeitserklärung

Ich, Fazeel Mahmood Khan, erkläre hiermit, dass ich die vorgelegte Dissertation selbst verfasst und mich dabei keiner anderen als der von mir ausdrücklich bezeichneten Quellen und Hilfen bedient habe.